ALTERING THE WORK FUNCTION OF SURFACES: THE INFLUENTIAL ROLE OF SURFACE MODIFIERS FOR TUNING PROPERTIES OF METALS AND TRANSPARENT CONDUCTING OXIDES

A Thesis
Presented to
The Academic Faculty

by

Anthony J. Giordano

In Partial Fulfillment
of the Requirements for the Degree
Doctor of Philosophy in the
School of Chemistry and Biochemistry

Georgia Institute of Technology
August 2014

ALTERING THE WORK FUNCTION OF SURFACES: THE INFLUENTIAL ROLE OF SURFACE MODIFIERS FOR TUNING PROPERTIES OF METALS AND TRANSPARENT CONDUCTING OXIDES

Approved by:

Dr. Seth R. Marder, Advisor
School of Chemistry and Biochemistry
Georgia Institute of Technology

Dr. Bernard Kippelen
School of Electrical Engineering
Georgia Institute of Technology

Dr. Jean-Luc Brédas
School of Chemistry and Biochemistry
Georgia Institute of Technology

Dr. Elisa Riedo
School of Physics
Georgia Institute of Technology

Dr. Stefan France
School of Chemistry and Biochemistry
Georgia Institute of Technology

Date Approved: April 14, 2014

To my parents and grandparents.

ACKNOWLEDGEMENTS

I wish to thank the many individuals who I had the opportunity to work with and learn from over the course of my Ph.D. First and foremost, I would like to thank my advisor, Dr. Seth Marder for his willingness to allow me to join his research group, for consistently affording me with the tools (both intellectual and instrumental) to complete this process, and for providing guidance along the way. I am also particularly grateful to Dr. Sergio Paniagua, Dr. O'Neil Smith, Dr. Yulia Getmanenko, Dr. Steve Barlow, Dr. Mariacristina Rumi, Dr. Peter Hotchkiss, Dr. Reddy Dasari, and Dr. Timothy Parker for their friendship and wonderful scientific insights. Particular thanks go to Steve for taking the time to edit and discuss this dissertation with me. Over the years the members of the Marder group have been extremely helpful and collaborative with one another and I do not think I could have asked to work on a day-to-day basis with a more welcoming and insightful group of people.

I also wish to thank the many collaborators that I have had the opportunity to work with over the years. Thanks to Dr. Bernard Kippelen for allowing me to conduct research in his lab the summer before finishing my undergraduate degrees as well as the members of his group who were always willing to help teach me new techniques and prepare samples for me, particularly Dr. Canek Fuentes Hernandez, Dr. Yinhua Zhou, Dr. Jae Won Shim, Amir Dindar, Talha Khan, Dr. William Potscavage, and Keith Knauer. Also, big thanks to Dr. Jean-Luc Brédas and the members of his group; Alexander Hyla, Dr. Hong Li, Dr. Paul Winget, and Dr. Chad Risko for providing complex calculations to complement experimental results and continually demonstrating such a collaborative

nature. Thanks to Dr. Elisa Riedo, Dr. Jennifer Curtis, Dr. Keith Carroll, and Dr. Jan Scrimgeour for all their help relating to work on thermochemical nanolithography. I wish to particularly thank Keith for his friendship over the years and for always being willing to work late into the night to try out new ideas or to help me prepare surfaces for TCNL.

I also wish to thank my collaborators from different universities including Dr. Matthew Gliboff, Kristina Knesting and Dr. David Ginger from the University of Washington for all their help with NEXAFS measurements and data processing as well as synchrotron beamline time. Thanks also to the individuals from the University of Arizona that I had the opportunity to work with: Dr. Mariola Macech, Dr. Erin Ratcliff, Dr. Neal Armstrong, Dr. Hsiao-Chu Lin, Yilong Zheng, Dr. Scott Saavedra, Lingzi Sang, and Dr. Jeanne Pemberton.

Thanks also to my fellowships for funding during my Ph.D. work from the National Defense Science and Engineering Graduate Fellowship program and an NSF Graduate Research Fellowship DGE-0644493.

Finally, I am grateful to my parents and my family for their continual support, encouragement, and love throughout my entire life. They truly made this possible.

TABLE OF CONTENTS

ACKNOWLEDGEMENTS iv

LIST OF TABLES xvii

LIST OF FIGURES xxi

LIST OF SYMBOLS AND ABBREVIATIONS xxxix

SUMMARY xliii

CHAPTER 1 INTRODUCTION AND BACKGROUND INFORMATION xliii

1.1 Surface Science 2

1.1.1 The Study of Surface Science – A Historical Perspective 2

1.1.2 The Importance of Surface Cleanliness 4

1.2 Surface Modification with Monolayers 5

1.2.1 A Note about Chemisorption and Physisorption 7

1.2.2 Binding Groups for Monolayer Surface Modification 8

1.2.2.1 Monolayer Terminology and Formation 9

1.2.2.2 Organosulfur Compounds for Surface Modification 11

1.2.2.3 Organosilicon Compounds for Surface Modification 12

1.2.2.4 Carboxylic Acids for Surface Modification 13

1.2.2.5 Phosphonic Acids for Surface Modification 15

1.3 Energy Level Definitions 17

1.4 Analytical Methods for Examining Monolayers 18

1.4.1 Atomic Force Microscopy 19

1.4.2 X-ray Photoelectron Spectroscopy 22

1.4.3 Ultraviolet Photoelectron Spectroscopy 25

1.4.4 Kelvin Probe 27

1.4.5 Infrared Reflection-Absorption Spectroscopy 29

1.4.6 Near Edge X-ray Absorption Fine Structure 32

1.5 Work Function Tuning with Surface Modifiers 37

1.5.1 Applications of Work Function Tuning 38

1.5.2 Work Function Changes Induced by Surface Modifiers 40

1.6 Organization of Thesis and General Overview 41

1.7 References 45

CHAPTER 2 SYNTHESIS AND CHARACTERIZATION OF MOLECULES FOR SURFACE MODIFICATION 57

2.1 General Phosphonic Acid Synthetic Techniques 57

2.1.1 The Michaelis-Arbuzov Reaction 57

2.1.2 Palladium Catalyzed Formation of Phosphonates 58

2.1.3 Formation of Phosphonic Acids by Hydrolysis of Phosphonates 59

2.2 NMR Spectroscopy of Phosphonic Acids 60

2.3 Design and Synthesis of Surface Modifiers 61

2.3.1 Phosphonic Acids for Compatibilization with poly(3-hexylthiophene) (P3HT) . 62

2.3.2 Phosphonic Acids for Use as Gate Dielectrics in Organic Field Effect Transistors (OFETs) 63

2.3.3 Perylene Diimide Surface Modifiers to Probe Charge Transfer 65

2.3.4 Phosphonic Acids for Altering the Work Function and Wettability of Metal Oxides 66

2.3.5 Surface Modifiers for Nanolithography and Crosslinking 68

2.4 Conclusions 71

2.5 Experimental 72

2.5.1 (5-Hexylthiophen-2-yl)methylphosphonic acid 73

2.5.2 (4-Hexylthiophen-2-yl)methylphosphonic acid 74

2.5.3 3-Hexylthiophen-2-ylphosphonic acid 76

2.5.4 Thiophen-2-ylmethylphosphonic acid 78

2.5.5 11-(Perfluorophenoxy)undecylphosphonic acid 79

2.5.6 11-(Perfluorobenzyloxy)undecylphosphonic acid 81

2.5.7 Diethyl (10-((8-hydroxyoctyl)oxy)decyl)phosphonate 83

2.5.8 (10-((8-(Perfluorophenoxy)octyl)oxy)decyl)phosphonic acid 87

2.5.9 (10-((8-((Perfluorophenyl)methoxy)octyl)oxy)decyl)phosphonic acid 89

2.5.10 *N*-(1-Undecyl-dodecyl)-perylene-3,4-dicarboxylicmonoanhydride-9,10-dicarboxylicmonoimide 91

2.5.11 4-(1,3,8,10-Tetraoxo-9-(tricosan-12-yl)-9,10-dihydroanthra[2,1,9-*def*:6,5,10-*d*'*e*'*f*']diisoquinolin-2(1*H*,3*H*,8*H*)-yl)benzoic acid 93

2.5.12 Diethyl (4-aminophenyl)phosphonate 94

2.5.13 (4-(1,3,8,10-Tetraoxo-9-(tricosan-12-yl)-9,10-dihydroanthra[2,1,9-def:6,5,10-d'e'f']diisoquinolin-2(^{1}H,3H,8H)-yl)phenyl)phosphonic acid 95

2.5.14 Diethyl (4-(4,4,5,5-tetramethyl-1,3,2-dioxaborolan-2-yl)phenyl)phosphonate. 97

2.5.15 (4'-(1,3,8,10-Tetraoxo-9-(tricosan-12-yl)-9,10-dihydroanthra[2,1,9-*def*:6,5,10-*d*'*e*'*f*']diisoquinolin-2(1*H*,3*H*,8*H*)-yl)-[1,1'-biphenyl]-4-yl)phosphonic acid 98

2.5.16 Benzylphosphonic acid 100

2.5.17 (2-Fluorobenzyl)phosphonic acid 101

2.5.18 2-(Trifluoromethyl)benzylphosphonic acid 102

2.5.19 3-Fluorobenzylphosphonic acid 103

2.5.20 3-(trifluoromethyl)benzylphosphonic acid 105

2.5.21 3,4-Difluorobenzylphosphonic acid 106

2.5.22 2,3-Difluorobenzylphosphonic acid 107

2.5.23 (4-Fluorobenzyl)phosphonic acid 109

2.5.24 (4-(Trifluoromethyl)benzyl)phosphonic acid 110

2.5.25 (4-Methoxybenzyl)phosphonic acid 111

2.5.26 (2,6-Difluorobenzyl)phosphonic acid 112

2.5.27 (2,6-Bis(trifluoromethyl)benzyl)phosphonic acid 114

2.5.28 (Perfluoro–1,4–phenylene)bis(methylene)diphosphonic acid 116

2.5.29 4-Nitrobenzylphosphonic acid 117

2.5.30 (3,4,5-Trifluorophenyl)phosphonic acid 118

2.5.31 Hydrogen 4-ammoniobenzylphosphonate 119

2.5.32 (4-(Dimethylamino)benzyl)phosphonic acid 120

2.5.33 (1-Cyano-2-(4-(diethylamino)phenyl)vinyl)phosphonic acid 122

2.5.34 4-Cyanophenylphosphonic acid 124

2.5.35 4-Nitrophenylphosphonic acid 125

2.5.36 (4-Bromophenyl)phosphonate 126

2.5.37 Octylphosphonic acid 127

2.5.38 (3,3,4,4,5,5,6,6,7,7,8,8,8-Tridecafluorooctyl)phosphonic acid 128

2.5.39 Dodecylphosphonic acid 129

2.5.40 (3,3,4,4,5,5,6,6,7,7,8,8,9,9,10,10,11,11,12,12,12-Henicosafluorododecyl)phosphonic acid 130

2.5.41 2-(3,5-Dimethoxyphenyl)propan-2-yl 3-(triethoxysilyl)propylcarbamate 131

2.5.42 3-(4-Benzoylphenoxy)propylphosphonic acid 133

2.5.43 4-(3'-Chlorodimethylsilyl)propyloxybenzophenone 133

2.6 References 135

CHAPTER 3 FLUORINATED BENZYL PHOSPHONIC ACIDS ON ITO: EXAMINING THE WORK FUNCTION, COVERAGE, AND ORIENTATION 144

3.1 Transparent Conducting Oxides 144

3.1.1 Indium Tin Oxide 144

3.2 Phosphonic Acid Modification of ITO 145

3.3 Literature Precedents Regarding Analyzing Phosphonic Acid Monolayers 147

3.3.1 Work Function Tuning of ITO and Dipolar Phosphonic Acids 148

3.3.2 Molecular Orientation of Phosphonic Acids 154

3.3.3 Tilt Angle Studies of Phenyl and Alkyl Phosphonic Acids on IZO and ITO.... 157

3.4 Selection of Phosphonic Acid Molecules for Study 159

3.4.1 Comparison of Dipole Moments for Analogous Tolyl Compounds..... 160

3.5 ITO Selection and Surface Modification with Benzyl Phosphonic Acids..... 163

3.6 Coverage Analysis of Benzyl Phosphonic Acids on ITO Using XPS 164

3.6.1 Determination of Correction Factor for Experimental Data 165

3.6.2 Calculation of Coverage – Comparing Experimental Data with Surface Models 166

3.7 Coverage Analysis of Fluorinated Benzyl Phosphonic Acids on ITO 169

3.7.1 Comparison of Monolayer Purity through C 1s Spectra..... 170

3.7.2 Monolayer Purity from F/C Atomic Ratios 173

3.7.3 Phosphonic Acid Coverage on ITO 175

3.8 Work-Function Modification of ITO with Fluorinated Benzyl Phosphonic Acids 180

3.8.1 Experimental UPS Results..... 180

3.8.2 Relating Work Function, Interface Dipole, and Coverage 185

3.8.3 Theoretically Calculated Work Function Changes 187

3.9 Examination of Molecular Ordering of Fluorinated Benzyl Phosphonic Acids... 190

3.9.1 NEXAFS Data Analysis Overview..... 190

3.9.2 Tilt Angles from NEXAFS and DFT Calculations..... 194

3.10 Conclusions 197

3.11 Experimental 200

3.11.1 Materials 200

3.11.2 ITO Surface Cleaning and Modification 200

3.11.3 Surface Characterization 201

3.11.3.1 XPS and UPS 201

3.11.3.2 NEXAFS 202

3.11.3.3 Tapping Mode AFM 204

3.11.4 Theoretical Calculations 205

3.11.4.1 Substituted Toluene Compounds 205

3.11.4.2 DFT Phosphonic Acids on ITO Calculations 206

3.12 References 208

CHAPTER 4 SURFACE MODIFICATION OF ATOMIC LAYER DEPOSITED ZINC OXIDE WITH DIPOLAR PHOPHONIC ACIDS 217

4.1 Zinc Oxide 217

4.1.1 Defects in Zinc Oxide 218

4.2 Atomic Layer Deposition 220

4.2.1 Atomic Layer Deposition of Zinc Oxide 222

4.3 Literature Precedent Regarding Phosphonic Acid Modification of ZnO 223

4.4 Selection of Phosphonic Acids for Modification of ALD ZnO 226

4.5 Comparison of Phosphonic Acid Modification Conditions for ZnO 227

4.5.1 Comparison of Immersion Conditions 227

4.5.1.1 XPS Analysis – Comparison of Immersion Protocols 227

4.5.1.2 Kelvin Probe Analysis 233

4.5.1.2.1 Kelvin Probe - Comparison of Pre- and Post-Modification Conditions 233

4.5.1.2.2 Kelvin Probe - Comparison of Concentration and Modification Time 234

4.5.1.3 IRRAS Analysis of PFBPA and DABPA on ALD ZnO 236

4.5.2 Examination of ZnO Etching by Phosphonic Acids 237

4.5.2.1 Tracking ZnO Etching by AFM Analysis 237

4.5.2.2 Correlation between ZnO Etching and Acidity of Phosphonic Acids (pK_a measurements) 242

4.6 Comparison of Work Function Changes from Phosphonic Acid Modification on ZnO and ITO (Kelvin Probe and UPS) 245

4.7 Spin Coating of Phosphonic Acid Surface Modifiers on ZnO 247

4.8 Conclusions 252

4.9 Experimental 253

4.9.1 Materials 253

4.9.2 ITO and ALD ZnO Film Preparation and Cleaning 253

4.9.3 ALD ZnO Phosphonic Acid Modification 254

4.9.4 Surface Characterization 255

4.9.4.1 XPS and UPS Measurements 255

4.9.4.2 Kelvin Probe 255

4.9.4.3 IR Analysis 256

4.9.4.4 Tapping Mode AFM 256

4.9.5 Determination of pK_a Values 257

4.10 References 258

CHAPTER 5 SURFACE MODIFICATION OF METALS AND METAL OXIDES USING REDOX-ACTIVE ORGANIC AND METAL-ORGANIC COMPOUNDS TO ALTER WORK FUNCTION 265

5.1 Redox Active Dopants to Tailor Work Function 265

5.1.1 Doping of Inorganic and Organic Materials 265

5.1.2 Doping of Inorganic Surfaces by Adsorption 267

5.1.3 Redox-Active Metal-Organic Compounds for Doping 271

5.2 Selection of Dopants for Treatment of ITO, ZnO, and Gold 274

5.3 n-Doping of Metals and Metal Oxides with Metal-Organic Species 277

5.3.1 Surface Treatment 277

5.3.2 XPS Analysis 278

5.3.2.1 XPS Analysis of ITO Treated with $[IrCpCp^*]_2$ 278

5.3.2.2 XPS Analysis of ITO Treated with $[RuMesCp^*]_2$ and $[RhCpCp^*]_2$ 285

5.3.2.3 XPS Analysis of Au and ALD ZnO Treated with $[IrCpCp^*]_2$ 288

5.3.3 UPS Analysis of ITO, ZnO, and Au Treated with n-Dopants 291

5.3.3.1 Work Function Modification by n-Dopants 291

5.3.3.2 Interface Dipole Contribution from Monomer Cation Species on the Surface 294

5.3.3.3 Work Function Stability in Air after Modification 297

5.3.4 Summary of Results for n-Dopants 300

5.4 p-Doping of Metals and Metal Oxides with Organic and Metal-Organic Species 301

5.4.1 Surface Treatment 301

5.4.2 Optimization of ITO Modification Conditions for p-type Materials 302

5.4.3 XPS Analysis of Surfaces Treated with Magic Blue 305

5.4.4 UPS Analysis of Surfaces Treated with Magic Blue 308

5.4.5 Summary of Results for p-Dopants 311

5.5 Conclusions 312

5.6 Experimental 314

5.6.1 Materials 314

5.6.2 Surface Preparation, Cleaning, and Modification 314

5.6.3 Surface Characterization 316

5.6.3.1 XPS and UPS Measurements 316

5.6.3.2 Kelvin Probe 317

5.7 References 318

CHAPTER 6 CONCLUSIONS AND OUTLOOK 324

6.1 References 334

APPENDIX A SURFACE MODIFICATION FOR MONOLAYER THERMOCHCEMICAL NANOLITHOGRAPHY 337

A.1 Overview of Thermochemical Nanolithography 337

A.2 Selection of Protecting Group for Monolayer Based TCNL 340

A.3 Thermal Deprotection of the DDZ Protecting Group 342

A.4 ^{1}H NMR Analysis of DDz Deprotection *via* Heating 343

A.5 ^{13}C NMR Analysis of DDz Deprotection *via* Heating 347

A.6 Analysis of Surface Bound DDz Deprotection 348

A.6.1 IRRAS Analysis 348

A.6.2 Surface Deprotection and Binding 350

A.7 Attempts at TCNL Patterning of DDz Si 353

A.8 Conclusions 356

A.9 Experimental 357

A.9.1 Materials 357

A.9.2 Surface Treatment 357

A.9.3 IRRAS 357

A.9.4 TGA-MS 357

A.9.5 AFM Patterning 358

A.10 References 359

APPENDIX B COVERAGE ANALYSIS – DETERMINATION OF CORRECTION FACTOR FOR EXPERIMENTAL DATA 363

B.1 References 366

LIST OF TABLES

Table 3.1 Summary of literature work function values of various phosphonic acid modifiers on the surface of ITO. The measurement technique PYS measures the photocurrent while irradiating a sample with monochromatic light of variable energy and is detailed in the supplementary information of Lacher.[37] The details regarding LIXPS are given in the supporting information of MacLeod.[39] Work function values provided in red are values where a difference from the bare substrate was reported. 150

Table 3.2 Summary of phosphonic acids for which experimental determinations of molecular tilt angle have been conducted. The substrate being modified, modification conditions, and method used for determining the tilt angle are also provided. Note that PM-ATR is potential-modulated attenuated total reflectance. See footnote for the tilt angle regarding clarification of reference point for tilt angle..... 155

Table 3.3 Summary of phosphonic acid molecules examined by NEXAFS and DFT on the surface of ITO as reported in Gliboff.[49] All values are reported relative to the surface normal and use the angle convention discussed in 3.9.1. Note that no appreciable differences were observed by DFT for the tilt angles of the two phenyl molecules. Differences depending on the binding geometry were noted..... 158

Table 3.4 Atomic ratio of fluorine to carbon of phosphonic acids on the surface of ITO. Shown are the abbreviation for the molecule, the number of fluorine atoms present in the molecule (since all compounds have 7 carbon atoms), the ideal atomic ratio of F/C in the molecule, the atomic ratio given by F 1s/C 1s, and the ratio of experimental F/C to F/C in the compound expressed as a percentage (Monolayer Purity). Experimental atomic ratios are averaged over 3 spots with the given error as the standard deviation of these spots. 174

Table 3.5 Comparison of fluorinated benzyl phosphonic acid coverage values. The molecular footprints given were calculated at the DFT level on surface-bound, geometry optimized phosphonic acids on a slab of ITO. The percent coverage values were obtained from the calculations shown in 3.6.2, and the ideal absolute coverage values obtained using the footprint of the phosphonic acid. The percent coverage values can then be expressed in absolute terms of molecules/cm^2. 176

Table 3.6 DFT level calculations of work function (both calculated WF and WF change relative to that calculated for a bare ITO unit cell) and intrinsic molecular dipole moment of each virtually isolated phosphonic acid in its surface optimized geometry are shown (calculated results courtesy of Alexander Hyla). In this instance coverage values of 2.8×10^{13} molecules/cm^2 were used for the calculations. Shown for reference are the experimentally determined WF values and changes relative to DSC ITO from Figure 3.15. Recall negative dipoles have electron density away from the surface and positive dipoles have electron density closer to the surface. 188

Table 4.1 Summary of phosphonic acids that have been used to modify the surface of ZnO either experimentally or through theoretical calculations as noted. Values for WF are noted when available. Abbreviations for techniques not previously used in this thesis are as follows: transmission electron microscopy (TEM), Fourier transform infrared spectroscopy (FTIR), diffuse reflectance infrared Fourier transform spectroscopy (DRIFT), phosphorus magic angle spinning nuclear magnetic resonance spectroscopy (^{31}P MAS NMR), dynamic light scattering (DLS), thermogravimetric analysis (TGA), quartz crystal microbalance (QCM), scanning electron microscopy (SEM)..... 224

Table 4.2 Summary of modification methods used to treat ALD ZnO. The triethylamine (TEA) wash after modification is commonly used to remove any unbound/physisorbed phosphonic acid molecules from the surface of the substrate 228

Table 4.3 Comparison of RMS roughness values for ZnO modified with the phosphonic acids shown. Concentrations of 1 mM and/or 10 mM are shown depending on the extent of etching observed. In some cases, the RMS roughness value showed minimal changes, while the topography had clearly been altered from that of the bare substrate. Instances where the ZnO experienced severe etching have extremely low roughness values. Standard deviation originates from averaging the RMS values over a t least 3 spots. 242

Table 4.4 Summary of substituted phenyl phosphonic acid pK_a values found in the literature. Values were determined either in pure water or in a mixture of 50:50 ethanol:water (unless otherwise noted). Various references provided[51-53] have more compounds reported than those provided in this table. 243

Table 4.5 Summary of substituted benzyl phosphonic acid pK_a values found in the literature. Values were determined either in pure water or in methanol..... 244

Table 4.6 Summary of pK_a values experimentally determined for phosphonic acids used to modify the surface of ALD ZnO. All measurements were conducted in a solvent system of 75:25 ethanol:H_2O under inert atmosphere. All measurements were conducted at 20 °C using a standardized solution of NaOH at least 3 times with the average and standard deviation reported for both pK_{a1} and pK_{a2}. 245

Table 4.7 Comparison of UPS data for spin-coated phosphonic acid layers on ZnO. Values are the average of 7 spots on each surface. Plasma cleaned ZnO is shown for reference..... 249

Table 5.1 Summary of WF modification by various n-dopant materials thermally evaporated on gold and/or ITO. The substrate used, along with the WF value of the substrate before and after treatment are noted as well as the overall change in WF. 271

Table 5.2 Comparison of $[IrCpCp^*]^+$ coverage on either plasma or detergent solvent cleaned ITO treated with a 2 mM solution of $[IrCpCp^*]_2$ under the conditions shown. The coverage values are expressed in both percent coverage (percent of an ideal monolayer) and absolute coverage (molecules/cm^2). Coverage values obtained from a comparison of Ir/In atomic ratios obtained from XPS data with Ir/In ratio obtained from a theoretical slab of ITO..... 285

Table 5.3 Comparison of coverage values for DSC ITO treated with 2 mM solutions of $[IrCpCp^*]_2$, $[RuMesCp^*]_2$, and $[RhCpCp^*]_2$ for 60 s. The coverage values are expressed in both percent coverage (percent of an ideal monolayer) and absolute coverage (molecules/cm^2). Coverage values obtained from a comparison of M/In (where M = Ir, Ru, or Rh) atomic ratios obtained from XPS data with M/In ratio obtained from a theoretical slab of ITO. 288

Table 5.4 Summary of experimental UPS data shown in Figure 5.14 along with the change in WF after modification. 291

Table 5.5 Comparison of WF values before and after treatment of DSC ITO with $[IrCpCp^*]_2$ (2 mM, 60 s), TDAE (2 mM 60 s), and NaOH (10 M, overnight). Error bar originates from standard deviation over 7 spots on each surface.. 294

Table 5.6 Summary of VBM values shown in Figure 5.15 to obtain changes in VBM (ΔVBM) along with changes in WF (ΔWF), which afford the interface dipole contribution to the shift in WF (ΔWF + ΔVBM)..... 297

Table 5.7 Summary of VBM values for the UPS data of ITO treated with Magic Blue shown in Figure 5.22. The VBM before and after surface modification are provided along with the changes in VBM (ΔVBM) changes in WF (ΔWF), and the interface dipole contribution to the shift in WF (ΔWF + ΔVBM)... 310

Table 5.8 Summary of UPS results showing changes in WF before and after modification, comparing ITO treated with a 2 mM solution of Magic Blue in DCM for 60 s carried out under either inert atmosphere or ambient air..... 311

LIST OF FIGURES

Figure 1.1 Portion of cuneiform writing discussing divination through the art of lecanomancy.[13] This section of the tablet in particular discusses the spreading of oil on water and describes actions that would be taken by Hammurabi's army or outcomes of the sick and dying based on the interaction of these two fluids. Tabor provides a complete translation of this portion of the text in his article.[12] 3

Figure 1.2 General components of a typical monolayer on the surface of a substrate. The three main components of the monolayer are highlighted and their purpose discussed in the text above. This figure was adapted from the literature.[33-34] . 7

Figure 1.3 Cartoon representation of steps that occur during the self-assembly of alkanethiols on a gold substrate: (a) physisorption, (b) lying down phase, (c) nucleation of vertical molecules, and (d) completion of vertical phase. It should be noted that the binding groups in all cases are thiols, with red binding groups indicating chemisorbed molecules and blue representing physisorbed molecules. This figure is adapted from those found in the literature.[46-47] 10

Figure 1.4 Generalized scheme for the reaction of a trialkoxysilane or trichlorosilane containing a spacer and terminal functional group (R) with a substrate terminated with surface hydroxyl groups. Note that the linking group (X) can be either an alkoxy or halogen group. This scheme shows the hydrolysis and condensation reactions that occur in solution as well as those that occur in order to covalently bind with the surface. This figure is adapted from the literature.[56-57] 14

Figure 1.5 Representative examples demonstrating the impact that water content has on the ability of an organosilane to form a high quality monolayer. In this example both chlorosilanes as well as alkoxysilanes are shown. Figure adapted from those found in the literature.[55, 58] 14

Figure 1.6 Mechanism of phosphonic acid binding to Lewis acidic metal oxides (**a**) and poorly Lewis acidic metal oxides (**b**). This figure demonstrates the varieties of binding modes that are possible and outlines what type of reaction is

occurring at each step. This figure was adapted from those in the literature.[77-78, 81] 16

Figure 1.7 Schematic view of an AFM showing the principal components required for operation. Image reproduced from the literature.[86] 20

Figure 1.8 Schematic demonstrating the collection of phase imaging in tapping mode (**a**) and changes in phase oscillation when a probe comes into contact with different portions of the surface (**b**). Image modified from the literature.[86] .. 21

Figure 1.9 Representative examples of AFM topography (left) and phase (right) images showing the features present on a spin coated film of a styrene-butadiene-styrene block copolymer. 22

Figure 1.10 Schematic diagram of a typical XPS instrument (**a**) showing the main components as well as the ability to translate (φ) and tilt (ϑ) the sample relative to the X-ray source along with typical spectra acquired by XPS for some representative elements (**b**). Images are modified from Jacobs.[94] 23

Figure 1.11 Example of peak separation observed in XPS due to non-equivalent atoms. The above is the spectrum of the C 1s peak for pentafluorobenzylphosphonic acid on the surface of ITO. The spectrum shows the presence of two main peaks with the peak originating from the **C-F** bonded atoms at higher binding energy due to the electronegative nature of fluorine, removing electron density from the adjacent carbon and thus decreasing the kinetic energy of electrons removed from the C 1s orbital. Both **C-C** and **C-P** bonds appear at similar binding energies and **carbonaceous** carbon originates from environmental contaminants on the surface. 24

Figure 1.12 Band diagram showing the excitation of a core level electron at an energy of E_{B2} by a photon of energy hν. The electron then travels to the analyzer where it is detected as a peak in the spectrum which is schematically shown to occur at a kinetic energy of E_{K2}. In XPS, the Fermi level is used as the reference point and energy units are commonly shown in Binding Energy (BE) rather than the Kinetic Energy that is directly detected by the analyzer. The bottom equation shows how BE is obtained from the X-ray photon energy (hν), work function of the analyzer ($WF_{analyzer}$) and the excess kinetic energy of the excited electron at the analyzer ($KE_{analyzer}$), which are all expressed with respect to the Fermi level. Image based on XPS explanations by Matolín[95] and Smart.[96] 25

Figure 1.13 Example spectra of bare ZnO obtained from UPS analysis with important features noted. Both the work function (ϕ) and valence band maximum (E_{VBM}) are directly determined from the spectra as shown; ϕ = (He I Source Energy) – (Secondary Electron Edge) and E_{VBM} = (Valence Band Maximum) - E_F. The intensity of the Secondary Electron Edge comes from inelastically scattered electrons that have escaped to vacuum, but lost energy in the process..... 27

Figure 1.14 Schematic diagram for the principle of KP. Two materials with different WFs (**a**) are brought into contact with one another (**b**) causing Fermi level alignment. A nulling potential is applied and at the charge free point the nulling potential is equivalent to the CPD (**c**). Image adapted from Subrahmanyam[100] and Schlaf.[102] 29

Figure 1.15 Schematic showing the external reflection method used in IRRAS of a generic monolayer deposited on a highly reflective gold substrate. The angle of incidence relative to the surface normal, θ, is typically 80°. Image adapted from Brune.[85] 31

Figure 1.16 IRRAS spectra of octradecylphosphonic acid modified ZnO[106] (left) and ITO[79] (right). In the case of the ITO surface the top spectrum is the powder form of the phosphonic acid while the lower spectrum was collected by IRRAS. The inset for both ZnO and ITO highlight the C-H vibrational regions..... 32

Figure 1.17 Two common measurement modes for NEXAFS, transmission (left) and electron yield (center). In transmission mode the intensity is dependent on the thickness of the sample being used (*t*), and in electron yield the intensity is dependent on the sampling depth (inelastic mean free path) of the X-rays (*L*). Image adapted from Stöhr.[107] 33

Figure 1.18 Comparison of XPS (left) and NEXAFS (right) spectra for a generic polymer containing carbon, oxygen, nitrogen, and fluorine. Peaks labelled on the bottom of the XPS data are Auger peaks and originate from Auger electrons as discussed below (image reproduced from literature).[107] Note the energy scale for XPS is in kinetic energy while the scale for NEXAFS is in photon energy..... 34

Figure 1.19 Schematic energy diagram for the absorption of an X-ray by a sample and the subsequent radiative and non-radiative decay processes that can occur when the resulting hole is filled. When the hole is filled radiatively there is a resulting fluorescence observed and when the hole is filled non-radiatively there is the emission of an Auger electron. In the case of low molecular weight molecules (such as surface modifiers) the Auger electron yield far surpasses that of the fluorescence yield.[109] 35

Figure 1.20 Example of the angular dependence of NEXAFS data due to the use of a polarized synchrotron light source for the case of benzene on silver. The benzene molecular orbitals have π-orbitals that are out of plane of the ring and σ-orbitals that are in the same plane as the benzene ring (left). Experimentally, when the X-ray electric field vector is parallel to these molecular orbitals they are selectively excited as observed in the resulting spectra. Sweeping over a range of angles allows for the determination of molecular orientations on the surface.[107] 36

Figure 1.21 Experimental NEXAFS data for phenylphosphonic acid on the surface of IZO collected at angles between 20° and 90° (left). The molecules on the right schematically demonstrate the angular dependence of the orbitals being excited based on the incident angle of the X-ray source. As can be readily observed, as the angle of incidence increases from 20° to 90° the intensity of the π*-transition also drastically increases. Image modified from Gliboff.[110] 37

Figure 1.22 Image showing band diagrams for an ITO electrode and a generic hole transporting layer before contact, with a barrier to hole injection into the HTL given as ΔE_{hole} (left). When the two materials are in contact the Fermi levels align with one another (center). The barrier to hole injection after contact (ΔE_{hole}) is still rather large. A surface modifier with a dipole (such as a phosphonic acid) is used to modify the surface of the ITO (right). The modified ITO and HTL surfaces are now brought into contact with one another and because the WF of the ITO has been increased by the modifier, the barrier to hole injection has been greatly diminished. Image adapted from Hotchkiss.[78] 39

Figure 2.1 Mechanism of the Arbuzov reaction using an alkylbromide and triethylphosphite. The product of the reaction is the desired phosphonate and a volatile side product such as ethylbromide in this case. 58

Figure 2.2 Hydrolysis mechanism for the formation of a phosphonic acid from a diethylphosphonate through the use of bromotrimethylsilane. 60

Figure 2.3 Thiophene based phosphonic acids designed for compatibilization and infiltration of P3HT with nanoporous titania. Note that new compounds are denoted in blue. 63

Figure 2.4 Phosphonic acids synthesized for use as a monolayer gate dielectric in OFET devices, consisting of a long alkyl chain to serve as a dielectric layer and fluorinated aryl termination for favorable interactions with aromatic overlayers. Note that new compounds are denoted in blue. 64

Figure 2.5 Perylene diimide phosphonic acid and carboxylic acid surface modifiers used to probe charge transfer on the surface of transparent conducting oxides..... 66

Figure 2.6 Aryl, alkyl, benzyl, and fluoroalkyl phosphonic acids synthesized for the purpose of altering the WF of metal oxides and enhancing wettability of organic overlayers on the modified surfaces. Note that new compounds are denoted in blue. 68

Figure 2.7 Summary of molecules synthesized for use in Thermochemical Nanolithography (alkoxysilane) and covalently binding polymer materials to the surface of a substrate (chlorosilane and phosphonic acid). 69

Figure 2.8 General scheme for the crosslinking of a generic polymer chain to the surface of a metal oxide upon exposure of a benzophenone phosphonic acid to irradiation. The same principle is also true in the case of the chlorosilane, only the substrate (silica or silicon in this case) would be different. 70

Figure 2.9 Expected decomposition products upon heating the alkoxkysilane containing the DDz protecting group..... 71

Figure 3.1 Schematic energy-band diagram for ITO films. The valence band originates from the O 2p orbitals with the In 5s orbitals making up the conduction band. The In 3d band is also shown for reference and it lies below that of the O 2p. V_O symbolizes oxygen vacancies, which already have a low barrier to conduction. The addition of tin doping adds additional donor levels. Image adapted from the literature.[1] 145

Figure 3.2 Schematic representation of tethering by aggregation and growth. Image adapted from the literature.[23] 147

Figure 3.3 Schematic representation of phosphonic acids with molecular dipoles pointing toward and away from the surface (top). Shown is a generalized variation in the electrostatic potential caused by the dipole present in the phosphonic acid between the surface of the solid and vacuum. Electrostatic potentials adapted from Appleyard.[32-33] 149

Figure 3.4 Summary of benzyl phosphonic acids used throughout the study along with the abbreviations for each molecule that will be used throughout the chapter… 160

Figure 3.5 Calculated dipole moments for analogous substituted toluene derivatives as calculated from Spartan. Note that the dipole moments in red correspond to the value for the vector shown with each compound. The values in blue correspond to the magnitude of the projection of the dipole moment onto the C1 – C4 axis in the molecule. This axis is explicitly labelled for the first row and follows the sign convention outlined below..... 162

Figure 3.6 Dipole moment convention used for tolyl compounds and phosphonic acids throughout this chapter. Note that the sign convention follows the dipole sign farthest away from the surface. That is the negative end points away from the surface then there is a negative dipole moment and when the positive end points away from the surface, a positive dipole moment is obtained. 163

Figure 3.7 Comparison of ITO used in this study (supersmooth ITO) with more commonly used "rough" ITO (Colorado Concepts). The top images are both 5 micron scales and the bottom image is a 1 micron area of the supersmooth ITO obtained directly from the center of the 5 micron image. 165

Figure 3.8 (Left) Bulk In_2O_3 unit cell with the (222) plane highlighted. (Right) Top view of hydroxyl terminated ITO (222) surface slab as optimized by DFT level of computation. The unit cell is indicated by the boundary box. Tin substitutions were randomly distributed over cationic positions in the slab. The unshaded polyhedral indicate chemically active surface sites including under-coordinated metal ions and surface hydroxyl groups. Image modified from the literature.[71] 168

Figure 3.9 Comparison of XPS survey spectra for DSC followed by plasma, DSC, DSC followed by plasma cleaning and immersion in ethanol, and PFBPA modified ITO. The core level peaks have been labelled for convenience. Note the lack of fluorine in the spectra without the phosphonic acid and the drastic changes observed in the carbon peak intensity. Note spectra have been normalized and offset for clarity..... 170

Figure 3.10 Comparison of C 1s peaks for 2-CF3BPA, 3-CF3BPA, and 4-CF3BPA. Spectra have been normalized and offset for clarity. Note the drastic difference in intensity for the CF_3-Ph peak between the 2-CF3BPA and 2,6-CF3BPA compared with both 3-CF3BPA and 4-CF3BPA. 172

Figure 3.11 Comparison of C 1s peaks for 2-FBPA, 3-FBPA, 4-FBPA, and 2,6-F2BPA. Spectra have been normalized and offset for clarity. As opposed to what was observed in Figure 3.10 similar spectral features are observed for all three of the monosubstituted phosphonic acids..... 173

Figure 3.12 Visual comparison of molecular footprint for each phosphonic acid on ITO ordered in increasing size from left to right, top to bottom. The red background box serves as a reference point to the phosphonic acid with the largest footprint, 2,6-CF3BPA and the blue box shows the size of each phosphonic acid in relation to this reference point. 177

Figure 3.13 Visual comparison of absolute coverage for each phosphonic acid on ITO ordered in increasing coverage from left to right, top to bottom. The molecular footprints from Figure 3.12 to show the relationship between coverage and footprint, with the smallest coverage being 2,6-CF3BPA. 177

Figure 3.14 Graph comparing the absolute coverage values for monosubstitued fluoro and trifluoromethyl benzyl phosphonic acids as a function of substitution position. 179

Figure 3.15 Comparison of experimental UPS data for the modified and control surfaces. Shown at left are the SEE spectra with the corresponding WF value shown in the table to the right. Values are obtained from an average of at least 5 spots on each substrate and standard deviation is the variation in WF from spot to spot. Graphs have been normalized and offset for clarity. Note that the graphs and table are ordered in increasing WF value, bottom to top and the dashed lines represent the extreme values to highlight the differences in SEE values. 181

Figure 3.16 Comparison of experimental VBM data for the modified and control surfaces. Shown at the left are the UPS spectra highlighting the VBM region and the corresponding numerical values are provided in the table to the right. Values are obtained from an average of at least 5 spots on each substrate and standard deviation is the variation in WF from spot to spot. Graphs have been normalized, offset and match the ordering of Figure 3.15 for clarity. The dashed lines represent the extreme values of 3,5-F2BPA and ethanol soaked ITO to highlight differences in VBM. 182

Figure 3.17 Energy-level diagram comparing the WF and VBM of different surfaces and modifiers with respect to DSC ITO. Data shown was collected by UPS. Both ΔWF and ΔVBM show the change occurring relative to DSC ITO. The interface dipole contribution originates from the sum of the change in WF and the change in VBM. Fermi levels are aligned. It should be noted that ITO is a degenerate n-doped semiconductor that has its Fermi level inside of the conduction band within the bulk,[1] however, the electrons that are detected by UPS originate from less than 1 nm below the surface.[5] In this regime, the Fermi level is below that of the conduction band and the conduction band is not shown in this diagram as UPS data does not provide information regarding its position. All values are reported in eV..... 184

Figure 3.18 3-dimensional plot comparing WF values from UPS (*x*), with absolute coverage (*y*), and the contribution of the interface dipole to the WF change (*z*). Data points are labelled according to colors and are consistent with the color convention for the UPS data shown in 3.8.1..... 186

Figure 3.19 3-dimensional plot comparing WF values from UPS (*x*), with absolute coverage (*y*), and the shift in VBM relative to DSC ITO (*z*). Data points are labelled according to colors and are consistent with the color convention for UPS data shown in 3.8.1..... 186

Figure 3.20 ITO unit cell utilized in DFT calculations showing side (left) and top-down (right) views of BPA bound to the surface of the ITO. Shown are the four binding sites that were used in the calculations. Image courtesy of Alexander Hyla..... 187

Figure 3.21 Comparison of change in WF values relative to DSC ITO for UPS and bare ITO for DFT, as determined by DFT calculations and by UPS experimental data as a function of calculated dipole moment for each phosphonic acid. The

overall trends between experiment and theory are quite good. Error bar for UPS data originates from standard deviation over multiple spots analyzed and highlighted data points correspond to those discussed in the text above..... 190

Figure 3.22 Generic phosphonic acids on the surface of ITO. Phenyl, alkyl, and benzyl phosphonic acids are shown to illustrate the differences in how the angle α is measured. Incident X-rays strike the surface at an angle θ. The angle α is formed between the transition dipole moment and the surface normal. In the case of the alkyl phosphonic acid, the transition dipole moment is along the axis of the chain, but in the case of phenyl and benzyl phosphonic acids this dipole is normal to the benzene ring. Thus, the angle reported is that of the benzene ring with respect to the surface normal. Note that benzyl phosphonic acids have an extra degree of rotational freedom (φ) that is not present in phenyl phosphonic acids. Image courtesy of Matthew Gliboff. 192

Figure 3.23 Carbon edge NEXAFS TEY spectra for BPA and PFBPA. Phenyl phosphonic acid (PPA) is shown for reference since that tilt angle has been previously determined.[49] All spectra were acquired at an incidence angle of 55°. Note the large decrease in the C=C π^* feature for PFBPA relative to BPA and PPA, and the prominent C-F σ^* transition. Image courtesy of Matthew Gliboff..... 192

Figure 3.24 Results of the angle α for benzyl phosphonic acids on the surface of ITO as obtained experimentally from NEXAFS data compared with the results calculated at the DFT level of theory. The magic angle (54.7°) is also highlighted since at values of α close to this angle the tilt angle of the molecules is indistinguishable from random orientations. At this tilt angle, the angle of incidence of the source X-ray radiation no longer impacts the intensity of the observed transitions.[74] NEXAFS data courtesy Matthew Gliboff and DFT data courtesy Alexander Hyla. 195

Figure 3.25 Summary of tilt angles obtained from theory for BPA and PFBPA at different sites on the unit cell of ITO and at different coverage concentrations. Data points in black correspond to a coverage of 2.8×10^{13} molecules/cm^2 while those in red correspond to 1.1×10^{14} molecules/cm^2. Binding sites correlate with those shown in Figure 3.20. Data courtesy of Alexander Hyla. 197

Figure 3.26 3-dimensional plot showing the relationship of experimentally determined values for changes in the WF of ITO (x) based on the substitution of the benzene ring, and how this relates to the absolute coverage (y) and orientation

(*z*) of the modifier on the surface of ITO. Blue drops lines were added to better aid in observing coverage values on the plot. 200

Figure 4.1 Position of Zn and O atoms in the ZnO würtzite crystal lattice. Figure has been adapted.[24] 219

Figure 4.2 Schematic band diagram for energy levels of intrinsic defects present within ZnO. The Zn_i and V_O states are donors and the V_{Zn} states are acceptors. Figure adapted from those found in the literature.[22, 25] 220

Figure 4.3 Schematic representation of a complete ALD cycle for the deposition of ZnO starting from diethyl zinc and water with ethane gas as a side product. A bare substrate is introduced into the ALD chamber, a precursor gas (diethyl zinc) is subsequently introduced, the chamber is purged. Water is then introduced reacting with the diethyl zinc, the chamber is purged again leaving behind solid zinc oxide. The cycle is then repeated *n* times until the desired thickness is achieved. 221

Figure 4.4 Phosphonic acids chosen for the modification of ZnO and ITO. The focus was on the use of phosphonic acids containing molecular dipoles that would be anticipated to create a decrease in the WF of the surface (2,6-F2BPA, 2,6-CF3BPA, ABPA, DABPA, DMABPA, MeOBPA) along with molecules that would also increase the WF as a control (NO2BPA and PFBPA). 227

Figure 4.5 Comparison of F 1s/C 1s atomic ratios for the modification methods outlined in Table 4.2 for 2,6-F2BPA and 2,6-CF3BPA. Methods 4 and 5 do not have atomic ratios given as the method etched away ZnO from the underlying substrate leaving glass behind. The expected ratios originate from the F/C ratio found in the individual molecules. 230

Figure 4.6 XPS survey spectra for freshly plasma cleaned ZnO and the surface after 2,6-F2BPA had etched away the majority of ZnO. Data for this comparison was acquired using modification technique 4 and while there are small peaks left for Zn (and loss of Zn Auger peaks) the vast majority has been etched away leaving behind a small amount of phosphonic acid (evidenced by F 1s peak) and exposing the underlying glass substrate (Na 1s peak). Spectra have been normalized and offset for clarity. 231

Figure 4.7 Comparison of tapping-mode AFM images of ALD ZnO (left) and smooth ITO (right). In both cases 5 μm × 5 μm images are shown at the top and 1 μm × 1 μm are shown at the bottom with values for RMS roughness also provided. Note the differences in the height scales between the two substrates, which was necessary so as to not obscure all of the topographic features present on the ITO samples. 232

Figure 4.8 Comparison of KP data showing WF changes relative to a bare ZnO substrate after modification. In this instance, method 3 from Table 4.2 was used for the modification meaning that the substrates were soaked in 10 mM phosphonic acid solutions overnight (either with or without a plasma pre-treatment) and then subsequently either washed with TEA or not post-modification. WF values are the average of at least 5 spots on each substrate. An HOPG substrate was referenced and measured multiple times over the course of data collection to ensure instrumental consistency over the time scale of the experiment. 234

Figure 4.9 Comparison of three phosphonic acid modifiers examined under low/high concentration (1/10 mM) and short/long modification times (24/48 h). In the case of the 10 mM, 48 h modification for 2,6-F2BPA complete etching of ZnO was observed. Duplicate samples were analyzed to demonstrate the variability observed in WF changes, particularly at higher concentrations/longer modification times. 235

Figure 4.10 Comparison of transmission IR of PFBPA and DABPA powders (left) with the IRRAS data collected for ALD ZnO deposited on a gold surface for enhanced reflectivity and modified with either PFBPA or DABPA (right). Spectral features are highlighted and labelled in both cases. 237

Figure 4.11 Comparison of AFM images at spot sizes of 1 μm × 1 μm and 5 μm × 5 μm for bare, plasma cleaned, and 10 mM phosphonic acid modified ALD ZnO. When possible, vertical scales were attempted to be maintained constant within a given image size (1 μm or 5 μm). 240

Figure 4.12 Comparison of AFM images of spot sizes 1 μm × 1 μm (left) and 5 μm × 5 μm (right) for bare, plasma cleaned, and 1 mM phosphonic acid modified ALD ZnO. When possible, vertical scales were attempted to be maintained constant within a given image size (1 μm or 5 μm) and with those images shown in Figure 4.11.[32] 241

Figure 4.13 Comparison of WF values for phosphonic acid modified ITO and ZnO. All surfaces were modified using 10 mM solutions of phosphonic acid overnight, followed by a bake at 140 °C and a rinse with a solution of 5 % TEA in ethanol. Etching was not observed for these surfaces of ZnO. UPS data (left) is the average over 7 spots on each surface and KP data (right) originates from the average of 5 spots on each surface. The same surfaces were used during the measurements, first measuring with KP then by UPS. 247

Figure 4.14 AFM comparison of ZnO before (top) and after (center) spin-coating a 10 mM solution of 2,6-F2BPA on the surface. Subsequent washing with an ethanolic solution of TEA does seem to remove the multilayers (bottom), but affords irregular WF values. Scan sizes of 1 μm × 1 μm (left) and 5 μm × 5 μm (right) were obtained and the RMS roughness values (averaged over 3 spots on each surface) are also provided..... 250

Figure 4.15 XPS survey comparison of ZnO before and after spin-coating 2,6-F2BPA as well as after washing with a solution of TEA. Note the near loss of Zn Auger peaks after the spin coating stop and the presence of the large P2s peak, which then decreases after the TEA wash, but is still far more apparent than in a typical monolayer of phosphonic acid. 251

Figure 5.1 Schematic band diagram of doping in a semiconductor, showing the case of an intrinsic semiconductor (e.g. silicon) without any impurities (undoped, left), with donor impurities (n-doped, e.g. phosphorus, center), and with acceptor impurities (p-doped, e.g. boron, right). Image adapted from Sze.[4]..... 266

Figure 5.2 Examples of p- (top) and n- (bottom) dopants that have been used to treat the surfaces of various types of substrates including metals, metal oxides, and graphene. Also provided are the abbreviations used throughout the text. ... 269

Figure 5.3 Redox-active metal-organic species recently examined by the Marder group for p- (top) and n-doping (bottom).[8-9, 33-34] 272

Figure 5.4 The two mechanisms by which electron transfer occurs using $[RhCpCp^*]_2$ as an example. The first step can either be the dissociation of the dimer (mechanism I) or electron transfer from the dimer to the acceptor (mechanism II). Mechanisms adapted from Guo.[8, 35] 273

Figure 5.5 Summary of p- and n-dopants that were used in the treatment of ITO, ZnO, and gold surfaces. Abbreviations for these materials are also provided. 275

Figure 5.6 Electrochemical potentials for materials investigated in this chapter as well as for materials previously used in the literature to treat surfaces. The solvent in which the electrochemical data was collected is noted. In the case of the n-type dimer materials, the oxidation of the dimer $[M]_2$ and the more reactive monomer $[M^+/M]$ are shown. Also shown is the thermodynamic estimate of doping strength, $E_{eff}(M^+/0.5M_2)$, as afforded from Equation **3.3** based on electrochemical data and DFT calculations (two values are reported for $[IrCpCp^*]_2$ as the dominant isomer and the minor isomer afford slightly different values for both dimer oxidation and effective oxidation.[38] In the case of p-type materials, only first reduction potentials are reported. All potentials reported are *vs.* the ferrocenium/ferrocene (Fc^+/Fc) couple. References for data are as follows: $[RuMesCp^*]_2$,[8, 35] $[RhCpCp^*]_2$,[35] MV0,[39] TDAE,[40-41] $Mo(tfd)_3$,[33] $Mo(tfa\text{-}tf)_3$,[42] Magic Blue,[43] F_4-TCNQ.[33, 44] 276

Figure 5.7 Comparison of survey spectra obtained by XPS. Spectra shown are for an ITO sample that was initially detergent solvent cleaned and subsequently immersed in a 2 mM solution of $[IrCpCp^*]_2$ in anhydrous toluene for 1 h. Important core ionizations are labeled. Spectra have been normalized and offset for clarity..... 279

Figure 5.8 Comparison of high-resolution spectra obtained by XPS in the region where Ir 4f ionizations typically occur. These high resolution spectra correspond to the same sample used to obtain Figure 5.7. Note that there is no Ir present on the surface of ITO prior to treatment with $[IrCpCp^*]_2$. Spectra have been normalized..... 280

Figure 5.9 XPS high-resolution Ir 4f spectra (shown are the Ir $4f_{5/2}$ and $4f_{7/2}$ peaks) comparing DSC ITO that was treated for either 60 s or 1 h with a 2 mM solution of $[IrCpCp^*]_2$ in anhydrous toluene. Also shown is a DSC ITO sample onto which was drop-cast a thick film of $[IrCpCp^*]_2$ from a concentrated solution in anhydrous toluene. There is good agreement between the high binding energy shoulders present in the thick film, correspond with what is observed for the solution soaked samples, thereby indicating the presence of monomer cation on the surface after treatment. The structure of $[IrCpCp^*]_2$ and its monomer cation form are also shown, and the labeled oxidation states color coded to correspond with the structures shown (inset). Spectra have been normalized. 281

Figure 5.10 Monomer cation of $[IrCpCp^*]_2$ as a space-filling model in a close-packed geometry (represented by the red line). The radius of the molecule is shown in yellow and the centroid-to-centroid distance is shown in peach. The area formed by the light green shaded rhombus best represents the molecular footprint, taking into account the hexagonal packing that is shown. 284

Figure 5.11 XPS survey spectra for DSC ITO and ITO after treatment in 2 mM solutions of $[RuMesCp^*]_2$ and $[RhCpCp^*]_2$ for 60 s or 10 s, respectively. Note in the case of the Ru dopant, the Ru 3d peak occurs in the same area as the peak originating from C 1s. Also note that in the case of the Rh dopant, there are peaks originating from Si 2s and Si 2p (~150 and 100 eV, respectively). These peaks originate from contamination due to the antechamber of the glovebox (silicon oil) and was how (as mentioned previously) it was determined substrates should not be directly exposed to the antechamber of a glove box. 286

Figure 5.12 High resolution spectra acquired by XPS after DSC ITO was treated with the Ru (**A**) and Rh (**B**) dimers. The respective dimer and monomer cations are shown below the spectral data for each dopant. In the case of the Ru dopant, no oxidation state change occurs when going from the dimer to the cation form. Also it should be noted that only the Ru $3d_{5/2}$ peak is visible since the Ru $3d_{3/2}$ peak overlaps with the C 1s peak. In the case of the Rh dimer, both the dimer as Rh (I) and the cation as Rh (III) are present on the surface, which is consistent with what was observed with this dopant on graphene.[37] 287

Figure 5.13 Comparison of survey and high-resolution Ir 4f spectra from XPS analysis for Au (**A** and **C**) and ZnO (**B** and **D**) after treatment with $[IrCpCp^*]_2$ (2 mM in anhydrous toluene for 60 s). In the case of the Au substrate the Ir 4f peak occurs at the tail of the Au 5p and the onset of the Au 4f peak making reliable quantification difficult. For both the Au and ZnO treated surfaces, the Ir present appears to originate only from the Ir (III) oxidation state, indicating the presence of monomer cation on the surface. Survey spectra have been normalized, offset, and core ionizations labeled for clarity. 290

Figure 5.14 Comparison of WF values for ITO, ZnO, and gold with the noted n-dopants. All samples were treated for 60 s in the solution of the dopant unless otherwise noted on the graph. Cleaning protocols included detergent solvent cleaning or plasma cleaning for ITO, rinsing with ethanol for ZnO, and piranha cleaning for the gold surface. Substrates were examined in a minimum of 7 spots to ensure consistency of the data over the whole surface. Red data points indicate a measurement after modification and black data

points indicate measurements prior to modification. Different shapes correspond to different substrate types as shown in the legend. 292

Figure 5.15 Valence band maximum values for ITO and ZnO surfaces before and after treatment under the noted modification conditions. Values shown are with respect to the Fermi level. As gold is a metal it has no clear VBM, only a Fermi level step, and thus no shift was observed. 296

Figure 5.16 Summary of WF shifts for ITO and ZnO surfaces that were treated with $[IrCpCp^*]_2$ and subsequently exposed to atmosphere for 5 min, 2 h, 16 h, and 72 h. WF was tracked *via* UPS analysis and when samples were not being exposed to atmosphere the substrates were stored under vacuum. Each data point originates from the average and standard deviation of 7 spots on the surface. 299

Figure 5.17 Comparison of Ir 4f peaks for a drop-cast film of the dimer on ITO, a solution soaked sample of ITO immediately after treatment without exposure to air, and after varying amounts of time exposed to atmospheric conditions. The vertical dashed lines serve as guides to show the subtle difference in binding energy observed for the Ir 4f peak position after treatment and after air exposure. Graphs have been normalized and vertically offset for clarity. 300

Figure 5.18 Comparison of WF values obtained from different modification conditions of ITO using solutions of Magic Blue in DCM. All data was collected using KP, with the error bar originating from the average of at least 5 spots on each surface. All data is referenced to freshly cleaved HOPG surfaces and show WF changes relative to that reference point. Modification conditions examined include different concentrations (**A**) all treated for 10 min, different modification times using 2 mM (**B**) and 8.7 mM (**C**) solutions of Magic Blue in DCM, and examining the impact of concentration, time, and modification temperature (**D**) with samples modified at 25 °C in blue and those modified at 40 °C in red. A freshly DSC ITO sample is provided for each set of measurements. Samples in (**D**) were prepared outside of the glove box. 303

Figure 5.19 Summary of KP data for 2 mM solutions of $Mo(tfa\text{-}tf)_3$ in solutions of toluene or DCM for varying amounts of time. Data originates from the average of at least 5 spots on each surface with the error bar from the standard deviation of these measurements. Values shown are relative to freshly cleaved HOPG and all samples were kept under inert atmosphere until just before measurement by KP. 305

Figure 5.20 Comparison of survey spectra for a thick film of Magic Blue drop-cast on the surface of ITO, a DSC ITO sample, and ITO after treatment with low and high concentrations of Magic Blue for either 60 s or 1 h. Spectra have been normalized, offset, and important ionizations labeled for clarity. 307

Figure 5.21 Comparison of high-resolution XPS data for the In $3d_{5/2}$ peaks of surfaces before and after modification with Magic Blue. The color coded dashed lines indicate the position of the peak, which does not change after modification with Magic Blue. 308

Figure 5.22 Comparison of WF for DSC ITO treated with solutions of Magic Blue in DCM at either 2 mM for 60 s or 8.7 mM for 1 h (left). The numerical values obtained from the average of 7 spots on each surface are also provided (right) with the error bar originating from the standard deviation among these spots. Note the trend to observe a higher WF value for the more concentrated solution at longer modification times. Spectra have been normalized and the onset of the secondary electron edge is denoted by the color coded vertical line intersecting the *x*-axis. 309

Figure 6.1 Compilation of work function data for phosphonic acids synthesized in the Marder group and used at a variety of institutions for the modification of multiple metal oxide surfaces. Data presented is a compilation of KP, UPS, and LIXPS WF measurements with the most representative value shown for phosphonic acids on a given metal oxide measured using multiple techniques. The data shown here originates from a variety of sources including this thesis, unpublished results by this author, and published sources as well.[1-10] Note that the dashed lines represent the WF of the bare substrate. 326

Figure A.1 Schematic representation of thermochemical nanolithography using a polymer containing a THP carbamate protecting group. The resistively heated AFM tip serves to perform the desired chemical deprotection, which exposes the desired functionality on the surface (in this case a primary amine) so that other materials (such as nanoparticles, small molecules, cells, etc.) can be attached at these newly formed binding sites. Note that the use of the chlorosilane benzophenone is to form a covalent linkage between the surface and the polymer layer to avoid delamination in subsequent processing steps. 339

Figure A.2 Complex patterns generated using TCNL in the case of (a) (left) the original image of the Mona Lisa is shown with the experimental rendition (right) of the same image reproduced at a size of ~32 μm through the use of TCNL and subsequent binding of NHS-DyLight 633 to the surface. (b) (Left) Original image by Ansel Adams entitled "Rose and Driftwood" and the TCNL reproduction of the image (right). In both cases the scale bar is 10 μm. Image has been reproduced from the literature.[25] 340

Figure A.3 Structure of monolayer for surface modification (top) and schematic of surface deprotection through the use of an AFM tip and applied bias (bottom). The molecule undergoes a heterolytic bond cleaveage (a) followed by the release of carbon dioxide and 3,5-dimethoxy-α-methylstyrene (b), which yields a primary amine. Image modified from the literature. [28] 341

Figure A.4 Structure of silane utilized throughout the monolayer TCNL studies (DDzSi) along with the expected products from a thermal decomposition of the material. 342

Figure A.5 TGA under inert atmosphere (blue trace) of DDzSi overlaid with the derivative TGA graph (green trace). The detector intensity of the mass spectrometer (red trace) is for CO_2 and corresponds well with the derivative TGA. 343

Figure A.6 Comparison of ^{1}H NMR spectra for heating of DDz Si at various temperatures as indicated below the figure. Note the inset shows the aromatic region of the spectrum (top) and the alkyl region (bottom). All spectra were obtained on a Varian 400 MHz NMR in $CDCl_3$ utilizing the residual solvent peak for reference at 7.26 ppm. 344

Figure A.7 Enlarged aromatic ^{1}H region for 200 °C DDz Si sample. 345

Figure A.8 Overlay of ^{1}H NMR spectra of DDz Si at room temperature (blue) and heated to 200 °C (red). The peaks of interest are highlighted with the color corresponding to the molecule provided in the image. 346

Figure A.9 ^{13}C NMR comparison of DDz Si at room temperature (top) and after heating to 200 °C for 8-10 minutes. The peak assignments are based on literature values for the molecules in question. 348

Figure A.10 Comparison of KBr pellet of DDz Si and IRRAS spectrum of the modified Glass:Ti:Au:SiOx:Silane surface. Note that the IRRAS spectrum was obtained utilizing 2000 scans, reference to an unmodified substrate, water was subtracted from the spectrum, and the baseline corrected. 350

Figure A.11 (Top) Experimental scheme for examining the deprotection of DDzSi on the surface of a glass slide. APTES modified surface served as the control, and the structure of FITC after attachment to the surface bound amine is shown. (center) Absorbance as a function of the amount of time DDzSi modified and FITC treated slides were heated. Note the lack of signal without heating and the decrease with extended heating. (Bottom, right) Absorbance of APTES modified and FITC treated slides as a control. 352

Figure A.12 Topography and phase images before (left) and after (right) patterning using the template shown at right. Note that triangles appear to form at lower voltages and at higher voltages, but is more spread out after patterning at higher voltages. The scales are in nm for topography and mV for friction. . 354

Figure A.13 (Top) Contact and tapping mode AFM images after patterning of a DDzSi modified silica sample with streptavidin. Shapes are visible in the friction image above approximately 14 V, which may be indicative of the onset of deprotection. The phase image, however, does not corroborate the friction image if streptavidin had bound to the patterned areas. (Bottom) Desired patterns programmed to vary tip temperature at the surface..... 355

Figure B.1 Graph showing the probability of detection of an electron in XPS analysis as a function of analysis depth in units of inelastic mean free paths (λ)..... 363

Figure B.2 Graphical representation for the origin of the correction factor to account for signal attenuation in experimental XPS data. The red curve is the same signal decay shown in Figure B.1 and the dotted blue line is the ideal case where no attenuation occurs. The ratio of these two areas provides the desired correction factor. 365

LIST OF SYMBOLS AND ABBREVIATIONS

^{31}P MAS	Phosphorous magic angle spinning
NMR	Nuclear magnetic resonance spectroscopy
AEY	Auger electron yield
AFM	Atomic Force Microscopy
ALD	Atomic layer deposition
AOB	Acridine orange base
APTES	Aminopropyl triethoxy silane
CB	Conduction Band
CMA	Cylindrical mirror analyzer
CPD	Contact potential difference
CVD	Chemical vapor deposition
DCM	Dichloromethane
DDZ	α,α-dimethyl-3,5-dimethoxybenzyloxycarbonyl
DFT	Density functional theory
DLS	Dynamic light scattering
DSC	Detergent solvent cleaned
EA	Electron affinity
EF	Fermi Level
EI	Electron impact
EVAC	Vacuum Level
F_4-TCNQ	Tetrafluoro-tetracyanoquinodimethane

FITC	Fluorescein isothiocyante
FTIR	Fourier transform infrared spectroscopy
HOPG	Highly ordered pyrolytic graphite
HTL	Hole transporting layer
IP	Ionization potential
IR	Infrared
IRRAS	Infrared Reflection-Absorption Spectroscopy
ITO	Indium tin oxide
IZO	Indium zinc oxide
KP	Kelvin Probe
LFM	lateral force microscopy
LIXPS	Low-intensity X-ray photoelectron spectroscopy
MALDI	Matrix assisted laser desorption ionization
MV0	Methyl viologen
NEXAFS	Near Edge X-ray Absorption Fine Structure Spectroscopy
NMR	Nuclear magnetic resonance spectroscopy
NREL	National renewable energy laboratory
ODPA	Octadecylphosphonic acid
OFETs	Organic Field Effect Transistors
OLED	Organic light emitting diode
P3HT	Poly(3-hexylthiophene)
PDI	Perylene diimide
PEIE	Polytheylenimine ethoxylated

PM-ATR	Potential-modulated attenuated total reflectance
PM-IRRAS	Polarization modulation infrared reflection absorption spectroscopy
PPA	Phenyl phosphonic acid
PYS	Photoelectron yield spectroscopy
QCM	Quartz crystal microbalance
RAIRS	Reflection absorption infrared spectroscopy
SAM	Self-assembled monolayer
SEM	Scanning electron microscopy
SPM	Scanning Probe Microscopy
SSRL	Stanford Synchrotron Radiation Lightsource
T-BAG	Tethering by aggregation and growth
TCNL	Thermochemical nanolithography
TCOs	Transparent conducting oxides
TDAE	Tetrakis(dimethylamino)ethylene
TEA	Triethylamine
TEM	Transmission electron microscopy
TEY	Total electron yield
TGA	Thermogravimetric analysis
TGA-MS	Thermogravimetric analysis coupled with mass spectrometry
THF	Tetrahydrofuran
TMSBr	Trimethylbormosilane
UHV	Ultra-high vacuum
UPS	Ultraviolet photoelectron spectroscopy

VB	Valence Band
VBM	Valence band maximum
WF	Work function
XPS	X-ray photoelectron spectroscopy
ZnO	Zinc Oxide
ZnPcPAs	Zinc phthalocyanine phosphonic acids

SUMMARY

This thesis focuses on the use of surface modifiers to tune the properties of both metals and metal oxides. Particular attention is given to examine the modification of transparent conducting oxides (TCOs) including indium tin oxide and zinc oxide both through the use of phosphonic acids as well as organic and metal-organic dopants. In this thesis a variety of known and new phosphonic acids are synthesized. A subset of these molecules are then used to probe the relationship between the ability of a phosphonic acid to tune the work function of ITO and how that interrelates with the coverage and molecular orientation of the modifier on the surface. Experimental techniques including XPS, UPS, and NEXAFS are coupled with theoretical DFT calculations in order to more closely examine this relationship.

Literature surrounding the modification of zinc oxide with phosphonic acids is not as prevalent as that found for the modification of ITO. Thus, effort is placed on attempting to determine optimal modification conditions for phosphonic acids on zinc oxide. As zinc oxide is already a low work function metal oxide, modifiers were synthesized in an attempt to further decrease the work function of this substrate in an effort to minimize the barrier to carrier collection/injection. Etching of the substrate by phosphonic acids is also examined.

In a related technique, n- and p-dopants are used to modify the surfaces of ITO, zinc oxide, and gold and it was found that the work function can be drastically altered, to approximately 3.3 – 3.6 eV for all three of the substrates examined. Surface reactions are straightforward to conduct typically taking only 60 s to achieve this change in work function.

CHAPTER 1

INTRODUCTION AND BACKGROUND INFORMATION

This chapter is intended to inform a reader unfamiliar with the topic of surface science (especially the modification and characterization of surfaces) prior to delving into the body of the thesis. The overarching theme of this thesis is the design of surface modifiers, their use in the modification of metal oxides, and characterization of the resulting modified surfaces with the goals understanding how surface modifiers bind at the interface and how these modifiers alter the work function of the substrate. Before getting into the details surrounding the experimental results in later chapters, this chapter begins by first introducing the broad concept of surface science and placing it in an historical context. Subsequently, focus then turns to the particular subset of surface science involving the use of monolayers. Since there are a wide variety of binding groups available, section 1.2.2 discusses the most commonly used types of modifiers, as well as provides some comparison as to the use case of each modifier.

Central to the study of surfaces is the use of analytical techniques to characterize the surface subsequent to modification since, while there are some macroscopic properties that can be observed upon modification, the vast majority of changes require techniques that can probe down to the molecular level of detail. Techniques to examine the topography, elemental composition, molecular tilt angle, and changes in surface energetics are detailed in 1.4. A discussion regarding energy levels, work function, band diagrams, and how these relate with surface modification is also provided. This

knowledge is central to understanding the changes in work function that are occurring after surface modification, which is an important aspect of this thesis.

1.1 Surface Science

The study of surfaces and interfaces encompass both the boundary between a material and the environment surrounding it as well as the interactions that can take place between the surface and the environment.[1] Over the past several decades, the examination of surfaces has seen a marked increase both in knowledge about surface chemistry as a whole and the development of techniques for surface analysis and modification.[2-5] As will be discussed below there are both scientific and technical reasons that have spurred increased interest in surface science, but from a more practical standpoint surface science and chemistry at the surface has become an important aspect to everyday life. In fact, it has become so commonplace for surfaces to be modified and tuned that the average consumer now expects anti-fog lenses for their glasses,[6-7] smaller and faster microprocessors, waterproof mobile electronics devices,[8] and safe, long lasting batteries.[9] All of these technologies and many more rely on altering the natural properties of a given surface to enhance their utility for a particular application.

1.1.1 The Study of Surface Science – A Historical Perspective

The study of surface science can be broadly defined as the exploration of the atomic arrangements and chemical compositions that occur at the surfaces of condensed matter. This definition can then be further extended to include examining the theory and observation of the chemical, mechanical, and electronic properties of these materials.[10] While the observation of the physical properties that are associated with condensed matter have been studied since the time of antiquity,[11] one of the earliest written records

of such an observation comes from the time of the Akkadian empire under the rule of Hammurabi. A portion of this text is shown in Figure 1.1 and discusses what the ancient Greeks would later call the practice of lecanomancy, or the art of divination by examining the interaction of oil and water.[12]

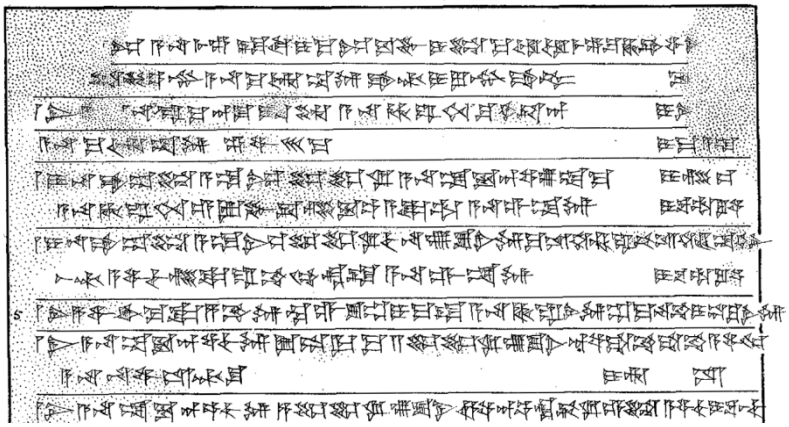

Figure 1.1 Portion of cuneiform writing discussing divination through the art of lecanomancy.[13] This section of the tablet in particular discusses the spreading of oil on water and describes actions that would be taken by Hammurabi's army or outcomes of the sick and dying based on the interaction of these two fluids. Tabor provides a complete translation of this portion of the text in his article.[12]

Studies of surfaces continued throughout history, but the actual science of surfaces began closer to the 19th century. Important examples in the history of this science include examples such as Faraday's study of the reaction of hydrogen and oxygen at well below their normal combustion temperature in the presence of platinum (which later was recognized as catalytic action by Jöns Berzelius).[14] Karl Ferdinand Braun observed that conduction of current through a sandwich of copper and iron (II) sulfide deviated from Ohm's law and posited that the asymmetrical resistance must originate at the interface of the metal and metal oxide.[11, 15] Yet, while the aforementioned discoveries

were important, it was the efforts of Irving Langmuir who provided the true momentum that eventually led to the widespread recognition of surface science as a discipline unto itself. Langmuir examined a broad range of topics related to surfaces and phenomena occurring at surfaces including heterogeneous catalysis, adsorption kinetics, and work function.[11, 16-17]

In addition to scientific breakthroughs, surface science was also aided in becoming its own field of study by the technical advancement of commercially available ultra-high vacuum (UHV) systems.[18] While the history of vacuum pumps dates back to the mid-1600s,[19-21] it was not until the 1950s that it started to become possible to achieve pressures below 10^{-8} Torr (pressures below this threshold are commonly used in instrumentation that relies on UHV today).[22] Overcoming this technical limitation allowed for the production of atomically clean surfaces and also provided an environment in which surface studies could be conducted with negligible molecular contaminants from the residual atmosphere in the UHV chamber over the time scale of a typical experiment.[10]

1.1.2 The Importance of Surface Cleanliness

As mentioned above, UHV allows for the formation of ultra-clean surfaces, but not all manipulations that need to be done with a given surface can occur under UHV conditions. Thus, a tremendous amount of research and development has gone into the removal of contaminants from the surface and the eventual production of clean surfaces.[23] Each type of surface has its own particular cleaning protocol that is determined by the properties of the surface, the likely contaminants present prior to cleaning, and the ultimate final use of the material in question. This means that cleaning

technologies for glass[24-25] can differ greatly from those used to clean silicon[26-27] and preparing a clean surface for nanoscale architectures (typically the removal of small particles and film-like contaminants) can differ from preparation of a sterile surface for biological studies (removal of microbial contaminants).[23, 28]

While utilizing a cleaning technique, however, it is critically important to keep in mind that the cleaning protocol itself can lead to not only a removal of surface contaminants, but also changes to the underlying substrate.[29] One example of this is changes to the roughness of a silicon-based substrate depending on whether wet or gaseous cleaning protocols are used.[30] Another example is changing the level of surface hydroxyl groups present and thus altering the hydrophobicity/hydrophilicity of a substrate such as indium tin oxide (ITO), thereby increasing or decreasing the ability of a modifier to bind to the surface.[31-32]

1.2 Surface Modification with Monolayers

As previously mentioned an important aspect to surface science is the ability to tune the interface of a material in order to allow the substrate to exhibit more desirable properties (for instance better wetting or the mitigation of film delamination). Achieving this goal has often been accomplished in the literature by the deposition of ultra-thin films on the substrate. Such an ultra-thin film can be anywhere from a sub-monolayer amount of molecules on the surface to multiple layers of a material. The focus of this thesis (as well as a vast amount of literature) is on the use of a single layer of molecules (or less in some cases) adsorbed to the surface of the substrate. This single layer of adsorbates on the surface can significantly alter the interfacial properties of the pristine surface. Thus, through careful molecular design it is possible to produce a layer of

molecules that can minimize surface aggregation, alter surface wetting, serve as an electrically insulating or conducting layer, or even provide corrosion resistance.[33]

In order to make judicious decisions regarding molecular design, it is first necessary to understand the basic components of a monolayer. Monolayers at the surface are generally broken down into three distinct components, as can be seen in Figure 1.2. These different parts of the molecule are the head group (binding group), the spacer, and the terminal functional group or tail. The head or binding group is the portion of the molecule that serves as the bridge between the substrate and the rest of the molecular structure. This group can be linked to the surface through simple physisorption, but typically chemisorption is preferable in order to make a more robust monolayer (for more on this distinction see 1.2.1), and the selection of this binding group will be discussed in greater detail in 1.2.2. The spacer group serves multiple purposes, the most important of which is determining the physical separation between the substrate and the potentially reactive terminal group. The composition of this portion of the monolayer can be made flexible or rigid through the use of saturated alkane chains or unsaturated/conjugated chains and rings. The third and final portion of a representative monolayer is the terminal functional group, which is what primarily determines the surface properties and chemistry after modification.[33]

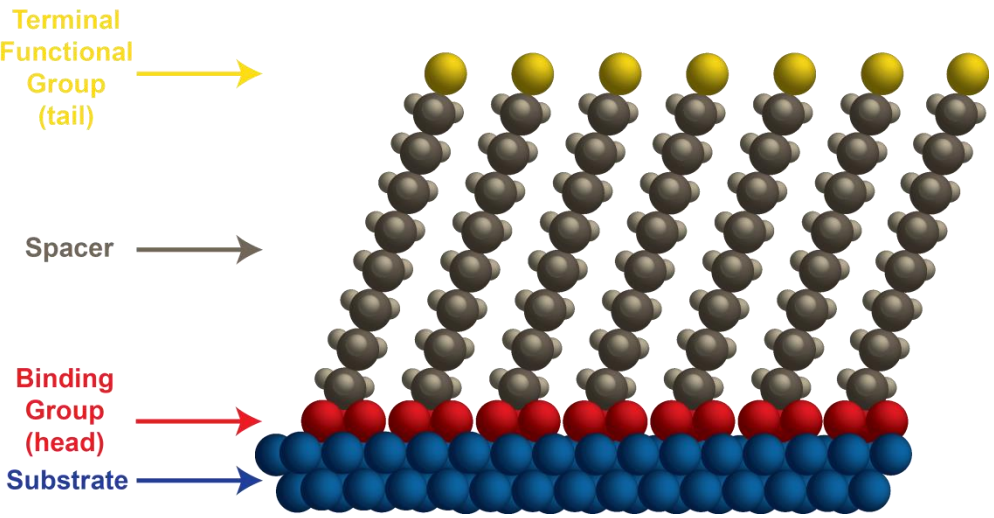

Figure 1.2 General components of a typical monolayer on the surface of a substrate. The three main components of the monolayer are highlighted and their purpose discussed in the text above. This figure was adapted from the literature.[33-34]

1.2.1 A Note about Chemisorption and Physisorption

As previously noted, it is possible to have molecules bind to the surface of a substrate in various manners. These types of adsorption can be classified as either weak (physisorption) or strong (chemisorption) interactions with the surface. It should be noted, however, that there is not a sharp distinction between these two types of adsorption; by convention it is typically accepted that the distinction occurs at a binding energy of approximately 0.5 eV per molecule (1 eV/molecule = 23.06 kcal/mol = 96.49 kJ/mol). In the case of physisorption the interaction that occurs between the substrate and the adsorbate is weak due to van der Waals forces and adsorption energies on the order of 0.01 – 0.1 eV.[35] Others will define this adsorption as bonds that can only occur at low temperatures on the surface such as the low temperature adsorption of noble gas atoms on a metal surface.[36] This definition, however, needs to be used with care since virtually any species will physisorb given low enough temperature conditions.[37]

In contrast to physisorption, chemisorption involves the formation of strong chemical bonds between the surface modifier and the substrate. The resulting bonds can be either ionic or covalent with typical energies on the order of 1 – 10 eV, which result in a robust layer of adsorbate at the surface.[35] Consequently, while physisorbed materials can easily be removed with the aid of heat or solvents, chemisorbed materials are not readily removed from the surface and require much harsher conditions for deliberate removal. Another important aspect that accompanies the chemisorption of a material at the surface is changes to the substrate structure due to relaxation or reconstruction at the surface (section 1.5.2 discusses this further).[37]

1.2.2 Binding Groups for Monolayer Surface Modification

The selection of binding group for monolayer surface modification greatly depends on the composition of the surface that is to be modified since not all binding groups behave the same on different surfaces. These differences in behavior are expected in the case of chemisorption where the chemical functionalities of the surface and the modifier have to react with one another. For instance, while it is possible to modify the surface of silicon, silica, or glass with alkoxy or halosilanes, the same surface modifiers have minimal interaction with surfaces lacking hydroxyl groups such as gold.[38-39] The following sections briefly discuss surface modifiers such as carboxylic acids, silanes, thiols, and phosphonic acids along with the various substrates that they readily modify. A very comprehensive list indicating binding groups that are best suited for a particular substrate can be found in Love *et al*.[33]

1.2.2.1 Monolayer Terminology and Formation

The seminal work on the formation of monolayers of acids on glass came from the work conducted by Langmuir[40] utilizing the antecedent work on surface tension conducted by Agnes Pockels.[41] Katharine Blodgett furthered this work while in Langmuir's lab by showing the successive deposition of many single layers of fatty acids on a glass substrate.[42-43] Due to the lack of available tools at the time it was not possible to focus on the structure and formation of such monolayers at the molecular level and instead the work mainly examined macroscopic properties such as wettability. With the discovery that alkanethiols could modify the surface of gold[44-45] and the advent of readily available analytical techniques to examine monolayers at the molecular level (discussed further in 1.4) it became possible to probe these modifiers at the molecular level and it was discovered that there appeared to be a self-organizing order to the monolayers that are formed. Thus, the term self-assembled monolayer (SAM) began to be applied to the formation of such monolayers due to this supramolecular like organization of molecules on the surface of the substrate.[34] Unfortunately, the term SAM, while an appropriate literal description for certain systems, has been used so widely throughout the literature that it has lost its core meaning and now colloquially applies to any material that can modify a surface whether there is evidence for self-assembly or not. Therefore, the term SAM will be avoided throughout this thesis as there is no readily available evidence that the modifiers discussed in the following chapters actually undergo self-assembly on the surface in an ordered manner. The term monolayer, which is a better expression of the current state of knowledge regarding the ordering of these systems, will be used instead.

A representative example of monolayer formation on the surface of a substrate can be seen in Figure 1.3. In particular, this type of scheme refers particularly to the case of thiols on a gold substrate and is representative of true self-assembly on the surface. The formation of a monolayer depends greatly on the type of binding group that is used, which is why only one representative example is shown here. In the case of this particular type of modification the thiol molecules begin physisorbed to the gold substrate, which is followed by the disordered chemisorption of molecules. The initial chemisorbed molecules that were previously lying down on the surface serve as nucleation sites and vertically directed orientation begins to occur, which is followed by growth outward from these sites until complete coverage of the surface is achieved, resulting in the formation of a monolayer.[46-47]

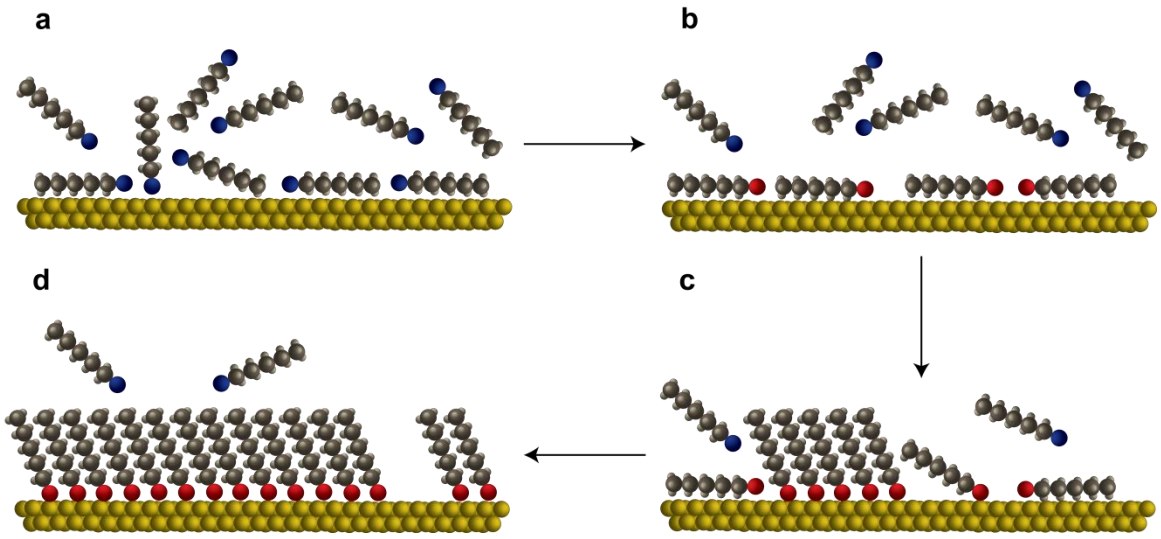

Figure 1.3 Cartoon representation of steps that occur during the self-assembly of alkanethiols on a gold substrate: (a) physisorption, (b) lying down phase, (c) nucleation of vertical molecules, and (d) completion of vertical phase. It should be noted that the binding groups in all cases are thiols, with red binding groups indicating chemisorbed molecules and blue representing physisorbed molecules. This figure is adapted from those found in the literature.[46-47]

1.2.2.2 Organosulfur Compounds for Surface Modification

Thiol surface modifiers have become increasingly commonplace in the literature ever since the discovery that such organic molecules can chemisorb to the surface of gold substrates.[44] In addition to thiols, organosulfur compounds such as disulfides and sulfides can also be used for surface modification and form monolayers on the surface of substrates by spontaneous adsorption from either solution or vapor deposition. Typically, solution deposition is desirable as it avoids the need for UHV systems, requiring only a clean substrate and an ethanolic solution of the thiol. Common materials that can be modified with thiols in such a manner include gold, silver, palladium, mercury, and zinc. Thiols are also more commonly utilized than other organosulfur materials such as disulfides due to better overall solubility.[33]

Thiols on coinage metals, particularly gold, do afford a robust monolayer with temperature stability above 120 °C due to the strong linkage of the thiol with the surface through the formation of S-Au bonds. As noted in Figure 1.3, the modification of the surface with thiols involves not only chemisorption, but initially physisorbed and mobile thiols that come on and off the surface, which aids in self-assembly of these monolayers.[33] The conditions required to form reproducible monolayers, while not as straightforward as those used for phosphonic acid modification (1.2.2.5), are more straightforward to control in comparison with silane surface modification (1.2.2.3) requiring deoxygenated solvent and inert atmosphere.[48-49] Due to the ability of thiols to react with oxygen, however, some chemical instability can exist under atmospheric conditions causing deterioration of the monolayer.[50-51] Even with this limitation, however, thiols are an excellent choice as surface modifiers given the underlying

substrate for modification is a coinage metal, and applications as diverse as examining the electrochemistry of monolayers, preparing biocompatibile surfaces, and the binding of proteins and nano-objects utilizing thiol-based monolayers have been demonstrated in the literature.[52] It is also possible to regain a pristine gold surface through the use of hydrogen-plasma cleaning to remove the monolayer.[52]

1.2.2.3 Organosilicon Compounds for Surface Modification

Silane-based surface modifiers encompass a range of binding groups including alkoxy and halosilanes, and have been commonly examined due to their ability to modify surfaces that are not easily modified by other binding groups such as silicon, silica, and glass. They also have been extensively studied due to the stability of the silicon-oxygen-carbon bond that is formed between the substrate and the surface modifier, making for a robust monolayer.[53] As with organosulfur compounds there are multiple types of organosilicon molecules that can be utilized in surface modification such as chlorosilanes and silyl ethers.[54] One of the drawbacks to the use of this type of surface modifier, however, is the overall limited reproducibility of the monolayer that is formed (particularly in the case of trichlorosilanes).[53, 55]

The irreproducibility of silane monolayers can be linked by the formation of homocondensation products that form a cross-linked polymeric like network of silane multilayers on the surface, rather than a pristine monolayer of material.[34] Such a formation of multilayers is dependent on the amount of water present in the organic solvent used for the surface modification. The general mechanism for the surface modification with a trialkoxysilane or trichlorosilane is shown in Figure 1.4 and illustrates that water plays an important role in surface modification with these

compounds. The water content thus determines the overall quality of the resulting monolayer as can be seen in Figure 1.5; completely anhydrous conditions lead to an incomplete monolayer as the initial hydrolysis reaction is slow, whereas, if too much water is present, the hydrolysis reaction occurs so quickly that homocondensation reactions dominate rather than reactions between the modifier and the substrate. Therefore, an optimum amount of water is needed to form a high quality monolayer; this amount differs from silane to silane depending on the functionality of the spacer and terminal functional group and is hard to control. Figure 1.5 also shows that the amount of water is important regardless of whether alkoxy or chlorosilanes are used since the surface modification in either case relies initially on hydrolysis to form the silanol, with the main difference being the speed with which the formation of the silanol takes place, with chlorosilanes reacting faster than alkoxysilanes.

1.2.2.4 Carboxylic Acids for Surface Modification

While thiols and silanes represent a large majority of surface modifiers used in the literature for the formation of monolayers on substrates, carboxylic acids are also an important binding group. Carboxylic acids have aided in expanding the variety of substrates that can be modified with a monolayer, allowed for the use of metals that are less costly than noble metals modified by thiols, and they have allowed for an examination of the important role that the chemistry between the metal or metal oxide and anchoring group play.[59] The chemisorption of carboxylic acids is based on an acid-base reaction between the binding group and the substrate. The overall driving force for surface binding in this case is the formation of a surface salt between the carboxylate anion and surface metal cation.[60-61] There is a diverse array of substrates that can be

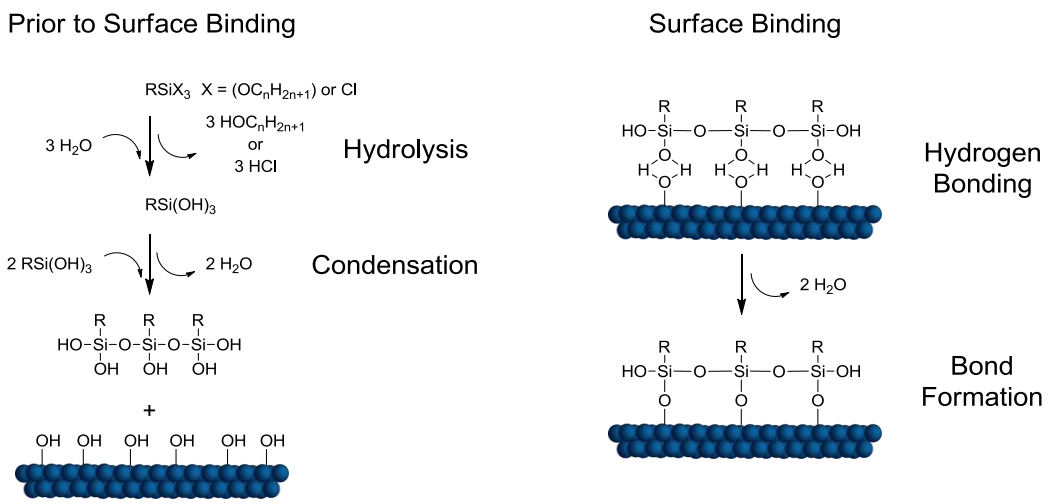

Figure 1.4 Generalized scheme for the reaction of a trialkoxysilane or trichlorosilane containing a spacer and terminal functional group (R) with a substrate terminated with surface hydroxyl groups. Note that the linking group (X) can be either an alkoxy or halogen group. This scheme shows the hydrolysis and condensation reactions that occur in solution as well as those that occur in order to covalently bind with the surface. This figure is adapted from the literature.[56-57]

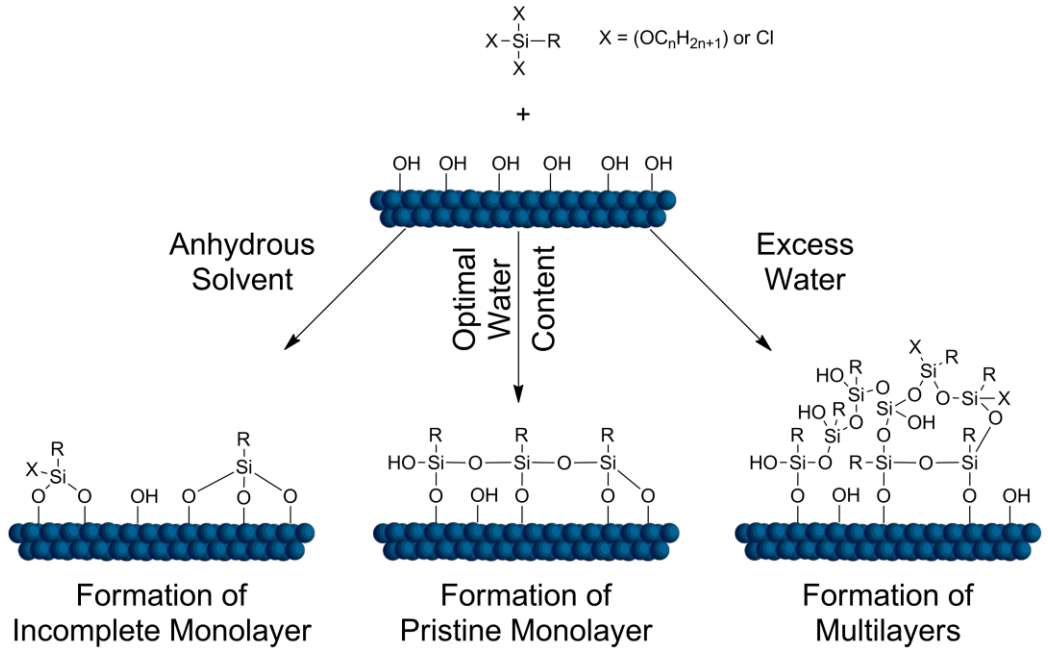

Figure 1.5 Representative examples demonstrating the impact that water content has on the ability of an organosilane to form a high quality monolayer. In this example both chlorosilanes as well as alkoxysilanes are shown. Figure adapted from those found in the literature.[55, 58]

modified with carboxylic acids (e.g. alkanonic acids), including alumina,[62] zirconia,[63] gold,[62, 64] silver,[65] and ITO.[66] The strength of binding of carboxylic acids compared with phosphonic acids (discussed in the next section and the focus of surface modifiers used in this thesis) to metal oxides has been shown to be weaker, resulting in a lower coverage monolayer when compared with an analogous phosphonic acid.[67]

1.2.2.5 Phosphonic Acids for Surface Modification

Phosphonic acids have been studied for surface modification relatively recently in comparison with the other binding groups previously discussed. Research surrounding this particular surface modifier dates back to work done in 1996 by Woodward, Ulman, and Schwartz who initially used a long chain alkyl phosphonic acids to modify the surface of mica.[68] This work was quickly followed up with two more studies examining the growth[69] and kinetics[70] of phosphonic acid monolayers. Prior to these studies it was known that phosphonic acids could modify the surface of zirconia,[71] titania,[72] alumina,[73-74] or could be used to form multilayers on gold[75] or silica.[76] Yet, the work from the Schwartz group was the first set of studies into the chemisorption of phosphonic acids on metal oxides directed to better understand the formation of the monolayer. Depending on the nature of the substrate, this monolayer can form in two different ways, both of which are shown in Figure 1.6. In the case of Lewis acidic metal oxides, the monolayer forms by coordination of the phosphoryl oxygen to the metal oxide surface followed by a heterocondensation reaction as shown in Figure 1.6a. In the case of metal oxides that are weakly Lewis acidic, heterocondensation takes place first without the phosphoryl coordination (Figure 1.6b).[77-78] This reaction can form up to three P-O-M bonds (where M is the metal oxide substrate); in the case of ITO modification is predominantly a

bidentate linkage with the surface.[79] The strength of these covalent bonds is what leads to the formation of such a robust monolayer, requiring harsh basic conditions or plasma etching for removal of the monolayer from the substrate.[80]

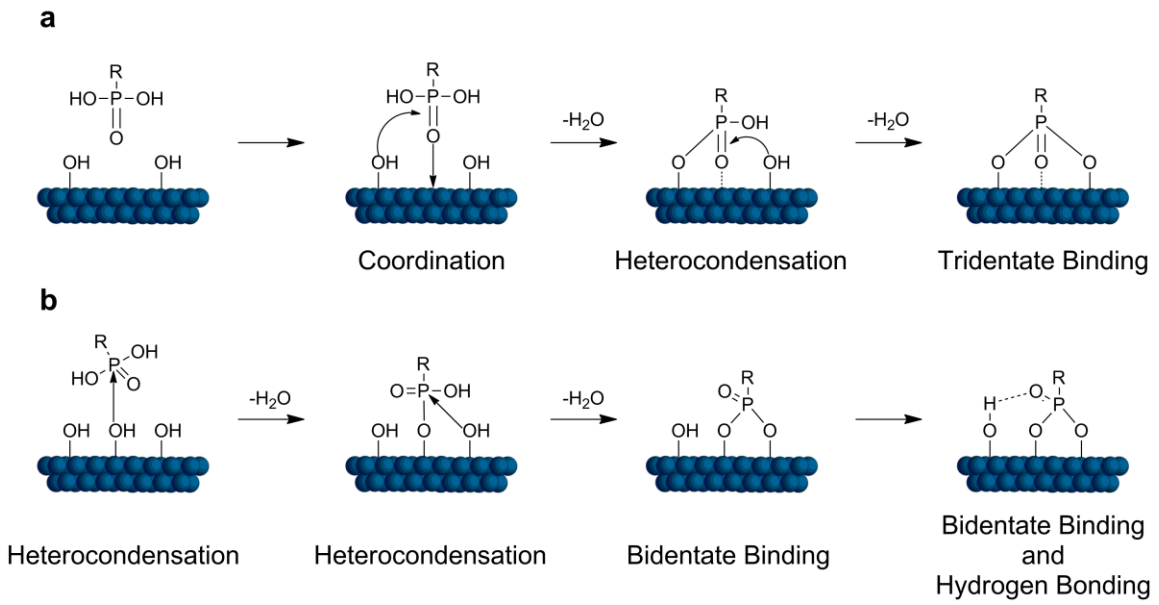

Figure 1.6 Mechanism of phosphonic acid binding to Lewis acidic metal oxides (**a**) and poorly Lewis acidic metal oxides (**b**). This figure demonstrates the varieties of binding modes that are possible and outlines what type of reaction is occurring at each step. This figure was adapted from those in the literature.[77-78, 81]

Phosphonic acids have both the advantage of creating strong bonds with metal oxide surfaces (similar to thiols and silanes), but in a more reproducible manner than silanes due to the inability of this type of binding mechanism to produce homocondensation products.[55] In contrast to thiols, phosphonic acids are not sensitive to the amount of oxygen present during the modification protocol and most experimental procedures utilize millimolar concentrations in ethanol or tetrahydrofuran (THF) for anywhere from several hours to multiple days depending on the intended use of the

monolayer. Any physisorbed multilayers are readily removed with sonication in a mildly basic solution,[79] and results in a high quality, highly reproducible monolayer. Phosphonic acids combine the binding strength of thiols and silanes with the lack of homocondensation products and ease of modification conditions found for carboxylic acids. This is why phosphonic acids are of particular interest and were chosen to be examined in this thesis in the context of modifying metal oxides of importance for electrode applications.

1.3 Energy Level Definitions

Before discussing the various analytical techniques that are used to analyze monolayers on a surface it is important to introduce the various terms that are used to describe electronic structure. As will be seen, both XPS and ultraviolet photoelectron spectroscopy (UPS) can be more readily understood with a prior knowledge of the Fermi level and work function.

- **Vacuum level (E_{VAC})** – In the context of solid surfaces and electronic measurements is defined as the energy of a stationary electron at a distance that is infinitely far away from the solid surface such that it is beyond the influence of any significant electrostatic interactions with the surface (E_{VAC}^{∞}).[82] However, the vacuum level that will be used throughout this thesis (allowing for the measurement of work function and other experimentally determined quantities) is better defined as the energy of an electron at rest just outside the solid and consequently is still affected by the potential of the solid surface.[83] From a practical standpoint this means that E_{VAC} as determined from experimental results is not from an electron infinitely away from the surface and

is therefore *not* an invariant reference point. An excellent discussion regarding the disambiguation of these two definitions can be found in Ishii.[83]

- **Conduction band (CB)** – the band consisting of unoccupied orbitals to which electrons can be excited; in the case of semiconductors that have a small gap between the valence band and conduction band it takes little energy to cause this excitation and thus conduction of electricity
- **Valence band (VB)** – the band consisting of occupied orbitals; in the case of semiconductors and conductivity, the band from which electrons are excited into the conduction band
- **Fermi level (E_F)** – thermodynamically, the work required to add an electron to a material, in the case of semiconductors, the level at thermodynamic equilibrium that has a 50 % probability of being occupied at any given time, and when the temperature is 0 K no electron population will exist in bands above that of the Fermi level[84]
- **Work function (ϕ, WF)** - the energy required to remove an electron from the Fermi level to the vacuum level

1.4 Analytical Methods for Examining Monolayers

Analyzing a surface after modification can run the gamut between a straightforward and simple approach such as goniometry (more commonly known as contact angle) to something far more complex and involved such as synchrotron-based techniques like Near Edge X-Ray Absorption Fine Structure Spectroscopy (NEXAFS, discussed below). Choosing from the myriad of techniques requires a careful understanding of what surface properties need to be probed (e.g. orientation, surface energy, work function, roughness, compatibilization, etc.) and whether the technique is

sufficiently sensitive to detect the quantity of modifier on the surface. The following sections provide a brief introduction to the types of characterization techniques that will be discussed throughout the remainder of this thesis. The references herein also serve as recommended reading regarding further in-depth details about the technique. A comprehensive summary of surface analysis techniques including characterization parameters, information obtained, equipment/techniques required, and resolution can be found in pages 33 – 52 of Brune *et. al*.[85]

1.4.1 Atomic Force Microscopy

Atomic force microscopy (AFM) is a type of scanning probe microscopy (SPM) that allows for the collection of high-resolution structural details of a surface on a scale of microns to angstroms. This technique can be conducted under UHV, but more commonly is performed under standard atmospheric conditions and relies on the measurement of differential forces between a sharp probe and the surface being imaged.[86-87] The scanning probe may be kept at a distance less than a few nanometers from the surface or in direct, mechanical contact with the surface; in the case of AFM these are referred to as tapping mode or contact mode, respectively.[88] The basic components of an AFM include a cantilever with a sharp probe at the end that is attached to a piezo, a laser beam, and a photodetector. Application of voltages to the piezoelectric scanner (often a four quadrant tube scanner) allow for the tip to be moved in three-dimensional space. A laser beam is then focused on the cantilever and reflected onto a photodetector as a means of measuring the forces acting on the tip, which cause changes in the deflection of the cantilever. While there are other options available for the measurement of this feedback, the use of a laser and photodetector has the advantage of

magnifying surface features by a factor of 750 – 1500 when using long cantilevers (100 – 200 μm in length), allowing for detection of cantilever deflection changes in the sub-angstrom range.[88] A schematic view of an AFM is shown in Figure 1.7.

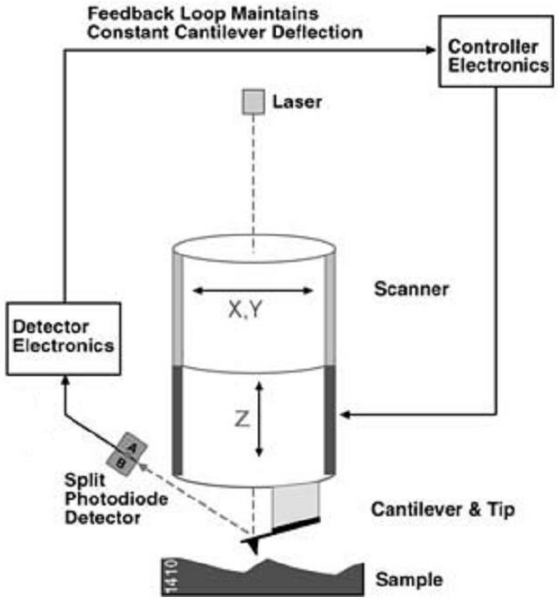

Figure 1.7 Schematic view of an AFM showing the principal components required for operation. Image reproduced from the literature.[86]

AFM analysis of modified surfaces is commonly carried out in tapping mode. In this intermittent-contact mode the cantilever is oscillated by a piezoelectric actuator at its resonance frequency and the amplitude of this oscillation is specified by the user. As the tip intermittently contacts the surface, the tip-sample force interactions that are encountered cause changes to the amplitude, phase, and resonance frequency of the vibrating cantilever. Thus, depending on whether the tip is attracted or repelled from the surface there is either a decrease or an increase in resonance frequency, respectively. Adjustments are made by a feedback controller in order to keep the cantilever at a

constant frequency of oscillation, which in turn allows for the formation of a topographical image indicative of the height changes that are present in the sample.[86] Analysis of fine morphological features is simultaneously collected and turned into a phase image based on the differences between the phase of the oscillation at the resonance frequency and the phase when the tip interacts with the surface.[86, 88] This difference is graphically demonstrated in Figure 1.8 and representative data showing the difference between topography and phase data (which can be simultaneously collected) is shown in Figure 1.9.

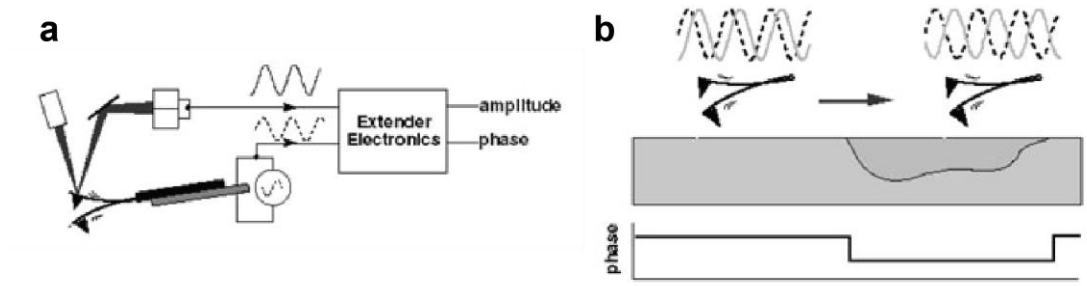

Figure 1.8 Schematic demonstrating the collection of phase imaging in tapping mode (**a**) and changes in phase oscillation when a probe comes into contact with different portions of the surface (**b**). Image modified from the literature.[86]

In the particular case of surface modifiers on a substrate, the information that can be gleaned from AFM greatly depends on the nature of the underlying substrate. In the case of atomically flat surfaces such as gold and mica it is possible to probe the development of the monolayer with time[69] as well as the packing and crystalline order that forms from self-assembly.[89-90] In the case of substrates that are not atomically flat, such as ITO or zinc oxide (ZnO), the underlying surface roughness precludes the ability to image the monolayer structural features. Instead AFM images are used to examine the

overall morphology of a surface after modification to examine whether the modifier changed the surface in any way (such as differences in roughness due to etching).

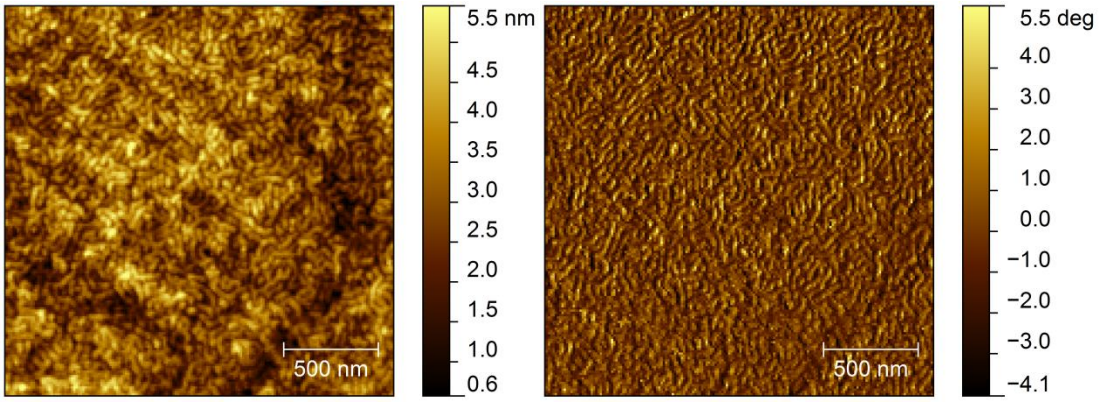

Figure 1.9 Representative examples of AFM topography (left) and phase (right) images showing the features present on a spin coated film of a styrene-butadiene-styrene block copolymer.

1.4.2 X-ray Photoelectron Spectroscopy

Another important aspect to examining surfaces is the ability to probe the chemical composition of the substrate both before and after modification. Obtaining such analytical information is most commonly accomplished through the use of X-ray photoelectron spectroscopy (XPS). This UHV technique relies on the bombardment of the sample surface with high-energy X-rays. When these X-rays strike the atoms on the surface there is a concomitant ejection of inner shell electrons and the atom becomes ionized. Thus, if E_0 is the energy of the X-ray source being used and E_j is the energy of the core electron being removed from the atom, then the difference in these energies, $E_0 - E_j$, will be the energy of the emitted electron, which is characteristic of both the atom and shell from which the electron originated. These emitted electrons are collected by an

energy analyzer, which filters the electrons based on their kinetic energies. Furthermore, since the number of ejected electrons is proportional to the number of atoms present, the technique can provide compositional data quantitatively. Thus, each element has its own set of characteristic peaks in the spectra (Moulder and Chastain serves as a good reference handbook for this)[91] and a determination of the relative amounts of each element can be obtained.[92-93] It is important to note that, since the probability of detecting an electron from a surface can be represented as the exponential e^{-x}, there is a limit to the detection depth of XPS. This limit means that XPS typically only probes to a depth of approximately 10 nm, which is well suited for the study of monolayers. A generalized schematic of XPS, as well as representative spectra are shown in Figure 1.10.

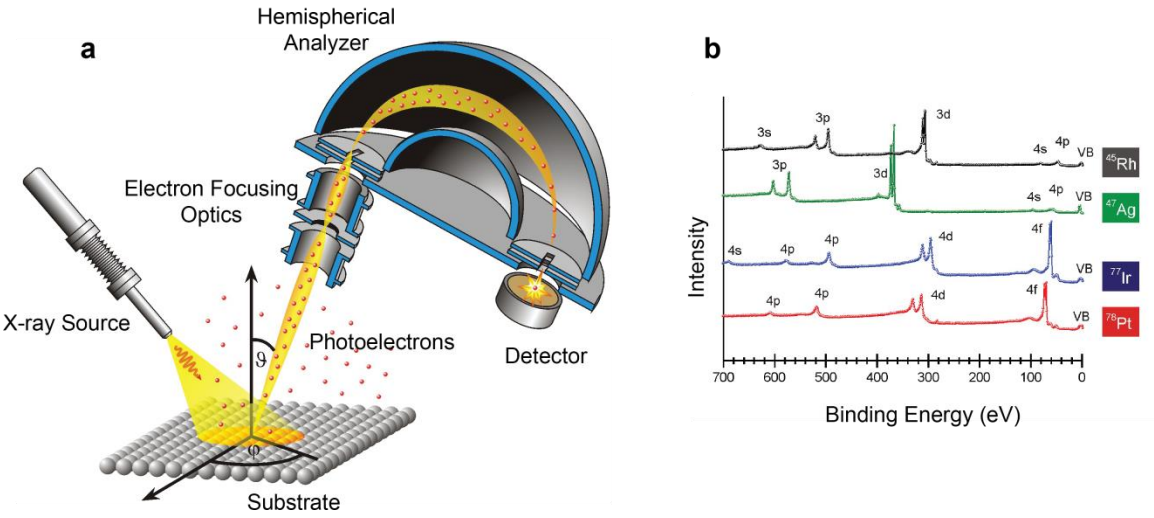

Figure 1.10 Schematic diagram of a typical XPS instrument (**a**) showing the main components as well as the ability to translate (φ) and tilt (ϑ) the sample relative to the X-ray source along with typical spectra acquired by XPS for some representative elements (**b**). Images are modified from Jacobs.[94]

Another important set of information afforded by XPS analysis is the ability to obtain information on the chemical state of the elements present on the surface being

examined. The binding energy (defined in Figure 1.12) of a specific ionization depends on the chemical state of the atom in question and chemically inequivalent atoms of the same element give rise to peaks in the XPS spectra that occur at measurably different energies (analogous to chemical shifts that are observed in nuclear magnetic resonance spectroscopy, NMR). These inequivalent atoms can originate from differences such as oxidation state or chemical environment, and a representative example of non-equivalent carbon atoms in a surface monolayer is provided in Figure 1.11. Figure 1.12 provides a band diagram for excitation caused by X-rays in XPS to better show how binding energy (the common energy unit used when plotting data), kinetic energy (what is detected by the analyzer), and the Fermi level relate to one another in this type of spectroscopy.

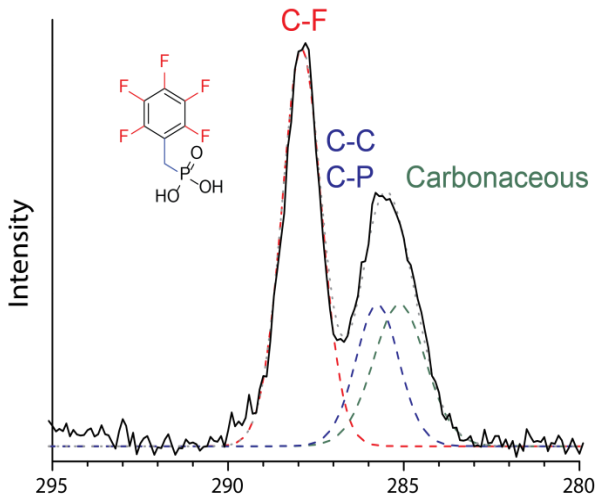

Figure 1.11 Example of peak separation observed in XPS due to non-equivalent atoms. The above is the spectrum of the C 1s peak for pentafluorobenzylphosphonic acid on the surface of ITO. The spectrum shows the presence of two main peaks with the peak originating from the **C-F** bonded atoms at higher binding energy due to the electronegative nature of fluorine, removing electron density from the adjacent carbon and thus decreasing the kinetic energy of electrons removed from the C 1s orbital. Both **C-C** and **C-P** bonds appear at similar binding energies and **carbonaceous** carbon originates from environmental contaminants on the surface.

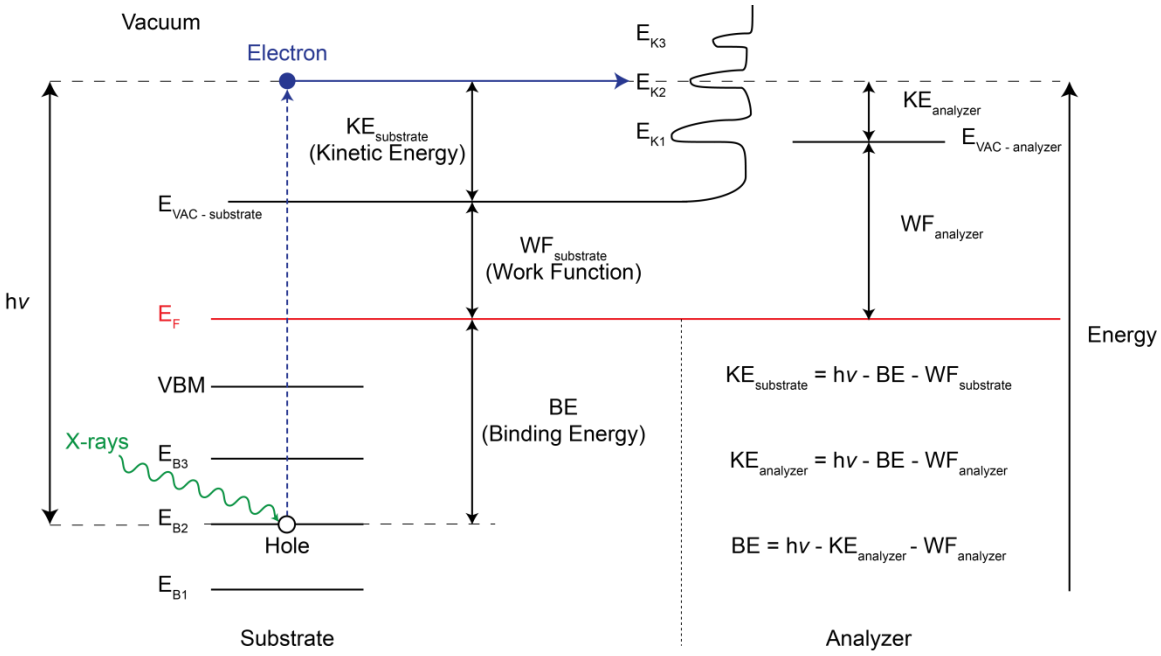

Figure 1.12 Band diagram showing the excitation of a core level electron at an energy of E_{B2} by a photon of energy hν. The electron then travels to the analyzer where it is detected as a peak in the spectrum which is schematically shown to occur at a kinetic energy of E_{K2}. In XPS, the Fermi level is used as the reference point and energy units are commonly shown in Binding Energy (BE) rather than the Kinetic Energy that is directly detected by the analyzer. The bottom equation shows how BE is obtained from the X-ray photon energy (hν), work function of the analyzer ($WF_{analyzer}$) and the excess kinetic energy of the excited electron at the analyzer ($KE_{analyzer}$), which are all expressed with respect to the Fermi level. Image based on XPS explanations by Matolín[95] and Smart.[96]

1.4.3 Ultraviolet Photoelectron Spectroscopy

UPS is a powerful technique that is highly surface sensitive and allows for the measurement of ionization energies for valence states. UPS in the context of this work focuses on the ability of this technique to quantify work function and valence band maximum values. This is also a UHV technique that is typically conducted using the same instrument as in XPS. In this case, however, rather than using X-rays as the excitation source, a helium discharge source is typically used (other UV sources such as those from synchrotron radiation can also be used), which allows for the production of

high intensity ultraviolet light. The source energy can be tuned to use either He I (21.22 eV) or He II (44.8 eV), which is significantly lower in energy than the Al Kα radiation that is typically used in XPS (1486.6 eV). Thus, rather than probing core level electrons, UPS examines the low binding energy valence electrons. The features that are observed in the spectrum depend on the density of states in the material being examined in addition to the ease with which electrons can be photoexcited from a given orbital. It should be noted that there are also secondary electrons (primary electrons are those that did not suffer inelastic collisions and secondary electrons are primary electrons that have lost varying amounts of energy) that comprise the background of the spectrum and originate from inelastically scattered secondary electrons, causing an intense spectral feature that is used to determine the WF of a material.[97] The important spectral features present and values that can be obtained from UPS are shown in Figure 1.13.

UPS is an extremely surface-sensitive technique and even the presence of a monolayer of material on the surface can drastically alter the spectrum obtained. Thus, since UPS does not utilize a very high-energy excitation source and the depth from which electrons can escape from a surface before being scattered is extremely dependent on the energy of the escaping electron, UPS only probes the top 2 – 3 nm of a material.[98] From this technique it is possible to determine the position of the valence band maximum (E_{VBM}), the Fermi level, and the WF of the material. This also means that the ionization potential (IP) of the material can be known as it is the sum of the E_{VBM} and the WF. The technique, however, does not afford direct information regarding the conduction band minimum and consequently the electron affinity of the material cannot be measured.

This information can be obtained from inverse photoemission spectroscopy,[99] which is beyond the scope of this thesis.

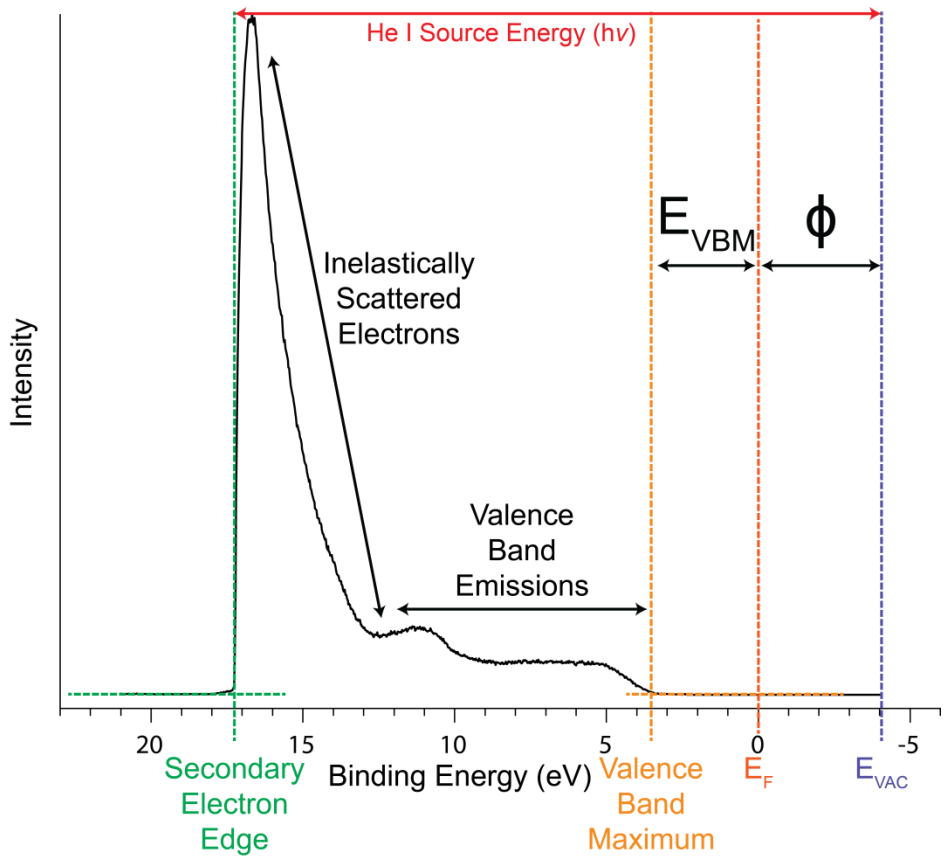

Figure 1.13 Example spectra of bare ZnO obtained from UPS analysis with important features noted. Both the work function (ϕ) and valence band maximum (E_{VBM}) are directly determined from the spectra as shown; ϕ = (He I Source Energy) – (Secondary Electron Edge) and E_{VBM} = (Valence Band Maximum) - E_F. The intensity of the Secondary Electron Edge comes from inelastically scattered electrons that have escaped to vacuum, but lost energy in the process.

1.4.4 Kelvin Probe

Kelvin probe (KP) is another technique that allows for the measurement of WF by probing the contact potential difference (CPD) between two materials. The technique

itself was originally proposed by Lord Kelvin in 1898 to obtain the CPD between metallic surfaces and has grown in popularity over the years as it does not need UHV and does not promote surface damage or desorption of weakly bound adsorbates, unlike photoemission spectroscopy techniques.[100] The technique relies on the fact that the two materials being examined have different WF values and when these materials are brought into physical contact with one another (typically through the use of a wire or metallic arm) the Fermi levels align with one another. This alignment causes an electrical potential to be formed between the substrate being examined and the KP, which is the CPD. The system then applies a nulling potential in the direction opposite the CPD and once a charge-free state has been achieved then the nulling potential is equal to the negative CPD (V_{Null} = -CPD). This is graphically shown in Figure 1.14. It should be noted that KP does not directly provide the WF of a material without calibration. Typically reference materials with well-known WF values are measured prior to the sample being analyzed. Highly-oriented pyrolytic graphite (HOPG) is commonly used for calibration as it can be readily cleaved to expose a fresh surface using the scotch tape technique and the material itself is very chemically inert (i.e. it does not form interface dipoles with adsorbed materials from the atmosphere).[101]

Various studies have been conducted to compare the WF obtained by KP with photoemission spectroscopy techniques.[100, 103-104] In general, the values obtained are relatively close to one another and both techniques afford reproducible results. From a practical standpoint, however, the recommendations of those conducting such studies has been to use techniques such as UPS when an absolute value for WF is needed, and to use

KP when conducting measurements on a large number of samples due to its ability to serve as a high-throughput screening technique.[104] A similar comparison has also been

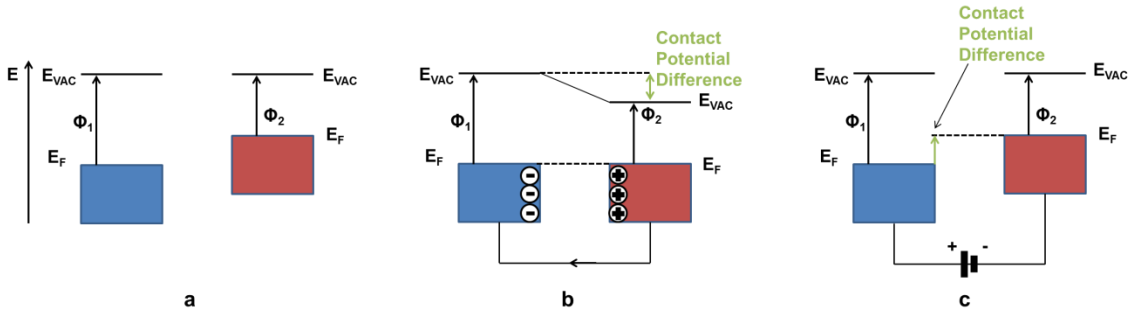

Figure 1.14 Schematic diagram for the principle of KP. Two materials with different WFs (**a**) are brought into contact with one another (**b**) causing Fermi level alignment. A nulling potential is applied and at the charge free point the nulling potential is equivalent to the CPD (**c**). Image adapted from Subrahmanyam[100] and Schlaf.[102]

conducted as part of the work reported in this thesis resulting in the same conclusion. On surfaces having different crystal orientations (or inhomogeneous modification) where there are non-uniform areas of WF, UPS tends to be biased toward lower values due to its smaller area of analysis causing the patches of lower WF values to skew the results. KP is less susceptible to this bias as it averages its measurement over a much larger area of the sample surface.[100]

1.4.5 Infrared Reflection-Absorption Spectroscopy

Infrared reflection-absorption spectroscopy (IRRAS) is an infrared (IR) based technique that relies on the use of an IR beam reflected off a surface at a grazing angle of incidence, rather than more commonly used IR techniques where light is transmitted directly through the sample on its way to the detector. Note that this technique is also known as reflection absorption infrared spectroscopy (RAIRS). Standard IR collected in

transmission mode is not applicable for studying surfaces as the sample would need to be both transparent in the IR region of the electromagnetic spectrum as well as be extremely thin so no absorption would be observed due to sample thickness.[99] Transmission mode also has the problem of passing through the monolayer of material over a small area and therefore does not have sufficient absorption for detection. Just like in any IR technique, however, the vibrational "fingerprint" of molecules on the surface is being examined, particularly those that are chemisorbed, and thus an analysis of the presence or absence of certain vibrational bands allows for characterizing the adsorbed layer down to as low a coverage of 0.5 % of a monolayer.[105] The highly sensitive nature of this technique is due partially to the need to conduct the measurement on a highly reflective surface such as gold and partly from the use of *p*-polarized IR light (IR light with its electric field along the plane of incidence).[93] As seen in Figure 1.15 the reflective substrate serves the purpose of allowing the incident light to pass through the monolayer twice, enhancing the signal-to-noise ratio of the resulting spectrum, and the use of the grazing angle greatly enhances the intrinsic electric field. The use of the *p*-polarized light then allows for only vibrational modes with dipole moments perpendicular to the surface to be observed. The technique can be enhanced by altering the polarization used (polarization modulation IRRAS, PM-IRRAS) and examining both *p*- and *s*-polarized light to determine tilt angle of modifiers from careful modelling and comparison with experimental vibrational mode intensities.

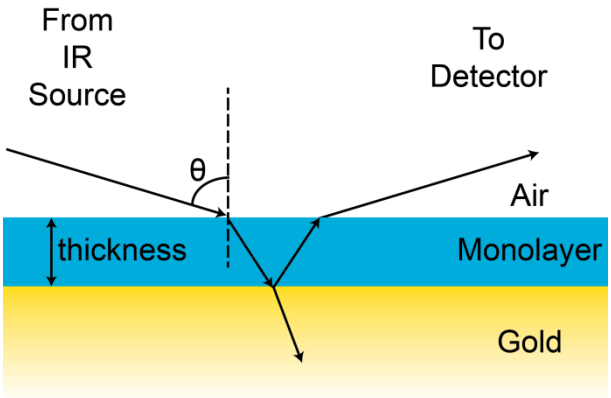

Figure 1.15 Schematic showing the external reflection method used in IRRAS of a generic monolayer deposited on a highly reflective gold substrate. The angle of incidence relative to the surface normal, θ, is typically 80°. Image adapted from Brune.[85]

IRRAS has proven to be an invaluable technique in determining the binding of modifiers on the surface, particularly in the case of phosphonic acids. The spectra collected by IRRAS are compared with the transmission IR of the phosphonic acid in powder form. Figure 1.16 shows two phosphonic acid modified surfaces, ZnO and ITO. In the case of these two metal oxides the phosphonic acids reflect the different binding modes that were shown in Figure 1.6. In the case of ZnO, due to the lack of P=O and P-O-H bands, it can be concluded that the binding of the surface modifier occurs mainly through a tridentate linkage with the surface.[106] In contrast, on ITO there is still a relatively intense P=O peak observed along with a small number of vibrational modes originating from P-O-H bonds leading to the conclusion that mainly a bidentate linkage is present.[79] Thus, while being a relatively straightforward technique, IRRAS provides a level of detail that can simultaneously confirm modification of the surface and provide information regarding molecular binding and confirmation of the modifier on the surface.

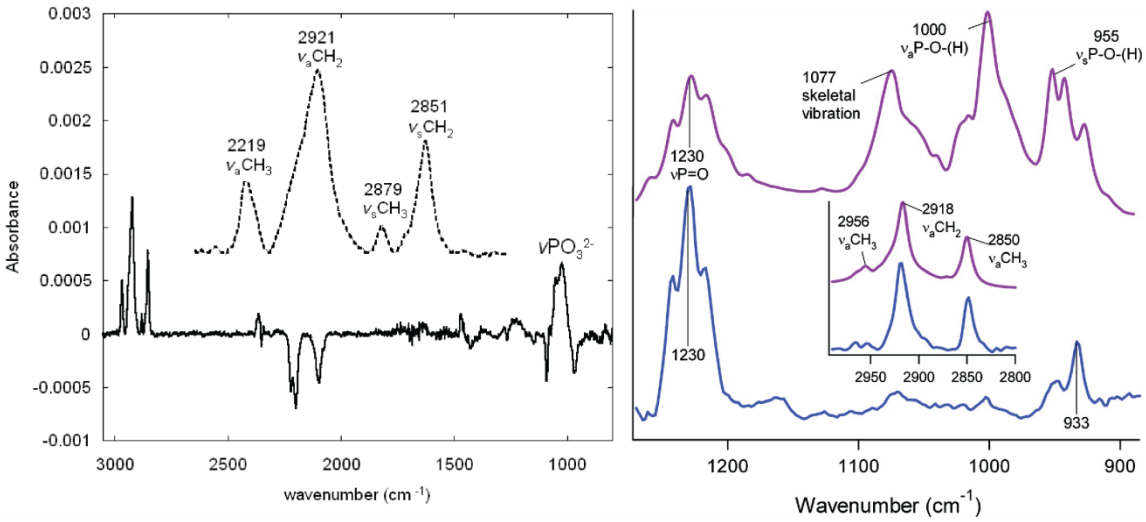

Figure 1.16 IRRAS spectra of octradecylphosphonic acid modified ZnO[106] (left) and ITO[79] (right). In the case of the ITO surface the top spectrum is the powder form of the phosphonic acid while the lower spectrum was collected by IRRAS. The inset for both ZnO and ITO highlight the C-H vibrational regions.

1.4.6 Near Edge X-ray Absorption Fine Structure

Near edge X-ray absorption fine structure (NEXAFS) is another X-ray based technique that is similar in basic principle to what has been previously discussed for other photoemission spectroscopic techniques such as XPS and UPS. Just like in XPS, X-rays are used to excite core level electrons, however, unlike XPS, NEXAFS does not use a fixed energy for the X-ray emission and a subsequent measurement of electron intensity as a function of kinetic energy. Instead the energy of the X-rays is varied around an ionization edge and the absorbed X-ray intensity is measured. There are two common ways in which the spectra are then recorded, either by transmission or electron yield as shown in Figure 1.17. In this case μ is the absorption coefficient of the X-rays and is logarithmically related to the detected intensity I_t in the case of transmission mode and directly proportional to I_e in the case of electron yield mode. Of the two techniques,

electron yield will be discussed in this thesis as this mode was used for the collection of data discussed in Chapter 4 and is more generally applicable as transmission mode requires the use of extremely thin, foil-like samples. Figure 1.18 shows a comparison of XPS and NEXAFS data.

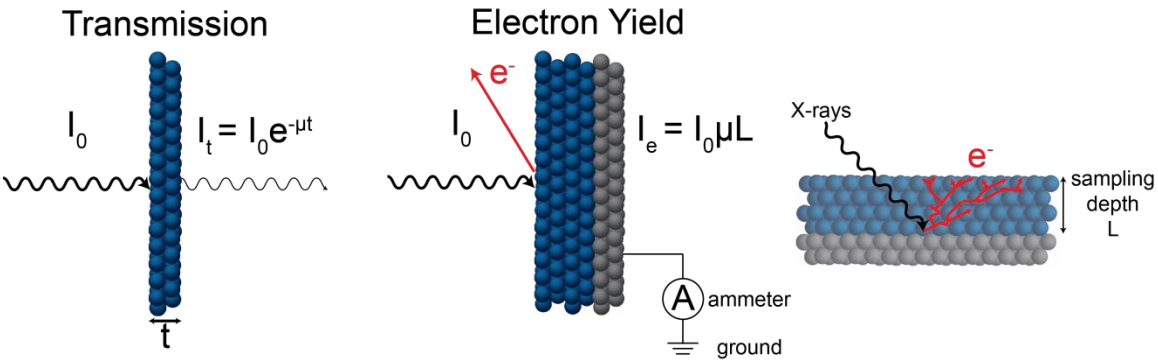

Figure 1.17 Two common measurement modes for NEXAFS, transmission (left) and electron yield (center). In transmission mode the intensity is dependent on the thickness of the sample being used (*t*), and in electron yield the intensity is dependent on the sampling depth (inelastic mean free path) of the X-rays (*L*). Image adapted from Stöhr.[107]

Measurements performed using the electron yield regime actually see the simultaneous collection of two distinct sets of data, the total electron yield (TEY) and the Auger electron yield (AEY) and the discrepancy between the two measurements results in a measure of the systematic uncertainty associated with the measurement and background removal (in the case of a modified substrate where the bare substrate background needs to be removed to better isolate the modifier). The measurement of AEY originates from the photoelectrons that are created by the absorption of the X-rays since as these high-energy particles are absorbed and subsequently displace electrons

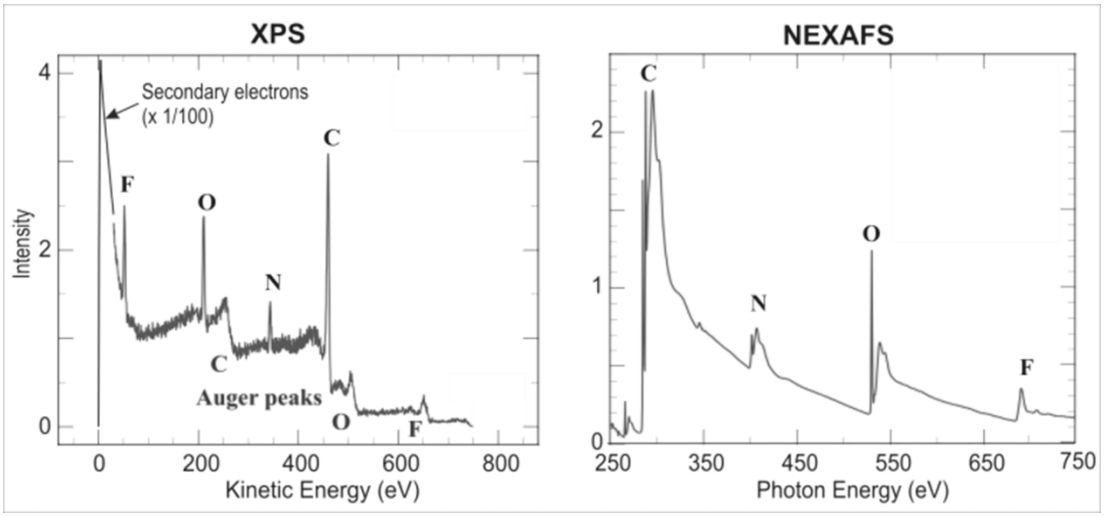

Figure 1.18 Comparison of XPS (left) and NEXAFS (right) spectra for a generic polymer containing carbon, oxygen, nitrogen, and fluorine. Peaks labelled on the bottom of the XPS data are Auger peaks and originate from Auger electrons as discussed below (image reproduced from literature).[107] Note the energy scale for XPS is in kinetic energy while the scale for NEXAFS is in photon energy.

from within an atom to higher lying empty states the resulting holes that are left behind are filled by higher lying electrons. The excess energy is released in the form of an Auger electron and since there is a direct correlation between the absorption of an X-ray and the emission of an Auger electron, AEY is a direct measure of the X-ray absorption in the sample. This process is schematically shown in Figure 1.19. Measurement of the TEY results from the formation of scattered secondary electrons created as Auger electrons escape the sample. Thus, electrons too deep in the sample do not have enough energy to overcome the WF and cannot escape the sample, which is why the sampling depth, *L*, is taken into account as shown in Figure 1.17.[107-108]

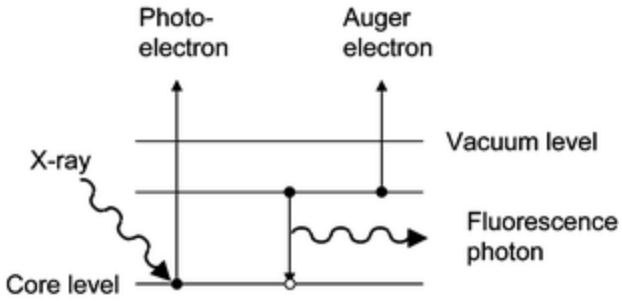

Figure 1.19 Schematic energy diagram for the absorption of an X-ray by a sample and the subsequent radiative and non-radiative decay processes that can occur when the resulting hole is filled. When the hole is filled radiatively there is a resulting fluorescence observed and when the hole is filled non-radiatively there is the emission of an Auger electron. In the case of low molecular weight molecules (such as surface modifiers) the Auger electron yield far surpasses that of the fluorescence yield.[109]

Just like XPS, NEXAFS is extremely sensitive to the environment surrounding an atom, however, unlike XPS, NEXAFS has the ability to determine the orientation of a material on the surface, for instance the tilt angle of a surface modifier. The tilt angle is able to be determined since NEXAFS is polarization dependent, meaning that the X-rays coming from the synchrotron light source are polarized and thus collection of data at multiple angles of incidence can afford this tilt angle information because only chemical bonds that are in plane with the polarized light source will be excited. This is best represented with an example, such as benzene as shown in Figure 1.20. Benzene has unoccupied sigma and pi antibonding orbitals (σ^* and π^*). When the electric field vector *E* is aligned almost parallel with the surface normal, only those orbitals having the same orientation experience excitation from the absorption of X-rays, which in this case is a π to π^*-excitation as seen in the experimental data (top right). Analogously, when the X-ray source has its electric field perpendicular to the surface normal only those orbitals which are also perpendicular to the surface normal are excited, which in this case are σ to

σ*-transitions (bottom right). This can be seen in representative experimental data also shown in the figure since at these extreme angles (20° and 90°) only one type of orbital dominates each spectrum. These intensities are proportional to the angle of incidence, and thus as can be seen from experimental data collected of a phenylphosphonic acid on the surface of indium zinc oxide (IZO), Figure 1.21, as the angle of incidence is swept from 20° to 90° the intensity of the π*- and σ*-transitions increase and decrease, respectively. Thus, NEXAFS affords molecular level detail not possible with other techniques, and when combined with experimental data from the other methods discussed in 1.4 a picture of not only how the molecule packs on the surface, but also its coverage, impact on the WF, and surface roughness is able to be determined.

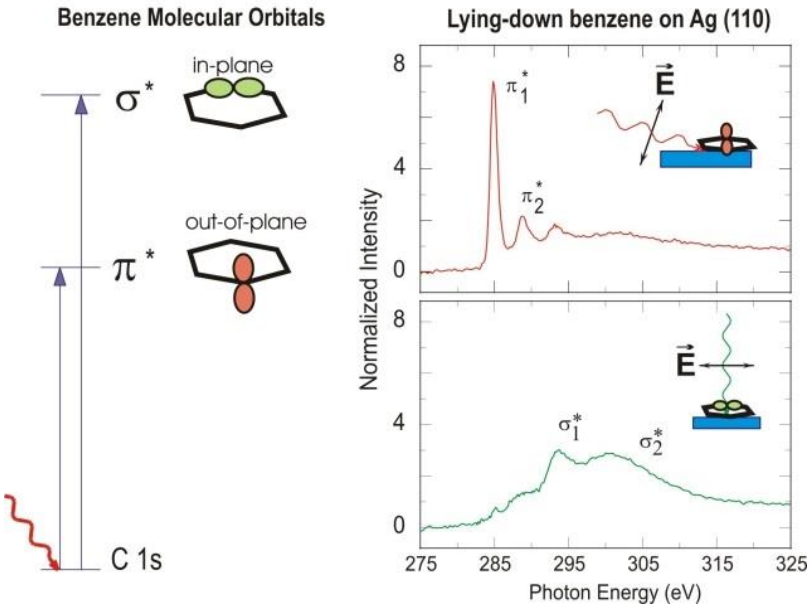

Figure 1.20 Example of the angular dependence of NEXAFS data due to the use of a polarized synchrotron light source for the case of benzene on silver. The benzene molecular orbitals have π-orbitals that are out of plane of the ring and σ-orbitals that are in the same plane as the benzene ring (left). Experimentally, when the X-ray electric field vector is parallel to these molecular orbitals they are selectively excited as observed in the resulting spectra. Sweeping over a range of angles allows for the determination of molecular orientations on the surface.[107]

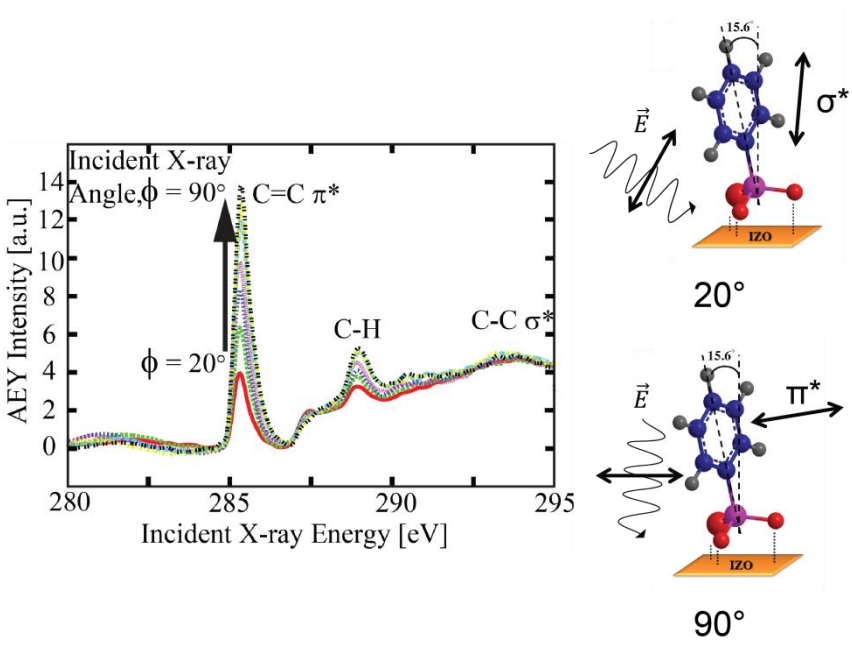

Figure 1.21 Experimental NEXAFS data for phenylphosphonic acid on the surface of IZO collected at angles between 20° and 90° (left). The molecules on the right schematically demonstrate the angular dependence of the orbitals being excited based on the incident angle of the X-ray source. As can be readily observed, as the angle of incidence increases from 20° to 90° the intensity of the π*-transition also drastically increases. Image modified from Gliboff.[110]

1.5 Work Function Tuning with Surface Modifiers

A large portion of this work is dedicated to the use of examining the ability of various surface modifiers to alter the work function of metals and metal oxides. Chapters 3, 4, and 5 all see the use of either phosphonic acids or molecular dopants to tune the work function of surfaces such as gold, ITO, and ZnO, and then measure these changes with KP and/or UPS. Before addressing how these surface modifiers tune the work function, however, it is helpful to discuss why such tuning is needed and the potential application of surfaces that have had their work function altered in this manner.

1.5.1 Applications of Work Function Tuning

Tuning the work function of a substrate is particularly important in order to control the interface energetics of a semiconductor on top of an electrode, particularly if the semiconductor is organic in nature. Altering the interface between the underlying metal or metal oxide and the organic over layer can serve the purpose of enhancing the wettability of the inorganic substrate by the organic material leading to more homogeneous films. In the current context, however, work function tuning allows for better energy-level alignment in organic optoelectronic devices thereby decreasing the energetic barriers for carrier injection depending on the device. Decreasing such injection barriers enhances the efficiency of the device by minimizing the energy barrier that must be overcome before current can flow.[111] Take for instance the case of an organic light emitting diode (OLED) using an ITO electrode and a generic hole-transporting layer (HTL), as shown in Figure 1.22. In this case, there is a barrier to the injection of holes from the electrode to the HTL given by ΔE_{hole}. Until this barrier is energetically overcome, current cannot flow into the OLED device and consequently it will not turn on. If a surface modifier (such as a phosphonic acid) is used to modify the surface of ITO and increase its work function (in the case of the electron-injecting electrode a decrease in work function would be desirable) this means there is also an increase in the vacuum level relative to the bare ITO surface. Thus, when the HTL is deposited on top of the modified ITO the energetic barrier to have emission from the OLED, ΔE_{hole}, is drastically decreased, thereby enhancing overall device performance.[78]

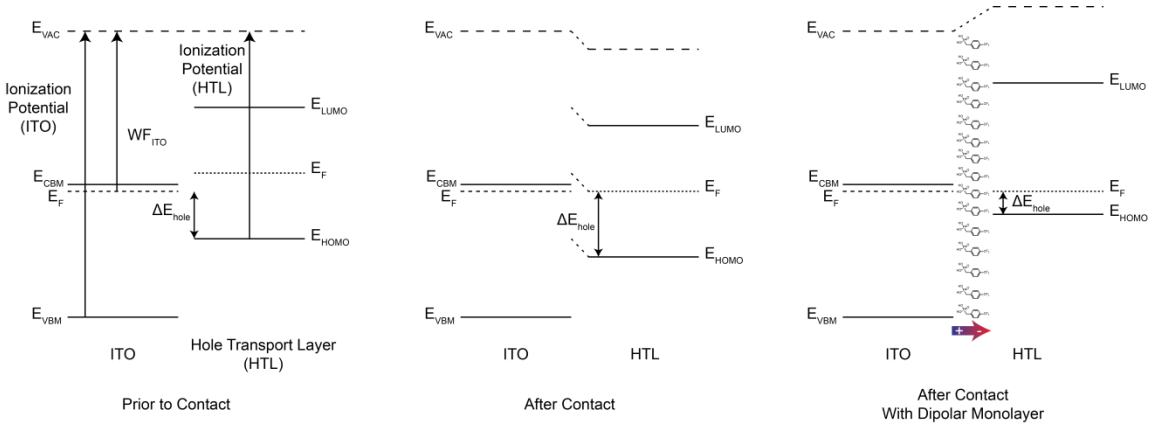

Figure 1.22 Image showing band diagrams for an ITO electrode and a generic hole transporting layer before contact, with a barrier to hole injection into the HTL given as ΔE_{hole} (left). When the two materials are in contact the Fermi levels align with one another (center). The barrier to hole injection after contact (ΔE_{hole}) is still rather large. A surface modifier with a dipole (such as a phosphonic acid) is used to modify the surface of the ITO (right). The modified ITO and HTL surfaces are now brought into contact with one another and because the WF of the ITO has been increased by the modifier, the barrier to hole injection has been greatly diminished. Image adapted from Hotchkiss.[78]

The previous scenario discussed the increase of work function through the use of surface modifiers to allow for a decreased barrier to hole injection into a device, but typical optoelectronic devices also require the presence of a low WF metal for the collection or injection of electrons. Both increasing and decreasing the WF of metals and metal oxides is a major aspect of this work, but it is particularly important to highlight the need to decrease the WF of substrates. That is because most low WF metals that can be used are typically alkaline earth metals such as calcium or magnesium or have thin coatings of alkali metals on top (e.g. lithium or cesium). Such materials, while having an intrinsically low WF, are also extremely reactive with oxygen and water and therefore do not maintain this low WF without some form of encapsulation.[112] Thus, an effort has been made to examine ways in which electrodes with higher native WF values such as ITO can be modified to serve as a low WF electrode thereby mitigating the need for

highly reactive alternatives. Success has been made modifying surfaces with small molecules[113-115] and amine containing polymers[112] to accomplish this goal, furthering the importance a surface modifier can have in the overall architecture and performance of a device.

1.5.2 Work Function Changes Induced by Surface Modifiers

Through the use of theoretical modelling, it has been possible to better characterize the components that contribute to the WF modification of a substrate through the use of a surface modifier such as a phosphonic acid. This relationship is summarized in Equation 1.1.

$$\Delta\phi = \Delta\phi_{SD} + \Delta\phi_{GEOM} + BD \qquad \text{Equation 1.1}$$

This means that the overall WF change ($\Delta\phi$) can be approximated as the sum of three distinct components, which are:

- the chemical bonding of the surface modifier to the underlying substrate, which is the bond dipole (BD)
- the change in surface geometry (and thus electron distribution) that occurs between the geometry optimized bare surface and the surface in its post-modified optimized geometry ($\Delta\phi_{GEOM} = \phi_{modified} - \phi_{pristine}$)
- the surface dipole that is induced by the modifier once attached to the surface ($\Delta\phi_{SD}$), which changes the vacuum level[111, 116]

It is important to note that the component $\Delta\phi_{SD}$ includes within it contributions that come from the molecular dipole as it sits relative to the surface normal and the coverage of the modifier since modifiers tend to interact with one another at higher coverage densities causing depolarization of their dipoles.

1.6 Organization of Thesis and General Overview

This general introduction to surface science, analytical techniques, and surface modification serves as the gateway to the later chapters. The basic concepts discussed within the previous underpin the concepts and studies that will be explored in greater detail throughout the subsequent chapters. While all the chapters have a focus on surface modification, each one examines different particular aspects of the modification process ranging from synthesis, modification methods, characterizing monolayers, surface doping, and surface etching.

Chapter 2 focuses on the design and synthesis of the surface modifiers that are employed throughout the remainder of the thesis. These surface modifiers include binding groups that should already be familiar from 1.2.2 including phosphonic acids, alkoxy silanes, chlorosilanes, and carboxylic acids. The bulk of this chapter focuses on the experimental methods that are involved in the synthesis of the 38 compounds that have been made related to surface modification. There is also a discussion regarding NMR analysis of phosphorus based compounds, as the presence of ^{31}P tends to complicate the coupling observed in ^{1}H and ^{13}C NMR. Similarly, heteroatom techniques such as ^{31}P and ^{19}F NMR are discussed since both provide useful demonstrations of purity for the fluorinated and non-fluorinated phosphonic acids that have been synthesized. While not all of the compounds shown in this chapter have been directly used in the remainder of the document, references are provided to published literature articles or patents using the compounds.

Chapter 3 highlights work conducted in collaboration with members of David Ginger's group at the University of Washington and Jean-Luc Brédas' group at the

Georgia Institute of Technology. This chapter focuses on examining phosphonic acids on the surface of ITO in an effort to better understand the relationship that exists between the orientation and coverage of such modifiers on the surface of ITO, the resulting WF that is measured after modification, and how these factors interrelate with one another. This work is an extension of material that has already been published in the literature investigating orientation of phenyl and alkyl phosphonic acids[110, 117] and specifically uses benzyl phosphonic acids on ITO, as this type of modifier has also been utilized in device architectures,[118-120] but no examination of molecular ordering had thus far been performed.

Chapter 4 expands upon previous work that was conducted to determine the binding of phosphonic acids to the surface of ZnO.[106] Previous work laid the initial ground work demonstrating the ability of phosphonic acids to modify the surface of ZnO in a mainly tridentate manner with minimal impact to the underlying surface. However, no work had been done to examine if the modifiers had an impact on the WF of ZnO that mirrored what had already been reported for ITO. Thus, phosphonic acids containing inherent molecular dipoles anticipated to either increase or decrease the WF of ZnO that has been deposited by atomic layer deposition (ALD) have been examined. Investigations have probed whether modification conditions impact the measured WF, the ability to spin coat phosphonic acids onto the surface of ZnO, and a direct comparison with ITO to determine whether both metal oxides have similar trends in WF changes when using the same phosphonic acid modifiers. Etching of ZnO by these surface modifiers has also been examined and pKa measurements conducted in an effort to determine the origin of the observed etching.

Chapter 5 discusses research done in collaboration with members of Seth Marder's and Jean-Luc Brédas' groups at Georgia Tech. The central theme of the chapter is again on the tuning of WF, but instead of examining the use of phosphonic acids, redox-active materials that serve as surface dopants are utilized. As briefly mentioned in 1.5.1 research in this area has already shown the ability of small molecules and polymers to drastically decrease the WF of gold, ITO, and ZnO. This chapter expands upon that work by examining both *n*- and *p*-type dopants that are more strongly reducing or oxidizing, respectively, than materials already reported in the literature. The goal of the chapter is to determine if there is a correlation between the oxidation or reduction strength of a material and its ability to alter the WF of a metal or metal oxide. Similar research has recently been conducted on grapheme using some of the same *n*-type redox active molecules with significant WF decreases.[121] The chapter presents not only experimental evidence, but also theoretical calculations, to examine the origin of the WF change due to these surface dopants.

Chapter 6 serves as an opportunity to summarize the findings reported throughout the thesis and better put these results in context with one another. This chapter also includes a summary of WF values achieved by numerous different phosphonic acids on a variety of substrates. Also presented is a discussion regarding the possible future directions of this research.

Appendix A focuses on work that was conducted in collaboration with members from Elisa Riedo's and Jennifer Curtis' groups at Georgia Tech. This work, while still involving the use of surface modification, has been placed in an appendix as its theme is significantly different from that of the other chapters. The goal of this work was to create

monolayers with thermally labile protecting groups that could be selectively removed through the use of a heated AFM cantilever, a technique known as thermochemical nanolithography (TCNL). Similar work has been previously conducted on polymer based samples.[122-124] However, non-specific binding of materials to the surface is a current limitation as well as being limited to only two different polymers that can be used as a platform for patterning. These limitations are what spurred investigation into monolayers for use with TCNL. Reported in this section are the efforts to characterize the thermal deprotection of a dimethoxybenzyloxycarbonyl amine protecting group and bulk studies conducted on surfaces to examine the ability to deprotect the monolayer and subsequently bind materials to the newly created active sites.

Appendix B provides a more detailed explanation of how coverage of monolayers on surfaces are calculated based on a comparison of XPS data with theoretically modelled surfaces.

1.7 References

[1] Somorjai, G. A.; Li, Y., Impact of Surface Chemistry. *Proceedings of the National Academy of Sciences* **2011,** *108*, 917-924.

[2] Somorjai, G. A., *Introduction to Surface Chemistry and Catalysis*. Wiley: New York, 1994.

[3] Ertl, G., *Reactions at Solid Surfaces*. Wiley: Hoboken, N.J., 2009.

[4] Noguera, C., *Physics and Chemistry at Oxide Surfaces*. Digitally printed 1st pbk. ed.; Cambridge University Press: Cambridge ; New York, 2005.

[5] Altman, E. I.; Bienfait, M.; Bonzel, H. P.; Brune, H.; Diehl, R.; Jung, M. Y. L.; Lifshitz, V. G.; Michel, M. E.; Miranda, R.; McGrath, R.; Oura, K.; Saranin, A. A.; Seebauer, E. G.; Zeppenfeld, P.; Zotov, A. V., *Group Iii: Condensed Matter. Vol. 42, Physics of Covered Solid Surfaces. Subvolume a Adsorbed Layers on Surfaces*. Springer: 2002.

[6] Howarter, J. A.; Youngblood, J. P., Self-Cleaning and Next Generation Anti-Fog Surfaces and Coatings. *Macromolecular Rapid Communications* **2008,** *29*, 455-466.

[7] Chevallier, P.; Turgeon, S. p.; Sarra-Bournet, C.; Turcotte, R. l.; Laroche, G. t., Characterization of Multilayer Anti-Fog Coatings. *ACS Applied Materials & Interfaces* **2011,** *3*, 750-758.

[8] Technology | Liquipel. http://www.liquipel.com/about/technology/ (accessed January 24, 2014).

[9] Lee, K. T.; Jeong, S.; Cho, J., Roles of Surface Chemistry on Safety and Electrochemistry in Lithium Ion Batteries. *Accounts of Chemical Research* **2012,** *46*, 1161-1170.

[10] Prutton, M., *Introduction to Surface Physics*. Oxford University Press: Oxford, 1994.

[11] Zangwill, A., *Physics at Surfaces*. Cambridge University Press: Cambridge Cambridgeshire ; New York, 1988.

[12] Tabor, D., Babylonian Lecanomancy: An Ancient Text on the Spreading of Oil on Water. *Journal of Colloid and Interface Science* **1980,** *75*, 240-245.

[13] Cuneiform Texts from Babylonian Tablets in the British Museum Part V. British Museum: London, 1898; pp Plate IV, 22446.

[14] Williams, L. P., *Michael Faraday, a Biography*. Basic Books: New York, 1965.

[15] Susskind, C., In *Advances in Electronics and Electron Physics*, Marton, L. M. a. C., Ed. Academic Press: New York, 1980; Vol. 50, pp 241-260.

[16] Desjonquères, M. C.; Spanjaard, D., *Concepts in Surface Physics*. 2nd ed.; Springer: Berlin ; New York, 1996.

[17] Kiejna, A.; Wojciechowski, K., *Metal Surface Electron Physics*. 1st ed.; Elsevier Science Ltd.: Kidlington, Oxford, 1996.

[18] Woodruff, D. P., *Surface Dynamics*. Elsevier: Amsterdam ; London, 2003.

[19] da C. Andrade, E. N., The History of the Vacuum Pump. *Vacuum* **1959,** *9*, 41-47.

[20] Hablanian, M. H., Comments on the History of Vacuum Pumps. *Journal of Vacuum Science & Technology A* **1984,** *2*, 118-125.

[21] Redhead, P., History of Vacuum Devices. *CERN European Organization for Nuclear Research - Reports* **1999**, 281-290.

[22] Redhead, P. A., Vacuum Science and Technology: 1950–2003. *Journal of Vacuum Science & Technology A* **2003,** *21*, S12-S14.

[23] Mittal, K. L., *Surface Contamination and Cleaning*. VSP: Utrecht ; Boston, 2003.

[24] Pulker, H. K., *Coatings on Glass*. 2nd, rev. ed.; Elsevier: Amsterdam ; New York, 1999.

[25] Cras, J. J.; Rowe-Taitt, C. A.; Nivens, D. A.; Ligler, F. S., Comparison of Chemical Cleaning Methods of Glass in Preparation for Silanization. *Biosensors and Bioelectronics* **1999,** *14*, 683-688.

[26] Kern, W., The Evolution of Silicon Wafer Cleaning Technology. *Journal of the Electrochemical Society* **1990,** *137*, 1887-1892.

[27] *Handbook of Silicon Wafer Cleaning Technology*. 2nd ed.; William Andrew: Norwich, NY, 2008.

[28] Birch, W. R. Coatings: An Introduction to the Cleaning Procedures. http://www.solgel.com/articles/June00/Birch/cleaning.htm (accessed July 8, 2009).

[29] Chung, Y., *Practical Guide to Surface Science and Spectroscopy*. Academic Press: San Diego, 2001.

[30] Henke, L.; Nagy, N.; Krull, U. J., An Afm Determination of the Effects on Surface Roughness Caused by Cleaning of Fused Silica and Glass Substrates in the Process of Optical Biosensor Preparation. *Biosensors and Bioelectronics* **2002,** *17*, 547-555.

[31] Donley, C.; Dunphy, D.; Paine, D.; Carter, C.; Nebesny, K.; Lee, P.; Alloway, D.; Armstrong, N. R., Characterization of Indium−Tin Oxide Interfaces Using X-Ray Photoelectron Spectroscopy and Redox Processes of a Chemisorbed Probe Molecule: Effect of Surface Pretreatment Conditions. *Langmuir* **2001,** *18*, 450-457.

[32] Brumbach, M.; Veneman, P. A.; Marrikar, F. S.; Schulmeyer, T.; Simmonds, A.; Xia, W.; Lee, P.; Armstrong, N. R., Surface Composition and Electrical and Electrochemical Properties of Freshly Deposited and Acid-Etched Indium Tin Oxide Electrodes. *Langmuir* **2007,** *23*, 11089-11099.

[33] Love, J. C.; Estroff, L. A.; Kriebel, J. K.; Nuzzo, R. G.; Whitesides, G. M., Self-Assembled Monolayers of Thiolates on Metals as a Form of Nanotechnology. *Chemical Reviews* **2005,** *105*, 1103-1169.

[34] Ulman, A., Formation and Structure of Self-Assembled Monolayers. *Chemical Reviews* **1996,** *96*, 1533-1554.

[35] Oura, K.; Lifshits, V. G.; Saranin, A. A.; Zotov, A. V., *Surface Science: An Introduction*. Springer: 2010.

[36] Norsko, J. K., Chemisorption on Metal Surfaces. *Reports on Progress in Physics* **1990,** *53*, 1253.

[37] Kolasinski, K. K.; Kolasinski, K. W., *Surface Science: Foundations of Catalysis and Nanoscience*. Wiley: 2012.

[38] Arkles, B.; Pan, Y.; Mi Kim, Y.; Eisenbraun, E.; Miller, C.; Kaloyeros, A. E. A., Hydridosilane Modification of Metals: An Exploratory Study. *Journal of Adhesion Science and Technology* **2012,** *26*, 41-54.

[39] Neouze, M. A.; Schubert, U., Surface Modification and Functionalization of Metal and Metal Oxide Nanoparticles by Organic Ligands. *Monatshefte für Chemie* **2008,** *139*, 183-195.

[40] Langmuir, I., The Constitution and Fundamental Properties of Solids and Liquids Ii. Liquids. *Journal of the American Chemical Society* **1917,** *39*, 1848-1906.

[41] Schreiber, F., Structure and Growth of Self-Assembling Monolayers. *Progress in Surface Science* **2000,** *65*, 151-257.

[42] Blodgett, K. B., Films Built by Depositing Successive Monomolecular Layers on a Solid Surface. *Journal of the American Chemical Society* **1935,** *57*, 1007-1022.

[43] Blodgett, K. B., Monomolecular Films of Fatty Acids on Glass. *Journal of the American Chemical Society* **1934,** *56*, 495-495.

[44] Nuzzo, R. G.; Allara, D. L., Adsorption of Bifunctional Organic Disulfides on Gold Surfaces. *Journal of the American Chemical Society* **1983,** *105*, 4481-4483.

[45] Nuzzo, R. G.; Zegarski, B. R.; Dubois, L. H., Fundamental Studies of the Chemisorption of Organosulfur Compounds on Gold(111). Implications for Molecular Self-Assembly on Gold Surfaces. *Journal of the American Chemical Society* **1987,** *109*, 733-740.

[46] Vericat, C.; Vela, M. E.; Benitez, G.; Carro, P.; Salvarezza, R. C., Self-Assembled Monolayers of Thiols and Dithiols on Gold: New Challenges for a Well-Known System. *Chemical Society Reviews* **2010,** *39*, 1805-1834.

[47] Schwartz, D. K., Mechanisms and Kinetics of Self-Assembled Monolayer Formation. *Annual Review of Physical Chemistry* **2001,** *52*, 107-137.

[48] Love, J. C.; Wolfe, D. B.; Haasch, R.; Chabinyc, M. L.; Paul, K. E.; Whitesides, G. M.; Nuzzo, R. G., Formation and Structure of Self-Assembled Monolayers of Alkanethiolates on Palladium. *Journal of the American Chemical Society* **2003,** *125*, 2597-2609.

[49] Folkers, J. P.; Laibinis, P. E.; Whitesides, G. M., Self-Assembled Monolayers of Alkanethiols on Gold: Comparisons of Monolayers Containing Mixtures of Short- and Long-Chain Constituents with Methyl and Hydroxymethyl Terminal Groups. *Langmuir* **1992,** *8*, 1330-1341.

[50] Vericat, C.; Benitez, G. A.; Grumelli, D. E.; Vela, M. E.; Salvarezza, R. C., Thiol-Capped Gold: From Planar to Irregular Surfaces. *Journal of Physics: Condensed Matter* **2008,** *20*, 184004.

[51] Yang, G.; Amro, N. A.; Starkewolfe, Z. B.; Liu, G.-y., Molecular-Level Approach to Inhibit Degradations of Alkanethiol Self-Assembled Monolayers in Aqueous Media. *Langmuir* **2004,** *20*, 3995-4003.

[52] Kind, M.; Wöll, C., Organic Surfaces Exposed by Self-Assembled Organothiol Monolayers: Preparation, Characterization, and Application. *Progress in Surface Science* **2009,** *84*, 230-278.

[53] Vioux, A.; Le Bideau, J.; Mutin, P. H.; Leclercq, D., Hybrid Organic-Inorganic Materials Based on Organophosphorus Derivatives. *New Aspects in Phosphorus Chemistry Iv* **2004,** *232*, 145-174.

[54] Haensch, C.; Hoeppener, S.; Schubert, U. S., Chemical Modification of Self-Assembled Silane Based Monolayers by Surface Reactions. *Chemical Society Reviews* **2010,** *39*, 2323-2334.

[55] Mutin, P. H.; Guerrero, G.; Vioux, A., Hybrid Materials from Organophosphorus Coupling Molecules. *Journal of Materials Chemistry* **2005,** *15*, 3761-3768.

[56] VanDerVoort, P.; Vansant, E. F., Silylation of the Silica Surface a Review. *Journal of Liquid Chromatography & Related Technologies* **1996,** *19*, 2723-2752.

[57] Vansant, E. F.; Voort, P. v. d.; Vrancken, K. C., *Characterization and Chemical Modification of the Silica Surface*. Elsevier: Amsterdam ; New York, 1995.

[58] Mutin, P. H.; Guerrero, G.; Vioux, A., Organic-Inorganic Hybrid Materials Based on Organophosphorus Coupling Molecules: From Metal Phosphonates to Surface Modification of Oxides. *Comptes Rendus Chimie* **2003,** *6*, 1153-1164.

[59] Jadhav, S., Self-Assembled Monolayers (Sams) of Carboxylic Acids: An Overview. *Central European Journal of Chemistry* **2011,** *9*, 369-378.

[60] Allara, D. L.; Nuzzo, R. G., Spontaneously Organized Molecular Assemblies. 1. Formation, Dynamics, and Physical Properties of N-Alkanoic Acids Adsorbed from Solution on an Oxidized Aluminum Surface. *Langmuir* **1985,** *1*, 45-52.

[61] Allara, D. L.; Nuzzo, R. G., Spontaneously Organized Molecular Assemblies. 2. Quantitative Infrared Spectroscopic Determination of Equilibrium Structures of Solution-Adsorbed N-Alkanoic Acids on an Oxidized Aluminum Surface. *Langmuir* **1985,** *1*, 52-66.

[62] Colvin, V. L.; Goldstein, A. N.; Alivisatos, A. P., Semiconductor Nanocrystals Covalently Bound to Metal Surfaces with Self-Assembled Monolayers. *Journal of the American Chemical Society* **1992,** *114*, 5221-5230.

[63] Pawsey, S.; Yach, K.; Halla, J.; Reven, L., Self-Assembled Monolayers of Alkanoic Acids: A Solid-State Nmr Study. *Langmuir* **2000,** *16*, 3294-3303.

[64] Paik, W.; Han, S.; Shin, W.; Kim, Y., Adsorption of Carboxylic Acids on Gold by Anodic Reaction. *Langmuir* **2003,** *19*, 4211-4216.

[65] Bandyopadhyay, K.; Patil, V.; Vijayamohanan, K.; Sastry, M., Adsorption of Silver Colloidal Particles through Covalent Linkage to Self-Assembled Monolayers. *Langmuir* **1997,** *13*, 5244-5248.

[66] Gardner, T. J.; Frisbie, C. D.; Wrighton, M. S., Systems for Orthogonal Self-Assembly of Electroactive Monolayers on Au and Ito: An Approach to Molecular Electronics. *Journal of the American Chemical Society* **1995,** *117*, 6927-6933.

[67] Vercelli, B.; Zotti, G.; Schiavon, G.; Zecchin, S.; Berlin, A., Adsorption of Hexylferrocene Phosphonic Acid on Indium−Tin Oxide Electrodes. Evidence of Strong Interchain Interactions in Ferrocene Self-Assembled Monolayers. *Langmuir* **2003,** *19*, 9351-9356.

[68] Woodward, J. T.; Ulman, A.; Schwartz, D. K., Self-Assembled Monolayer Growth of Octadecylphosphonic Acid on Mica. *Langmuir* **1996,** *12*, 3626-3629.

[69] Woodward, J. T.; Schwartz, D. K., In Situ Observation of Self-Assembled Monolayer Growth. *Journal of the American Chemical Society* **1996,** *118*, 7861-7862.

[70] Woodward, J. T.; Doudevski, I.; Sikes, H. D.; Schwartz, D. K., Kinetics of Self-Assembled Monolayer Growth Explored Via Submonolayer Coverage of Incomplete Films. *The Journal of Physical Chemistry B* **1997,** *101*, 7535-7541.

[71] Rigney, M. P.; Funkenbusch, E. F.; Carr, P. W., Physical and Chemical Characterization of Microporous Zirconia. *Journal of Chromatography A* **1990,** *499*, 291-304.

[72] Randon, J.; Blanc, P.; Paterson, R., Modification of Ceramic Membrane Surfaces Using Phosphoric Acid and Alkyl Phosphonic Acids and Its Effects on Ultrafiltration of Bsa Protein. *Journal of Membrane Science* **1995,** *98*, 119-129.

[73] Wieserman, L. F.; Martin, E. S.; Wefers, K.; Novak, J. W., Jr.; Cross, K.; Conroy, C. M. Active Material Useful as a Multipurpose Adsorbent Comprising Metal Oxide/Hydroxide Particles Reacted with One or More Phosphorus-Containing Materials. EP273756A2, 1988.

[74] Wieserman, L. F.; Wefers, K.; Cross, K.; Martin, E. S. Adsorbents from Metal Oxide/Hydroxide Particles Reacted with Phosphorus-Containing Organic Acids. US4994429A, 1991.

[75] Yang, H. C.; Aoki, K.; Hong, H. G.; Sackett, D. D.; Arendt, M. F.; Yau, S. L.; Bell, C. M.; Mallouk, T. E., Growth and Characterization of Metal(Ii) Alkanebisphosphonate Multilayer Thin Films on Gold Surfaces. *Journal of the American Chemical Society* **1993,** *115*, 11855-11862.

[76] Chidsey, C. E. D.; Loiacono, D. N., Chemical Functionality in Self-Assembled Monolayers: Structural and Electrochemical Properties. *Langmuir* **1990,** *6*, 682-691.

[77] Guerrero, G.; Mutin, P. H.; Vioux, A., Organically Modified Aluminas by Grafting and Sol-Gel Processes Involving Phosphonate Derivatives. *Journal of Materials Chemistry* **2001,** *11*, 3161-3165.

[78] Hotchkiss, P. J.; Jones, S. C.; Paniagua, S. A.; Sharma, A.; Kippelen, B.; Armstrong, N. R.; Marder, S. R., The Modification of Indium Tin Oxide with Phosphonic Acids: Mechanism of Binding, Tuning of Surface Properties, and Potential for Use in Organic Electronic Applications. *Accounts of Chemical Research* **2012,** *45*, 337-346.

[79] Paniagua, S. A.; Hotchkiss, P. J.; Jones, S. C.; Marder, S. R.; Mudalige, A.; Marrikar, F. S.; Pemberton, J. E.; Armstrong, N. R., Phosphonic Acid Modification of Indium-Tin Oxide Electrodes: Combined Xps/Ups/Contact Angle Studies. *Journal of Physical Chemistry C* **2008,** *112*, 7809-7817.

[80] Queffélec, C.; Petit, M.; Janvier, P.; Knight, D. A.; Bujoli, B., Surface Modification Using Phosphonic Acids and Esters. *Chemical Reviews* **2012**, 3777–3807.

[81] Hotchkiss, P. J. The Design, Synthesis, and Use of Phosphonic Acids for the Surface Modification of Metal Oxides. Ph.D. Thesis, Georgia Institute of Technology, Atlanta, GA, 2008.

[82] Cahen, D.; Kahn, A., Electron Energetics at Surfaces and Interfaces: Concepts and Experiments. *Advanced Materials* **2003,** *15*, 271-277.

[83] Ishii, H.; Sugiyama, K.; Ito, E.; Seki, K., Energy Level Alignment and Interfacial Electronic Structures at Organic/Metal and Organic/Organic Interfaces. *Advanced Materials* **1999,** *11*, 605-625.

[84] Myers, H. P., *Introductory Solid State Physics*. 2nd ed.; Taylor & Francis: London, 1997.

[85] Brune, D.; Hellborg, R.; Whitlow, H. J.; Hunderi, O., *Surface Characterization: A User's Sourcebook*. Wiley: 2008.

[86] Yao, N.; Wang, Z. L., Handbook of Microscopy for Nanotechnology. Kluwer Academic Publishers: Boston, 2005.

[87] Bubert, H.; Jenett, H., *Surface and Thin Film Analysis : Principles, Instrumentation, Applications*. Wiley-VCH: Weinheim, 2002.

[88] Magonov, S. N.; Whangbo, M.-H., *Surface Analysis with Stm and Afm : Experimental and Theoretical Aspects of Image Analysis*. VCH: Weinheim ; New York, 1996.

[89] Touzov, I.; Gorman, C. B., Tip-Induced Structural Rearrangements of Alkanethiolate Self-Assembled Monolayers on Gold. *The Journal of Physical Chemistry B* **1997,** *101*, 5263-5276.

[90] Barrena, E.; Ocal, C.; Salmeron, M., Evolution of the Structure and Mechanical Stability of Self-Assembled Alkanethiol Islands on Au(111) Due to Diffusion and Ripening. *The Journal of Chemical Physics* **1999,** *111*, 9797-9802.

[91] Moulder, J. F.; Chastain, J., *Handbook of X Ray Photoelectron Spectroscopy: A Reference Book of Standard Spectra for Identification and Interpretation of Xps Data*. Physical Electronics Division, Perkin-Elmer Corporation: 1995.

[92] Robinson, J. W.; Frame, E. M. S.; Frame, G. M., *Undergraduate Instrumental Analysis*. 6th ed.; M. Dekker: New York, 2005.

[93] Ulman, A., *Characterization of Organic Thin Films*. Butterworth-Heinemann, Manning: Boston, Greenwich, 1995.

[94] Jacobs, K. Ultra High Vacuum Lab. http://jacobs.physik.uni-saarland.de/instrumentation/uhvl.htm (accessed 2-10-2014).

[95] Matolín, V. Principles of Photoemission Spectroscopy (Pes). http://physics.mff.cuni.cz/kfpp/povrchy/method/xps-ve (accessed 3-14-2014).

[96] Smart, R.; McIntyre, S.; Bancroft, M.; Bello, I. X-Ray Photoelectron Spectroscopy. http://mmrc.caltech.edu/SS_XPS/XPS_PPT/XPS_Slides.pdf (accessed 3-14-2014).

[97] O'Connor, D. J.; Sexton, B. A.; Smart, R. S. C., *Surface Analysis Methods in Materials Science*. 2nd ed.; Springer: Berlin ; New York, 2003.

[98] Eland, J. H. D., *Photoelectron Spectroscopy : An Introduction to Ultraviolet Photoelectron Spectroscopy in the Gas Phase*. 2nd ed.; Butterworths: London ; Boston, 1984.

[99] Rivière, J. C.; Myhra, S., *Handbook of Surface and Interface Analysis : Methods for Problem-Solving*. 2nd ed.; CRC Press: Boca Raton, 2009.

[100] Subrahmanyam, A.; Kumar, C. S., *Kelvin Probe for Surface Engineering : Fundamentals and Design*. Ane Books Pvt Ltd: New Delhi, 2010.

[101] Hansen, W. N.; Hansen, G. J., Standard Reference Surfaces for Work Function Measurements in Air. *Surface Science* **2001,** *481*, 172-184.

[102] Schlaf, R. Tutorial on Kelvin Probe Measurements. http://rsl.eng.usf.edu/Documents/Tutorials/TutorialsKelvinProbe.pdf (accessed 6-23-2011).

[103] Beerbom, M. M.; Lagel, B.; Cascio, A. J.; Doran, B. V.; Schlaf, R., Direct Comparison of Photoemission Spectroscopy and in Situ Kelvin Probe Work Function Measurements on Indium Tin Oxide Films. *Journal of Electron Spectroscopy and related Phenomena* **2006,** *152*, 12-17.

[104] Kim, J. S.; Lagel, B.; Moons, E.; Johansson, N.; Baikie, I. D.; Salaneck, W. R.; Friend, R. H.; Cacialli, F., Kelvin Probe and Ultraviolet Photoemission Measurements of Indium Tin Oxide Work Function: A Comparison. *Synthetic Metals* **2000,** *111*, 311-314.

[105] Bordo, V. G.; Rubahn, H. G., *Optics and Spectroscopy at Surfaces and Interfaces*. Wiley-VCH: Weinheim, 2005.

[106] Hotchkiss, P. J.; Malicki, M.; Giordano, A. J.; Armstrong, N. R.; Marder, S. R., Characterization of Phosphonic Acid Binding to Zinc Oxide. *Journal of Materials Chemistry* **2011,** *21*, 3107-3112.

[107] Stöhr, J. Nexafs Spectroscopy. http://www-ssrl.slac.stanford.edu/stohr/nexafs.htm (accessed 9-15-2012).

[108] Stöhr, J., *Nexafs Spectroscopy*. 1st ed.; Springer: Berlin ; New York, 1996.

[109] Hahner, G., Near Edge X-Ray Absorption Fine Structure Spectroscopy as a Tool to Probe Electronic and Structural Properties of Thin Organic Films and Liquids. *Chemical Society Reviews* **2006,** *35*, 1244-1255.

[110] Gliboff, M.; Sang, L. Z.; Knesting, K. M.; Schalnat, M. C.; Mudalige, A.; Ratcliff, E. L.; Li, H.; Sigdel, A. K.; Giordano, A. J.; Berry, J. J.; Nordlund, D.; Seidler, G. T.; Bredas, J. L.; Marder, S. R.; Pemberton, J. E.; Ginger, D. S., Orientation of Phenylphosphonic Acid Self-Assembled Monolayers on a Transparent Conductive Oxide: A Combined Nexafs, Pm-Irras, and Dft Study. *Langmuir* **2013,** *29*, 2166-2174.

[111] Heimel, G.; Romaner, L.; Zojer, E.; Bredas, J. L., The Interface Energetics of Self-Assembled Monolayers on Metals. *Accounts of Chemical Research* **2008,** *41*, 721-729.

[112] Zhou, Y. H.; Fuentes-Hernandez, C.; Shim, J.; Meyer, J.; Giordano, A. J.; Li, H.; Winget, P.; Papadopoulos, T.; Cheun, H.; Kim, J.; Fenoll, M.; Dindar, A.; Haske, W.; Najafabadi, E.; Khan, T. M.; Sojoudi, H.; Barlow, S.; Graham, S.; Bredas, J. L.; Marder, S. R.; Kahn, A.; Kippelen, B., A Universal Method to Produce Low-Work Function Electrodes for Organic Electronics. *Science* **2012,** *336*, 327-332.

[113] Broker, B.; Blum, R. P.; Frisch, J.; Vollmer, A.; Hofmann, O. T.; Rieger, R.; Mullen, K.; Rabe, J. P.; Zojer, E.; Koch, N., Gold Work Function Reduction by 2.2 Ev with an Air-Stable Molecular Donor Layer. *Applied Physics Letters* **2008,** *93*, 243303.

[114] Lindell, L.; Unge, M.; Osikowicz, W.; Stafstrom, S.; Salaneck, W. R.; Crispin, X.; de Jong, M. P., Integer Charge Transfer at the Tetrakis(Dimethylamino)Ethylene/Au Interface. *Applied Physics Letters* **2008,** *92*, 163302.

[115] Osikowicz, W.; Crispin, X.; Tengstedt, C.; Lindell, L.; Kugler, T.; Salaneck, W. R., Transparent Low-Work-Function Indium Tin Oxide Electrode Obtained by Molecular Scale Interface Engineering. *Applied Physics Letters* **2004,** *85*, 1616-1618.

[116] Li, H.; Paramonov, P.; Bredas, J.-L., Theoretical Study of the Surface Modification of Indium Tin Oxide with Trifluorophenyl Phosphonic Acid

Molecules: Impact of Coverage Density and Binding Geometry. *Journal of Materials Chemistry* **2010,** *20*, 2630-2637.

[117] Gliboff, M.; Li, H.; Knesting, K. M.; Giordano, A. J.; Nordlund, D.; Seidler, G. T.; Brédas, J.-L.; Marder, S. R.; Ginger, D. S., Competing Effects of Fluorination on the Orientation of Aromatic and Aliphatic Phosphonic Acid Monolayers on Indium Tin Oxide. *The Journal of Physical Chemistry C* **2013,** *117*, 15139-15147.

[118] Sharma, A.; Haldi, A.; Hotchkiss, P. J.; Marder, S. R.; Kippelen, B., Effect of Phosphonic Acid Surface Modifiers on the Work Function of Indium Tin Oxide and on the Charge Injection Barrier into Organic Single-Layer Diodes. *Journal of Applied Physics* **2009,** *105*, 074511.

[119] Sharma, A.; Haldi, A.; Potscavage Jr, W. J.; Hotchkiss, P. J.; Marder, S. R.; Kippelen, B., Effects of Surface Modification of Indium Tin Oxide Electrodes on the Performance of Molecular Multilayer Organic Photovoltaic Devices. *Journal of Materials Chemistry* **2009,** *19*, 5298-5302.

[120] Sharma, A.; Hotchkiss, P. J.; Marder, S. R.; Kippelen, B., Tailoring the Work Function of Indium Tin Oxide Electrodes in Electrophosphorescent Organic Light-Emitting Diodes. *Journal of Applied Physics* **2009,** *105*, 084507.

[121] Paniagua, S. A.; Baltazar, J.; Sojoudi, H.; Mohapatra, S. K.; Zhang, S.; Henderson, C. L.; Graham, S.; Barlow, S.; Marder, S. R., Production of Heavily N- and P-Doped Cvd Graphene with Solution-Processed Redox-Active Metal-Organic Species. *Materials Horizons* **2013**, 111-115.

[122] Wang, D. B.; Szoszkiewicz, R.; Lucas, M.; Riedo, E.; Okada, T.; Jones, S. C.; Marder, S. R.; Lee, J.; King, W. P., Local Wettability Modification by Thermochemical Nanolithography with Write-Read-Overwrite Capability. *Applied Physics Letters* **2007,** *91*, 243104.

[123] Wang, D.; Kodali, V. K.; II, W. D. U.; Jarvholm, J. E.; Okada, T.; Jones, S. C.; Rumi, M.; Dai, Z.; King, W. P.; Marder, S. R.; Curtis, J. E.; Riedo, E., Thermochemical Nanolithography of Multifunctional Nanotemplates for Assembling Nano-Objects. *Advanced Functional Materials* **2009,** *19*, 3696-3702.

[124] Carroll, K. M.; Giordano, A. J.; Wang, D.; Kodali, V. K.; Scrimgeour, J.; King, W. P.; Marder, S. R.; Riedo, E.; Curtis, J. E., Fabricating Nanoscale Chemical Gradients with Thermochemical Nanolithography. *Langmuir* **2013,** *29*, 8675-8682.

CHAPTER 2

SYNTHESIS AND CHARACTERIZATION OF MOLECULES FOR SURFACE MODIFICATION

2.1 General Phosphonic Acid Synthetic Techniques

There are multiple synthetic pathways that can be used to make phosphonic acids with the common intermediate being the formation of a dialkylphosphonate. Within the context of this thesis, techniques such as the Michaelis-Arbuzov reaction and catalytic formation of C-P bonds have been utilized. The final step is to then dealkylate the phosphonate and form the phosphonic acid (typically through the use of concentrated HCl or trimethylbromosilane (TMSBr)). There have been multiple review articles as well as various books published focusing on the formation of C-P bonds.[1-5]

2.1.1 The Michaelis-Arbuzov Reaction

The most common reaction to form dialkylphosphonates used in this chapter is that of the Michaelis-Arbuzov reaction, which is also commonly referred to as the Arbuzov reaction. This particular type of reaction is S_N2 in nature and requires the use of an alkyl group adjacent to a good leaving group, and a trivalent phosphorus compound such as triethylphosphite. The lone pair on the triethylphosphite attacks the carbon adjacent to the halogen (typically bromine or iodine, but other good leaving groups work as well). The leaving group then attacks the carbon adjacent to the O-P bond and the now free oxygen lone pair is shared with the phosphorus to create a phosphoryl group, with concomitant evolution of an alkyl group attached to the leaving group (often ethylbromide or ethyliodide). The mechanism of this reaction is schematically illustrated

in Figure 2.1. It should be noted that this type of reaction does not work when phosphorus is attached to a sp^2 hybridized carbon, as in the case of aryl halides.

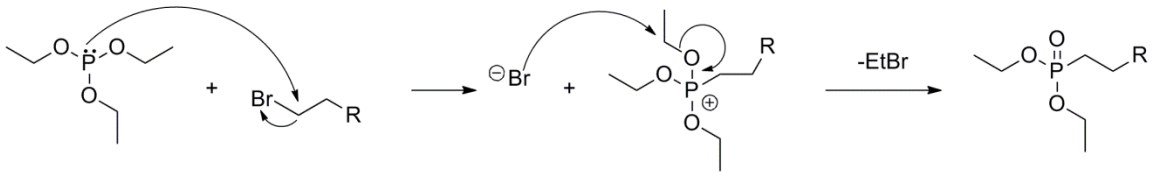

Figure 2.1 Mechanism of the Arbuzov reaction using an alkylbromide and triethylphosphite. The product of the reaction is the desired phosphonate and a volatile side product such as ethylbromide in this case.

From a practical standpoint, reactions such as these are straightforward to carry out by combining the two starting materials (the halide and triethylphosphite) in a round bottom flask and heating the reaction vessel to reflux (140 °C). The reaction can be done solvent free with triethylphosphite serving as the solvent in a large excess (often 3 equivalents). It is also possible to conduct this type of reaction through the use of microwave irradiation[6] going to completion on the order of minutes. Purification can then be conducted by distillation of the excess triethylphosphite, as the newly formed phosphonate will typically have a boiling point in excess of 200 °C.

2.1.2 Palladium Catalyzed Formation of Phosphonates

In order to form phosphonates where the C-P bond forms between an sp^2 hybridized carbon and phosphorus, transition metal catalysts are commonly used. An early report used $NiCl_2$ at high temperatures in order to form aryl phosphonates[7] with the use of palladium catalysis later explored as well.[8] In the case of this chapter, palladium catalysis was more commonly used. The reaction requires the use of an aryl halide and a

palladium species where an oxidative addition occurs between the palladium species and the aryl halide affording a newly formed complex between the palladium and the arene. Dialkylphosphite is then used, which attacks the arene-palladium complex, leading to the formation of the arylphosphonate and a base regenerates the palladium catalyst.

2.1.3 Formation of Phosphonic Acids by Hydrolysis of Phosphonates

In order to convert the typically formed diethylphosphonate to the phosphonic acid there are two commonly used techniques available. The most straightforward is the dealkylation of phosphonates by refluxing in an excess of hydrochloric acid (typically 8 M) for several hours. The phosphonic acid generally precipitates upon cooling. While these conditions are useful for compounds that are very acid stable, an alternative technique exists for molecules containing more acid sensitive groups. This milder approach uses trimethylsilylhalides, most typically bromotrimethylsilane (TMSBr).[9] Use of this technique leads to the conversion of the alkyl groups present in the phosphonate to trimethylsilyl groups, which can easily be cleaved in an aqueous solution. Typically mixtures of methanol and water are used for this step. The mechanism of hydrolysis for phosphonates is outlined in Figure 2.2.

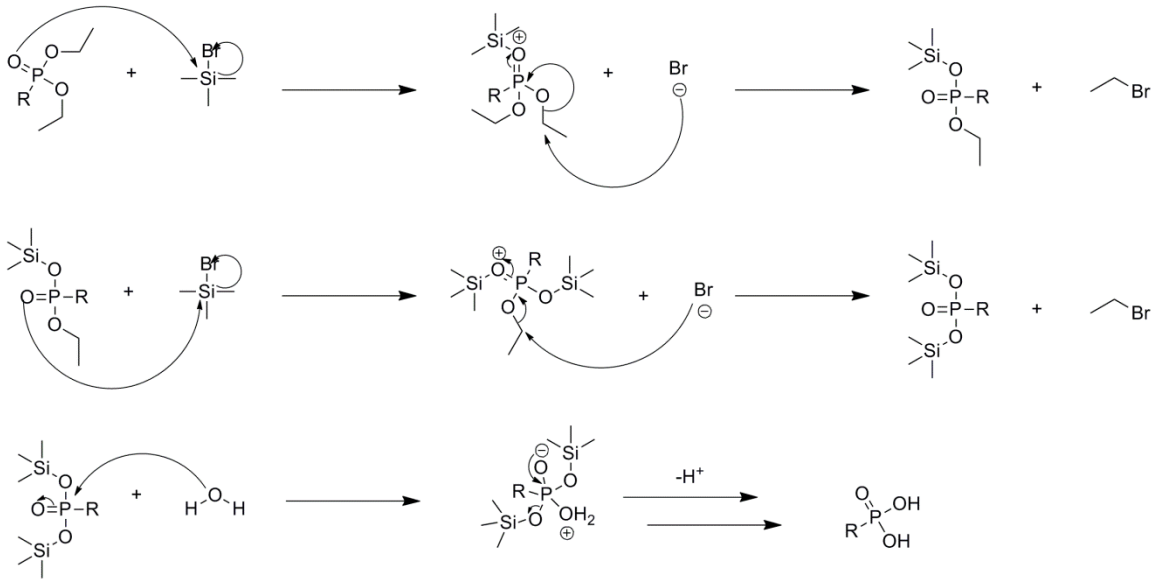

Figure 2.2 Hydrolysis mechanism for the formation of a phosphonic acid from a diethylphosphonate through the use of bromotrimethylsilane.

2.2 NMR Spectroscopy of Phosphonic Acids

Phosphorus has a spin of $\frac{1}{2}$ similar to ^{1}H and ^{13}C, and thus ^{31}P spectroscopy can be utilized in order to characterize phosphonic acids and their precursors. ^{31}P has a natural abundance of 100 % which means acquiring ^{31}P NMR data is relatively straightforward. Also, due to its spin, phosphorus coupling can be observed in both ^{1}H and ^{13}C NMR spectroscopy. In the case of ^{13}C NMR it is not possible to simultaneously run ^{1}H and ^{31}P decoupled NMR, thus, one must be chosen at a time and if ^{31}P decoupling is used then coupling to ^{1}H will then be observed, and vice versa. ^{31}P NMR spectroscopy is of great use in analyzing purity of phosphonates and phosphonic acids as it provides another analytical method by which a reaction can be monitored. In the case of comparing phosphonic acids and phosphonates, the phosphonic acid generally appears more upfield relative to the phosphonate precursors. From a practical standpoint, in order to provide a

reference point by which to calibrate the spectrum, typically phosphoric acid is used as an external reference (capillary tube filled with a solution of phosphoric acid) and referenced to 0 ppm.[10]

In the case of this chapter, another powerful technique is the use of ^{19}F NMR spectroscopy to characterize compounds and determine purity. Fluorine has only one naturally occurring isotope, which is ^{19}F and the overall sensitivity of ^{19}F is about 83 % that of ^{1}H NMR. Similarly to ^{31}P, ^{1}H, and ^{13}C, ^{19}F has a nuclear spin of $\frac{1}{2}$ and thus ^{19}F spectra that are acquired are typically proton decoupled. As expected, however, the presence of both ^{31}P and ^{19}F in close proximity to one another, as is the case for many of the molecules shown in this chapter, leads to complex splitting patterns. There are more reference standards available for use in ^{19}F NMR compared to that of ^{31}P, however, one of the more commonly used is that of trifluoroacetic acid, which has a chemical shift set to -76.55 ppm. It should also be noted that chemical shifts for fluorine-containing compounds are often difficult to predict and rationalize as the shielding of the ^{19}F nucleus consists mainly of paramagnetic shielding rather than the more well-understood diamagnetic shielding.[10]

2.3 Design and Synthesis of Surface Modifiers

Prior to examining the experimental details regarding the surface modifiers that have been synthesized for use in this thesis, it is important to understand the properties that were desired from such modifiers and therefore why particular choices in molecular design were made. It will be noted throughout the text which compounds are new, and which compounds have been previously reported in the literature. Note that in all cases

new compounds are blue in color in order to differentiate them from those materials previously reported in the literature.

2.3.1 Phosphonic Acids for Compatibilization with poly(3-hexylthiophene) (P3HT)

As noted in Chapter 1, one of the common uses for surface modification is the compatibilization of two materials with one another. This is of particular interest in optoelectronic applications such as organic photovoltaics (OPVs) where an organic active layer needs to properly interact (e.g. good wetting, minimize delamination, etc.) with an inorganic electrode. One such option to enhance compatibilization is through the modification of the surface with a material such as a phosphonic acid having a tail group that is similar in nature to the overlayer that will be deposited. Thus, in the case of an organic photovoltaic where materials such as poly(3-hexylthiophene) (P3HT) are commonly used, having a surface modifier that is similar in nature to the polymer will enhance wetting. In the case of the phosphonic acids that were designed and synthesized in Figure 2.3, the specific application was for a collaboration with Jenny Nelson's group at Imperial College London focused on porous metal oxide:polymer OPVs where device performance can be limited mainly by the infiltration of the polymer into the pores of the metal oxide (such as titania).[11] Thus, in an effort to enhance compatibility between the titania and P3HT, it was hypothesized that modifying the surface of titania with a phosphonic acid similar in structure to a monomer of P3HT, that better polymer infiltration (wetting) into the pores of the metal oxide would be observed. Thus, four phosphonic acids were synthesized all containing either a thiophene or hexylthiophene moiety. Both rigid and flexible phosphonic acids were made based on either direct phosphorus-thiophene linkage or phosphorus-methylene-thiophene bond, respectively.

The position of the hexyl group was also varied thinking that this bulky substituent would likely influence the orientation of the modifier on the surface and it was unclear whether it would be advantageous to have either the alkylchain or the thiophene group closest to the surface. The results from the use of these phosphonic acids on titania have been summarized elsewhere,[11] but based on initial results, control surfaces without modification using these phosphonic acids tended to have higher overall device efficiencies. It remains unclear whether there was an intrinsic problem with the use of these modifiers in particular, or if the correct modification conditions for a nanoporous structure had not been found. In either case, further research using these phosphonic acids to modify planar substrates would be required before re-examining nanoparticle modification.

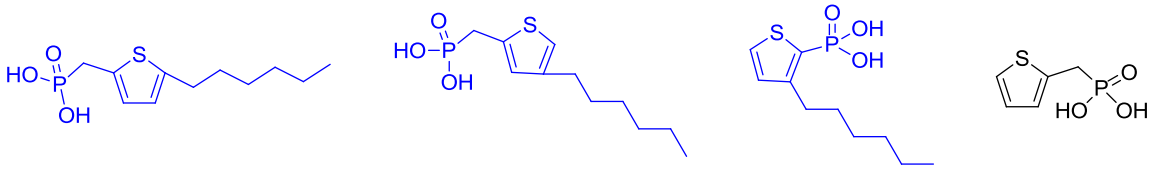

Figure 2.3 Thiophene based phosphonic acids designed for compatibilization and infiltration of P3HT with nanoporous titania. Note that new compounds are denoted in blue.

2.3.2 Phosphonic Acids for Use as Gate Dielectrics in Organic Field Effect Transistors (OFETs)

Recent results from Thomas Anthopoulos' group in Imperial College London have demonstrated the ability to fabricate low-voltage n-channel transistors using phosphonic acids both as a means of compatibilization and to serve as the gate dielectric

within the device.[12] The phosphonic acid used in this previously reported study was a long chain alkyl phosphonic acid (octadecylphosphonic acid, ODPA) using fullerene and pentacene based active layers. The molecules shown in Figure 2.4 were designed with two expectations in mind: the long alkyl chain should act in a manner similar to what was previously observed for ODPA (acting as a dielectric layer as well as enhancing the packing ability of the phosphonic acid), and that the termination of the chain with a fluorinated arene would allow for favorable interaction between the aromatic semiconductor deposited on top of the phosphonic acid monolayer. Non-fluorinated analogues of these molecules were also synthesized in the Marder group by Peter Hotchkiss.[13] Initial exploratory studies using the non-fluorinated modifiers were included in a recent patent application, however these particular modifiers have not been tested at this time.[14]

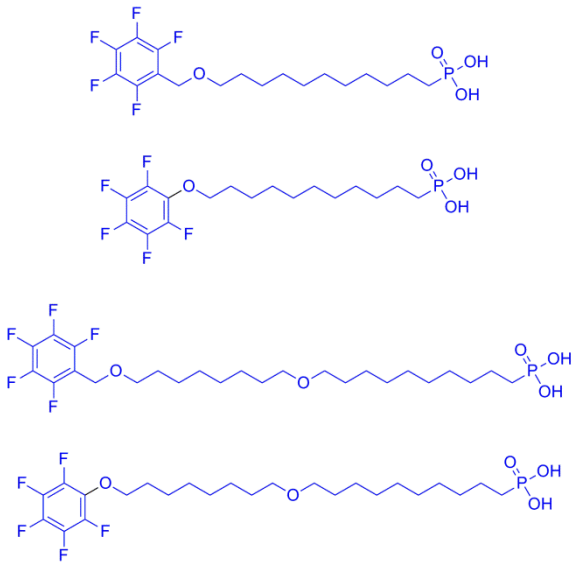

Figure 2.4 Phosphonic acids synthesized for use as a monolayer gate dielectric in OFET devices, consisting of a long alkyl chain to serve as a dielectric layer and fluorinated aryl termination for favorable interactions with aromatic overlayers. Note that new compounds are denoted in blue.

2.3.3 Perylene Diimide Surface Modifiers to Probe Charge Transfer

The efficiency of charge transfer in organic optoelectronic devices can be greatly influenced based on the interface between organic active layers and inorganic electrodes. The rate of charge transfer between these interfaces depends on multiple factors such as charge mobilities, reorganization energies, and offsets in frontier orbital energies. It is also true that when the inorganic surface is modified with a material such as a phosphonic acid the structural parameters of the monolayer such as the packing and orientation, may greatly influence the efficiency of charge transfer.[15] Recenly, zinc phthalocyanine phosphonic acids (ZnPcPAs) have been used to examine the relationship that exists between molecular orientation and charge transfer rates.[15] One of the issues with using this type of modifier to probe such processes on the surface is the tendency of the ZnPcPAs to aggregate and form multiple domains on the surface consisting of monomeric and aggregated forms of the molecules. The ZnPcPAs that had been originally examined had a long alkyl chain linking the phosphonic acid binding group with the core of the zinc phthalocyanine. It was thought that such aggregation may be minimized if a more rigid linker was chosen. Furthermore, rather than use a phthalocyanine core it would be advantageous to be able to conduct electrochemical as well as photoluminescence techniques (in addition to more standard characterization such as XPS, UPS, and AFM) to probe charge transfer on the surface after modification. Thus, perylene diimide (PDI) cores containing aromatic linkers between the binding group and the PDI core were thought to fit both of the requirements. In addition, it was unclear how the choice in binding group would impact the charge transfer dynamics after modification so in addition to phosphonic acids, carboxylic acid PDI structures would

also be examined. The molecules synthesized for this purpose containing PDI cores and either phosphonic or carboxylic acid binding groups are shown in Figure 2.5. These materials were examined by Yilong Zheng from Scott Saavedra's group and Luis Torres-Figueroa from Oliver Monti's group, both at the University of Arizona. Initial results indicated that aggregation was still a problem with these PDI molecules and current next-generation PDI phosphonic acids are currently being synthesized in the Marder group by Fadi Jradi containing steric bulk that would minimize the degree to which such modifiers could aggregate with one another.

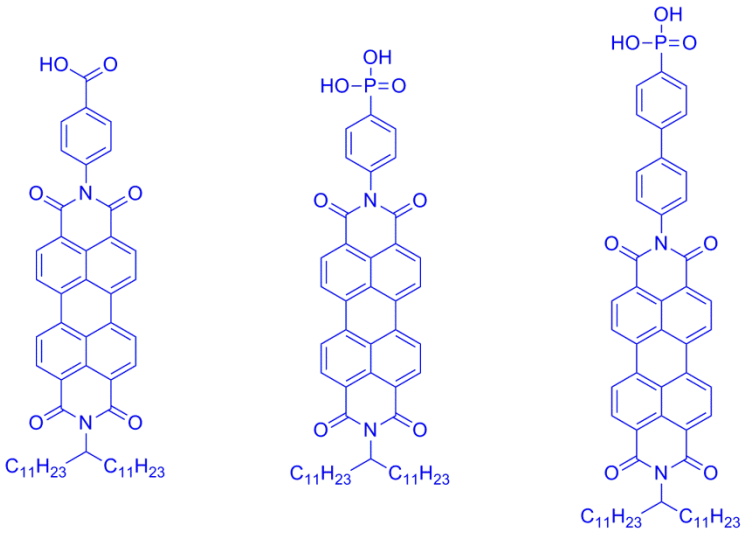

Figure 2.5 Perylene diimide phosphonic acid and carboxylic acid surface modifiers used to probe charge transfer on the surface of transparent conducting oxides.

2.3.4 Phosphonic Acids for Altering the Work Function and Wettability of Metal Oxides

A series of substituted benzyl, alkyl, and fluoroalkyl phosphonic acids were synthesized with the purpose of tuning the WF of metal oxide substrates such as ITO

(Chapter 3) and ZnO (Chapter 4). In the case of these surface modifiers, the origin of the change in surface properties comes from the molecular dipole inherent within the molecule, which, when put on the surface of a metal oxide, forms an interface dipole causing a change in properties such as WF. Similarly, the wettability of a surface can be altered by turning what was previously a hydroxyl terminated surface and thus hydrophilic, as is the case with materials such as ITO and ZnO, into a surface terminated with hydrophobic benzyl, alkyl, and fluoroalkyl groups. Thus, from a compatibility standpoint, surfaces modified with phosphonic acids such as those shown in Figure 2.6 are more likely to enhance wetting of organics on the surface compared to the bare, unmodified metal oxide. In addition to the use of some of the modifiers as outlined in Chapters 3 and 4 many of these compounds have been utilized by collaborators at the University of Washington, University of Arizona, National Renewable Energy Laboratory, and Princeton, and some of these results have already been published in the literature.[16-23]

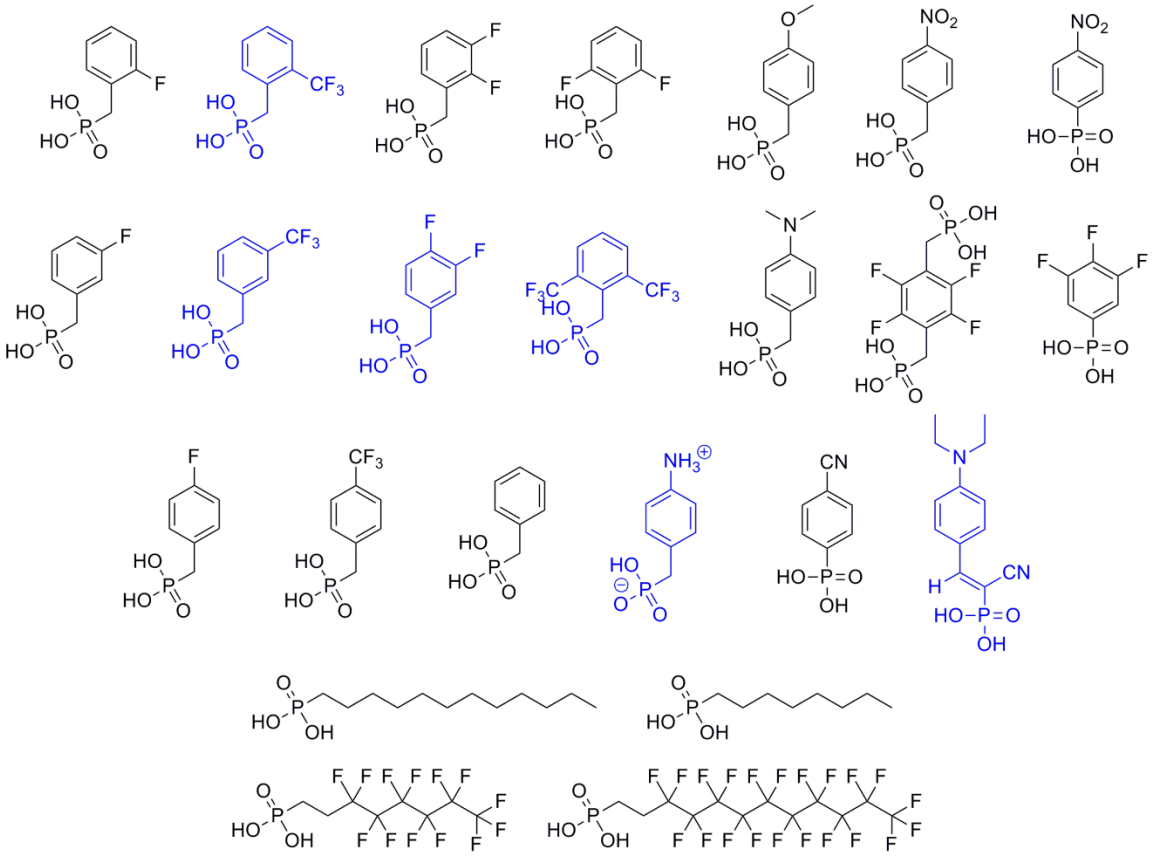

Figure 2.6 Aryl, alkyl, benzyl, and fluoroalkyl phosphonic acids synthesized for the purpose of altering the WF of metal oxides and enhancing wettability of organic overlayers on the modified surfaces. Note that new compounds are denoted in blue.

2.3.5 Surface Modifiers for Nanolithography and Crosslinking

The ability to attach a disparate material to a surface is highly desirable. One of the more common uses of such an attachment is the crosslinking of polymers to the surface of metal oxides. Implementing this type of system could prevent problems such as delamination[24] within devices, as well as making them more robust to multiple solution based processing procedures by covalently linking the polymer to the surface of the substrate. Figure 2.7 summarizes the molecules that were made for the purposes of binding other materials to the substrate. In the case of the benzophenone terminated (Ar-

CO-Ar) phosphonic acid and chlorosilane, these modifiers were made with the purpose of binding polymeric overlayers to the surface of silicon (in the case of the silane) and ITO or other metal oxides (in the case of the phosphonic acid). The photochemistry of benzophenone has been well characterized[25-26] and involves the formation of C-C bonds through a process that is shown in Figure 2.8.[27-28] It is important to note that the benzophenone crosslinking shown in Figure 2.8 is not specific to this particular system and can be applied to other benzophenone derivatives. Upon photon absorption, benzophenone undergoes several photophysical processes, affording a *n*, π^* triplet state, which proceeds to the formation of a radical on benzophenone to produce benzophenone*. This radical can perform hydrogen abstraction from the polymer chain leaving two radical species, which can then recombine to produce a crosslinked product. Examination of using a benzophenone phosphonic acid on indium-tin oxide (ITO) may prove useful for organic electronic devices.

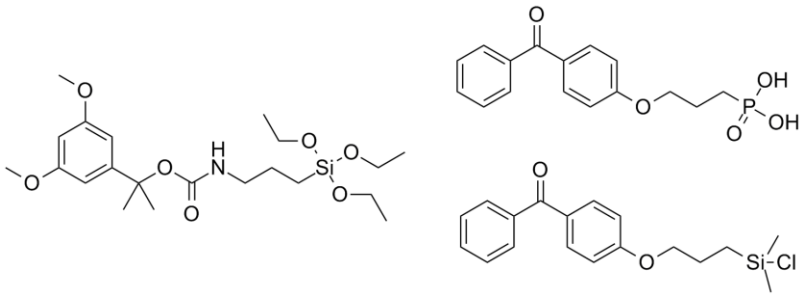

Figure 2.7 Summary of molecules synthesized for use in Thermochemical Nanolithography (alkoxysilane) and covalently binding polymer materials to the surface of a substrate (chlorosilane and phosphonic acid).

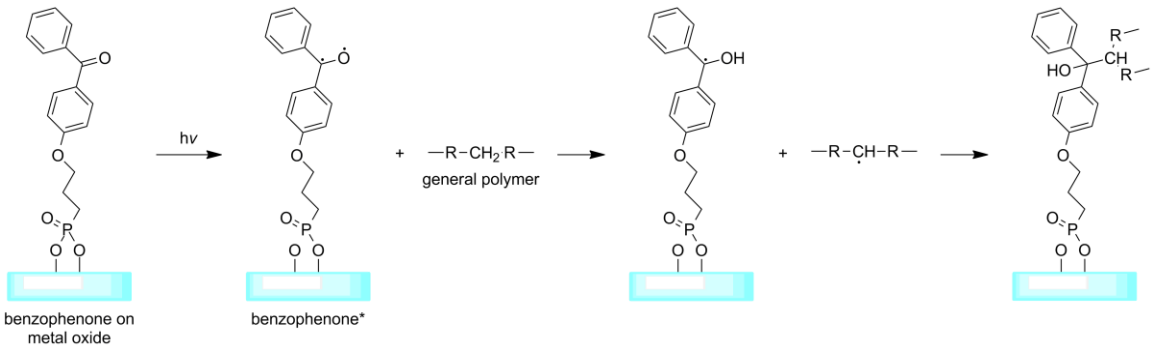

Figure 2.8 General scheme for the crosslinking of a generic polymer chain to the surface of a metal oxide upon exposure of a benzophenone phosphonic acid to irradiation. The same principle is also true in the case of the chlorosilane, only the substrate (silica or silicon in this case) would be different.

In the case of the alkoxysilane, this modifier was designed for the purpose of Thermochemical Nanolithography (TCNL), which is a technique utilizing a heated atomic force microscope cantilever to cause the selective thermal deprotection of a protecting group on the surface of a substrate (as discussed in greater detail in Appendix A). The protecting group for this particular modifier is an α,α-dimethyl-3,5-dimethoxybenzyloxycarbonyl (DDz), which forms a primary amine after deprotection. The deprotection products for this molecule are shown in Figure 2.9. Selectively forming this amine on the surface of a substrate enables the subsequent binding in specific areas of materials ranging from dyes, nanoparticles, cells, and other molecules. The basic technique is similar to TCNL that has been previously conducted using polymer materials that contain protecting groups such as a tetrahydropyran carbamate.[29-30]

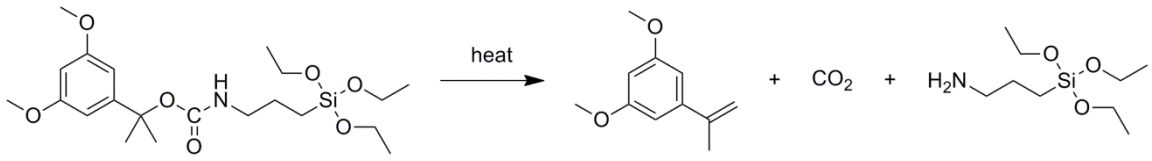

Figure 2.9 Expected decomposition products upon heating the alkoxkysilane containing the DDz protecting group.

2.4 Conclusions

Some of the more commonly used synthetic techniques to form phosphonates and phosphonic acids have been briefly outlined in this chapter, as they have been covered in greater detail throughout the literature.[1-4] Dealkylation is an important step in the formation of phosphonic acid final products and for the purposes of this thesis, TMSBr was used almost exclusively for this conversion. While the number of commercially available phosphonic acids has increased over the last several years, as is evidenced by the number and variety of compounds synthesized that the commercially available materials do not currently meet the needs of individuals looking to tailor surface properties. However, phosphonic acids are relatively straightforward to synthesize and easily purified by recrystallization meaning that phosphonic acids can be readily tailored to the needs of a particular type of surface, interface, or application. In total, 17 compounds not previously reported in the literature have been synthesized for use in this thesis or in projects working with research groups (as noted above). The following experimental section serves as the central location of synthetic details for this thesis and subsequent chapters refer back to this section when materials are used. The only materials not discussed in this section are the dimers discussed in Chapter 5 as those were synthesized by other members of the Marder group.

2.5 Experimental

Unless otherwise specified, reactions were conducted at room temperature utilizing reagent grade chemicals that were used as received without further purification.

^{1}H and ^{13}C NMR spectra were acquired on either a Varian 300 MHz or 400 MHz spectrometer using the internal solvent peak as reference.

^{31}P NMR spectra were measured using a Varian 400 MHz spectrometer using a capillary tube filled with a solution of 85 % phosphoric acid as an external reference (H_3PO_4, δ = 0 ppm). Spectra acquired were proton decoupled.

^{19}F NMR spectra were measured using a Varian 400 MHz spectrometer using a capillary tube filled with a dilute solution of trifluoro acetic acid in ethanol (CF_3COOH, δ = -76.55 ppm). Spectra acquired were proton decoupled.

Elemental analyses were conducted by Atlantic Microlabs, Atlanta, GA always analyzing for C and H as well as F and N where applicable.

Mass spectra were measured by the Georgia Institute of Technology Bioanalytic Mass Spectrometry Facility using either electron impact (EI) on a MicroMass AutoSpec M, electrospray ionization (ESI) on an Applied Biosystems QSTAR-XL, or matrix assisted laser desorption ionization (MALDI) on an Applied Biosystems 4700 Proteomics Analyzer.

Compounds that have been previously reported in the literature were characterized by NMR spectroscopy and references providing NMR spectra consistent with that acquired in-house are provided. All other compounds not fully characterized in the literature were analyzed by ^{1}H and ^{13}C NMR as well as ^{19}F and ^{31}P NMR where

applicable, high-resolution mass spectrometry, and elemental analysis. Any exceptions where parts of this data could not be acquired is noted in the text below.

2.5.1 (5-Hexylthiophen-2-yl)methylphosphonic acid

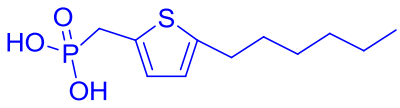

A solution of *n*-butyllithium (7.3 mL, 2.5 M in hexanes, 18.3 mmol) was added over 10 minutes to a stirred solution of 3.05 g (18.1 mmol) of 2-hexylthiophene in 50 mL of freshly distilled THF at -78 °C under nitrogen. The solution was allowed to stir for one hour at -78 °C and removed from the reaction flask, *via* syringe, and 3.4 g (18.0 mmol) of copper (I) iodide was added in 5 mL of THF. The reaction mixture in the syringe was then added to the THF/CuI solution in one portion and a slight exotherm was noted. The temperature of the bath was allowed to increase to between -30 °C and -20 °C and the mixture stirred for two hours at this temperature. Diethyl iodomethylphosphonate was then added (5.0 g, 18.1 mmol) in one portion and the solution was allowed to stir overnight at room temperature. The resulting dark brown/orange reaction mixture was diluted with 100 mL of diethyl ether. This mixture was then filtered through silica gel, eluting with ethyl acetate. Volatiles were removed under reduced pressure and the resulting residue purified by column chromatography packed with silica gel (1:1 hexanes:ethyl acetate), affording diethyl (5-hexylthiophen-2-yl)methylphosphonate as a yellow oil (3.61 g, 63%). ^{1}H NMR (399.96 MHz, $CDCl_3$) δ 6.74 (t, *J* = 3.60 Hz, 1H), 6.58 (d, *J* = 3.20 Hz, 1H), 4.05 (m, 4H), 3.27 (d, *J* = 20.80 Hz),

2.72 (t, *J* = 7.20 Hz, 2H), 1.62 (quin, *J* = 7.60 Hz, 2H), 1.29 (m, 12H), 0.86 (t, *J* = 6.80 Hz, 3H). $^{13}C\{^{1}H\}$ NMR (100.58 MHz, $CDCl_3$) δ 145.3 (d, *J* = 4.1 Hz), 129.4 (d, *J* = 10.4 Hz), 126.9 (d, *J* = 8.8 Hz), 123.8 (d, *J* = 3.4 Hz), 62.3 (d, *J* = 6.8 Hz), 31.5 (d, *J* = 1.71 Hz), 30.0, 28.8, 28.7, 27.4, 22.5, 16.3 (d, *J* = 6.0 Hz), 14.0. $^{31}P\{^{1}H\}$ NMR (161.91 MHz, $CDCl_3$): δ 25.24. EI-MS exact mass calculated (found) for [M^+], m/z: 318.1419 (318.14311).

The phosphonate (1.5 g, 4.7 mmol) was dissolved in 10 mL of anhydrous dichloromethane and bromotrimethylsilane (1.9 mL, 14.4 mmol) was added *via* syringe. The system was sealed with a greased stopper and allowed to stir for three hours. Volatiles were removed under reduced pressure to produce a yellow-orange oil, which was dissolved in a solution of methanol/water (30 mL and 4 mL, respectively) and allowed to stir overnight. After removal of solvent under reduced pressure crystals slowly formed. The product was recrystallized from acetonitrile to produce the title compound as slightly off-white crystals (0.99 g, 81%). ^{1}H NMR (399.96 MHz, DMSO-d_6) δ 6.48 (t, *J* = 2.20 Hz, 1H), 6.42 (d, *J* = 3.20 Hz, 1H), 2.88 (d, *J* = 20.40 Hz, 2H), 2.50 (t, *J* = 7.60 Hz, 2H), 1.36 (quin, *J* = 7.20 Hz, 2H), 1.09 (m, 6H), 0.66 (t, *J* = 6.80 Hz, 3H). $^{13}C\{^{1}H\}$ NMR (100.58 MHz, DMSO-d_6) δ 143.3 (d, *J* = 4.9 Hz), 132.5 (d, *J* = 13.0 Hz), 126.0 (d, *J* = 11.4 Hz), 123.6 (d, *J* = 3.9 Hz), 31.2, 30.9, 29.8 (d, *J* = 182.9 Hz), 29.3, 28.1, 22.0, 13.9. $^{31}P\{^{1}H\}$ NMR (161.91 MHz, DMSO-d_6): δ 20.74. EI-MS exact mass calculated (found) for [M^+], m/z: 262.0793 (262.07914). Analysis calculated (found) %: C 50.37 (50.22), H 7.30 (7.33).

2.5.2 (4-Hexylthiophen-2-yl)methylphosphonic acid

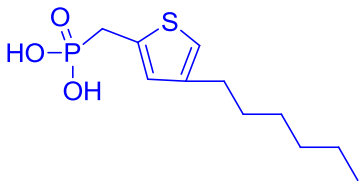

A solution of *n*-butyllithium (7.8 mL, 2.5 M in hexanes, 18.3 mmol) was added over 10 minutes to a stirred solution of 3.1 g (18.1 mmol) of 3-hexylthiophene in 50 mL of freshly distilled THF at -78 °C under nitrogen. The solution was allowed to stir for one hour at -78 °C and removed from the reaction flask, *via* syringe, and 3.5 g (18.1 mmol) of copper (I) iodide was added in 5 mL of THF. The reaction mixture in the syringe was then added to the THF/CuI solution in one portion and a slight exotherm was noted. The temperature of the bath was allowed to increase to between -30 °C and -20 °C and the mixture stirred for two hours at this temperature. Diethyl iodomethylphosphonate was then added (5.0 g, 18.1 mmol) in one portion and the solution was allowed to stir overnight at room temperature. The resulting dark orange reaction mixture was then filtered through silica gel, eluting with ethyl acetate. Volatiles were removed under reduced pressure and the resulting residue purified by column chromatography packed with silica gel (1:1 hexanes:ethyl acetate), affording diethyl (4-hexylthiophen-2-yl)methylphosphonate as a dark orange oil (2.52 g, 44%). ^{1}H NMR (399.96 MHz, $CDCl_3$) δ 6.80 (dd, *J* = 4.40, 0.80 Hz, 1H), 6.72 (s, br, 1H), 4.05 (quind, *J* = 7.00, 1.20, 4H), 3.29 (dd, *J* = 20.59, 0.40 Hz, 2H), 2.52 (t, *J* = 7.60 Hz, 2H), 1.55 (quin, *J* = 6.00 Hz, 2H), 1.27 (m, 12H), 0.86 (t, *J* = 6.80 Hz, 3H). ^{13}C{^{1}H} NMR (100.58 MHz, $CDCl_3$) δ 143.2 (d, *J* = 3.1 Hz), 131.9 (d, *J* = 10.1 Hz), 128.7 (d, *J* = 8.3 Hz), 119.1 (d, *J* = 3.4 Hz), 62.3 (d, *J* = 6.7 Hz), 31.6, 30.3 (d, *J* = 11.6 Hz), 28.9, 28.8, 27.4, 22.5, 16.3 (d,

J = 6.0 Hz), 14.0. $^{31}P\{^{1}H\}$ NMR (161.91 MHz, $CDCl_3$): δ 25.01. EI-MS exact mass calculated (found) for [M^+], m/z: 318.1419 (318.14044). Analysis calculated (found) %: C 56.58 (56.31), H 8.55 (8.56).

The phosphonate (1.5 g, 4.8 mmol) was dissolved in 10 mL of anhydrous dichloromethane and bromotrimethylsilane (1.9 mL, 14.4 mmol) was added *via* syringe. The system was sealed with a greased stopper and allowed to stir for three hours. Volatiles were removed under reduced pressure to produce an oil, which was dissolved in 5:1 methanol:water (42 mL) and allowed to stir overnight. After removal of solvent under reduced pressure crystals slowly formed. The product was recrystallized from acetonitrile to produce the title compound as slightly off-white, shiny, fluffy crystals (1.1 g, 85%). ^{1}H NMR (399.96 MHz, DMSO-d_6) δ 6.88 (s, 1H), 6.76 (d, J = 2.00 Hz, 1H), 3.1 (d, J = 20.80 Hz, 2H), 2.48 (t, J = 7.60 Hz, 2H), 1.53 (quin, J = 7.60 Hz, 2H), 1.27 (m, 6H), 0.86 (t, J = 6.80 Hz, 3H). $^{13}C\{^{1}H\}$ NMR (100.58 MHz, DMSO-d_6) δ 141.9 (d, J = 3.0 Hz), 134.9 (d, J = 9.4 Hz), 127.8 (d, J = 8.0 Hz), 118.5 (d, J = 3.4 Hz), 31.0, 30.4, 29.8 (d, J = 7.7 Hz), 29.1, 28.4, 22.0, 13.9. $^{31}P\{^{1}H\}$ NMR (161.91 MHz, DMSO-d_6): δ 20.68. EI-MS exact mass calculated (found) for [M^+], m/z: 262.0793 (262.07509). Analysis calculated (found) %: C 50.37 (50.52), H 7.30 (7.24).

2.5.3 3-Hexylthiophen-2-ylphosphonic acid

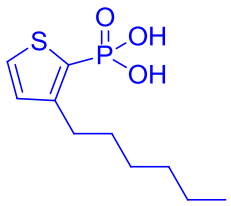

In a microwave tube under a flow of nitrogen was combined 2-bromo-3-hexylthiophene (1.00 g, 4.05 mmol), palladium (II) chloride (73 mg, 0.4 mmol), and triethyl phosphite (0.73 mL, 4.20 mmol). The vessel was sealed and irradiated in a CEM Discover microwave for five minutes at 100 Watts (generally reaching a maximum temperature of 150 °C). The resulting dark reaction was diluted in 20 mL of diethyl ether and gravity filtration used to remove the catalyst. Removal of solvent under reduced pressure produced a dark oil, which was purified by column chromatography packed with silica gel (2:1 hexanes:ethyl acetate) to afford diethyl 3-hexylthiophen-2-ylphosphonate (1.42 g, 58% for a combination of two runs). ^{1}H NMR (399.96 MHz, $CDCl_3$) δ 7.53 (t, *J* = 3.60 Hz, 1H), 7.03 (t, *J* = 6.00 Hz, 1H), 4.11 (m, 4H), 2.84 (td, *J* = 4.00, 1.20 Hz, 2H), 1.61 (quin, *J* = 7.60 Hz, 2H), 1.32 (m, 12H), 0.87 (t, *J* = 4.80 Hz, 3H). ^{13}C{^{1}H} NMR (100.58 MHz, $CDCl_3$) δ 152.4 (d, *J* = 13.2 Hz), 131.9 (d, *J* = 7.8 Hz), 130.5 (d, *J* = 19.2 Hz), 121.4 (d, *J* = 104.6 Hz), 62.3 (d, *J* = 5.3 Hz), 31.6, 30.8, 29.7 (d, *J* = 2.2 Hz), 29.2, 22.5, 16.2 (d, *J* = 6.7 Hz), 14.0. ^{31}P{^{1}H} NMR (161.91 MHz, $CDCl_3$): δ 13.45. EI-MS exact mass calculated (found) for [M^+], m/z: 304.1262 (304.12724). Analysis calculated (found) %: C 55.24 (55.23) H 8.28 (8.30).

The phosphonate (1.0 g, 3.35 mmol) was dissolved in 10 mL of dry dichloromethane and 1.2 mL (9.2 mmol) of bromotrimethylsilane was added *via* syringe. The system was sealed with a greased stopper and allowed to stir overnight. Volatiles were removed under reduced pressure to produce a viscous, brown oil, which was dissolved in a mixture of methanol/water (16 mL and 3.5 mL, respectively) and allowed to stir overnight. After removal of solvent under reduced pressure crystals slowly formed. The resulting solid was recrystallized from hexanes to produce the title

compound as light tan colored crystals (0.5 g, 93%). ^{1}H NMR (399.96 MHz, DMSO-d_6) δ 7.65 (m, 1H), 7.04 (t, J = 4.00 Hz, 1H), 2.77 (t, J = 8.00 Hz, 2H), 1.55 (m, 2H), 1.26 (m, 6H), 0.86 (m, 3H). ^{13}C{^{1}H} NMR (100.58 MHz, DMSO-d_6) δ 148.8 (d, J = 6.2 Hz), 130.2 (d, J = 71.5 Hz), 129.9 (d, J = 6.9 Hz), 127.7 (d, J = 199.5 Hz), 31.1, 30.3, 29.0 (d, J = 2.4 Hz), 28.7, 22.1, 13.9. ^{31}P{^{1}H} NMR (161.91 MHz, DMSO-d_6): δ 7.70. EI-MS exact mass calculated (found) for [M^{+}], m/z: 248.0636 (248.06319). Analysis calculated (found) %: C 48.38 (48.55), H 6.90 (6.82).

2.5.4 Thiophen-2-ylmethylphosphonic acid

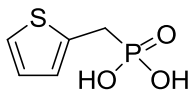

A solution of *n*-butyllithium (7.1 mL, 2.5 M in hexanes, 17.8 mmol) was added over 10 minutes to a stirred solution of 1.50 g (17.8 mmol) of thiophene in 50 mL of freshly distilled THF at -78 °C under nitrogen. The solution was allowed to stir for one hour at -78 °C and removed from the reaction flask, *via* syringe, and 3.4 g (17.9 mmol) of copper (I) iodide was added in 5 mL of THF. The reaction mixture in the syringe was then added to the THF/CuI solution in one portion and a slight exotherm was noted. The temperature of the bath was allowed to increase to between -30 °C and -20 °C and the mixture stirred for two hours. Diethyl iodomethylphosphonate was then added (5.0 g, 18.0 mmol) in one portion and the solution was allowed to stir overnight at room temperature. The resulting dark brown/orange reaction mixture was diluted with 100 mL of diethyl ether. This mixture was then filtered through silica gel, eluting with ethyl

acetate. Volatiles were removed under reduced pressure and the resulting viscous dark orange oil purified by column chromatography packed with silica gel (1:1 hexanes:ethyl acetate), affording diethyl thiophen-2-ylmethylphosphonate as a yellow oil (1.7 g, 40%) of 93% pure product. ^{1}H NMR (300.23 MHz, $CDCl_3$) δ 6.96 (m, 1H), 6.83 (m, 1H), 6.74 (m, 1H), 3.90 (m, 4H), 3.14 (m, 2H), 2.62 (impurity), 1.00 (t, J = 7.21, 6H). This is a commercially available product and has been previously reported in the literature.[31]

The phosphonate (1.0 g, 4.4 mmol) was dissolved in 18 mL of anhydrous dichloromethane and bromotrimethylsilane (2.5 mL, 18.9 mmol) was added *via* syringe. The system was sealed with a greased stopper and allowed to stir for three hours. Volatiles were removed under reduced pressure to produce a yellow-orange oil, which was dissolved in a solution 10:1 methanol:water (33 mL) and allowed to stir overnight. After removal of solvent under reduced pressure a solid formed. The product was recrystallized from acetonitrile to crystallize and form the title compound as fluffy, colorless needles (0.50 g, 66%). ^{1}H NMR (300.23 MHz, DMSO-d_6) δ 7.31 (m, 1H), 6.92 (m, 2H), 3.17 (d, J = 20.42 Hz, 2H). ^{13}C{^{1}H} NMR (100.58 MHz, DMSO-d_6) δ 135.2 (d, J = 9.2 Hz), 126.6 (d, J = 3.0 Hz), 126.5 (d, J = 8.2 Hz), 124.2 (d, J = 3.3 Hz), 29.5 (d, J = 136.9 Hz). ^{31}P{^{1}H} NMR (161.91 MHz, DMSO-d_6): δ 20.6. EI-MS exact mass calculated (found) for [M^+], m/z: 177.9854 (177.98791). Analysis calculated (found) %: C 33.71 (33.87), H 3.96 (3.92). This product has been previously reported in the literature,[32] but had not been fully characterized.

2.5.5 11-(Perfluorophenoxy)undecylphosphonic acid

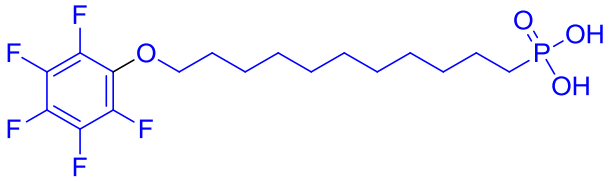

In a microwave tube under a flow of nitrogen was combined hexafluorobenzene (1.97 g, 10.6 mmol), diethyl 11-hydroxyundecylphosphonate (4.23 g, 13.7 mmol), and solid sodium hydroxide (0.85 g, 21.3 mmol). The vessel was sealed and irradiated in a CEM Discover microwave ramping to 135 °C and holding that temperature for 2 minutes. The resulting yellow mixture was poured into water, acidified with 1 M HCl, and extracted with ether. The organic layer was washed three times each with dilute aqueous sodium hydroxide, water, brine, and dried over magnesium sulfate. Volatiles were removed under reduced pressure to afford a slightly yellow, viscous oil which was purified by column chromatography packed with silica gel (1:1 chloroform:ethyl acetate) to afford diethyl 11-hydroxyundecylphosphonate (1.71 g, 34%). ^{1}H NMR (399.96 MHz, $CDCl_3$) δ 4.06 (m, 6H), 1.73 (m, 4H), 1.57 (m, 2H), 1.37 (m, 20H). $^{13}C\{^{1}H\}$ NMR (125.8 MHz, $CDCl_3$) δ 141.7 (d, J = 248.6 Hz), 138.9 (d, J = 101.3 Hz), 136.6 (d, J = 111.1 Hz,), 133.7 (d, J = 4.5 Hz), 75.8, 61.3 (d, J = 6.5 Hz), 30.6 (d, J = 17.0 Hz), 29.8, 29.4, 29.2, 29.1, 29.0, 26.2, 25.4, 25.1, 22.4 (d, J = 2.6 Hz). $^{31}P\{^{1}H\}$ NMR (161.91 MHz, $CDCl_3$): δ 33.30. ^{19}F NMR (376.28 MHz, $CDCl_3$): δ -155.86 (m, 2F), -162.44 (m, 2F), 162.81 (m, 1F), from trifluoro acetic acid. EI-MS exact mass calculated (found) for [M^+], m/z: 474.1958 (474.1951). Analysis calculated (found) %: C 53.16 (52.98), H 6.80 (6.97), F 20.02 (19.79).

A solution of diethyl 11-hydroxyundecylphosphonate (1.01 g, 2.1 mmol) in 15 mL of dry dichloromethane and 1.1 mL (8.3 mmol) of bromotrimethylsilane was made. The system was sealed with a greased stopper and allowed to stir overnight. Volatiles were removed under reduced pressure to produce a viscous, brown oil, which was dissolved in 20 mL of a 4:1 methanol:water solution and allowed to stir for six hours. After removal of solvent under reduced pressure an off white solid formed, which was recrystallized from acetonitrile to afford while crystals of 11-(perfluorophenoxy)undecylphosphonic acid (0.84 g, 94%). ^{1}H NMR (399.96 MHz, DMSO-d_6) δ 4.17 (t, J = 1.20 Hz, 2H), 1.69 (m, 2H), 1.50-1.25 (m, 18H). ^{13}C{^{1}H} NMR (100.58 MHz, DMSO-d_6) δ 75.5, 30.0 (d, J = 16.0 Hz), 29.1, 28.9, 28.8, 28.6, 28.5, 28.1, 26.8, 24.9, 22.6 (d, J = 4.5 Hz) aromatic carbons not observed due to strong fluorine coupling. ^{31}P{^{1}H} NMR (161.91 MHz, DMSO-d_6) δ 27.71. ^{19}F NMR (376.28 MHz, DMSO-d_6): δ 155.47 (m, 2F), 162.20 (m, 2F), 162.82 (m, 1F), from trifluoro acetic acid. Analysis calculated (found) %: C 48.81 (48.95), H 5.78 (5.68), F 22.71 (22.76).

2.5.6 11-(Perfluorobenzyloxy)undecylphosphonic acid

Under an inert atmosphere was combined potassium hydroxide (0.57g, 10.2 mmol), pentafluorobenzylbromide (1.4 mL, 9.95 mmol), diethyl 11-hydroxyundecylphosphonate (3.05 g, 9.89 mmol), and tetrabutylammonium iodide (0.01

g, 0.03 mmol) with anhydrous THF. The mixture was allowed to stir at 65 °C for approximately 9 hours and filtered through a thin layer of silica gel, eluting with THF. Volatiles were removed under reduced pressure and the reaction mixture was distilled utilizing Kugelrohr distillation (0.18 Torr, 250 °C) to afford impure diethyl 11-(perfluorobenzyloxy)undecylphosphonate. The impure material was subsequently purified by column chromatography packed with silica gel (hexane:ethyl acetate gradient) to afford 0.91 g (19%) of diethyl 11-(perfluorobenzyloxy)undecylphosphonate. ^{1}H NMR (399.96 MHz, $CDCl_3$) δ 4.56 (t, *J* = 1.8 Hz, 2H), 4.08 (m, 4H), 3.47 (t, *J* = 6.6 Hz, 2H), 1.73-1.24 (m, 26 H). $^{13}C\{^{1}H\}$ NMR (125.8 MHz, $CDCl_3$) δ 145.6 (d, *J* = 246.4 Hz), 141.2 (d, *J* = 261.8 Hz), 137.3 (d, *J* = 270.7 Hz), 111.5, 71.1, 61.3 (d, *J* = 6.5 Hz), 59.4, 32.8, 30.7, 30.5, 29.5, 29.3, 29.0, 26.2, 25.9, 25.1, 22.4 (d, *J* = 5.3 Hz), 16.4 (d, *J* = 6.0 Hz). Analysis calculated (found) %: C 54.09 (54.30), H 7.02 (7.07), F 19.45, 19.16). Exact mass calculated (found) for $[M+H]^+$, m/z: 488.2115 (488.2115).

A solution of diethyl 11-(perfluorobenzyloxy)undecylphosphonate (0.63 g, 1.3 mmol) in 15 mL of dry dichloromethane and 0.7 mL (5.3 mmol) bromotrimethylsilane was made. The system was sealed with a greased stopper and allowed to stir overnight. Volatiles were removed under reduced pressure to produce a viscous, brown oil, which was dissolved in 25 mL of a 4:1 methanol:water solution and allowed to stir for six hours. After removal of solvent under reduced pressure an off white solid formed, which was recrystallized from a minimal amount of acetonitrile to afford white crystals of 11-(perfluorobenzyloxy)undecylphosphonic acid (0.49 g, 92%). ^{1}H NMR (399.96 MHz, DMSO-d_6) δ 4.55 (s, 2H), 3.42 (t, *J* = 6.4 Hz, 2H), 1.49-1.44 (m, 6H), 1.34-1.18 (m, 14 H). $^{13}C\{^{1}H\}$ NMR (100.58 MHz, DMSO-d_6) δ 104.5, 69.9, 58.8, 30.1, 29.9, 28.9, 28.8,

28.8, 28.7, 28.1, 26.8, 25.4, 22.648 (d, J = 4.8 Hz). $^{31}P\{^{1}H\}$ NMR (161.91 MHz, DMSO-d_6) δ 27.63. ^{19}F NMR (376.28 MHz, DMSO-d_6): δ -141.86 (m, 2F), -152.95 (m, 1F), -160.88 (m, 2F), from trifluoro acetic acid. Analysis calculated (found): C 50.00 (50.16), H 6.06 (6.23), F 21.97 (21.79). Exact mass calculated (found) for $[M–H]^-$, m/z: 432.1489 (432.1487).

2.5.7 Diethyl (10-((8-hydroxyoctyl)oxy)decyl)phosphonate

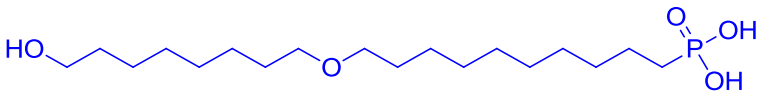

A solution of 10-bromodecan-1-ol (25.5 mL, 127.9 mmol) in 200 mL of anhydrous dichloromethane was cooled to 0 °C. Triethylamine (17.8 mL, 127.7 mmol) dried over molecular sieves was subsequently added and allowed to stir for several minutes before adding a solution of acetyl chloride (10.8 mL, 151.8 mmol) in 50 mL of anhydrous dichloromethane to the reaction flask over the course of an hour. To the resulting cloudy solution was added an additional 100 mL of anhydrous dichloromethane and the solution was allowed to stir at 0 °C for an additional 2 hours and subsequently allowed to stir at room temperature for 5 hours. The reaction was quenched by adding water and the organic layer was collected and washed twice with water, three times with a saturated sodium bicarbonate solution, three times with brine, and dried over magnesium sulfate. After filtering and subsequent removal of volatiles under reduced pressure 10-bromodecyl acetate was obtained as a clear oil (32.3 g, 91.3%, AJG-II-197B). ^{1}H NMR (399.96 MHz, $CDCl_3$) δ 4.04 (t, J = 6.8 Hz, 2H), 3.40 (t, J = 6.8 Hz,

2H), 2.04 (s, 3H), 1.85 (quin, 6.8 Hz, 2H), 1.60 (m, 2H), 1.43-1.29 (m, 12H). $^{13}C\{^{1}H\}$ NMR (100.58 MHz, $CDCl_3$) δ 171.3, 64.8, 34.1, 33.0, 29.5 (two distinct peaks separated by 5.0 Hz, 2C), 29.3, 28.9, 28.7, 28.3, 26.0, 21.2. Elemental Analysis calculated (found): C 51.62 (51.58), H 8.30 (8.52). EI-MS exact mass calculated (found), m/z: 278.0881 (278.0908).

A mixture of 10-bromodecyl acetate (30.2 g, 108.2 mmol) and triethyl phosphite (57.0 mL, 327.6 mmol) was heated under a nitrogen atmosphere at 130 °C for two days. Excess triethyl phosphite and other side products were removed under reduced pressure (0.3 torr) at 90 °C overnight. Unreacted starting material was removed on a silica gel plug, eluting with 2:1 hexane:ethyl acetate then slowly increasing to pure ethyl acetate in order to isolate the desired compound, 10-(diethoxyphosphoryl)decyl acetate as a clear oil (25.5 g, 94%, AJG-II-199E). ^{1}H NMR (300.23 MHz, $CDCl_3$) δ 4.08 (m, 6H), 2.04 (s, 3H), 1.80-1.59 (m, 6H), 1.36-1.27 (m, 18H). EI-MS exact mass calculated (found), m/z: 336.2066 (336.2049).

10-(Diethoxyphosphoryl)decyl acetate (25.4 g, 75.5 mmol) was dissolved in 150 mL of methanol and to this solution added potassium carbonate (13.5 g, 97.7 mmol) dissolved in 150 mL of water. The resulting mixture was heated at 85 °C for two days. The reaction mixture was washed three times with diethyl ether. The collected organic phases were subsequently washed three times each with water followed by brine and dried over magnesium sulfate. After filtering and removing volatiles under reduced pressure the crude material was purified on a silica gel plug eluting first with chloroform and then 95:5 ethyl acetate:methanol, which afforded diethyl 10-hydroxydecylphosphonate as a light yellow oil (19.0 g, 85%, AJG-II-207C). ^{1}H NMR

(300.23 MHz, $CDCl_3$) δ 4.07 (m, 4H), 3.61 (appears as q, *J* = 6.3 Hz, 5.1, 2H), 1.73-1.52 (m, 6H), 1.36-1.20 (m, 18H). $^{13}C\{^1H\}$ NMR (100.58 MHz, $CDCl_3$) δ 62.9, 61.5 (d, *J* = 7.0 Hz, 2C), 32.9, 30.7 (d, *J* = 17.1 Hz), 29.6, 29.5, 29.4, 29.1 (d, *J* = 1.0 Hz), 25.9, 25.8 (d, *J* = 140.7 Hz), 22.4 (d, *J* = 5.0 Hz), 16.5 (d, *J* = 6.0 Hz, 2C). $^{31}P\{^1H\}$ NMR (161.91 MHz, $CDCl_3$): δ 33.4. EI-MS exact mass calculated (found), m/z: 294.1960 (294.1960).

Diethyl 10-(8-bromooctyloxy)decylphosphonate (7.1 g, 24.1 mmol), potassium hydroxide (1.5 g, 26.7 mmol), and aliquat 336 (0.22 mL, 0.5 mmol) were allowed to stir for approximately 15 minutes. 1,8-dibromooctane (18 mL, 97.1 mmol) was then added *via* syringe and the bright yellow solution turned cloudy. The reaction mixture was heated to 50 °C for 6 hours and then 80 °C overnight. Excess dibromide was removed with a silica gel plug, eluting with hexanes followed by 95:5 ethyl acetate:methanol to isolate a clear, slightly yellow oil of diethyl 10-(8-bromooctyloxy)decylphosphonate (6.7 g, 81%, AJG-II-221C). ^1H NMR (300.23 MHz, $CDCl_3$) δ 4.06 (m, 4H), 3.35 (m, 6H), 1.84-1.51 (m, 10H), 1.33-1.23 (m, 26H). $^{13}C\{^1H\}$ NMR (75.5 MHz, $CDCl_3$) δ 71.1 (two close but distinct peaks separated by 7.6 Hz, 2C), 61.5 (d, *J* = 9.0 Hz, 2C), 34.2, 32.9, 30.8 (d, *J* = 23.1 Hz), 29.9, 29.8, 29.7, 29.6, 29.4, 29.2 (two closely spaced peaks separated by 0.8 Hz), 28.9, 28.3, 26.3, 26.2, 25.8 (d, *J* = 139.7 Hz), 22.5 (d, *J* = 5.3 Hz), 16.6 (d, *J* = 6.0 Hz, 2C). Elemental Analysis calculated (found): C 54.43 (54.52), H 9.55 (9.80). EI-MS exact mass calculcated (found): 484.2317 (484.2295).

Diethyl 10-(8-bromooctyloxy)decylphosphonate (5.6 g, 11.5 mmol), was dissolved in 50 mL of anhydrous DMF under a flow of nitrogen. Glacial acetic acid was then added to this solution (4.4 mL, 73.0 mmol) *via* syringe along with solid potassium carbonate (12.7 g, 92.2 mmol). The mixture was allowed to stir at room temperature for

three days. Water was added to the reaction mixture and the desired product extracted with dichloromethane. The organic washings were collected, washed three times each with water followed by brine and dried over solid sodium sulfate. Volatiles were removed under reduced pressure to afford 8-((10-(diethoxyphosphoryl)decyl)oxy)octyl acetate as a clear oil (4.5 g, 9.7 mmol, 85%). ^{1}H NMR (399.96 MHz, $CDCl_3$) δ 4.08-3.97 (m, 6H), 3.33 (td, *J* = 8.0 Hz, 4.0 Hz, 4H), 1.98 (s, 3H), 1.70 – 1.50 (m, 10H), 1.28-1.22 (m, 26 H). ^{13}C{^{1}H} NMR (100.58 MHz, $CDCl_3$) δ 171.4, 71.1, 71.0, 64.8, 61.5 (d, *J* = 7.0 Hz, 2C), 30.7 (d, *J* = 17.1 Hz), 29.9 (two close but distinct carbons separated by 3.0 Hz, 2C), 29.7, 29.6, 29.5 (two close but distinct peaks separated by 3.0 Hz, 2C), 29.3, 29.2 (d, *J* = 2.0 Hz), 28.73, 26.3 (two peaks seaparated by 7.0 Hz, 2C), 26.0, 25.8 (d, *J* = 139.7 Hz), 22.5 (d, *J* = 5.0 Hz), 21.2, 16.6 (d, *J* = 6.0 Hz, 2C). ^{31}P{^{1}H} NMR (161.91 MHz, $CDCl_3$): δ 33.32. EI-MS exact mass calculated (found), m/z: 464.3267 (464.3246).

8-((10-(Diethoxyphosphoryl)decyl)oxy)octyl acetate (4.7 g, 10.1 mmol) was dissolved in 50 mL of methanol and a solution of potassium carbonate (1.9 g, 13.7 mmol) in approximately 30 mL of water was added. This milky white solution was stirred under nitrogen at 85 °C for two days. The desired product was extracted with ethyl acetate three times and combined. The combined organic layers were subsequently washed three times each with water and brine, dried over sodium sulfate, filtered, and volatiles removed under reduced pressure. The resulting oil was purified by Kugelrohr distillation (0.09 Torr, 235 °C) to produce diethyl (10-((8-hydroxyoctyl)oxy)decyl)phosphonate as a clear oil (3.4 g, 81%). ^{1}H NMR (300.23 MHz, $CDCl_3$) δ 4.13-4.02 (m, 4H), 3.62 (t, *J* = 9.0 Hz, 2H), 3.37 (t, *J* = 6.0 Hz, 4H), 1.71-1.50 (m, 10H), 1.33-1.26 (m, 26H). ^{13}C{^{1}H}

NMR (100.58 MHz, $CDCl_3$) δ 71.0 (two close but distinct peaks separated by 2.0 Hz, 2C), 62.9, 61.5 (d, *J* = 7.0 Hz, 2C), 32.9, 30.7 (d, *J* = 17.1 Hz), 29.9, 29.6 (two close but distinct peaks separated by 6.0 Hz, 2C), 29.5 (two close but distinct peaks separated by 1.0 Hz, 2C), 29.4, 29.2 (two close but distinct peaks separated by 1.0 Hz, 2C), 26.3 (two close but distinct peaks separated by 4.0 Hz, 2C), 25.9, 25.8 (d, *J* = 140.7 Hz), 22.5 (d, *J* = 5.0 Hz), 16.6 (d, *J* = 6.0 Hz, 2C). $^{31}P\{^{1}H\}$ NMR (161.91 MHz, $CDCl_3$): δ 33.39. Elemental analysis calculated (found): C 62.53 (62.28), H 11.21 (11.13). EI-MS exact mass calculated (found), m/z: 422.3161 (422.3131).

2.5.8 (10-((8-(Perfluorophenoxy)octyl)oxy)decyl)phosphonic acid

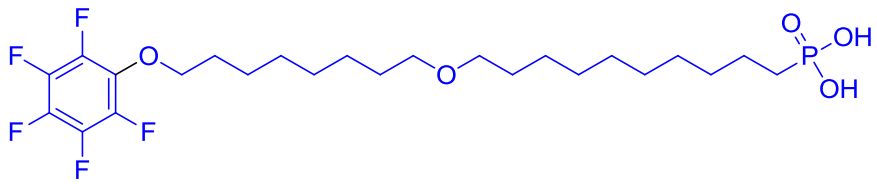

In a microwave tube equipped with a stir bar was combined diethyl (10-((8-hydroxyoctyl)oxy)decyl)phosphonate (0.4 g, 0.9 mmol), hexafluorobenzene (0.25 mL, 2.2 mmol), and finely ground sodium hydroxide (0.06 g, 1.5 mmol). The vessel was sealed, purged with nitrogen, and placed in a CEM Discover microwave. The tube was irradiated with 100 Watts for a total of 7 minutes (achieving a maximum temperature of approximately 175 °C). The reaction mixture was purified by silica gel column chromatography (1:1 hexanes:ethyl acetate) to isolate 0.2 g of diethyl (10-((8-(perfluorophenoxy)octyl)oxy)decyl)phosphonate as a clear oil (41%). The reaction conditions were repeated utilizing at most 0.5 g of starting alcohol in order to obtain more

material. ^{1}H NMR (399.96 MHz, $CDCl_3$) δ 4.10-3.99 (m, 6H), 3.33 (td, *J* = 8.0, 4.0 Hz, 4H), 1.72-1.62 (m, 4H), 1.56-1.45 (m, 6H), 1.40-1.22 (m, 26H). ^{13}C{^{1}H} NMR (100.58 MHz, $CDCl_3$) δ 143.4-140.7 (m, 2C), 139.6-136.81 (m, 2C), 138.6-136.1 (m), 134.0 (m), 76.0, 71.0 (two closely spaced peaks separated by 9.0 Hz, 2C), 61.5 (d, *J* = 6.0 Hz, 2C), 30.7 (d, *J* = 17.1 Hz), 29.9 (three closely spaced peaks separated by 2.0 and 4.0 Hz, respectively), 29.7, 29.6, 29.5, 29.3, 29.2, 26.5, 26.3 (two closely spaced peaks separated by 9.0 Hz, 2C), 25.6, 25.2, 22.5 (d, *J* = 5.0 Hz), 16.6 (d, *J* = 6.0 Hz, 2C). ^{31}P{^{1}H} NMR (161.91 MHz, $CDCl_3$): δ 33.29. ^{19}F{^{1}H} NMR (376.28 MHz, $CDCl_3$): δ -155.84 (apparent d, *J* = 18.82 Hz, 2F), -162.56 (broad t, *J* = 18.82 Hz, 2F), -162.95 (m, 1F) trifluoro acetic acid standard. Elemental analysis calculated (found): C 57.13 (56.89), H 7.88 (7.89), F 16.14 (15.92). EI-MS exact mass calculated (found), m/z: 588.3003 (588.2969).

A solution of diethyl (10-((8-(perfluorophenoxy)octyl)oxy)decyl)phosphonate (0.5 g, 0.8 mmol) in 30 mL of dry dichloromethane and 0.5 mL (3.8 mmol) of bromotrimethylsilane was made. The system was sealed with a greased stopper and allowed to stir for 8 hours. Volatiles were removed under reduced pressure to produce a viscous oil, which was dissolved in 30 mL of a 4:1 methanol:water solution and allowed to stir overnight. After removal of solvent under reduced pressure a white solid was collected and subsequently recrystallized from acetonitrile. This produced (10-((8-(perfluorophenoxy)octyl)oxy)decyl)phosphonic acid as a white solid (0.37 g, 83%). ^{1}H NMR (399.96 MHz, DMSO-d_6) δ 4.17 (t, *J* = 8.0 Hz, 2H), 3.31 (t, *J* = 8 Hz, 4H), 1.69 (quin, *J* = 8 Hz, 2H), 1.54-1.18 (m, br, 28 H). ^{13}C{^{1}H} NMR (100.58 MHz, THF-d_8) δ 144.4-141.7 (m, 2C), 139.1 (dtt, *J* = 249.2, 12.1, 4.0 Hz, 2C), 138.2 (dtt, *J* = 250.2, 13.1,

4.0 Hz), 135.1 (td, *J* = 13.1, 6.0 Hz), 76.9 (t, *J* = 2.6 Hz), 71.7 (2 close peaks separated by 6.4 Hz, 2C), 31.8 (d, *J* = 16.6 Hz), 31.0, 30.9 (2 close peaks separated by 5.8 Hz, 2C), 30.8, 30.6 (2 close peaks separated by 3.5 Hz, 2C), 30.5, 30.4, 30.3, 28.0 (d, *J* = 142.2 Hz), 27.4, 27.3, 26.6, 23.9 (d, *J* = 4.7 Hz); $^{13}C\{^{19}F\}$ NMR (100.58 MHz, THF-d_8) δ 143.1 (2C), 139.1 (2C), 138.2, 135.1. $^{31}P\{^{1}H\}$ NMR (161.91 MHz, THF-d_8): δ 32.96. $^{19}F\{^{1}H\}$ NMR (376.28 MHz, THF-d_8): δ -157.12 (m, 2F), -164.59 (m, 2F), -165.26 (apparent tt, *J* = 21.8, 3.0 Hz, 1F) trifluoro acetic acid standard. Elemental analysis calculated (found): C 54.13 (54.43), H 7.19 (7.23), F 17.84 (17.75). EI-MS exact mass calculated (found) for $[M+H]^+$, m/z: 532.2377 (532.2344).

2.5.9 (10-((8-((Perfluorophenyl)methoxy)octyl)oxy)decyl)phosphonic acid

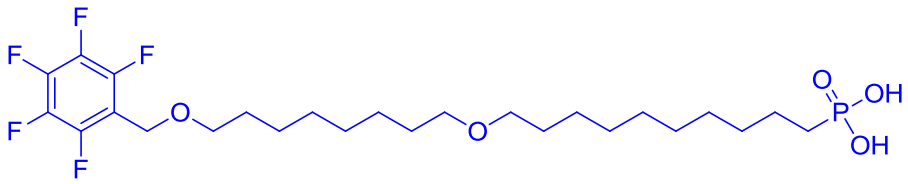

A mixture of diethyl (10-((8-hydroxyoctyl)oxy)decyl)phosphonate (1.5 g, 3.5 mmol), solid, finely ground potassium hydroxide (0.3 g, 5.3 mmol), and Aliquat 336 (0.2 mL, 0.4 mmol) was made in a round bottom flask equipped with a magnetic stirrer. The mixture was allowed to stir for 10 minutes, after which pentafluorobenzyl bromide was added (1 mL, 7.1 mmol). The mixture was allowed to stir at room temperature for two days. The reaction mixture was filtered through silica gel (eluting with ethyl acetate) to afford a yellow tinged oil. The oil was purified by silica gel column chromatography (1:1 hexanes:ethyl acetate) to give diethyl (10-((8-

((perfluorophenyl)methoxy)octyl)oxy)decyl)phosphonate as a clear oil (1.0 g, 1.8 mmol, 49%). ^{1}H NMR (399.96 MHz, $CDCl_3$) δ 4.57 (broad s, 2H), 4.13-4.03 (m, 4H), 3.47 (t, *J* = 8.0 Hz, 2H), 3.38 (t, *J* = 8.0 Hz, 4H), 1.75-1.27 (m, 36H). ^{13}C{^{1}H} NMR (100.58 MHz, $CDCl_3$) δ 147.1-145.9 (m, 2C), 142.8-140.0 (m, 2C), 138.98-136.11 (m), 111.9-111.5 (m), 71.2, 71.1 (two close but distinct peaks separated by 5.0 Hz, 2C), 61.5 (d, *J* = 6.0 Hz, 2C), 59.6, 30.7 (d, *J* = 17.1 Hz), 29.9 (two close but distinct peaks separated by 3.0 Hz, 2C), 29.6 (three close but distinct peaks separated by 2.0 and 4.0 Hz, respectively, 3C), 29.5, 29.4 (two close but distinct peaks separated by 2.0 Hz, 2C), 29.2 (two close but distinct peaks separated by 1.0 Hz), 26.3 (two close but distinct peaks separated by 6.0 Hz, 2C), 26.1, 25.8, (d, *J* = 139.7 Hz), 22.5 (d, *J* = 5.0 Hz), 16.6 (d, *J* = 6.0 Hz, 2C). ^{31}P{^{1}H} NMR (161.91 MHz, $CDCl_3$): δ 33.33. ^{19}F{^{1}H} NMR (376.28 MHz, $CDCl_3$): δ -141.82 - -141.90 (m, 2F), -153.06 (t, *J* = 20.70 Hz, 1F), -161.02, -161.13 (m, 2F) trifluoro acetic acid standard. Elemental analysis calculated (found): C 57.80 (57.52), H 8.03 (8.10), F 15.76 (15.50). EI-MS exact mass calculated (found), m/z: 602.3160 (302.3147).

A solution of diethyl (10-((8-((perfluorophenyl)methoxy)octyl)oxy)decyl)phosphonate (0.5 g, 0.83 mmol) in 30 mL of dry dichloromethane and bromotrimethylsilane (0.5 mL, 3.8 mmol) was made. The system was sealed with a greased stopper and allowed to react for approximately 8 hours. Volatiles were removed under reduced pressure to produce a viscous oil, which was dissolved in 30 mL of 4:1 methanol:water solution and allowed to stir overnight to produce a solid suspended in the liquid. After removal of solvent under reduced pressure the white solid was recrystallized from acetonitrile to afford (10-((8-

((perfluorophenyl)methoxy)octyl)oxy)decyl)phosphonic acid as a white solid (0.4 g, 0.8 mmol, 94%). ^{1}H NMR (399.96 MHz, DMSO-d_6) δ 9.60 (s, 2H), 4.57 (s, 2H), 3.46 (t, *J* 4.0 Hz, 2H), 3.33 (t, *J* = 4.0 Hz, 4H), 1.55 (m, br, 10H), 1.31 (s, br, 20H). ^{13}C{^{1}H} NMR (100.58 MHz, THF-d_8) δ 148.1-145.4 (m, 2C), 143.6-140.77 (m, 2C), 139.9-137.1 (m), 113.3 (td, *J* = 18.1 Hz, 3.0 Hz), 71.7 (3 close peaks separated by 1.9 and 4.0 Hz from center peak), 60.2, 31.8 (d, *J* = 17.1 Hz), 31.0 (2 close peaks separated by 4.2 Hz, 2C), 30.8, 30.7 (2 close peaks separated by 1.8 Hz, 2C), 30.6 (2 close peaks separated by 4.8 Hz, 2C), 30.5, 30.4, 28.0 (d, *J* = 142.1 Hz), 27.4 (2 close peaks separated by 6.7 Hz, 2C), 27.1, 23.9 (d, *J* = 5.0 Hz). ^{31}P{^{1}H} NMR (161.91 MHz, DMSO-d_6): δ 27.74. ^{19}F{^{1}H} NMR (376.28 MHz, DMSO-d_6): δ -141.82 (m, 2F), -153.00 (apparent t, *J* = 20.7 Hz, 1F), -160.88 (m, 2F); trifluoro acetic acid standard. Elemental analysis calculated (found): C 54.94 (54.89), H 7.38 (7.27), F 17.38 (17.19). EI-MS exact mass calculated (found) for [M-H]$^{-}$, m/z: 546.2534 (546.2497).

2.5.10 *N*-(1-Undecyl-dodecyl)-perylene-3,4-dicarboxylicmonoanhydride-9,10-dicarboxylicmonoimide

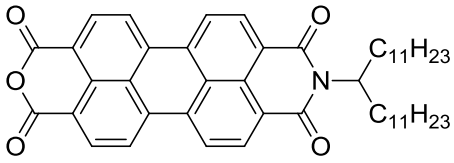

In an oven dried three neck round bottom flask equipped with a septum, addition funnel, and reflux condenser under nitrogen was added lithium aluminum hydride (5.2 g, 135.7 mmol) and anhydrous THF (32 mL, 395.9 mmol). The slurry was cooled to 0 °C

under inert atmosphere and a solution of tricosan-12-one oxime (20 g, 56.6 mmol) in anhydrous THF was added dropwise over the course of 5 minutes. Following complete addition the reaction mixture was allowed to warm to room temperature, stirred at room temperature for one hour, and heated to reflux for 3 hours. The mixture was then allowed to cool to room temperature and stir overnight. Excess lithium aluminum hydride was quenched by cooling the mixture to 0 °C and slowly adding water to the reaction mixture. The desired product was extracted three times with ethyl acetate, washed with 20 % NaOH in DI water, water, dried over magnesium sulfate. Drying under reduced pressure afforded tricosan-12-amine as a white solid (17.1 g, 89 %). ^{1}H NMR (399.96 MHz, $CDCl_3$) δ 1.40 – 1.26 (m, br, 42H), 0.88 (t, J = 6.8 Hz, 6H). The ^{1}H NMR spectrum was consistent with that reported in the literature.[33]

In a round bottom flask 1,2-tricosanone (80 g, 236.3 mmol), hydroxylamine hydrochloride (39.3 mL, 945 mmol), pyridine (133.8 mL, 1653.8 mmol), and ethanol (200 mL) were combined. The solution was allowed to stir under nitrogen and heated to reflux overnight. Upon cooling, the reaction mixture was poured into water and the desired product extracted with hexane, washed with water, dried over magnesium sulfate, filtered, and volatiles removed under reduced pressure to afford tricosan-12-amine (81.4 g, 97 %). ^{1}H NMR (399.96 MHz, $CDCl_3$) δ 2.34 – 2.30 (m, 2H), 2.17 – 2.13 (m, 2H), 1.49 – 1.45 (m, 4H), 1.26 (s, br, 32 H), 0.88 (t, 6H, J = 6.4 Hz).

In a pressure vessel 3,4,9,10-perylenetetracarboxylic dianhydride (6.0 g, 15.3 mmol), tricosan-12-amine (12.0 g, 35.1 mmol), zinc (II) acetate (1.7 g, 9.2 mmol), and imidazole (70.6 g, 1037.7 mmol) were combined. The pressure vessel was flushed with nitrogen, sealed, and the mixture of solids was heated to 180 °C overnight. Upon cooling

400 mL of 2 N HCl was added and the desired product extracted with chloroform. The organic phase was washed with water, dried over magnesium sulfate, and purified on a silica gel plug eluting with 1:1 chloroform:hexane. Removal of volatiles afforded *N*,*N*'-bis(1-undecyl-dodecyl)-perylene-3,4,9,10-tetracarboxylic diimide as a red solid (12.5 g, 79 %, AJG-III-090A). ^{1}H NMR (399.96 MHz, $CDCl_3$) δ 8.64 (m, 8H), 5.22 – 5.15 (m, 2H), 2.26 – 2.18 (m, 4H), 1.88 – 1.83 (m, 4H), 1.36 – 1.14 (m, br, 74H), 0.84 (t, 12H, *J* = 6.8 Hz). The ^{1}H NMR spectrum was consistent with that reported in the literature.[34]

In a round bottom flask *N*,*N*'-Bis(1-undecyl-dodecyl)-perylene-3,4,9,10-tetracarboxylic diimide (1.3 g, 1.3 mmol), powdered potassium hydroxide (0.25 g, 4.4 mmol), and *t*-butanol (24 mL, 251 mmol) were heated to 120 °C for 50 minutes under an inert nitrogen atmosphere. After cooling a 2 N HCl (13 mL) solution in DI water and acetic acid (25 mL) were added to the mixture and the solution allowed to stir at room temperature overnight. The product was purified on a silica gel plug eluting with chloroform. Volatiles were removed to afford the desired compound as a burgundy colored solid which was dissolved in a minimal amount of chloroform and precipitated from methanol (0.52 g, 58 %). ^{1}H NMR (300.23 MHz, $CDCl_3$) δ 8.71 – 8.64 (m, 8H), 5.21 – 5.11 (m, 1H), 2.27 – 2.15 (m, 2H), 1.87 – 1.80 (m, 2H), 1.40 – 1.17 (m, 36 H), 0.81 (t, 6H, *J* = 6.6 Hz). The ^{1}H NMR spectrum was consistent with that reported in the literature.[35]

2.5.11 4-(1,3,8,10-Tetraoxo-9-(tricosan-12-yl)-9,10-dihydroanthra[2,1,9-*def*:6,5,10-*d*'*e*'*f*']diisoquinolin-2(1*H*,3*H*,8*H*)-yl)benzoic acid

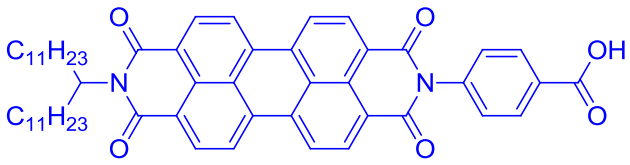

In a pressure vessel, *N*-(1-undecyl-dodecyl)-perylene-3,4-dicarboxylicmonoanhydride-9,10-dicarboxylicmonoimide (0.40 g, 0.6 mmol), 4-aminobenzoic acid (0.23 g, 1.7 mmol), zinc (II) acetate (0.08 g, 0.4 mmol), and imidazole (3.42 g, 50.4 mmol) were combined. The vessel was purged with nitrogen, sealed, and heated to 130 °C for 2 hours. Upon cooling, the mixture was diluted in chloroform, and washed twice with 2 N HCl. The product was then purified on silica gel eluting with 10:1 chloroform:ethanol. Volatiles were removed under reduced pressure to afford the title compound as a red solid, which was further purified by dissolving in minimal chloroform and precipitating slowly with methanol. The resulting solid was washed with methanol, dried and afforded the title compound (0.2 g, 47 %). ^{1}H NMR (399.96 MHz, THF-d_8) δ 11.52 (s, br, 1H), 8.52 – 8.43 (m, 8H), 8.18 (d, 2H, 8.0 Hz), 7.54 (d, 2H, J = 7.6 Hz), 5.18 (m, 1H), 2.35 – 2.28 (m, 2H), 1.92 – 1.85 (m, 2H), 1.46 – 1.13 (m, 36H), 0.85 (apparent triplet, 6H, J = 6.8 Hz). ^{13}C{^{1}H} NMR (100.58 MHz, THF-d_8) δ 167.3, 136.3 (2C), 140.6, 134.8, 134.3, 131.8, 131.2, 131.0, 130.2, 129.7, 129.6, 128.3, 126.4, 126.3, 124.1, 124.0, 115.3, 55.3, 33.4, 32.9, 30.7, 30.7, 30.6, 30.4, 28.2, 23.6, 14.5. MALDI-MS calculated (found) $[M+H]^+$: 833.4530 (833.4881). Elemental Analysis calculated (found) for $C_{54}H_{60}N_2O_6 + H_2O$: C 76.21 (76.27), H 7.34 (7.19), N 3.29 (3.19).

2.5.12 Diethyl (4-aminophenyl)phosphonate

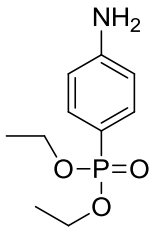

In a round bottom flask *p*-bromoaniline (10 g, 58.1 mmol), palladium (II) acetate (0.6 g, 2.9 mmol), and triphenylphosphine (2.3 g, 8.7 mmol) were combined. The reaction vessel was pumped under vacuum and refilled with dry nitrogen three times followed by the addition of diethyl phosphite (11.2 mL, 87.2 mmol), triethylamine (6.1 mL, 43.6 mmol), and ethanol (100 mL) *via* syringe, The reaction mixture was allowed to stir at reflux for 72 hours and upon cooling volatiles were removed under reduced pressure and the resulting off-white solid was purified by precipitation, first dissolving the solid in a mixture of 1:1 hexane:ethyl acetate followed by the addition of hexane until a white solid was formed. The solid was then further purified on silica gel eluting with chloroform followed by 5 % methanol in chloroform to produce diethyl (4-aminophenyl)phosphonate (3.0 g, 23 %). ^{1}H NMR (300.23 MHz, $CDCl_3$) δ 7.58 – 7.51 (m, 2H), 6.69 – 6.65 (m, 2H), 4.11 – 3.92 (m, 6 H, -OCH_2CH_3 and –NH_2), 1.27 (t, 6H, *J* = 6.0 Hz). The ^{1}H NMR spectrum was consistent with that reported in the literature.[36]

2.5.13 (4-(1,3,8,10-Tetraoxo-9-(tricosan-12-yl)-9,10-dihydroanthra[2,1,9-def:6,5,10-d'e'f']diisoquinolin-2(^{1}H,3H,8H)-yl)phenyl)phosphonic acid

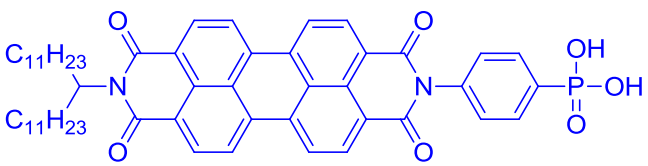

In a pressure vessel, *N*-(1-undecyl-dodecyl)-perylene-3,4-dicarboxylicmonoanhydride-9,10- dicarboxylicmonoimide (0.50 g, 0.7 mmol), zinc (II) acetate (0.10 g, 0.5 mmol), diethyl (4-aminophenyl)phosphonate (0.48 g, 2.1 mmol), and imidazole (4.29 g, 63.0 mmol) were combined. The vessel was purged with nitrogen, sealed, heated to 130 °C for 3 hours. Upon cooling, the mixture was diluted in chloroform, and washed twice with 2 N HCl. The product was then purified on silica gel eluting with 10:1 chloroform:ethanol. Volatiles were removed under reduced pressure to afford the title compound as a red solid, which was further purified by dissolving in minimal chloroform and precipitating slowly with methanol. The resulting solid was washed with methanol, dried and afforded ethyl hydrogen (4-(1,3,8,10-tetraoxo-9-(tricosan-12-yl)-3,8,9,10-tetrahydroanthra[2,1,9-*def*:6,5,10-*d*'*e*'*f*']diisoquinolin-2(1*H*)-yl)phenyl)phosphonate rather than the title compound (0.5 g, 80 %, AJG-III-100C). ^{1}H NMR (399.96 MHz, THF-d_8) δ 8.44 – 8.27 (m, br, 8H), 7.90 – 7.85 (m, 2H), 7.47 (apparent doublet, 2H, J = 8.0 Hz), 5.14 (apparent pentet, ^{1}H, J = 8.0 Hz), 4.12 (pentet, 2H, J = 7.2 Hz), 2.00 – 1.88 (m, 2H), 1.45 – 1.18 (m, 42H), 0.87 – 0.83 (m, 6H). ^{13}C{^{1}H} NMR (100.58 MHz, THF-d_8) δ 163.4, 139.8 (2C), 134.8, 134.1, 133.0, 132.9, 131.3, 130.4, 130.2, 126.3, 126.2, 124.0, 123.9, 62.59, 56.52, 33.5, 33.1, 30.9, 30.9, 30.8, 30.5, 28.5, 23.7, 17.1, 17.0, 14.6. ^{31}P{^{1}H} NMR (161.91 MHz, THF-d_8) δ 20.01. Elemental Analysis calculated (found) for $C_{55}H_{65}N_2O_7P$ C 73.64 (73.54), H 7.30 (7.25), N 3.12 (3.15). MALDI-MS $[M+H]^+$: 897.4.

The ethyl hydrogen (4-(1,3,8,10-tetraoxo-9-(tricosan-12-yl)-9,10-dihydroanthra[2,1,9-*def*:6,5,10-*d*'*e*'*f*']diisoquinolin-2(1*H*,3*H*,8*H*)-yl)phenyl)phosphonate (0.15 g, 1.7 mmol) was dissolved in dry dichloromethane (approximately 20 mL) and

bromotrimethylsilane (1.0 mL, 7.5 mmol) was added via syringe. The reaction vessel was sealed with a greased stopper and tallowed to stir at room temperature overnight. Volatiles were removed under reduced pressure and the resulting thick oil was dissolved in a 10:1 mixture of methanol:deionized water (approximately 20 mL) overnight. Volatiles were removed under reduced pressure and the resulting solid was recrystallized by dissolving the solid in a minimal amount of chloroform and precipitating with methanol to afford a dark red solid (0.12 g, 83 %). ^{1}H NMR (399.96 MHz, THF-d_8) δ 8.18 – 8.07 (m, 8H), 7.95 – 7.90 (m, 2H), 7.55 (m, 2H), 5.78 (s), 5.06 (pentet, ^{1}H, J = 7.2 Hz), 4.22 (t, 1H), 2.01 – 1.92 (m, 2H), 1.42 – 1.27 (m, 36H), 0.88 – 0.84 (m, 6H). Attempts to obtain ^{13}C both at room temperature, high temperature, and with various solvents afforded spectra that were extremely noisy. ^{31}P{^{1}H} NMR (161.91 MHz, THF-d_8) δ 16.01. MALDI-MS calculated (found) $[M+H]^+$: 869.4295 (869.4252). Elemental Analysis calculated (found) for $C_{53}H_{61}N_2O_7P + H_2O$: C 71.76 (71.55), H 7.16 (6.98), N 3.16 (3.19).

2.5.14 Diethyl (4-(4,4,5,5-tetramethyl-1,3,2-dioxaborolan-2-yl)phenyl)phosphonate

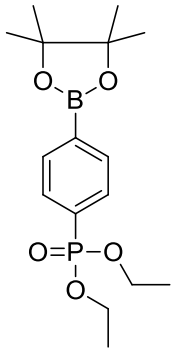

A two neck round bottom flask was charged with bis(pinacolato)diboron (2.63 g, 10.4 mmol), 1,1'-bis(diphenylphosphino)ferrocene-palladium(II)dichloride dichloromethane complex (0.23 g, 0.3 mmol), and potassium acetate (1.77 mL, 28.4 mmol) under inert nitrogen atmosphere. The mixture was dissolved in anhydrous dimethyl sulfoxide (45 mL) and diethyl (4-bromophenyl)phosphonate was added (2.77 g, 9.45 mmol) followed by heating of the system to 80 °C for approximately 30 hours. The product was extracted with ethyl acetate, washed with water, dried over magnesium sulfate, and filtered. Removal of volatiles under reduced pressure and Kugelrohr distillation (60 mTorr, 175 °C) afforded the title compound as an off white solid (1.15 g, 36 %, AJG-III-120H). ^{1}H NMR (399.96 MHz, $CDCl_3$) δ 7.91 – 7.88 (m, 2H), 7.83 – 7.78 (m, 2H), 4.19 – 4.01 (m, 4H), 1.35 (s, 12H), 1.31 (t, 6H, *J* = 7.2 Hz). ^{13}C{^{1}H} (100.58 MHz, $CDCl_3$) δ 134.8 (d, 2C, *J* = 14.5 Hz), 132.1, 131.1 (d, 2C, *J* =9.6 Hz), 130.2, 84.4 (2C), 62.3 (d, *J* = 5.3 Hz), 25.1 (4C), 16.5 (d, *J* = 6.4 Hz). ^{31}P{^{1}H} NMR (161.91 MHz, $CDCl_3$) δ 19.16. Elemental analysis calculated (found) C 56.49 (56.45), H 7.70 (7.73). EI-MS calculated (found) $[M]^+$: 340.1611 (340.1615).

2.5.15 (4'-(1,3,8,10-Tetraoxo-9-(tricosan-12-yl)-9,10-dihydroanthra[2,1,9-*def*:6,5,10-*d'e'f'*]diisoquinolin-2(1*H*,3*H*,8*H*)-yl)-[1,1'-biphenyl]-4-yl)phosphonic acid

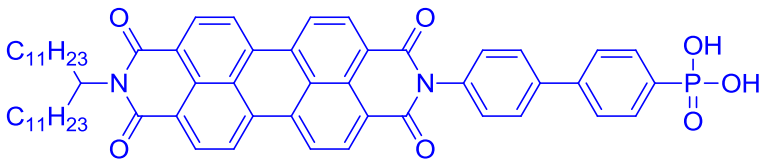

To a round bottom flask equipped with a reflux condenser was added 2-(4-bromophenyl)-9-(tricosan-12-yl)anthra[2,1,9-*def*:6,5,10-*d*'*e*'*f*']diisoquinoline-1,3,8,10(2*H*,9*H*)-tetraone (0.3 g, 0.4 mmol), diethyl (4-(4,4,5,5-tetramethyl-1,3,2-dioxaborolan-2-yl)phenyl)phosphonate (0.5 g, 1.5 mmol), and tetrakis(triphenylphosphine)palladium (0) (0.08 g, 0.1 mmol), which were dissolved in a solvent mixture of toluene (50 mL), methanol (14 mL), and 2 M potassium carbonate in DI water (14 mL). The reaction mixture was stirred under nitrogen at 75 °C for 15 hours under the exclusion of light. After cooling the reaction mixture was washed two times with DI water, two times with brine, the organic phase was dried over magnesium sulfate, and filtered. Volatiles were removed under reduced pressure and the resulting red solid was dissolved in a minimal amount of chloroform and precipitated slowly after addition of methanol. The precipitate was washed with methanol and filtered to afford the title compound as a red solid (0.29 g, 82 %, AJG-III-124B). ^{1}H NMR (399.96 MHz, THF-d_8) δ 8.71 – 8.67 (m, 4H), 8.58 – 8.51 (m, br, 4H), 7.92 – 7.83 (m, 6H), 7.52 (apparent doublet, 2H, J = 8.0 Hz), 5.24 – 5.16 (m, 1H), 4.16 – 4.04 (m, 4H), 2.37 – 2.31 (m, 2H), 1.92 – 1.84 (m, 2H), 1.41 – 1.16 (m, 42H), 0.86 – 0.83 (m, 6H). ^{13}C{^{1}H} NMR (100.58 MHz, THF-d_8) δ 163.6, 145.1, 145.1, 140.9, 136.9, 134.9, 134.5, 133.4, 133.3, 131.4, 130.9, 130.8, 129.8, 129.7, 128.9, 128.5, 128.1, 127.9, 126.5, 126.4, 124.2, 62.4 (d, 2C, J = 6.0 Hz), 55.4, 33.5, 33.1, 30.9, 30.9, 30.8, 30.8, 30.8, 30.5, 23.7, 17.0 (d, 2C, J = 6.0 Hz), 14.6. ^{31}P{^{1}H} NMR (161.91 MHz, $CDCl_3$) δ 18.58. MALDI-MS calculated (found) $[M+H]^+$: 1001.5234 (1001.5212).

The diethyl (4'-(1,3,8,10-tetraoxo-9-(tricosan-12-yl)-9,10-dihydroanthra[2,1,9-*def*:6,5,10-*d*'*e*'*f*']diisoquinolin-2(1*H*,3*H*,8*H*)-yl)-[1,1'-biphenyl]-4-yl)phosphonate (0.16 g,

0.2 mmol) was dissolved in dry dichloromethane (approximately 10 mL) and bromotrimethylsilane (1.5 mL, 11.4 mmol) was added via syringe. The reaction vessel was sealed with a greased stopper and tallowed to stir at room temperature overnight. Volatiles were removed under reduced pressure and the resulting solid was dissolved in a 10:1 mixture of methanol:deionized water (approximately 20 mL) overnight. Volatiles were removed under reduced pressure and the resulting solid was recrystallized by dissolving the solid in a minimal amount of chloroform and precipitating with methanol to afford a dark red solid (0.12 g, 86 %, AJG-III-128A). ^{1}H and ^{13}C NMR proved difficult to obtain at either room temperature or elevated temperature in a variety of solvents due to aggregation. Elemental Analysis calculated (found) for $C_{59}H_{65}N_2O_7P$ + H_2O: C 73.58 (73.02), H 7.01 (6.89), 2.91 (2.95). MALDI-MS calculated (found) $[M+H]^+$: 945.4608 (945.4592).

2.5.16 Benzylphosphonic acid

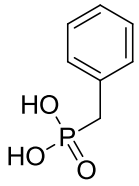

Benzyl bromide (34.7 mL, 292.1 mmol) and triethylphosphite (145 mL, 833.4 mmol) were combined in a round bottom flask and heated at 130 °C under inert nitrogen atmosphere overnight. Excess triethylphosphite and other side products were removed under reduced pressure (approximately 0.2 torr at 60 °C) overnight. Diethyl benzylphosphonate was obtained as a colorless oil (66.0 g, 99 %). ^{1}H NMR (300.23,

DMSO-d_6) 7.27 (m, 5H), 3.92 (m, 4H), 3.19 (d, J = 21.62 Hz, 2H), 1.14 (t, J = 6.91 Hz, 6H). Spectra was consistent with the desired product.[37]

Diethyl benzylphosphonate (29 g, 127.1 mmol) was dissolved in dry dichloromethane (75 mL). Bromotrimethylsilane (50.0 mL, 381.2 mmol) was added and the flask sealed with a greased stopper. After stirring at room temperature overnight volatiles were removed under reduced pressure to afford a dark, viscous oil that was subsequently dissolved in a solution of 10:1 methanol:water (200 mL) and allowed to stir at room temperature overnight. Volatiles were removed under reduced pressure and the resulting solid was recrystallized from 4:1 acetone:chloroform to yield a white crystalline powder (20.0 g, 91 %). ^{1}H (399.96 MHz, DMSO-d_6) 7.29-7.23 (m, 4H), 7.21-7.17 (m, ^{1}H), 2.95 (d, J = 21.20 Hz, 2H). ^{13}C{^{1}H} (100.58 MHz, DMSO-d_6) 134.1 (d, J = 8.8 Hz), 129.7 (d, J = 6.2 Hz), 128.0 (d, J = 2.8 Hz), 125.9 (d, J = 3.4 Hz), 35.3 (d, J = 132.4 Hz). ^{31}P{^{1}H} (161.91 MHz, DMSO-d_6) 22.48. ^{1}H NMR was consistent with that reported in the literature.[38]

2.5.17 (2-Fluorobenzyl)phosphonic acid

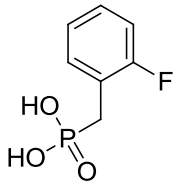

2-Fluorobenzylbromide (7.2 g, 38.1 mmol) was combined with triethylphosphite (55.2 mL, 317 mmol) and the mixture was heated with stirring at 130 °C overnight. Excess triethylphosphite and other side products were removed under vacuum

(approximately 0.2 torr) at 60 °C overnight to afford a clear oil (26.1 g, 98 %). NMR spectra was consistent with that reported in the literature.[39]

2-Fluorobenzylphosphonate (10.0 g, 40.6 mmol), was dissolved in dry dichloromethane (130 mL). Bromotrimethylsilane (16.0 mL, 121 mmol) was added *via* syringe. The reaction vessel was sealed with a greased stopper and allowed to stir at room temperature overnight. Volatiles were removed under reduced pressure yield a viscous oil. This oil was subsequently dissolved in a 4:1 methanol:water (50 mL) solution and allowed to stir overnight. After removal of the solvents, recrystallization from acetonitrile afforded a white, crystalline solid (7.5 g, 97 %). NMR spectra was consistent with that reported in the literature.[40-41]

2.5.18 2-(Trifluoromethyl)benzylphosphonic acid

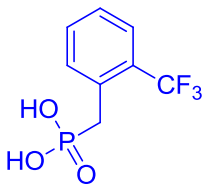

2-Trifluoromethylbenzylbromide (11.7g, 48.9 mmol) was combined with triethylphosphite (23.0 mL, 132.2 mmol) and the mixture was heated with stirring at 130 °C overnight. Excess triethylphosphite and other side products were removed under vacuum (approximately 0.2 torr) at 60 °C overnight to afford a clear oil (14.2 g, 98%). ^{1}H NMR (399.96 MHz, acetone-d_6), δ 7.72 (m, 2H), 7.62 (appears as triplet, J = 8.0 Hz, 1H), 7.46 (m, 1H), 4.00 (m, 4H), 3.36 (d, J = 22.4 Hz, 2H), 1.12 (t, J = 7.20 Hz, 6H). ^{13}C{^{1}H} NMR (100.58 MHz, acetone-d_6): δ 134.4 (d, J = 5.1 Hz), 133.7 (m), 133.2 (dd, J

= 10.0, 1.7 Hz), 130.3 (dd, *J* = 29.4, 7.9), 128.9 (d, *J* = 3.2 Hz), 127.8 (qd, *J* = 5.7, 2.5 Hz), 125.0 (d, *J* = 1.6 Hz), 63.4 (d, *J* = 6.6 Hz), 32.4 (q, *J* = 2.0 Hz), 17.6 (d, *J* = 5.8 Hz). $^{31}P\{^{1}H\}$ NMR (161.91 MHz, acetone-d_6): δ 25.67. ^{19}F (276.29 MHz, acetone-d_6, trifluoroacetic acid standard): δ -57.24. Analysis calculated (found) %: C 48.66 (48.37), H 5.44 (5.47). Exact Mass calculated (found) for $[M+H]^+$, m/z: 296.0789 (296.0789).

2-(Trifluoromethyl)benzylphosphonate (5.0 g, 16.9 mmol), was dissolved in dry dichloromethane (20 mL). Bromotrimethylsilane (8.9 mL, 67.5 mmol) was added *via* syringe. The reaction vessel was sealed with a greased stopper and allowed to stir at room temperature overnight. Volatiles were removed under reduced pressure yield a viscous oil. This oil was subsequently dissolved in a 4:1 methanol:water (50 mL) solution and allowed to stir overnight. After removal of the solvents, recrystallization from acetonitrile afforded a white, crystalline solid (AJG-II-164A, 4.0 g, 99 %). ^{1}H NMR (399.96 MHz, DMSO-d_6), δ 7.62 (m, 3H), 7.41 (t, *J* = 7.60 Hz, 1H), 3.16 (d, *J* = 22.00, 2H). $^{13}C\{^{1}H\}$ NMR (100.58 MHz, DMSO-d_6): δ 132.8 (m), 132.3 (d, *J* = 4.8 Hz), 131.8 (appears as doublet, *J* = 1.6 Hz), 127.5 (dd, *J* = 29.1, 7.6 Hz), 126.5 (d, *J* = 3.0 Hz), 125.6 (m), 122.9, 31.8 (d, *J* = 132.1 Hz). $^{31}P\{^{1}H\}$ NMR (161.91 MHz, DMSO-d_6): δ 20.4. ^{19}F (276.29 MHz, DMSO-d_6, trifluoroacetic acid standard): δ -55.9. Analysis calculated (found) %: C 40.02 (40.15), H 3.36 (3.22), F 23.74 (23.58). Exact Mass calculated (found) for $[M]^+$, m/z: 240.0163 (240.0166).

2.5.19 3-Fluorobenzylphosphonic acid

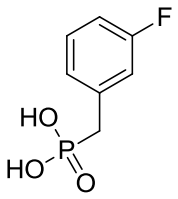

3-Fluorobenzylbromide (6.6 mL, 53.8 mmol) was combined with triethylphosphite (27.5 mL, 158.0 mmol) and the mixture was heated with stirring at 130 °C overnight. Excess triethylphosphite and other side products were removed under vacuum (approximately 0.2 torr) at 60 °C overnight to afford a clear, pale-yellow oil. (13.1 g, 99%) ^{1}H NMR (399.96 MHz, $CDCl_3$), δ 7.25 (m, 1H), 7.06, (m, 1H), 7.00 (m, 1H), 6.93 (m, 1H), 4.02 (m, 4H), 3.13 (d, *J* = 22.0, 2H), 1.24 (t, *J* = 6.80, 6H). Exact Mass calculated (found) for $[M+H]^+$, m/z: 248.0821 (246.0823). Spectra was consistent with that reported in the literature.[42]

Diethyl 3-fluorobenzylphosphonate (6.1 g, 24.8 mmol), was dissolved in dry dichloromethane (40 mL). Bromotrimethylsilane (10.0 mL, 75.8 mmol) was added *via* syringe. The reaction vessel was sealed with a greased stopper and allowed to stir at room temperature overnight. Volatiles were removed under reduced pressure yield a viscous oil. This oil was subsequently dissolved in a 4:1 methanol:water (50 mL) solution and allowed to stir overnight. After removal of the solvents, repeated recrystallizations from 1:1 dichloromethan:acetonitrile afforded a white, plate crystals (3.0 g, 65 %, AJG-II-173A-C). ^{1}H NMR (399.96 MHz, DMSO-d_6), δ 10.39 (s, br, 2H), 7.31 (apparent quartet, *J* = 7.20, 1H), 7.05 (m, 3H), 3.01 (d, *J* = 21.60 Hz, 2H). ^{13}C{^{1}H} NMR (100.58 MHz, DMSO-d_6): δ 162.0 (dd, *J* = 242.4, 3.3 Hz), 137.1 (t, *J* = 8.5 Hz), 129.8 (dd, *J* = 8.5, 2.8), 126.0 (dd, *J* = 6.4, 2.6 Hz), 116.4 (dd, *J* = 21.4, 6.0 Hz), 112.8

(dd, J = 20.9, 3.4), 35.0 (d, J = 131.8 Hz). $^{31}P\{^{1}H\}$ NMR (161.91 MHz, DMSO-d_6): δ 21.89. ^{19}F (276.29 MHz, DMSO-d_6, trifluoroacetic acid standard): δ -112.57. Analysis calculated (found) %: C 44.22 (44.17), H 4.24 (4.21), F 9.99 (9.88). Exact Mass calculated (found) for $[M]^+$, m/z: 240.0163 (240.0168).

2.5.20 3-(trifluoromethyl)benzylphosphonic acid

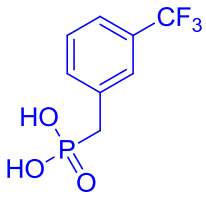

3-trifluoromethylbenzylbromide (6.5 mL, 42.6 mmol) was combined with triethylphosphite (22.0 mL, 126.4 mmol) and the mixture was heated with stirring at 130 °C overnight. Excess triethylphosphite and other side products were removed under vacuum (approximately 0.2 torr) at 60 °C overnight to afford a clear, pale-yellow oil. This oil was further purified by Kugelrohr distillation (0.17 Torr, 125 °C) to achieve the desired phosphonate as a clear oil (AJG-II-162H, 7.3 g, 58%) ^{1}H NMR (399.96 MHz, $CDCl_3$), δ 7.52 (m, 3H), 7.43 (m, 1H), 4.02 (m, 4H), 3.17 (d, J = 21.6 Hz, 2H), 1.23 (t, J = 7.20 Hz, 6H). Analysis calculated (found) %: C 48.66 (48.41), H 5.44 (5.52). Exact Mass calculated (found) for $[M+H]^+$, m/z: 296.0789 (296.0809). Spectra and analyses are consistent with those reported in the literature. [43-46]

3-(Trifluoromethyl)benzylphosphonate (4.0 g, 13.5 mmol), was dissolved in dry dichloromethane (30 mL). Bromotrimethylsilane (6.0 mL, 45.5 mmol) was added *via*

syringe. The reaction vessel was sealed with a greased stopper and allowed to stir at room temperature overnight. Volatiles were removed under reduced pressure yield a viscous oil. This oil was subsequently dissolved in a 4:1 methanol:water (50 mL) solution and allowed to stir overnight. After removal of the solvents, recrystallization from acetonitrile afforded a white, crystalline solid (2.1 g, 66 %, AJG-II-175A). ^{1}H NMR (399.96 MHz, DMSO-d_6), δ 10.52 (s, br, 2H), 7.61 (s, br, 1H), 7.53 (m, 3H), 3.10 (d, J = 21.20 Hz, 2H). ^{13}C{^{1}H} NMR (100.58 MHz, DMSO-d_6): δ 135.8 (d, J = 8.6 Hz), 133.8 (m), 128.9 (m), 126.0 (m), 126.0 (m), 124.3 (d, J = 272.3 Hz), 122.7 (quin, J = 3.6 Hz), 35.0 (d, J = 131.3 Hz). ^{31}P{^{1}H} NMR (161.91 MHz, DMSO-d_6): δ 21.65. ^{19}F (276.29 MHz, DMSO-d_6, trifluoroacetic acid standard): δ -59.38. Analysis calculated (found) %: C 40.02 (39.98), H 3.36 (3.23), F 23.74 (23.92). Exact Mass calculated (found) for $[M]^{+}$, m/z: 240.0163 (240.0168).

2.5.21 3,4-Difluorobenzylphosphonic acid

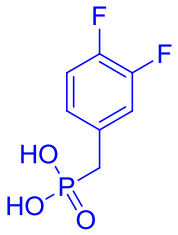

4-(bromomethyl)-1,2-difluorobenzene (6.0 mL, 46.7 mmol) was combined with triethylphosphite (25.0 mL, 143.7 mmol) and the mixture was heated with stirring at 130 °C overnight. Excess triethylphosphite and other side products were removed under vacuum (approximately 0.2 torr) at 60 °C overnight to afford a clear oil. (12.2 g, 99%)

^{1}H NMR (399.96 MHz, $CDCl_3$), δ 7.12 (m, 2H), 7.01, (m, 1H), 4.03 (m, 4H), 3.08 (d, *J* = 28.80 Hz, 2H), 1.25 (t, *J* = 9.20 Hz, 6H). Exact Mass calculated (found) for $[M+H]^+$, m/z: 264.0727 (264.0732). Spectra were consistent with that reported in the literature.[47-48]

Diethyl 3,4-difluorobenzylphosphonate (6.0 g, 22.7 mmol), was dissolved in dry dichloromethane (40 mL). Bromotrimethylsilane (9.0 mL, 68.2 mmol) was added *via* syringe. The reaction vessel was sealed with a greased stopper and allowed to stir at room temperature overnight. Volatiles were removed under reduced pressure yield a viscous oil. This oil was subsequently dissolved in a 4:1 methanol:water (50 mL) solution and allowed to stir overnight. After removal of the solvents, repeated recrystallizations from 1:1 dichloromethane:acetonitrile afforded a white crystals (3.2 g, 68 %). ^{1}H NMR (399.96 MHz, DMSO-d_6), δ 10.5 (s, br, 2H), 2.27 (m, 2H), 7.06 (m, 1H), 2.97 (d, *J* = 21.6 Hz, 2H). $^{13}C\{^{1}H\}$ NMR 148.9 (ddd, *J* = 245.1, 13.5, 5.1 Hz), 148.1 (ddd, *J* = 248.9, 12.4, 3.6 Hz), 132.1 (m), 126.4 (m), 118.4 (dd, *J* = 17.2, 6.0 Hz), 116.9 (dd, *J* = 16.9, 2.8 Hz), 34.2 (d, *J* = 131.9 Hz). $^{31}P\{^{1}H\}$ NMR (161.91 MHz, DMSO-d_6): δ 21.80. ^{19}F (276.29 MHz, DMSO-d_6, trifluoroacetic acid standard): δ -138.073 (quin, *J* = 10.16 Hz, 1F), -141.10 (m, 1F). Analysis calculated (found) %: C 40.40 (40.38), H 3.39 (3.26), F 18.26 (18.08). Exact Mass calculated (found) for $[M]^+$, m/z: 208.0101 (208.0103).

2.5.22 2,3-Difluorobenzylphosphonic acid

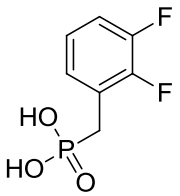

4-(Bromomethyl)-2,3-difluorobenzene (5.9 mL, 46.4 mmol) was combined with triethylphosphite (26.0 mL, 149.4 mmol) and the mixture was heated with stirring at 130 °C overnight. Excess triethylphosphite and other side products were removed under vacuum (approximately 0.2 torr) at 60 °C overnight to afford a clear oil. (12.2 g) ^{1}H NMR (399.96 MHz, $CDCl_3$), δ 7.11-7.00 (m, 3H), 4.05 (q, *J* = 7.20 4H), 3.20 (d, *J* = 21.60, 2H), 1.25 (t, *J* = 7.20, 6H). Exact Mass calculated (found) for $[M+H]^+$, m/z: 264.0727 (264.0729). ^{1}H NMR data consistent with that previously reported in the patent literature.[49]

Diethyl 2,3-difluorobenzylphosphonate (6.0 g, 22.7 mmol), was dissolved in dry dichloromethane (40 mL). Bromotrimethylsilane (9.0 mL, 68.2 mmol) was added *via* syringe. The reaction vessel was sealed with a greased stopper and allowed to stir at room temperature overnight. Volatiles were removed under reduced pressure yield a viscous oil. This oil was subsequently dissolved in a 4:1 methanol:water (50 mL) solution and allowed to stir overnight. After removal of the solvents, repeated recrystallizations from acetonitrile afforded a white plate crystals (4.4 g, yield over 2 steps: 93 %). ^{1}H NMR (399.96 MHz, DMSO-d_6), δ 10.03 (s, br, 2H), 7.25 (m, 1H), 7.13 (m, 2H), 3.03 (d, *J* = 21.60 Hz, 2H). ^{13}C{^{1}H} NMR(100.58 MHz, DMSO-d_6) δ 149.7 (ddd, *J* = 190.1, 13.2, 3.0), 148.1 (ddd, *J* = 245.9, 12.7, 6.7 Hz), 127.1 (m), 124.2, 124.1 (m), 115.0 (dd, *J* = 16.9, 3.5 Hz), 28.2 (d, *J* = 130.9 Hz). ^{31}P{^{1}H} NMR (161.91 MHz,

DMSO-d_6): δ 20.35. ^{19}F (276.29 MHz, DMSO-d_6, trifluoroacetic acid standard): δ 137.41 (m, 1F), 140.82 (m, 1F). Analysis calculated (found) %: C 40.40 (40.34), H 3.39 (3.27), F 18.26 (18.09). Exact Mass calculated (found) for $[M]^+$, m/z: 208.0101 (208.0101). Spectral data consistent with that previously reported in the literature.[50]

2.5.23 (4-Fluorobenzyl)phosphonic acid

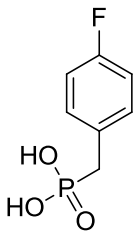

In a 250 mL round bottom flask *p*-fluorobenzyl bromide (3.5 g, 18.5 mmol) was combined with triethyl phosphite (10 mL, 56 mmol) and the mixture was allowed to stir at 135 °C overnight. Excess triethyl phosphite and other undesired side products were removed by heating at 70 °C under a vacuum of approximately 0.01 Torr overnight produce diethyl 4-fluorobenzylphosphonate as a light yellow oil (4.5 g, 99 %, AJG-III-106). ^{1}H NMR (399.96 MHz, $CDCl_3$) δ 7.30 – 7.25 (m, 2H), 7.02 – 6.98 (m, 2H), 4.06 – 3.97 (m, 4H), 3.12 (d, 2H, J = 21.6 Hz), 1.27 – 1.23 (m, 6H). The ^{1}H NMR spectrum was consistent with that reported in the literature.[51]

The diethyl 4-fluorobenzylphosphonate (4.51 g, 18.3 mmol) was dissolved in dry dichloromethane (approximately 50 mL) and bromotrimethylsilane (7.3 mL, 55.0 mmol) was added via syringe. The reaction vessel was sealed with a greased stopper and tallowed to stir at room temperature overnight. Volatiles were removed under reduced

pressure and the resulting thick oil was dissolved in a 10:1 mixture of methanol:deionized water (approximately 50 mL) overnight. Volatiles were removed under reduced pressure and the resulting solid was recrystallized from hot acetonitrile to obtain the title compound as an off white solid (2.21 g, 64 %). ^{1}H NMR (399.96 MHz, DMSO-d_6) δ 7.25 (m, 2H), 7.11 – 7.07 (m, 2H), 2.94 (d, 2H, J = 21.2 Hz). ^{31}P{^{1}H} NMR (161.91 MHz, DMSO-d_6) δ 21.96. ^{19}F{^{1}H} (376.28 MHz, $CDCl_3$) δ 115.70 (m, 1F). ^{1}H NMR consistent with that reported in the literature.[52]

2.5.24 (4-(Trifluoromethyl)benzyl)phosphonic acid

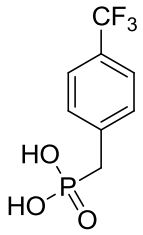

In a 250 mL round bottom flask 4-(trifluoromethyl)benzyl bromide (25.4 g, 106.3 mmol) was combined with an excess of triethyl phosphite (55 mL, 329.4 mmol) and the mixture was allowed to stir at 135 °C for 72 hours. Excess triethyl phosphite and other unwanted side products were removed under reduced pressure (approximately 1.5 Torr) at 80 °C overnight to afford diethyl 4-(trifluoromethyl)benzylphosphonate as a clear oil (30.8 g, 98% yield, AJG-II-294C). ^{1}H NMR (300.23 MHz, $CDCl_3$) 7.57-7.39 (m, 4H), 4.07-3.97 (m, 4H), 3.18 (d, J = 24.0 Hz, 2H), 1.24 (t, J = 9.0 Hz, 6H). Spectrum is consistent with that reported in the literature.[53]

Diethyl 4-(trifluoromethyl)benzylphosphonate (15.5 g, 52.2 mmol), was dissolved in dry dichloromethane (approximately 100 mL) and bromotrimethylsilane (20 mL, 151.5 mmol) was added *via* syringe. The reaction vessel was sealed with a greased stopper and the mixture stirred at room temperature for approximately 4 hours. Volatiles were removed under reduced pressure and the resulting thick oil was dissolved in a 10:1 mixture of methanol:DI water (50 mL) and allowed to stir overnight at room temperature. Removal of volatiles under vacuum afforded a white solid, which was recrystallized from hot acetonitrile to afford 4-(trifluoromethyl)beznylphosphonic acid (6.0 g, 50 % yield, AJG-II-298A). ^{1}H NMR (399.96 MHz, DMSO-d_6) δ 7.64 (d, J = 8.0 Hz, 2H), 7.46 (m, 2H), 3.07 (d, $J_{\text{P-H}}$ = 20.0 Hz, 2H). ^{19}F{^{1}H} NMR (376.28 MHz, DMSO-d_6) δ -59.12 (s, 3F), from trifluoro acetic acid. ^{31}P{^{1}H} NMR (161.91 MHz, DMSO-d_6) δ 21.00. Spectra are consistent with those reported in the literature.[54]

2.5.25 (4-Methoxybenzyl)phosphonic acid

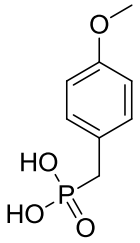

In a 250 mL round bottom flask 1-(chloromethyl)-4-methoxybenzene (13.0 mL, 95.8 mmol) was combined with triethyl phosphite (50 mL, 287.4 mmol) and the mixture allowed to stir under nitrogen at 135 °C for 24 hours. Excess triethyl phosphite and other undesired side products were removed by heating at 85 °C under vacuum (approximately

0.1 Torr) for 8 hours to afford diethyl 4-methoxybenzylphosphonate as a clear oil (21.6 g, 83.6 mmol, 88 % yield). ^{1}H NMR (399.96 MHz, $CDCl_3$) δ 7.17 (m, 2H), 6.80 (d, *J* = 8.0 Hz), 3.96 (m, 4H), 3.74 (s, 3H), 3.05 (d, JP-H = 20.0 Hz), 1.20 (t, *J* = 8.0 Hz, 6H). The ^{1}H NMR spectrum was consistent with that reported in the literature.[55]

The diethyl 4-methoxybenzylphosphonate (10.3 g, 38.9 mmol) was dissolved in dry dichloromethane (approximately 30 mL) and bromotrimethylsilane (15 mL, 113.7 mmol) was added via syringe. The reaction vessel was sealed with a greased stopper and allowed to stir at room temperature for approximately 8 hours. Volatiles were removed under reduced pressure and the resulting thick oil was dissolved in a 10:1 mixture of methanol:deionized water (approximately 50 mL. After approximately 10 minutes a white solid began to crash out of solution and the reaction mixture was allowed to continue stirring under ambient conditions overnight. Volatiles were removed under reduced pressure and the resulting solid was recrystallized from hot methanol to obtain white crystals of the title compound (4 g, 51 %). ^{1}H NMR (399.96 MHz, DMSO-d_6) δ 7.15 (m, 2H), 6.84 (m, 2H), 3.69 (s, 3H), 2.87 (d, J_{P-H} = 24.0 Hz). ^{31}P{^{1}H} NMR (161.91 MHz, DMSO-d_6) δ 22.79. ^{13}C{^{1}H} NMR (75.5 MHz, DMSO-d_6) δ 157.6 (d, *J* = 3.8 Hz), 130.5 (d, *J* = 6.0 Hz, 2C), 125.9 (d, *J* = 9.1 Hz), 113.4 (d, *J* = 2.3 Hz, 2C), 55.0, 34.2 (d, *J* = 133.6 Hz). Elemental analysis calculated (found): C 47.53 (47.77), H 5.48 (5.51). Exact mass calculated (found) for [M^+], m/z: 202.0395 (202.0395).

2.5.26 (2,6-Difluorobenzyl)phosphonic acid

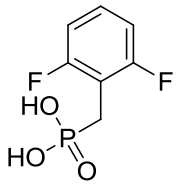

In a 250 mL round bottom flask 2,6-difluorobenzyl bromide (21.4 g, 103 mmol) was combined with triethyl phosphite (58 mL, 333 mmol) and the mixture allowed to stir at 135 °C for 48 hours. Excess triethyl phosphite and other unwanted side products were removed under vacuum, approximately 0.9 Torr at 90 °C overnight to afford diethyl d,6-difluorobenzylphosphonate as a clear oil (26.3 g, 96 % yield, AJG-II-293D). ^{1}H NMR (399.96 MHz, $CDCl_3$) 7.19 (m, 1H), 6.87 (m, 2H), 4.06 (m, 4H), 3.21 (d, J = 24.00 Hz, 2H), 1.25 (t, J = 8.00 Hz, 6 H). Spectrum consistent with that reported in the literature.[40]

Diethyl 2,6-difluorobenzylphosphonate (15.0 g, 56.8 mmol) was dissolved in dry dichloromethane (approximately 100 mL). Bromotrimethylsilane (22.5 mL, 170.3 mmol) was added *via* syringe. The reaction vessel was capped with a greased stopper and allowed to stir overnight at room temperature. Volatiles were removed under reduced pressure. The resulting oil was then dissolved in a 10:1 methanol:water mixture (50 mL) and allowed to stir overnight. Volatiles were removed under vacuum to afford a powdery solid that was subsequently recrystallized from hot acetonitrile to yield the title compound as a white, crystalline solid (11.3 g, 96% yield, AJG-II-295A-B). ^{1}H NMR (399.96 MHz, DMSO-d_6) δ 7.30 (m, 1H), 7.05 (m, 2H), 2.98 (d, $J_{P\text{-}H}$ = 20.00 Hz, 2H). ^{19}F{^{1}H} NMR (376.3 MHz, DMSO-d_6) δ -111.45 (q, $J_{P\text{-}F}$ = 3.8 Hz, 2F), from trifluoro acetic acid. ^{31}P{^{1}H} NMR (161.91 MHz, DMSO-d_6) 19.46. Spectra are consistent with those reported in the literature.[40]

2.5.27 (2,6-Bis(trifluoromethyl)benzyl)phosphonic acid

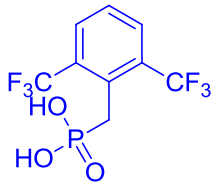

A slurry of potassium *tert*-butoxide (7.9 g, 70.4 mmol) with 100 mL of THF was made in a 250 mL round bottom flask equipped with a nitrogen inlet, septum, and stir bar. The mixture was cooled to -30 °C at which time 1,3-bis(trifluoromethyl)benzene (7.5 mL, 48.0 mmol) was added and the mixture cooled to -80 °C for 1 hour in a dry ice/acetone bath followed by addition of *n*-BuLi (24.5 mL, 70.0 mmol, 2.85 M in hexanes) dropwise over the course of 30 minutes. The temperature of the resulting dark red solution was maintained at -80 °C over the course of 7.5 hours at which point chloromethyl methyl ether (7.3 mL, 107.3 mmol) dropwise over 20 minutes. The reaction mixture was then allowed to warm to room temperature and stirred overnight. After quenching the reaction with deionized water, the aqueous layer was extracted with diethyl ether three times. The collected organic layers were then washed three times with brine, dried over magnesium sulfate, filtered, and volatiles removed under reduced pressure to afford a brown colored oil. The oil was distilled twice *via* Kugelrohr distillation (0.4 Torr, 40 °C) to afford 2-(methoxymethyl)-1,3-bis(trifluoromethyl)benzene (5.90 g, 49%). ^{1}H (300.23 MHz, $CDCl_3$) δ 7.99 (d, J = 6.00 Hz, 2H), 7.55 (t, J = 7.50 Hz, 1H), 4.64 (s, 2H), 3.42 (apparent doublet, J = 3.00 Hz, 3H).

$^{13}C\{^{1}H\}$ (75.50 MHz, $CDCl_3$) 135.4, 132.4, 130.1 (q, *J* = 6.04 Hz), 128.9, 122.1, 66.7, 59.0. Spectra are consistent with those reported in the literature.[56]

A round bottom flask charged with 2-(methoxymethyl)-1,3-bis(trifluoromethyl)benzene (5.90 g, 22.9 mmol) was cooled to -40 °C for 30 minutes in a dry ice/acetone bath followed by addition of BBr_3 (25.3 mL, 267.6 mmol). The mixture was stirred cold for 20 minutes then warmed to room temperature and allowed to stir for 4 hours. After cooling the mixture to 0 °C the solution was diluted with DCM and quenched with water. The aqueous layer was extracted with diethyl ether, and the collected organic layers washed with brine, dried over magnesium sulfate, and volatiles removed under reduced pressure. The resulting light brown oil was distilled by Kugelrohor distillation (0.3 Torr, 40 °C) to afford 2-(bromomethyl)-1,3-bis(trifluoromethyl)benzene as a colorless oil (6.1 g, 87%). ^{1}H (399.96 MHz, $CDCl_3$) δ 7.90 (d, *J* = 8.0 Hz, 2H), 7.57 (t, *J* = 8.40 Hz), 4.76 (s, 2H). $^{19}F\{^{1}H\}$ (376.28 MHz, $CDCl_3$) δ -57.79 (referenced to trifluoroacetic acid at -76.55). Spectra are consistent with those reported in the literature.[56]

In a 100 mL round bottom flask a mixture of 2-(bromomethyl)-1,3-bis(trifluoromethyl)benzene (0.89 g, 2.9 mmol) and triethyl phosphite (7.0 mL, 40.2 mmol) was made and stirred at 130 °C for 24 hours. Excess triethyl phosphite and other undesired side products were removed by heating at 40 °C under vacuum (approximately 0.2 Torr) overnight to afford a clear oil that formed crystals at room temperature. The product was then recrystallized from pentane to afford diethyl 2,6-bis(trifluoromethyl)benzylphosphonate as a white crystalline solid (0.7 g, 70%). ^{1}H (300.23 MHz, $CDCl_3$) δ 7.9 (d, *J* = 9.0 Hz, 2H), 7.50 (t, *J* = 9.0 Hz, 1H), 4.05 (m, 4H),

3.70 (d, J = 24.0 Hz, 2H), 1.25 (t, J = 4.5 Hz, 6H). $^{31}P\{^{1}H\}$ NMR (161.91 MHz, $CDCl_3$) δ 23.29. $^{19}F\{^{1}H\}$ (376.28 MHz, $CDCl_3$) δ -56.99 (referenced to trifluoroacetic acid at -76.55). Elemental Analysis calculated (found): C 42.87 (42.95), H 4.15 (4.26), F 31.30 (31.44). Exact mass calculated (found) for $[M^+]$, m/z: 364.0663 (364.0650).

In a 100 mL round bottom flask diethyl 2,6-bis(trifluoromethyl)benzylphosphonate (1.0 g, 2.7 mmol) was dissolved in anhydrous dichloromethane (approximately 30 mL). Bromotrimethylsilane (1.1 mL, 8.3 mmol) was added to the solution *via* syringe and the reaction vessel was sealed with a greased stopper before allowing it to stir at room temperature overnight. Volatiles were removed under reduced pressure and the resulting thick oil was dissolved in a 10:1 methanol:water mixture, which was allowed to stir at room temperature overnight. Removal of volatiles *in vacuo* gave rise to a white solid, which was recrystallized from acetonitrile to afford 2,6-bis(trifluoromethyl)benzylphosphonic acid (0.8 g, 94%). ^{1}H (399.96 MHz, DMSO-d_6) δ 8.03 (d, J = 8.0 Hz, 2H), 7.66 (t, J = 8.0 Hz, 1H), 3.47 (d, J = 20.0 Hz, 2H). $^{31}P\{^{1}H\}$ NMR (161.91 MHz, DMSO-d_6) δ $^{19}F\{^{1}H\}$ (376.28 MHz, $CDCl_3$) δ -54.65 (referenced to trifluoroacetic acid at -76.55). Elemental Analysis calculated (found): C 35.08 (35.34), H 2.29 (2.35), F 37.00 (36.82). Exact mass calculated (found) for $[M^+]$, m/z: 308.0037 (308.0042).

2.5.28 (Perfluoro–1,4–phenylene)bis(methylene)diphosphonic acid

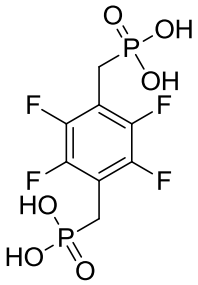

Tetraethyl (perfluoro-1,4-phenylene)bis(methylene)diphosphonate (1.1 g, 2.4 mmol) was dissolved in dry dichloromethane (20 mL). Bromotrimethylsilane (1.3 mL, 13.3 mmol) was added *via* syringe. The reaction vessel was sealed with a greased stopper and allowed to stir at room temperature overnight. Volatiles were removed under reduced pressure to yield a viscous oil. This oil was subsequently dissolved in a mixture of 4:1 methanol:water (20 mL) and allowed to stir overnight. Volatiles were removed under reduced pressure to afford a white solid whose spectra was consistent with that reported in the literature.[57]

2.5.29 4-Nitrobenzylphosphonic acid

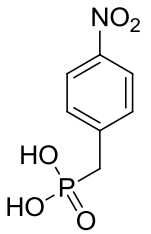

In a 250 mL round bottom flask 1-(bromomethyl-4-nitrobenzene (20.7 g, 95.8 mmol) was combined with triethyl phosphite (50 mL, 287.4 mmol) and the mixture was allowed to stir at 135 °C overnight. Excess triethyl phosphite and other undesired side

products were removed by heating at 90 °C under a vacuum of approximately 0.2 Torr for approximately 36 hours. The slightly impure material was then run through a silica gel plug (eluting with 95:5 ethyl acetate:methanol) and purified by silica gel column chromatography (100% ethyl acetate) to produce diethyl 4-nitrobenzylphosphonate (20.6 g, 79 %, AJG-III-004I). ^{1}H NMR (399.96 MHz, $CDCl_3$) δ 8.15 (m, 2H), 7.45 (m, 2H), 4.02 (m, 4H), 3.21 (d, $J_{P\text{-}H}$ = 20.0 Hz), 1.23 (t, J = 8.0 Hz). The ^{1}H NMR spectrum was consistent with that reported in the literature.[58]

The diethyl 4-nitrobenzylphosphonate (5.01 g, 18.3 mmol) was dissolved in dry dichloromethane (approximately 50 mL) and bromotrimethylsilane (7.5 mL, 56.8 mmol) was added *via* syringe. The reaction vessel was sealed with a greased stopper and tallowed to stir at room temperature overnight. Volatiles were removed under reduced pressure and the resulting thick oil was dissolved in a 10:1 mixture of methanol:deionized water (approximately 50 mL) overnight. Volatiles were removed under reduced pressure and the resulting solid was recrystallized from hot acetonitrile to obtain the title compound as an off-white solid (3.6 g, 90%). ^{1}H NMR (399.96 MHz, DMSO-d_6) δ 8.16 (d, J = 8.0 Hz, 2H), 7.51 (dd, J = 8.8, 2.4 Hz, 2H), 3.15 (d, J = 22.0 Hz, 2H). ^{31}P{^{1}H} NMR (161.91 MHz, DMSO-d_6) δ 20.26. ^{1}H NMR was consistent with that reported in the literature.[59]

2.5.30 (3,4,5-Trifluorophenyl)phosphonic acid

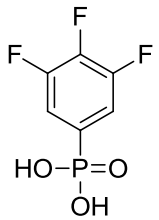

In a round bottom flask, diethyl (3,4,5-trifluorophenyl)phosphonate (2.5 g, 9.3 mmol) was dissolved in dry dichloromethane (approximately 30 mL) and bromotrimethylsilane (6 mL, 45.5 mmol) was added *via* syringe. The reaction vessel was sealed with a greased stopper and the mixture stirred at room temperature overnight. Volatiles were removed under reduced pressure and the resulting thick oil was dissolved in a 10:1 mixture of methanol:DI water (30 mL) and allowed to stir overnight at room temperature. Removal of solvent under vacuum afforded a tan colored solid, which was recrystallized from hot toluene to afford (3,4,5-trifluorophenyl)phosphonic acid as tan colored, fluffy crystals (1.7 g, 86 %, AJG-II-311A). ^{1}H NMR (399.96 MHz, DMSO-d_6) δ 7.52 - 7.41 (m, 2H). ^{31}P{^{1}H} NMR (161.91 MHz, DMSO-d_6) 9.22 (td, J(P-F) = 6.5, 3.2 Hz). Spectra are consistent with those previously reported.[13]

2.5.31 Hydrogen 4-ammoniobenzylphosphonate

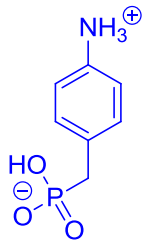

In a 500 mL round bottom flask diethyl 4-nitrobenzylphosphonate (11.9 g, 43.6 mmol) was dissolved in approximately 300 mL of ethanol. To the stirred solution was added tin (II) chloride dihydrate (49.5 g, 219.4 mmol) in portions, followed by the addition of 13.8 mL of concentrated hydrochloric acid. The reaction was subsequently heated to reflux overnight. After allowing to cool to room temperature, the pH of the

solution was adjusted to between 8 and 9 with 1M NaOH (approximately 250 mL). The desired product was then extracted with dichloromethane three times and the combined organic phases washed with water, brine, and dried over sodium sulfate. Removal of volatiles under reduced pressure afforded diethyl 4-aminobenzylphosphonate as a yellow crystalline solid that slowly changed color to light pink with time (AJG-III-014B, 9.6 g, 90%). The ^{1}H was consistent with that reported in the literature.[58]

The diethyl 4-aminobenzylphosphonate (2.0 g, 8.2 mmol) was dissolved in dry dichloromethane (approximately 30 mL) and bromotrimethylsilane (3.4 mL, 25.8 mmol) was added *via* syringe. The reaction vessel was sealed with a greased stopper and tallowed to stir at room temperature overnight. Volatiles were removed under reduced pressure and the resulting thick oil was dissolved in a 10:1 mixture of methanol:deionized water (approximately 50 mL) overnight. Volatiles were removed under reduced pressure and the resulting solid was recrystallized from hot acetonitrile to afford a tan colored solid. ^{1}H NMR (399.96 MHz, DMSO-d_6) δ 10.5-8.5 (s, br, 3H), 7.33 (m, 2H), 7.22 (m, 2H), 2.99 (d, $J_{P\text{-}H}$ = 20.0 Hz) – Note that the amine peak is not visible and this is indicative of having a zwitterionic compound. ^{31}P{^{1}H} NMR (161.91 MHz, DMSO-d_6) δ 21.66. EI-MS exact mass calculated (found) for [M^{+}], m/z: 187.0398 (187.0405).

2.5.32 (4-(Dimethylamino)benzyl)phosphonic acid

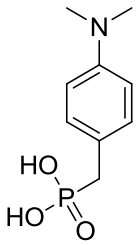

A solution of diethyl 4-nitrobenzylphosphonate (4.5 g, 18.5 mmol) in anhydrous THF (approximately 45 mL) and sodium borohydride (4.2 g, 111.0 mmol) was made. A solution of formaldehyde (37% in water, 6.2 mL, 25.3 mmol) and 3M sulfuric acid (4.8 mL) was also made. Half of the solution containing the phosphonate was added to formaldehyde/acid mixture. This was followed by addition of an extra 4.8 mL of 3M sulfuric acid and then addition of the remaining phosphonate solution. The mixture was allowed to stir overnight at room temperature. The reaction mixture was subsequently diluted with water (30 mL) and 1M sodium hydroxide was added (approximately 60 mL). The aqueous layer was then washed with diethyl ether three times. The combined organic layers were then washed with brine, dried over sodium sulfate, filtered, and volatiles removed under reduced pressure to afford a yellow oil that turned tan in color with time. The oil was purified on a silica gel column (eluting with 95:5 ethyl acetate:methanol) to afford diethyl 4-(dimethylamino)benzylphosphonate as a pale yellow oil (5.8 g, 87 %). ^{1}H and ^{31}P NMR were consistent with that reported in the literature.[58]

The diethyl 4-(dimethylamino)benzylphosphonate (3.4 g, 12.5 mmol) was dissolved in dry dichloromethane (approximately 50 mL) and bromotrimethylsilane (7.0 mL, 53.0 mmol) was added *via* syringe. The reaction vessel was sealed with a greased stopper and tallowed to stir at room temperature for 48 hours. Volatiles were removed under reduced pressure and the resulting thick oil was dissolved in a 10:1 mixture of methanol:deionized water (approximately 50 mL) overnight. Volatiles were removed under reduced pressure and the resulting tan solid turns to a gel-like material as it sits under atmospheric conditions. The solid was attempted to be recrystallized from

hexanes, acetonitrile, acetone, toluene, THF, DCM, petroleum ether, and IPA all of which the compound was insoluble in at room temperature and elevated temperatures. An appropriate solvent system of ethanol and THF was found to work best to afford a white solid in solution. When filtered, this white solid immediately turned brown and gel-like. ^{1}H (399.96 MHz, DMSO-d_6) 7.22 (apparent doublet, broad, 2H), 7.09 (s, broad, 2H), 3.00 (s, 6H), 2.91 (d, J = 24.0 Hz, 2H). ^{31}P{^{1}H} NMR (161.91 MHz, DMSO-d_6) δ 21.91. The ^{1}H NMR is consistent with the desired compound except for trapping both ethanol and THF.

2.5.33 (1-Cyano-2-(4-(diethylamino)phenyl)vinyl)phosphonic acid

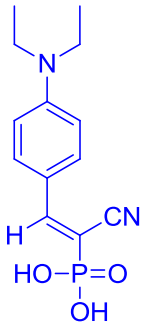

A solution of 4-diethylamino)benzaldehyde (5.0 g, 28.2 mmol) and diethyl cyanomethylphosphonate (4.5 mL, 28.6 mmol) in methanol (approximately 15 mL), The mixture was allowed to stir at room temperature and piperidine (20 drops) was added along with approximately 0.5 g of molecular sieves (4 A). The reaction mixture was allowed to stir at room temperature over the course of 48 hours. The reaction mixture was subsequently diluted with DCM. Volatiles were removed from the reaction vessel and the resulting thick oil was added to a silica gel column for purification (eluting with

3.5:1.5 DCM:ethyl acetate). Removal of volatiles afforded diethyl (1-cyano-2-(4-(diethylamino)phenyl)vinyl)phosphonate as a thick yellow oil (7.3 g, 77%). ^{1}H NMR (399.96 MHz, DMSO-d_6) δ 7.84 (d, J = 9.2 Hz, 2H), 7.74 (d, J = 21.2 Hz, 1H), 6.62 (d, J = 9.2 Hz, 2H), 4.14 (m, 4H), 3.40 (q, J = 7.2 Hz, 4H), 1.34 (td, J = 7.2, 0.4, 6H), 1.18 (t, J = 6.8 Hz, 6H). ^{31}P{^{1}H} NMR (161.91 MHz, $CDCl_3$) δ 15.72. ^{13}C{^{1}H} (100.58 MHz, $CDCl_3$) δ 158.5 (d, J = 7.9 Hz), 151.5, 133.8, 120.2 (d, J = 18.2 Hz), 117.5 (d, J = 11.1 Hz), 111.1, 88.4 (d, J = 203.1 Hz), 63.1 (d, J = 5.6 Hz), 44.9, 16.4 (d, J = 6.6 Hz), 12.7. Elemental Analysis calculated (found): C 60.70 (60.00), H 7.49 (7.46), N 8.33 (8.21). EI-MS exact mass calculated (found) for [M^+], m/z: 336.1603 (336.1605).

The (1-cyano-2-(4-(diethylamino)phenyl)vinyl)phosphonate (4.0 g, 11.9 mmol) was dissolved in dry dichloromethane (approximately 75 mL) and bromotrimethylsilane (6.4 mL, 47.7 mmol) was added *via* syringe. The reaction vessel was sealed with a greased stopper and tallowed to stir at room temperature overnight. Volatiles were removed under reduced pressure and the resulting thick oil was dissolved in a 10:1 mixture of methanol:deionized water (approximately 50 mL) 48 hours. Volatiles were removed under reduced pressure and the impure yellow solid was recrystallized from hot ethanol to afford the title compound as a bright yellow solid (2.9 g, 88%). ^{1}H NMR (300.23 MHz, DMSO-d_6) δ 7.81 (d, J = 9.9 Hz, 2H), 7.58 (d, J = 19.8 Hz, 1H), 7.76 (d, J = 9.0 Hz, 2H), 3.42 (m, 4H), 1.11 (t, J = 6.6 Hz, 6H). ^{13}C{^{1}H} NMR (75.50 MHz, DMSO-d_6) δ 153.9 (d, J = 6.8 Hz), 150.4, 132.4, 119.5 (d, J = 8.5 Hz), 118.5 (d, J = 10.9), 111.0, 94.8 (d, J = 190.8Hz), 43.9, 12.4. ^{31}P{^{1}H} NMR (161.91 MHz, DMSO-d_6) δ 8.93. Elemental Analysis calculated (found): C 55.71 (55.75), H 6.11 (6.18), N 10.00 (9.99). EI-MS found for [M+H]$^+$: 281.0.

2.5.34 4-Cyanophenylphosphonic acid

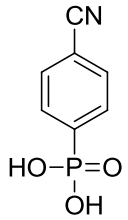

A solution of *p*-bromobenzonitrile (1.85 g, 10 mmol), dicyclohexylmethylamine (2.93 g, 15 mmol), and diethyl phosphite (1.55 mL 12 mmol) in 40 mL of ethanol was sparged under a flow of nitrogen. A mixture of triphenylphosphine (0.16 g, 0.6 mmol) and palladium (II) acetate (46 mg, 0.2 mmol) was added. After heating at reflux overnight, the solution was diluted with 300 mL of ethyl acetate and the organic layer was washed three times each with 1N HCl, saturated sodium bicarbonate, and saturated sodium chloride solution. The organic layer was dried over anhydrous magnesium sulfate, filtered, volatiles removed under reduced pressure to afford a dark, yellow oil. The oil was purified by column chromatography (1:3 hexane:ethyl acetate) to produce a bright yellow viscous oil (1.44 g, 60%). ^{1}H NMR (300.23 MHz, $CDCl_3$) δ 7.93 (m, 2H), 7.76 (m, 2H), 4.15 (m, 4H), 1.34 (t, *J* = 5.40 Hz, 6H). $^{13}C\{^{1}H\}$ NMR (75.49 MHz, $CDCl_3$) δ 135.1 (d, *J* = 140.8 Hz), 132.5 (d, *J* = 7.3 Hz), 132.3 (d, *J* = 11.2 Hz), 118.1 (d, *J* = 1.0 Hz), 116.2 (d, *J* = 2.7 Hz), 62.9 (d, *J* = 4.3 Hz), 16.6 (d, *J* = 4.8 Hz). $^{31}P\{^{1}H\}$ NMR (161.91 MHz, DMSO-d_6): δ 16.2. Spectra was consistent with that reported in the literature.[60]

A solution of diethyl 4-cyanophenyl phosphonate (0.50 g, 2.1 mmol) was made in 15 mL of dry dichloromethane and bromotrimethylsilane (0.95 mL, 7.2 mmol) was added *via* syringe. The mixture was capped with a greased stopper and allowed to stir for four hours. The volatiles were removed *in vacuo* to produce a light-yellow oil. This oil was dissolved in methanol (16 mL) and water (2 mL) and allowed to stir overnight. The removal of solvents under reduced pressure produced a dark oil and the addition of dichloromethane to this oil caused the precipitation of an off-white solid (0.26 g, 67.8%). ^{1}H NMR (300.23 MHz, DMSO-d_6) δ 7.93 (dd, J = 7.96 Hz, 3.21 Hz, 2H) 7.82 (dd, J = 12.61 Hz, 8.11 Hz, 2H). Spectra were consistent with the desired compound and that reported in the literature.[61]

2.5.35 4-Nitrophenylphosphonic acid

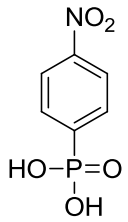

A solution of p-bromonitrobenzene (4.0 g, 20.0 mmol), dicyclohexylmethylamine (5.9 g, 30 mmol), and diethyl phosphite (3.1 mL, 23.7 mmol) in 80 mL of ethanol was spaged under a flow of nitrogen. A mixture of triphenylphosphine (0.32 g, 1.2 mmol) and palladium (II) acetate (90.5 mg, 0.4 mmol) was added under inert atmosphere. After heating at reflux for 16 hours the clear yellow mixture was diluted with 300 mL of ethyl acetate and the organic layer was washed three times each with 100 mL portions of 1N HCl, saturated sodium bicarbonate solution, and saturated sodium chloride solution. The

organic layer was dried over anhydrous magnesium sulfate, filtered, and volatiles removed under reduced pressure. The resulting impure oil was purified by column chromatography packed with silica gel (1:3 hexanes:ethyl acetate). Removal of volatiles under reduced pressure provided diethyl 4-nitrophenylphosphonate as a yellow oil (3.69 g, 71%). ^{1}H NMR (300.23 MHz, $CDCl_3$) δ 8.28 (ddd, J = 9.00 Hz, 3.3 Hz, 1.50 Hz, 2H), 7.98 (m, 2H), 4.14 (m, 4H), 1.32 (t, J = 7.20 Hz, 6H). ^{13}C{^{1}H} NMR (75 MHz, $CDCl_3$) δ 150.1 (d, J = 3.68 Hz), 135.7 (d, J = 93.0 Hz), 132.9 (d, J = 10.5 Hz), 123.3 (d, J = 15.2 Hz), 62.7 (d, J = 5.6 Hz), 16.3 (d, J = 6.2 Hz). NMR spectra was consistent with that previously reported in the literature.[62]

A solution of diethyl 4-nitrophenylphosphonate (1.5 g, 5.9 mmol) in 40 mL of dry dichloromethane was made and bromotrimethylsilane (2.3 mL, 17.4 mmol) was added *via* syringe. The system was sealed with a greased stopper and allowed to stir for four hours. The volatiles were removed *in vacuo* to produce a light yellow/orange oil. This oil was dissolved in a mixture of methanol (41 mL) and water (7 mL) and allowed to stir overnight. The removal of solvents under reduced pressure produced a dark yellow/orange oil. Crystallization was noted after several days to produce the title compound in 95% purity (0.85 g, 72%) contaminated with diethyl 4-nitrophenylphosphonate. ^{1}H NMR (300.23 MHz, DMSO-d_6) δ 7.93 (dd, J = 7.96 Hz, 3.21 Hz, 2H) 7.82 (dd, J = 12.61 Hz, 8.11 Hz, 2H). ^{1}H NMR consistent with that reported in the literature.[63-64]

2.5.36 (4-Bromophenyl)phosphonate

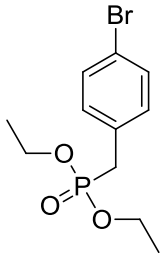

In a round bottom flask under inert nitrogen atmosphere 1-bromo-4-iodobenzene (5.00 g, 17.7 mmol) and tetrakis(triphenylphosphine)palladium (0) (0.37 g, 0.3 mmol) were combined and dissolved in anhydrous toluene (67 mL, 1148.8 mmol). Triethylamine (2.6 mL, 18.4 mmol) and triethylphosphite (3.1 mL, 17.7 mmol) were subsequently added and the mixture was heated to 50 °C. Upon observing no formation of desired product by GC-MS an additional 0.5 g of palladium catalyst (0.4 mmol) was added and the mixture heated to 90 °C for 72 hours. The reaction mixture was cooled, filtered, and purified by silica gel column chromatography eluting with 3:1 hexane:ethyl acetate followed by 95:5 dichloromethane:ethanol to afford a yellow oil (2.77 g, 54 %, AJG-III-113C). ^{1}H NMR (399.96 MHz, $CDCl_3$) δ 7.71 – 7.60 (m, 4H), 4.20 – 4.03 (m, 4H), 1.33 (t, *J* = 6.8 Hz, 6H). ^{31}P{^{1}H} NMR (161.91 MHz, $CDCl_3$) δ 18.31. ^{1}H NMR was consistent with that previously reported in the literature.[65]

2.5.37 Octylphosphonic acid

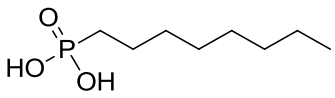

1-bromooctane (25.7 g, 133 mmol) was combined with triethylphosphite (68 mL, 391 mmol) and the mixture was allowed to stir at 140 °C overnight. Excess triethylphosphite was removed under reduced pressure (approximately 0.2 Torr) at 80 °C overnight to yield octylphosphonate as an oil (27.8 g, 86 %). ^{1}H NMR spectrum is consistent with the desired product.[66]

Octylphosphonate (10 g, 40.0 mmol) was dissolved in anhydrous dichloromethane (50 mL) and bromotrimethylsilane (15.0 mL, 114 mmol) was added *via* syringe. The system was sealed with a greased stopper and allowed to stir overnight. Volatiles were removed under reduced pressure and the resulting viscous oil was dissolved in a solution of 10:1 methanol:water (50 mL) and allowed to stir overnight. After removing volatiles, the product was recrystallized from acetronitrile to afford octylphosphonic acid as a white, crystalline solid (6.0 g, 77 %). ^{1}H NMR spectrum was consistent with that of the desired product.[67]

2.5.38 (3,3,4,4,5,5,6,6,7,7,8,8,8-Tridecafluorooctyl)phosphonic acid

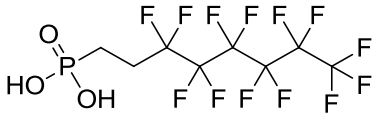

3,3,4,4,5,5,6,6,7,7,8,8,8-Tridecafluorooctylphosphonate (10.4 g, 21.5 mmol) was dissolved in anhydrous dichloromethane (100 mL) and bromotrimethylsilane (9.0 mL, 68.2 mmol) was added *via* syringe. The system was sealed with a greased stopper and allowed to stir overnight. Volatiles were removed under reduced pressure and the resulting viscous oil was dissolved in a solution of 4:1 methanol:water (50 mL) and

allowed to stir overnight. After removing volatiles, the product was recrystallized from acetronitrile to afford (3,3,4,4,5,5,6,6,7,7,8,8,8-tridecafluorooctyl)phosphonic acid as a white, crystalline solid (6.3 g, 71 %). ^{1}H NMR spectrum was consistent with that of the desired product.[68]

2.5.39 Dodecylphosphonic acid

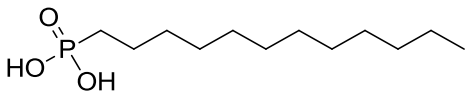

1-Bromododecane (25.2 g, 101 mmol) was combined with triethylphosphite (52 mL, 299 mmol) and the mixture was allowed to stir at 140 °C overnight. Excess triethylphosphite was removed under reduced pressure (approximately 0.2 Torr) at 80 °C overnight to yield diethyl dodecylphosphonate as an oil (29.6 g, 96 %). ^{1}H NMR spectrum is consistent with the desired product.[69]

Diethyl dodecylphosphonate (15.0 g, 49.0 mmol) was dissolved in anhydrous dichloromethane (50 mL) and bromotrimethylsilane (20.0 mL, 152 mmol) was added *via* syringe. The system was sealed with a greased stopper and allowed to stir for 48 hours. Volatiles were removed under reduced pressure and the resulting viscous oil was dissolved in a solution of 10:1 methanol:water (60 mL) and allowed to stir overnight. After removing volatiles, the product was recrystallized from acetronitrile to afford dodecylphosphonic acid as a white, crystalline solid (11.7 g, 96 %). ^{1}H NMR spectrum was consistent with that of the desired product.[69]

2.5.40 (3,3,4,4,5,5,6,6,7,7,8,8,9,9,10,10,11,11,12,12,12-Henicosafluorododecyl)phosphonic acid

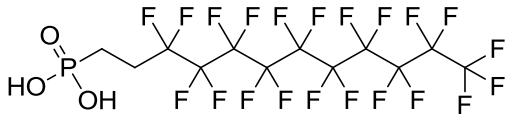

In a 250 mL round bottom flask ^{1}H, ^{1}H, 2H, 2H-perfluoro-1-iododododecane (20.1 g, 29.8 mmol) was combined with triethyl phosphite (16 mL, 92.0 mmol) and the mixture was allowed to stir at 130 °C for 48 hours. Excess triethyl phosphite and other undesired side products were removed by heating at 85 °C under vacuum (approximately 0.1 Torr) overnight. A substantial amount of starting material sublimed, and was added back to the impure material. Triethyl phosphite was then added to the combination of unreacted starting material and impure product (45 mL, 258.6 mmol) and reacted at 135 °C for an additional 72 hours. Removal of excess triethyl phosphite under vacuum (80 °C, approximately 0.2 Torr) overnight afforded a brown, waxy solid. A portion of this solid was purified by silica gel column chromatography eluting with a mixture of 9:1 ethyl acetate:hexanes to afford diethyl (3,3,4,4,5,5,6,6,7,7,8,8,9,9,10,10,11,11,12,12,12-henicosafluorododecyl)phosphonate as a white solid (3.1 g, 15.2 %). The ^{1}H NMR was consistent with that reported in the literature.[70]

The phosphonate from the previous step was placed in a 250 mL round bottom flask (2.76 g, 4.0 mmol) and dissolved in anhydrous dichloromethane (approximately 25 mL). Bromotrimethylsilane (2.2 mL, 16.7 mmol) was added *via* syringe. The reaction vessel was sealed with a greased stopper and the mixture allowed to stir at room

temperature overnight. Volatiles were removed under reduced pressure and the resulting thick oil was dissolved in a 10:1 methanol:water solution, which was allowed to stir at room temperature for 6 hours. After removal of volatiles *in vacuo* a white solid was obtained which was recrystallized from methanol to obtain the title compound (1.4 g, 55.3 %). ^{1}H NMR (399.96 MHz, CD_3OD) δ 2.43 (m, 2H), 1.94 (m, 2H). $^{31}P\{^{1}H\}$ NMR (161.91 MHz, CD_3OD) δ 26.51. $^{19}F\{^{1}H\}$ NMR (376.28 MHz, CD_3OD) δ -80.47 (t, J = 7.5 Hz, 2F), -114.50 (s, br, 3F), -120.80 (s, br, 10F), -121.80 (s, br, 2F), -122.57 (s, br, 2F), -125.37 (s, br, 2F). Elemental analysis calculated (found): C 22.95 (22.80), H 0.96 (0.89), F 63.52 (63.60). The ^{1}H NMR was consistent with that reported in the literature.[70]

2.5.41 2-(3,5-Dimethoxyphenyl)propan-2-yl 3-(triethoxysilyl)propylcarbamate

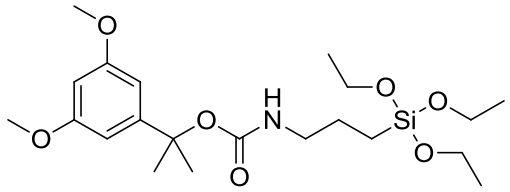

The methyl magnesium bromide Grignard reagent (18.8 mL, 56.4 mmol, 3.0 M in ether) was placed into an oven dried three neck flask under nitrogen equipped with a stir bar, addition funnel, reflux condenser, and a septum. The Grignard was allowed to cool to 0 °C for twenty minutes. A solution of methyl 3,5-dimethoxybenzoate (5.0 g, 25.5 mmol) in 50 mL of freshly distilled diethyl ether was made in a 250 mL schlenk flask that had been pumped under vacuum and filled with nitrogen three times prior to the addition of the ether. The benzoate solution was then added dropwise. The resulting milky white solution was allowed to stir at room temperature overnight. The reaction

mixture was cooled in an ice bath and 100 mL of deionized water was slowly added to quench the reaction. The resulting pH 10 solution was acidified to pH 3.5 with solid citric acid and subsequently washed three times with diethyl ether. The organic phase was then washed three times each with saturated potassium bicarbonate and deionized water and then dried over anhydrous sodium sulfate. Volatiles were removed to yield a brown oil, which crystallized after the addition of pentane. The mixture was recrystallized four times from hot pentane to afford 2-(3,5-dimethoxyphenyl)propan-2-ol as colorless needles (2.4 g, 48%). ^{1}H was consistent with that reported in the literature.[71-72]

A solution of 2-(3,5-dimethoxyphenyl)propan-2-ol (0.50 g, 2.5 mmol) in 5 mL of freshly distilled THF was added to an oven dried 100 mL two neck round bottom flask, equipped with a reflux condenser, under a flow of nitrogen. Dibutyltin dilaurate (0.05 mL, 0.1 mmol) was added to the flask followed by sparged 3-isocyanatopropyltriethoxysilane (0.73 mL, 3.0 mmol), dropwise over the course of several minutes. The mixture was allowed to stir at 50 °C for 32 hours. Volatiles were removed and the product was purified *via* column chromatography on silica gel (16:4:1 hexanes:ethyl acetate:triethylamine). Note that the column was *not* pretreated with triethylamine, and the compound was loaded utilizing the eluent to afford the title compound as a colorless oil (0.58 g, 55% after recovering 0.03 g of starting alcohol). ^{1}H NMR (399.96 MHz, $CDCl_3$) δ 6.51 (d, J = 2.0 Hz, 2H), 6.33 (t, J = 0.8 Hz, 1H), 4.93 (t, br, 1H), 3.81 (m, 6H), 3.77, (s, 6H), 3.1 (q, J = 6.4 Hz, 9H), 1.72 (s, 6H), 1.59 (s, 2H), 1.22 (t, J = 6.8 Hz, 9 H), 0.61 (t, J = 8.0 Hz, 2H). ^{13}C{^{1}H} NMR (100.58 MHz, $CDCl_3$) δ 160.8, 155.4, 149.6, 103.1, 93.4, 80.4, 60.8, 58.6, 55.4, 43.3, 29.2, 23.6, 18.4, 14.9, 7.8

ppm. HRMS (FAB+) exact mass calculated (found) for [M^+], m/z: 443.2339 (443.23576). NMR spectra and IR (KBr Pellet) were consistent with that reported in the literature.[73]

2.5.42 3-(4-Benzoylphenoxy)propylphosphonic acid

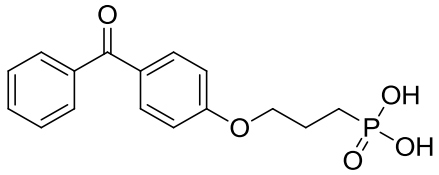

Diethyl 3-(4-benzoylphenoxy)propylphosphonate (2.13 g, 5 mmol) was dissolved in 20 mL of dry dichloromethane and 2.25 mL (19.5 mmol) of bromotrimethylsilane was added. The system was sealed with a greased stopper and allowed to stir overnight. Volatiles were removed to produce a brown oil, which was dissolved in methanol (33 mL) and water (8 mL) and allowed to stir overnight. After removal of solvent a white product was found in the reaction flask. The product was then washed with water and placed in a separatory funnel. Ethyl acetate was used to extract the insoluble phosphonic acid from the aqueous layer. Volatiles were removed to produce a slightly off-white/yellow free flowing solid. The ^{1}H NMR is consistent with what has been previously reported in the literature.[74]

2.5.43 4-(3'-Chlorodimethylsilyl)propyloxybenzophenone

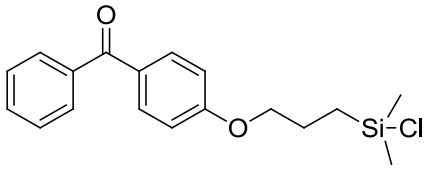

Synthesis of the title compound was conducted according to the procedure previously reported in the literature with ^{1}H NMR matching what was previously reported.[75]

2.6 References

[1] Kosolapoff, G. M.; Maier, L., *Organic Phosphorus Compounds*. Wiley-Interscience: 1976.

[2] Worms, K. H.; Schmidt-Dunker, M., Phosphonic Acids and Derivatives. In *Organic Phosphorous Compounds*, Maier, L.; Kosolapoff, G. M., Eds. John Wiley & Sons, Inc.: New York, 1976; Vol. 7, p 184.

[3] Doak, G. O.; Freedman, L. D., The Synthesis of Arylphosphonic and Diarylphosphinic Acids by the Diazo Reaction. *Journal of the American Chemical Society* **1951,** *73*, 5658-5660.

[4] Freedman, L. D.; Doak, G. O., The Preparation and Properties of Phosphonic Acids. *Chemical Reviews* **1957,** *57*, 479-523.

[5] Engel, R., *Synthesis of Carbon-Phosphorus Bonds*. CRC Press: Boca Raton, Fla., 1988.

[6] Kiddle, J. J.; Gurley, A. F., Microwave Irradiation in Organophosphorus Chemistry 1: The Michaelis-Arbuzov Reaction. *Phosphorus Sulfur and Silicon and the Related Elements* **2000,** *160*, 195-205.

[7] Tavs, P., Reaction of Aryl Halides with Trialkyl Phosphites and Dialkyl Benzenephosphonites to Aromatic Phosphonates and Phosphinates by Nickel Salt Catalysed Arylation. *Chemische Berichte-Recueil* **1970,** *103*, 2428-2436.

[8] Hirao, T.; Masunaga, T.; Yamada, N.; Ohshiro, Y.; Agawa, T., Palladium-Catalyzed New Carbon-Phosphorus Bond Formation. *Bulletin of the Chemical Society of Japan* **1982,** *55*, 909-913.

[9] Mckenna, C. E.; Higa, M. T.; Cheung, N. H.; Mckenna, M. C., Facile Dealkylation of Phosphonic Acid Dialkyl Esters by Bromotrimethylsilane. *Tetrahedron Letters* **1977**, 155-158.

[10] Silverstein, R. R. M.; Webster, F. X.; Kiemle, D. J., *The Spectrometric Identification of Organic Compounds*. John Wiley & Sons Australia, Limited: 2005.

[11] Ishwara, T. W. S. Optimisation of Hybrid Organic/Inorganic Solar Cells. Imperial College London, London, 2009.

[12] Wobkenberg, P. H.; Ball, J.; Kooistra, F. B.; Hummelen, J. C.; Leeuw, D. M. d.; Bradley, D. D. C.; Anthopoulos, T. D., Low-Voltage Organic Transistors Based on Solution Processed Semiconductors and Self-Assembled Monolayer Gate Dielectrics. *Applied Physics Letters* **2008,** *93*, 013303.

[13] Hotchkiss, P. J. The Design, Synthesis, and Use of Phosphonic Acids for the Surface Modification of Metal Oxides. Ph.D. Thesis, Georgia Institute of Technology, Atlanta, GA, 2008.

[14] Hotchkiss, P.; Marder, S.; Giordano, A.; Anthopoulos, T. D., Electronic Devices Comprising Novel Phosphonic Acid Surface Modifiers. Google Patents: 2010.

[15] Lin, H.-C.; Polaske, N. W.; Oquendo, L. E.; Gliboff, M.; Knesting, K. M.; Nordlund, D.; Ginger, D. S.; Ratcliff, E. L.; Beam, B. M.; Armstrong, N. R.; McGrath, D. V.; Saavedra, S. S., Electron-Transfer Processes in Zinc Phthalocyanine–Phosphonic Acid Monolayers on Ito: Characterization of Orientation and Charge-Transfer Kinetics by Waveguide Spectroelectrochemistry. *The Journal of Physical Chemistry Letters* **2012,** *3*, 1154-1158.

[16] Ratcliff, E. L.; Garcia, A.; Paniagua, S. A.; Cowan, S. R.; Giordano, A. J.; Ginley, D. S.; Marder, S. R.; Berry, J. J.; Olson, D. C., Investigating the Influence of Interfacial Contact Properties on Open Circuit Voltages in Organic Photovoltaic Performance: Work Function Versus Selectivity. *Advanced Energy Materials* **2013,** *3*, 647-656.

[17] MacLeod, B. A.; Horwitz, N. E.; Ratcliff, E. L.; Jenkins, J. L.; Armstrong, N. R.; Giordano, A. J.; Hotchkiss, P. J.; Marder, S. R.; Campbell, C. T.; Ginger, D. S., Built-in Potential in Conjugated Polymer Diodes with Changing Anode Work Function: Interfacial States and Deviation from the Schottky–Mott Limit. *The Journal of Physical Chemistry Letters* **2012,** *3*, 1202-1207.

[18] Gliboff, M.; Li, H.; Knesting, K. M.; Giordano, A. J.; Nordlund, D.; Seidler, G. T.; Brédas, J.-L.; Marder, S. R.; Ginger, D. S., Competing Effects of Fluorination on the Orientation of Aromatic and Aliphatic Phosphonic Acid Monolayers on Indium Tin Oxide. *The Journal of Physical Chemistry C* **2013,** *117*, 15139-15147.

[19] Gliboff, M.; Sang, L. Z.; Knesting, K. M.; Schalnat, M. C.; Mudalige, A.; Ratcliff, E. L.; Li, H.; Sigdel, A. K.; Giordano, A. J.; Berry, J. J.; Nordlund, D.;

Seidler, G. T.; Bredas, J. L.; Marder, S. R.; Pemberton, J. E.; Ginger, D. S., Orientation of Phenylphosphonic Acid Self-Assembled Monolayers on a Transparent Conductive Oxide: A Combined Nexafs, Pm-Irras, and Dft Study. *Langmuir* **2013,** *29*, 2166-2174.

[20] Knesting, K. M.; Hotchkiss, P. J.; MacLeod, B. A.; Marder, S. R.; Ginger, D. S., Spatially Modulating Interfacial Properties of Transparent Conductive Oxides: Patterning Work Function with Phosphonic Acid Self-Assembled Monolayers. *Advanced Materials* **2012,** *24*, 642-646.

[21] Gantz, J.; Placencia, D.; Giordano, A.; Marder, S. R.; Armstrong, N. R., Influence of Electrode Surface Composition and Energetics on Small-Molecule Organic Solar Cell Performance: Polar Versus Nonpolar Donors on Indium Tin Oxide Contacts. *Journal of Physical Chemistry C* **2013,** *117*, 1205-1216.

[22] Li, H.; Ratcliff, E. L.; Sigdel, A. K.; Giordano, A. J.; Marder, S. R.; Berry, J. J.; Brédas, J.-L., Modification of the Gallium-Doped Zinc Oxide Surface with Self-Assembled Monolayers of Phosphonic Acids: A Joint Theoretical and Experimental Study. *Advanced Functional Materials* **2014**, Early View.

[23] Cowan, S. R.; Schulz, P.; Giordano, A. J.; Garcia, A.; MacLeod, B. A.; Marder, S. R.; Kahn, A.; Ginley, D. S.; Ratcliff, E. L.; Olson, D. C., Chemically Controlled Reversible and Irreversible Extraction Barriers Via Stable Interface Modification of Zinc Oxide Electron Collection Layer in Polycarbazole-Based Organic Solar Cells. *Advanced Functional Materials* **2014**, Accepted.

[24] Reese, M. O.; Morfa, A. J.; White, M. S.; Kopidakis, N.; Shaheen, S. E.; Rumbles, G.; Ginley, D. S., Pathways for the Degradation of Organic Photovoltaic P3ht : Pcbm Based Devices. *Solar Energy Materials and Solar Cells* **2008,** *92*, 746-752.

[25] Dorman, G.; Prestwich, G. D., Benzophenone Photophores in Biochemistry. *Biochemistry* **1994,** *33*, 5661-5673.

[26] Turro, N. J., *Modern Molecular Photochemistry*. University Science Books: Sausalito, Calif. :, 1991.

[27] Millan, M. D.; Locklin, J.; Fulghum, T.; Baba, A.; Advincula, R. C., Polymer Thin Film Photodegradation and Photochemical Crosslinking: Ft-Ir Imaging, Evanescent Waveguide Spectroscopy, and Qcm Investigations. *Polymer* **2005,** *46*, 5556-5568.

[28] M. Doytcheva, D. D., R. Stamenova, A. Orahovats, Ch. Tsvetanov, J. Leder,, Ultraviolet-Induced Crosslinking of Solid Poly(Ethylene Oxide). *Journal of Applied Polymer Science* **1997,** *64*, 2299-2307.

[29] Wang, D.; Kodali, V. K.; II, W. D. U.; Jarvholm, J. E.; Okada, T.; Jones, S. C.; Rumi, M.; Dai, Z.; King, W. P.; Marder, S. R.; Curtis, J. E.; Riedo, E., Thermochemical Nanolithography of Multifunctional Nanotemplates for Assembling Nano-Objects. *Advanced Functional Materials* **2009,** *19*, 3696-3702.

[30] Carroll, K. M.; Giordano, A. J.; Wang, D.; Kodali, V. K.; Scrimgeour, J.; King, W. P.; Marder, S. R.; Riedo, E.; Curtis, J. E., Fabricating Nanoscale Chemical Gradients with Thermochemical Nanolithography. *Langmuir* **2013,** *29*, 8675-8682.

[31] Lukovskaya, E. V.; Bobylyova, A. A.; Fedorova, O. A.; Fedorov, Y. V.; Anisimov, A. V.; Didane, Y.; Brisset, H.; Fages, F., Synthesis, Structures, and Optical and Electrochemical Characteristics of Novel Crown-Containing Polythiophene Systems. *Russian Chemical Bulletin* **2007,** *56*, 967-974.

[32] Kosolapoff, G. M., Phosphite Isomerication in the Synthesis of Thiophene Phosphonic Acids. *Journal of the American Chemical Society* **1947,** *69*, 2248-2248.

[33] Sugandhi, E. W.; Falkinham Iii, J. O.; Gandour, R. D., Synthesis and Antimicrobial Activity of Symmetrical Two-Tailed Dendritic Tricarboxylato Amphiphiles. *Bioorganic & Medicinal Chemistry* **2007,** *15*, 3842-3853.

[34] Li, Y.; Wang, C.; Li, C.; Di Motta, S.; Negri, F.; Wang, Z., Synthesis and Properties of Ethylene-Annulated Di(Perylene Diimides). *Organic Letters* **2012,** *14*, 5278-5281.

[35] Ahrens, M. J.; Kelley, R. F.; Dance, Z. E. X.; Wasielewski, M. R., Photoinduced Charge Separation in Self-Assembled Cofacial Pentamers of Zinc-5,10,15,20-Tetrakis(Perylenediimide)Porphyrin. *Physical Chemistry Chemical Physics* **2007,** *9*, 1469-1478.

[36] Kohler, M. C.; Sokol, J. G.; Stockland Jr, R. A., Development of a Room Temperature Hirao Reaction. *Tetrahedron Letters* **2009,** *50*, 457-459.

[37] Vugts, D. J.; Koningstein, M. M.; Schmitz, R. F.; de Kanter, F. J. J.; Groen, M. B.; Orru, R. V. A., Multicomponent Synthesis of Dihydropyrimidines and Thiazines. *Chemistry – A European Journal* **2006,** *12*, 7178-7189.

[38] Blackburn, G. M.; Ingleson, D., The Dealkylation of Phosphate and Phosphonate Esters by Lodotrimethylsilane : A Mild and Selective Procedure. *Journal of the Chemical Society, Perkin Transactions 1* **1980**, 1150-1153.

[39] Chen, Z.-S.; Zhou, Z.-Z.; Hua, H.-L.; Duan, X.-H.; Luo, J.-Y.; Wang, J.; Zhou, P.-X.; Liang, Y.-M., Reductive Coupling Reactions: A New Strategy for C(Sp3)–P Bond Formation. *Tetrahedron* **2013,** *69*, 1065-1068.

[40] Montoneri, E.; Savarino, P.; Adani, F.; Ricca, G., Organosulphur Phosphorus Acid Compounds. Part 6. Preparation and Analytical Identification of Fluorobenzylphosphono-Disulphonic Acids. *Phosphorus, Sulfur, and Silicon and the Related Elements* **1995,** *106*, 37-45.

[41] Montoneri, E.; Savarino, P.; Viscardi, G.; Gallazzi, M. C., Organosulphur Phosphorus Acid Compounds. Part 4. Fluorobenzylphosphono-Sulphonic Acids. *Phosphorus, Sulfur, and Silicon and the Related Elements* **1994,** *86*, 145 - 155.

[42] Hong, M. C.; Kim, Y. K.; Choi, J. Y.; Yang, S. Q.; Rhee, H.; Ryu, Y. H.; Choi, T. H.; Cheon, G. J.; An, G. I.; Kim, H. Y.; Kim, Y.; Kim, D. J.; Lee, J.-S.; Chang, Y.-T.; Lee, K. C., Synthesis and Evaluation of Stilbene Derivatives as a Potential Imaging Agent of Amyloid Plaques. *Bioorganic & Medicinal Chemistry* **2010,** *18*, 7724-7730.

[43] Detert, H.; Schmitt, V., Quadrupolar Donor-Acceptor Substituted Oligo(Phenylenevinylene)S - synthesis and Solvatochromism of the Fluorescence. *Journal of Physical Organic Chemistry* **2004,** *17*, 1051-1056.

[44] Liu, J.; Boarman, K., Regiospecific Topochemical Reactions Controlled by Trifluoromethyl Directing Groups. *Chemical communications (Cambridge, England)* **2005**, 340.

[45] Skropeta, D.; Schmidt, R. R., Chiral, Non-Racemic [Alpha]-Hydroxyphosphonates and Phosphonic Acids Via Stereoselective Hydroxylation of Diallyl Benzylphosphonates. *Tetrahedron: Asymmetry* **2003,** *14*, 265-273.

[46] Detert, H.; Sugiono, E., Synthesis and Electronic Spectra of Substituted Oligo(Phenylenevinylene)S. *Journal of Physical Organic Chemistry* **2000,** *13*, 587-590.

[47] Lion, C. J.; Matthews, C. S.; Stevens, M. F. G.; Westwell, A. D., Synthesis, Antitumor Evaluation, and Apoptosis-Inducing Activity of Hydroxylated (E)-Stilbenes. *Journal of Medicinal Chemistry* **2005,** *48*, 1292-1295.

[48] Kurz, T.; Schlüter, K.; Kaula, U.; Bergmann, B.; Walter, R. D.; Geffken, D., Synthesis and Antimalarial Activity of Chain Substituted Pivaloyloxymethyl Ester Analogues of Fosmidomycin and Fr900098. *Bioorganic & Medicinal Chemistry* **2006,** *14*, 5121-5135.

[49] Iida, K.; Kawata, E.; Kobayashi, K.; Watanabe, S., Novel Amino Group-Containing Aromatic Compound, and Sensitizing Dye for Photoelectric Conversion, Containing the Aromatic Compound. Google Patents: 2008.

[50] Montoneri, E.; Savarino, P.; Quagliotto, P.; Adani, F.; Ricca, G., Organosulphur Phosphorus Acid Compounds. Part 7. Preparation and Analytical Identification of Difluorobenzylphosphono-Sulfonic Acids. *Phosphorus, Sulfur, and Silicon and the Related Elements* **1998,** *134*, 99 - 108.

[51] Iorga, B.; Eymery, F.; Savignac, P., Controlled Monohalogenation of Phosphonates: A New Route to Pure A-Monohalogenated Diethyl Benzylphosphonates. *Tetrahedron* **1999,** *55*, 2671-2686.

[52] Woo, H. Y.; Liu, B.; Kohler, B.; Korystov, D.; Mikhailovsky, A.; Bazan, G. C., Solvent Effects on the Two-Photon Absorption of Distyrylbenzene Chromophores. *Journal of the American Chemical Society* **2005,** *127*, 14721-14729.

[53] Shim, H. K.; Kang, I. N.; Jang, M. S.; Zyung, T.; Jung, S. D., Electroluminescence of Polymer Blend Composed of Conjugated and Nonconjugated Polymers. White-Light-Emitting Diode. *Macromolecules* **1997,** *30*, 7749-7752.

[54] Pogorelova, S. P.; Kharitonov, A. B.; Willner, I.; Sukenik, C. N.; Pizem, H.; Bayer, T., Development of Ion-Sensitive Field-Effect Transistor-Based Sensors for Benzylphosphonic Acids and Thiophenols Using Molecularly Imprinted Tio2 Films. *Analytica Chimica Acta* **2004,** *504*, 113-122.

[55] Murias, M.; Handler, N.; Erker, T.; Pleban, K.; Ecker, G.; Saiko, P.; Szekeres, T.; Jäger, W., Resveratrol Analogues as Selective Cyclooxygenase-2 Inhibitors: Synthesis and Structure-Activity Relationship. *Bioorganic & Medicinal Chemistry* **2004,** *12*, 5571-5578.

[56] Inoue, M.; Sato, T.; Hirama, M., Asymmetric Total Synthesis of (−)-Merrilactone A: Use of a Bulky Protecting Group as Long-Range Stereocontrolling Element. *Angewandte Chemie International Edition* **2006,** *45*, 4843-4848.

[57] Paniagua, S. A.; Hotchkiss, P. J.; Jones, S. C.; Marder, S. R.; Mudalige, A.; Marrikar, F. S.; Pemberton, J. E.; Armstrong, N. R., Phosphonic Acid Modification of Indium-Tin Oxide Electrodes: Combined Xps/Ups/Contact Angle Studies. *Journal of Physical Chemistry C* **2008,** *112*, 7809-7817.

[58] Gester, S.; Pietzsch, J.; Wuest, F. R., Synthesis of 18f-Labelled Stilbenes from 4-[18f]Fluorobenz-Aldehyde Using the Horner–Wadsworth–Emmons Reaction. *Journal of Labelled Compounds and Radiopharmaceuticals* **2007,** *50*, 105-113.

[59] Hand, J. K.; Stewart, A. L.; Sears, R. B.; McCall, T. R.; Davis-McGibony, C. M., A Novel Synthesis of P-Nitrobenzylphosphonic Acid and Its Action on Alkaline Phosphatase. *Letters in Organic Chemistry* **2008,** *5*, 563-565.

[60] Zhuang, R.; Xu, J.; Cai, Z.; Tang, G.; Fang, M.; Zhao, Y., Copper-Catalyzed C−P Bond Construction Via Direct Coupling of Phenylboronic Acids with H-Phosphonate Diesters. *Organic Letters* **2011,** *13*, 2110-2113.

[61] Kabachnik, M. M.; Solntseva, M. D.; Izmer, V. V.; Novikova, Z. S.; Beletskaya, I. P., Palladium-Catalyzed Phase-Transfer Arylation of Dialkyl Phosphonates. *Russian Journal of Organic Chemistry* **1998,** *34*, 93-97.

[62] Kalek, M.; Ziadi, A.; Stawinski, J., Microwave-Assisted Palladium-Catalyzed Cross-Coupling of Aryl and Vinyl Halides with H-Phosphonate Diesters. *Organic Letters* **2008,** *10*, 4637-4640.

[63] Latham, K.; Downs, J. E.; Rix, C. J.; White, J. M., Interactions of Guanidinium with Benzene-Sulphonic, -Phosphonic and -Arsonic Acids and Several of Their Nitro-Derivatives. *Journal of Molecular Structure* **2011,** *987*, 74-85.

[64] Berrino, R.; Cacchi, S.; Fabrizi, G.; Goggiamani, A.; Stabile, P., Arenediazonium Tetrafluoroborates in Palladium-Catalyzed C-P Bond-Forming Reactions.

Synthesis of Arylphosphonates, -Phosphine Oxides, and -Phosphines. *Organic & Biomolecular Chemistry* **2010,** *8*, 4518-4520.

[65] Andaloussi, M.; Lindh, J.; Sävmarker, J.; J. R. Sjöberg, P.; Larhed, M., Microwave-Promoted Palladium(Ii)-Catalyzed C□P Bond Formation by Using Arylboronic Acids or Aryltrifluoroborates. *Chemistry – A European Journal* **2009,** *15*, 13069-13074.

[66] Wu, S.-Y.; Casida, J. E., Stereospecific Intramolecular Cyclization for Asymmetric Synthesis of (Rp)- and (Sp)-Enantiomers of 2-Octyl- and 2-Phenyl-4h-1,3,2-Benzodioxaphosphorin 2-Oxides. *Phosphorus, Sulfur, and Silicon and the Related Elements* **1995,** *102*, 177-184.

[67] Bravo-Altamirano, K.; Montchamp, J.-L., A Novel Approach to Phosphonic Acids from Hypophosphorous Acid. *Tetrahedron Letters* **2007,** *48*, 5755-5759.

[68] Schulmeyer, T.; Paniagua, S. A.; Veneman, P. A.; Jones, S. C.; Hotchkiss, P. J.; Mudalige, A.; Pemberton, J. E.; Marder, S. R.; Armstrong, N. R., Modification of Batio3 Thin Films: Adjustment of the Effective Surface Work Function. *Journal of Materials Chemistry* **2007,** *17*, 4563-4570.

[69] Meziane, D.; Hardouin, J.; Elias, A.; Guénin, E.; Lecouvey, M., Microwave Michaelis–Becker Synthesis of Diethyl Phosphonates, Tetraethyl Diphosphonates, and Their Total or Partial Dealkylation. *Heteroatom Chemistry* **2009,** *20*, 369-377.

[70] Kraft, U.; Zschieschang, U.; Ante, F.; Kalblein, D.; Kamella, C.; Amsharov, K.; Jansen, M.; Kern, K.; Weber, E.; Klauk, H., Fluoroalkylphosphonic Acid Self-Assembled Monolayer Gate Dielectrics for Threshold-Voltage Control in Low-Voltage Organic Thin-Film Transistors. *Journal of Materials Chemistry* **2010,** *20*, 6416-6418.

[71] Birr, C.; Stahnke, G.; Lang, P.; Lochinge.W, Alpha,Alpha-Dimethyl-3,5-Dimethoxybenzyloxycarbonyl (Ddz) Residue, an N-Protecting Group Labile toward Weak Acids and Irradiation. *Annalen Der Chemie-Justus Liebig* **1972,** *763*, 162-172.

[72] Hartsel, J. A.; Craft, D. T.; Chen, Q.-H.; Ma, M.; Carlier, P. R., Access to "Friedel–Crafts-Restricted" Tert-Alkyl Aromatics by Activation/Methylation of Tertiary Benzylic Alcohols. *The Journal of Organic Chemistry* **2012,** *77*, 3127-3133.

[73] Fresco, Z. M.; Suez, I.; Backer, S. A.; Frechet, J. M. J., Afm-Induced Amine Deprotection: Triggering Localized Bond Cleavage by Application of Tip/Substrate Voltage Bias for the Surface Self-Assembly of Nanosized Dendritic Objects. *Journal of the American Chemical Society* **2004,** *126*, 8374-8375.

[74] Griep-Raming, N.; Karger, M.; Menzel, H., Using Benzophenone-Functionalized Phosphonic Acid to Attach Thin Polymer Films to Titanium Surfaces. *Langmuir* **2004,** *20*, 11811-11814.

[75] Prucker, O.; Naumann, C. A.; Ruhe, J.; Knoll, W.; Frank, C. W., Photochemical Attachment of Polymer Films to Solid Surfaces Via Monolayers of Benzophenone Derivatives. *Journal of the American Chemical Society* **1999,** *121*, 8766-8770.

CHAPTER 3

FLUORINATED BENZYL PHOSPHONIC ACIDS ON ITO: EXAMINING THE WORK FUNCTION, COVERAGE, AND ORIENTATION

3.1 Transparent Conducting Oxides

Transparent conducting oxides (TCOs) are a broad class of metal oxides that simultaneously have both high optical transparency and high electrical conductivity, thus enabling their use in optoelectronic devices.[2-3] Research regarding TCOs has drastically increased over the last decade thanks in part to the explosion of laptop computers and tablets, and the ubiquity of flat screen displays. This technological boom brings with it a global increase in energy consumption and has made research into alternative energy sources which use TCOs, such as organic photovoltaics (OPVs), very common as well.[4] Some of the more commonly used and studied metal oxides have been indium tin oxide (ITO), indium zinc oxide (IZO), and zinc oxide.[6-7]

3.1.1 Indium Tin Oxide

Indium tin oxide has one of the lowest resistivity values among TCOs ($1 - 2 \times 10^{-4}$ Ω cm), is mostly transparent in the visible region (> 90 %), and is readily available from commercial sources. ITO (as well as other indium based oxides) is a relatively hard (~ 5 – 6 on the Mohs hardness scale)[8] polycrystalline material when deposited, and has a conductivity that originates primarily from oxygen vacancies in the lattice structure, formed during annealing. Shallow donor levels from the In 5s electrons form around

these oxygen vacancies in indium oxide films, and the addition of tin doping serves to form another impurity band from the Sn 5s orbitals just below the conduction band, thereby decreasing the barrier to conduction.[1, 9] This is schematically shown in Figure 3.1. Because of this combination of properties, ITO is now commonly used in applications such as displays, photovoltaics, transistors, and sensors. Compatibilization of ITO with overlayers is therefore extremely important in device architectures and is why this substrate was selected for further analysis of phosphonic acid modification.

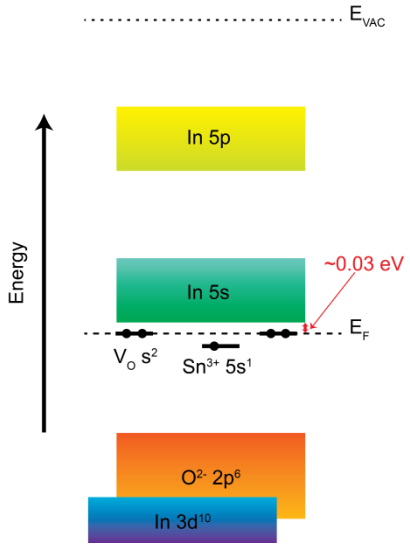

Figure 3.1 Schematic energy-band diagram for ITO films. The valence band originates from the O 2p orbitals with the In 5s orbitals making up the conduction band. The In 3d band is also shown for reference and it lies below that of the O 2p. V_O symbolizes oxygen vacancies, which already have a low barrier to conduction. The addition of tin doping adds additional donor levels. Image adapted from the literature.[1]

3.2 Phosphonic Acid Modification of ITO

As was discussed in 1.2.2.5 phosphonic acids have become an increasingly popular surface modifier and several review articles have been published about using this type of surface modifier.[10-11] There are many surfaces, including nanoparticles and

planar substrates, that have been modified by phosphonic acids (e.g. zirconia,[12] titania,[13] alumina,[14-15] zinc oxide,[16] etc.). ITO is of particular interest due to the various properties summarized in 3.1.1.[17-20] There are many methods of pre-treatment for ITO, including the use of acids, bases, plasma treatment, or thin layers of polymer prior to depositing an organic layer on its surface,[10, 21-22] the use of phosphonic acids, however, have the ability to produce a stable, robust monolayer. This monolayer can then aid in compatibilization of the ITO surface with an organic overlayer and allow for the work function of the ITO substrate to be tuned precisely.

Modification of the ITO substrate is also a relatively straightforward process, though it should be noted that multiple deposition conditions have been reported for the formation of phosphonic acid monolayers on ITO. In general, the modification occurs by making a dilute solution (on the order of 1 – 10 mM in concentration) of the phosphonic acid in a polar solvent and allowing the substrate to soak in a solution of the modifier. This soaking can occur through the use of a technique such as tethering by aggregation and growth (T-BAG) where the sample is held vertically in the phosphonic acid solution and the solvent allowed to evaporate until the substrate is no longer immersed, as schematically demonstrated in Figure 3.2.[23] Alternatively, a modified version of this technique places the sample horizontally in solution and allows the solvent to evaporate until the sample is above the level of the phosphonic acid solution.[16, 24] It is also possible to perform dip-coating,[25] microcontact printing,[26-27] spin coating,[28] and spray coating[29-30] to form monolayers of phosphonic acids on planar substrates. Simple solution soaking on the order of hours to days is still the most commonly employed technique to achieve successful modification of the surface with phosphonic acids.[31] Note that dilute solutions

of base are also often used to remove any excess physisorbed phosphonic acid from the surface and aid in ensuring a pristine monolayer has been formed after modification.

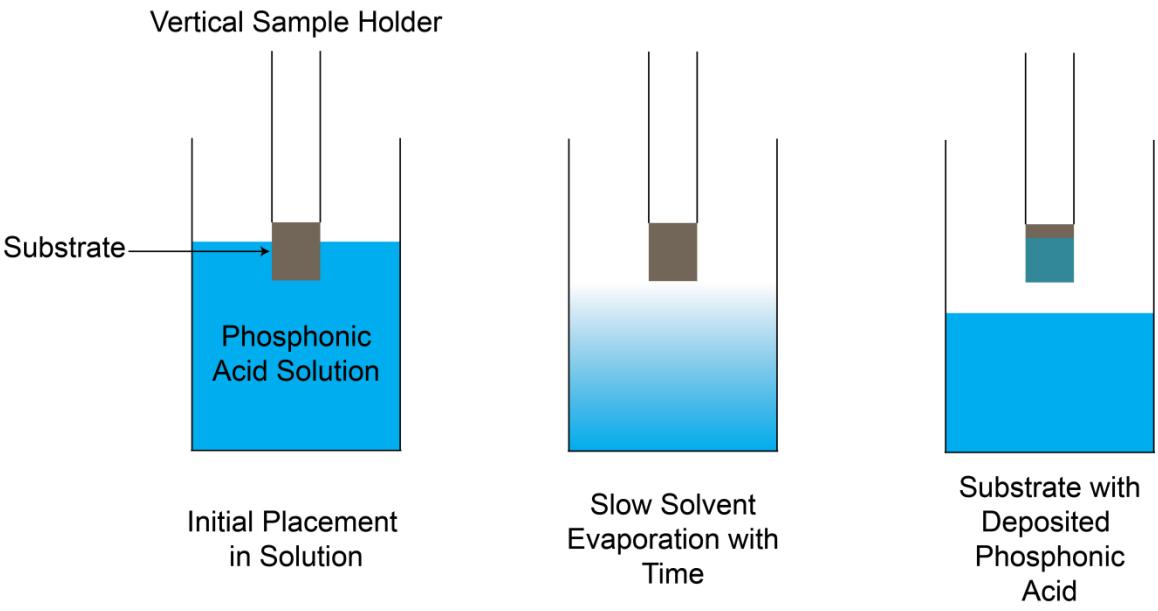

Figure 3.2 Schematic representation of tethering by aggregation and growth. Image adapted from the literature.[23]

3.3 Literature Precedents Regarding Analyzing Phosphonic Acid Monolayers

The central theme of this chapter is the examination of a variety of benzyl phosphonic acids on the surface of ITO to better understand the interrelationships that exist between work function changes, molecular orientation of the surface modifier, and its coverage. Some of the basic characterization, such as binding of phosphonic acids to the surface of ITO and ZnO, were discussed in 1.4.5. In order to put this particular chapter in context with work already published, a brief summary is provided to examine what has already been done to examine work function tuning and molecular orientation of phosphonic acid surface modifiers on ITO.

3.3.1 Work Function Tuning of ITO and Dipolar Phosphonic Acids

When utilizing a dipolar surface modifier to tune the work function of a material, the general rule of thumb is that placing a molecule with a dipole having the positive end point away from the surface (thus putting more electron density near the surface) causes a change in potential, making it easier to remove an electron, (i.e. a reduction of the work function). Alternatively, if the negative end of a dipole points away from the surface (thus removing electron density near the surface due to the nearby positive end of the dipole) then it becomes harder to remove electrons from the surface to vacuum, which causes an increase in the work function. This is demonstrated schematically in Figure 3.3. One of the earliest reports to use phosphonic acids in order to decrease the WF of ITO used 2-chloroethanephosphonic acid.[32] It should be noted, however, that this study did not provide WF measurements by UPS or KP, but instead posited that because OLED device performance when the modifier was used proved to be similar to that of a Mg:Ag electrode and thus that the WF had decreased. In a follow-up study to the previous one, amine, trichloro, nitro, and chloro terminated phosphonic acids were used and it was shown with KP that the WF had not decreased relative to bare ITO for 2-chloroethanephosphonic acid, and only the amine terminated phosphonic acid showed a decrease in WF of approximately 0.1 eV.[33] This work was later built upon by showing the changes in surface energy and wettability caused by phosphonic acid modification in comparison with other standard surface preparation protocols.[34]

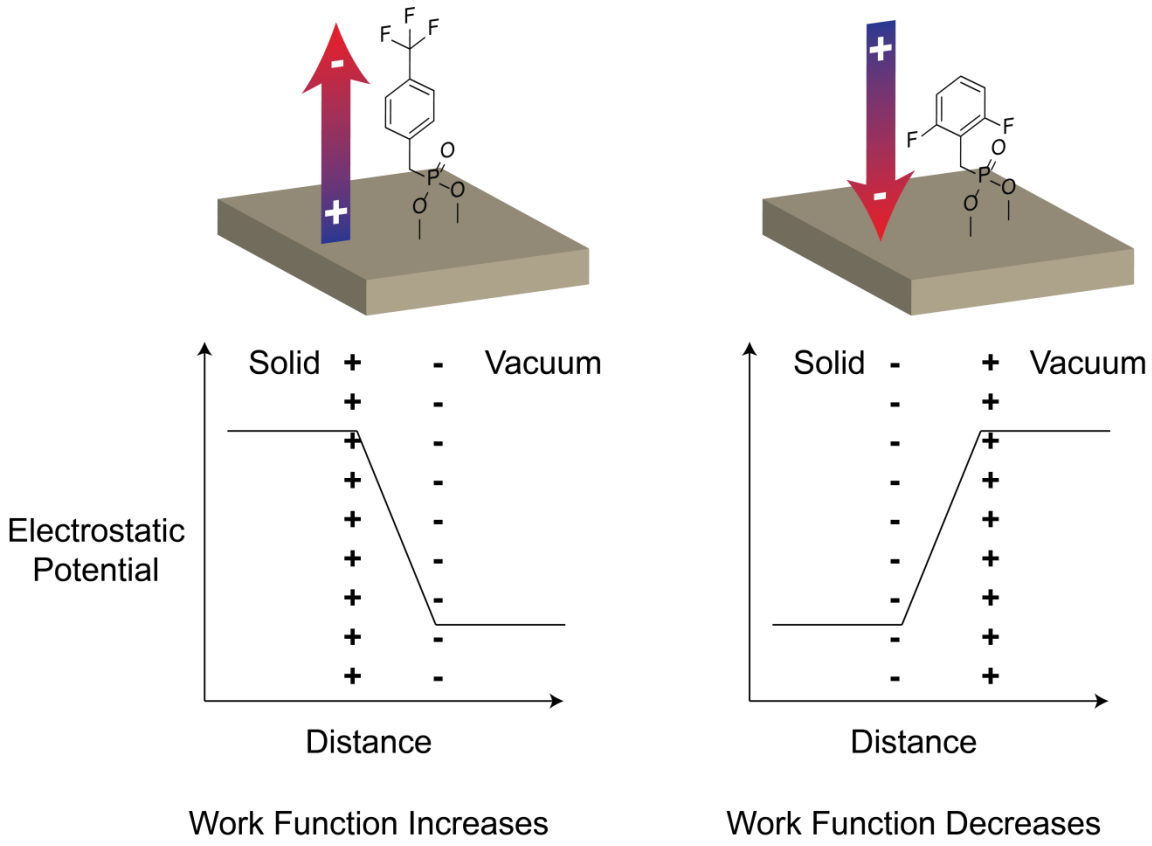

Figure 3.3 Schematic representation of phosphonic acids with molecular dipoles pointing toward and away from the surface (top). Shown is a generalized variation in the electrostatic potential caused by the dipole present in the phosphonic acid between the surface of the solid and vacuum. Electrostatic potentials adapted from Appleyard.[32-33]

While there have been some studies conducted to examine the lowering of work function through the use of phosphonic acids such as those discussed above, as well as one study involving the use of a quarterthiophene phosphonic acid derivative (ΔWF = -0.28 eV),[35] the majority of studies have focused on increasing the work function of ITO. A summary of the molecules used in these studies as well as work function values obtained by various techniques are shown in Table 3.1. There are several factors that this information highlights. The first of which being the reproducibility of phosphonic acid surface modification of ITO and the resulting work function obtained. There are a few

instances where, depending on the measurement technique, the WF differs by ~ 0.1 – 0.3 eV, but the vast majority of the measurements are highly consistent. For instance, ITO modified with pentafluorobenzylphosphonic acid (PFBPA) has been measured by KP, UPS, low-intensity X-ray photoelectron spectroscopy (LIXPS), and photoelectron yield spectroscopy (PYS) and in all cases a WF between 4.9 and 5.1 eV was obtained. PFBPA has also been used to examine the impact that modification conditions (and consequently phosphonic acid coverage and WF) have on ITO.[31] Data from these studies has also demonstrated that the interface dipole created by the phosphonic acid on the surface of ITO is largely responsible for these changes in WF values.[10, 36-38] Thus, it is possible to tune the WF of ITO to values between slightly below that of detergent solvent cleaned ITO (~ 4.6 eV) to values obtained through oxygen plasma cleaning (> 5.4 eV).

Table 3.1 Summary of literature work function values of various phosphonic acid modifiers on the surface of ITO. The measurement technique PYS measures the photocurrent while irradiating a sample with monochromatic light of variable energy and is detailed in the supplementary information of Lacher.[37] The details regarding LIXPS are given in the supporting information of MacLeod.[39] Work function values provided in red are values where a difference from the bare substrate was reported.

Phosphonic Acid	Work Function (eV)	Measurement Technique	Reference
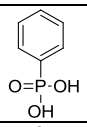	4.42	PYS	[37]
	4.51	Kelvin Probe	[40]
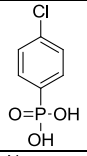	5.29	Kelvin Probe	[41]
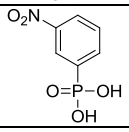	5.26	Kelvin Probe	[41]
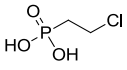	5.49	Kelvin Probe	[41]
	4.72	PYS	[37]

Phosphonic Acid	Work Function (eV)	Measurement Technique	Reference
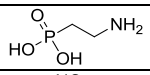	4.34	PYS	37
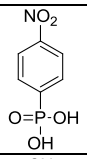	5.60	Kelvin Probe	42
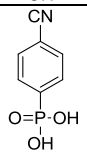	5.77	Kelvin Probe	42
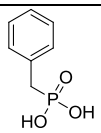	4.5	UPS	43
	4.45	LIXPS	39
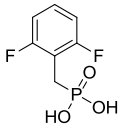	-0.1	UPS	38
	4.40	Kelvin Probe	44
	4.43	PYS	37
	4.1	UPS	43
	4.17	LIXPS	39
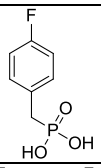	+0.5	UPS	38
	4.91	Kelvin Probe	45
	4.97	PYS	37
	4.96	LIXPS	39
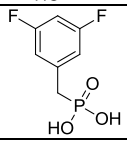	+0.7	UPS	38
	5.20	PYS	37
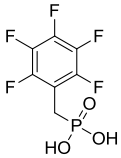	+0.7	UPS	38
	4.9	UPS	36, 44-46
	5.00	PYS	37
	4.9	UPS	43
	5.14	LIXPS	39
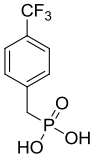	+1.1	UPS	38
	5.40	Kelvin Probe	45
	5.29	PYS	37
	5.5	UPS	43
	5.30	LIXPS	39
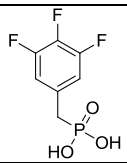	+0.8	UPS	38
	5.30	Kelvin Probe	44
	5.18	PYS	37
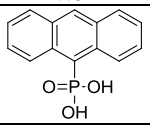	4.62	Kelvin Probe	40

Phosphonic Acid	Work Function (eV)	Measurement Technique	Reference
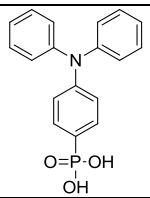	4.58	Kelvin Probe	[40]
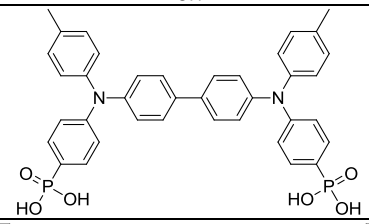	4.54	Kelvin Probe	[40]
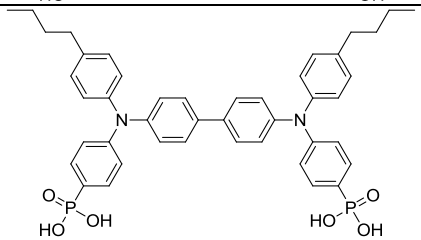	4.61	Kelvin Probe	[40]
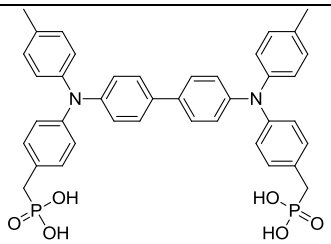	4.65	Kelvin Probe	[40]
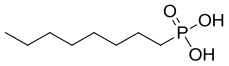	4.6	Kelvin Probe	[47]
	4.49	PYS	[37]
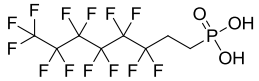	5.3	Kelvin Probe	[45-47]
	5.1	UPS	[36]
	5.40	PYS	[37]
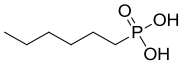	4.5	UPS	[36]
	4.48	PYS	[37]
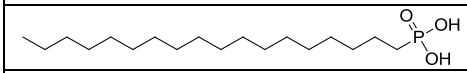	4.5	UPS	[36]
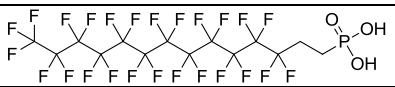	5.48	UPS	[48]
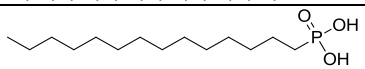	4.13	UPS	[48]
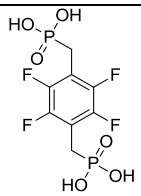	4.5	UPS	[36]

Phosphonic Acid	Work Function (eV)	Measurement Technique	Reference
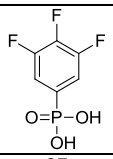	5.17	Kelvin Probe	44-45
	5.15	PYS	37
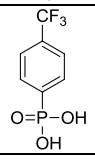	5.40	Kelvin Probe	44
	5.44	PYS	37
	5.15	PYS	37
	5.17	PYS	37
	5.24	PYS	37
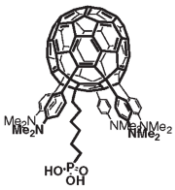	5.26	PYS	37
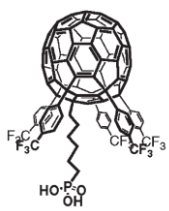	5.14	PYS	37

3.3.2 Molecular Orientation of Phosphonic Acids

Many aspects to phosphonic acid surface modification have become very well understood within the last 10 – 15 years such as materials that can be modified with phosphonic acids, modification methods, binding to the surface, influence on work function, and effectiveness in device architectures for enhancing efficiency. However, a molecular level understanding of how phosphonic acids orient themselves once on the surface of the substrate has not been greatly explored in comparison to other surface modifiers. Table 3.2 provides a summary of literature reports of phosphonic acid tilt angles on various substrates. Of these reports very few provided a systematic approach to examining tilt angle of these surface modifiers. Furthermore, while alkyl phosphonic acids had been examined in several cases, phenyl and benzyl phosphonic acids had not been examined prior to collaborative efforts between Georgia Tech, the University of Washington, the University of Arizona, the National Renewable Energy Laboratory, and the Stanford Synchrotron Radiation Lightsource (SSRL).[49-50]

The earliest report of measuring the tilt angle of phosphonic acids actually dates back to 2002 where multiple layers of zirconium bisphosphonates on the surface of ITO were examined. While spectroscopic ellipsometry indicated the molecules were not standing upright, a tilt angle for a terphenylbisphosphonic acid monolayer was reported to be between 45 – 60° (relative to the surface normal) based on carbon NEXAFS. No further details were provided and a reference cited as "in preparation" appears to never have been published.[51-52] The value reported, however, appears to be consistent with angles of ~ 55° for multilayers of a ruthenium complex bearing phosphonic acids on silica and zirconia.[53] One other more complex structure that has been examined is a

perylene based phosphonic acid on the surface of titania, which found the molecules tend to adopt orientations more parallel to the surface (66° relative to the surface normal) even though the linkers chosen are relatively rigid in nature.[54]

Table 3.2 Summary of phosphonic acids for which experimental determinations of molecular tilt angle have been conducted. The substrate being modified, modification conditions, and method used for determining the tilt angle are also provided. Note that PM-ATR is potential-modulated attenuated total reflectance. See footnote for the tilt angle regarding clarification of reference point for tilt angle.

Phosphonic Acid	**Tilt Angle (°)**	**Substrate**	**Notes & Technique**	**Reference**
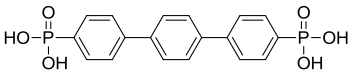	45-60[1]	ITO	Zr Complex ellipsometry NEXAFS	51-52
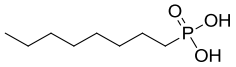	38[2]	HfO_2	NEXAFS	55
	47[b]	Ag		
	-	ITO	NEXAFS	56
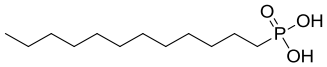	36[b]	HfO_2	NEXAFS	55
	38[b]	Ag		
	-	ITO	NEXAFS	56
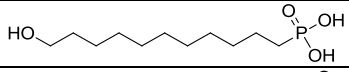	47[b]	SiO_2	NEXAFS	57
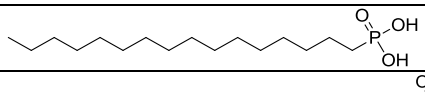 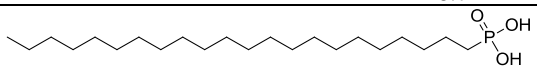	10-15[b]	Al_2O_3	IR	58
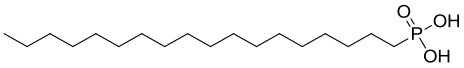	20-30[b]	glass	Langmuir-Blodgett films XPS	59
	37[b]	SiO_2	NEXAFS	57
	34[b]	HfO_2	NEXAFS	55
	30[b]	Ag		
	-	ITO	NEXAFS	56

[1] Angle between the transition dipole moment of the ring system and the surface normal. See Figure 3.22 for a similar orientation convention.
[2] For alkyl phosphonic acids the reported angle is between the surface normal and the backbone of the alkyl chain.

Phosphonic Acid	Tilt Angle (°)	Substrate	Notes & Technique	Reference
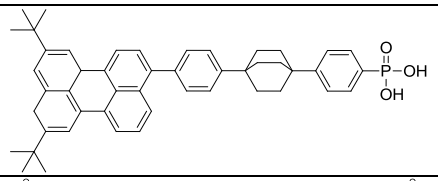	66[3]	TiO_2	two-photon photoelectron spectroscopy	54
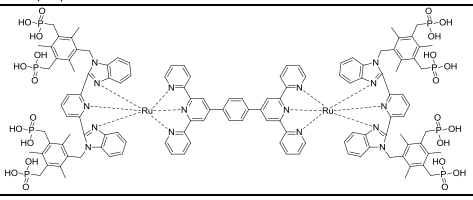	55[4]	SiO_2 SiO_2:Zr	ellipsometry	53
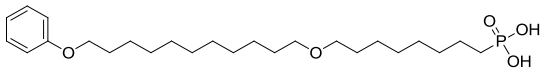	27 [b]	Al_2O_3	NEXAFS alkyl chain	60-61
	66[a]		NEXAFS phenyl ring	
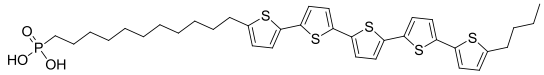	32[a]	Al_2O_3	NEXAFS thiophenes	62
	44 [b]	Al_2O_3	NEXAFS alkyl chain	
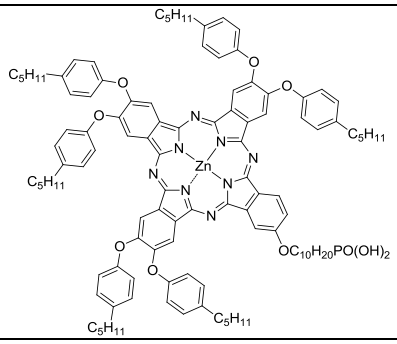	33[5]	ITO	PM-ATR monomer	63
	58[e]		PM-ATR aggregate	
	52[e]		NEXAFS monomer	
	53[e]		NEXAFS aggregate	

Alkyl phosphonic acids have been the most studied thus far in the literature. Work using alkyl phosphonic acids on alumina using IR spectroscopy (using reference alkyl thiols on gold) found that these long-chain phosphonic acid monolayers have a tilt angle between the alkyl backbone and the surface normal of between 10° and 15°, which is indicative of bidentate binding to the surface.[58] Similar alkyl phosphonic acid

[3] Specified as the long molecular axis versus the surface normal.
[4] Angle as multiple layers are formed with the assumption the first monolayer is upright and 55° from the surface normal thereafter.
[5] Angle that exists between the molecular plan normal and normal to the ITO surface

molecules were used to prepare Langmuir-Blodgett monolayers on glass substrates (20 – 30°)[59] as well as on silicon surfaces (37°).[64] Chain length variation was also found to have an impact on the ordering of the molecules as one study varied the alkyl chain length between 6 and 18 carbons on ITO. It was found that with increasing chain length comes a trend to form more upright packing going from tilt angles of ~ 48° to ~ 28° for C6 to C8 chains, respectively.[65] This is consistent with data from another NEXAFS study on ITO indicating that ordering increases with longer chain length, but no tilt angle values were supplied.[56]

3.3.3 Tilt Angle Studies of Phenyl and Alkyl Phosphonic Acids on IZO and ITO

As discussed in 3.3.2 there have been studies conducted to examine the orientation of some alkyl phosphonic acids on ITO. The purpose of this summary is to provide context of the results discussed later in the chapter by introducing the antecedent work that enabled the orientation studies of benzyl phosphonic acids on ITO. Gliboff's initial study focused on determining the orientation of phenylphosphonic acid on the surface of IZO experimentally through a combination of NEXAFS and PM-IRRAS then comparing these results to those of density functional theory (DFT) calculations.[50] IZO was chosen for this initial study both due to its recent use in organic optoelectronic devices and its ability to form conformal films on gold surfaces, which is critical for IRRAS measurements as discussed in 1.4.5. Very good agreement was found between the three methods affording average tilt angles between the plane of the benzene ring and the surface normal of 17 – 15°, 18 – 9°, and 11-12° by PM-IRRAS, NEXAFS, and theory, respectively.[50, 66]

The follow-up work to this initial study focused on fluorinated and non-fluorinated phenyl and alkyl phosphonic acids on the surface of ITO.[49] In this instance ITO was used instead of IZO, and thus it was necessary to confirm similar orientation values of phenylphosphonic acid on ITO before examining other surface modifiers. Indeed, the tilt angle of phenyl phosphonic acid on ITO (21 – 11°) was similar to that found for IZO and also agreed with theoretical calculations.[49] A summary of the molecules examined in this study and the tilt angles obtained are provided in Table 3.3. The overall conclusion from this study was that aryl and alkyl phosphonic acids behave very differently on the surface of a metal oxide and that introducing fluorination has a marked impact on the binding mode and packing of the modifier. Similarly, DFT calculations showed that the coverage of the surface modifier also played an impact on the calculated tilt angles. It should also be pointed out that in the case of octylphosphonic acid there was good agreement between these data and the data reported for alkyl phosphonic acids shown in Table 3.2.

Table 3.3 Summary of phosphonic acid molecules examined by NEXAFS and DFT on the surface of ITO as reported in Gliboff.[49] All values are reported relative to the surface normal and use the angle convention discussed in 3.9.1. Note that no appreciable differences were observed by DFT for the tilt angles of the two phenyl molecules. Differences depending on the binding geometry were noted.

Phosphonic Acid	**NEXAFS Tilt Angle (°)**	**DFT Tilt Angle (°)**
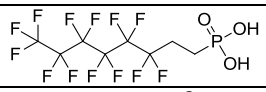	30 ± 5	-
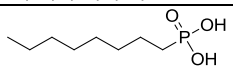	41 ± 8	-
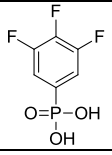	27 ± 4	bidentate: 22 – 15 tridentate: 12 – 11

Phosphonic Acid	NEXAFS Tilt Angle (°)	DFT Tilt Angle (°)
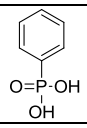	19 ± 4	

3.4 Selection of Phosphonic Acid Molecules for Study

Based on the results obtained for the alkyl and phenyl phosphonic acids it was determined that other potentially technically relevant phosphonic acids should also be examined on the surface of ITO. As can be seen in Table 3.1 a large number of phosphonic acids that have been currently studied in the literature or used in devices have been benzyl phosphonic acids. Therefore, in order to achieve a better understanding of these molecules on the surface of ITO, it was determined that the next logical step would be to apply the knowledge previously acquired in analyzing alkyl and phenyl phosphonic acids and apply them to benzyl phosphonic acids. In particular, fluorinated benzyl phosphonic acids were chosen due to their ability to drastically alter the work function of a substrate because of the molecular dipoles induced by the presence of the fluorine groups. Moreover, fluorination also has the added benefit of allowing more straightforward characterization of the surface after modification by XPS analysis as fluorine is not a common contaminant deposited on the surface by standard processing techniques. Fluorine (like the other halogens) has a large relative sensitivity factor compared with other elements and thus even small concentrations of fluorine on the surface of a substrate can be readily detected by XPS, which is ideal for the analysis of monolayers.

The phosphonic acids that have been chosen for this study are summarized in Figure 3.4. All of the compounds were made as discussed in Chapter 2. As there are a

number of molecules used for the study, abbreviations have been assigned to each compound; these are provided in Figure 3.4. Several of the compounds (e.g. PFBPA, 4-CF3BPA, 3,4,5-F3BPA, etc.) have already been well characterized in terms of work function changes as shown in Table 3.1, but the selection of these 14 phosphonic acids allows for a very systematic examination of the impact that molecular dipole has on altering the work function of a substrate. Analysis of molecular tilt angles allows for better understanding any outlier work function changes that differ from expectations based on molecular dipole alone. The inclusion of BPA also provides a point of comparison with a non-fluorinated compound.

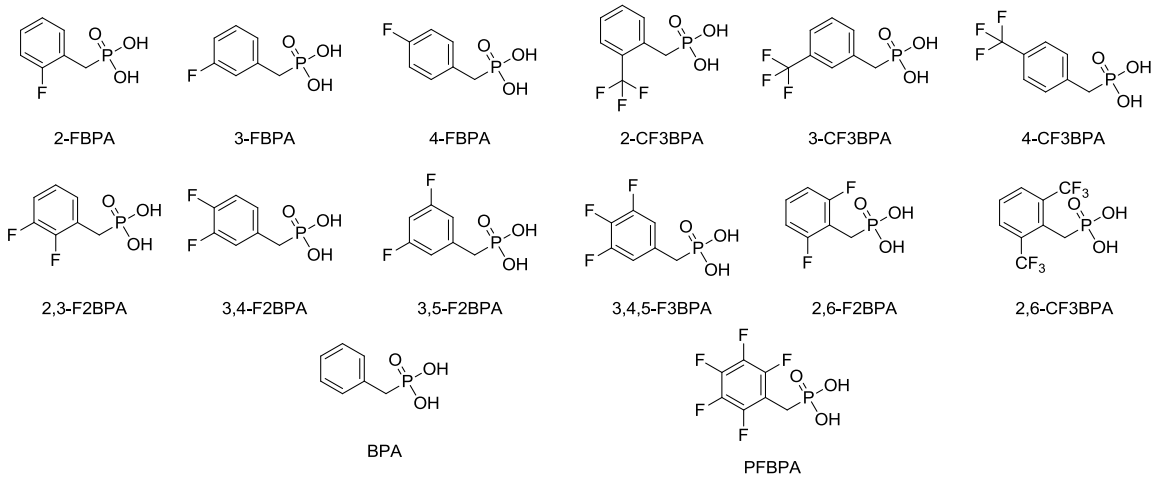

Figure 3.4 Summary of benzyl phosphonic acids used throughout the study along with the abbreviations for each molecule that will be used throughout the chapter.

3.4.1 Comparison of Dipole Moments for Analogous Tolyl Compounds

In an effort to better highlight the anticipated changes in molecular dipole, the dipole moment for the substituted toluene analogues of the substituted benzyl phosphonic

acids shown in Figure 3.4 (i.e. where the PO_3H_2 moiety is removed and replaced with H) was calculated in Spartan. These DFT level calculations were conducted on the molecule in its ground-state conformation using B3LYP/6-31G**. In order to allow comparison between these molecules an arbitrary axis needs to be chosen, which in this case was the axis defined by the line linking the CH_3 substituent to the carbon of the ring para to the CH_3 substituent (as labelled in the first row of Figure 3.5). The calculated dipole moment vectors were then projected onto this axis and a sign convention chosen based on using a molecule standing vertically on a substrate with the methyl group closest to the surface. Thus, if the negative end of the dipole is located away from the surface, then the value is negative, and if the negative end of the dipole is located close to the surface, then the value is positive. This sign convention will be used throughout the chapter and is shown in Figure 3.6.

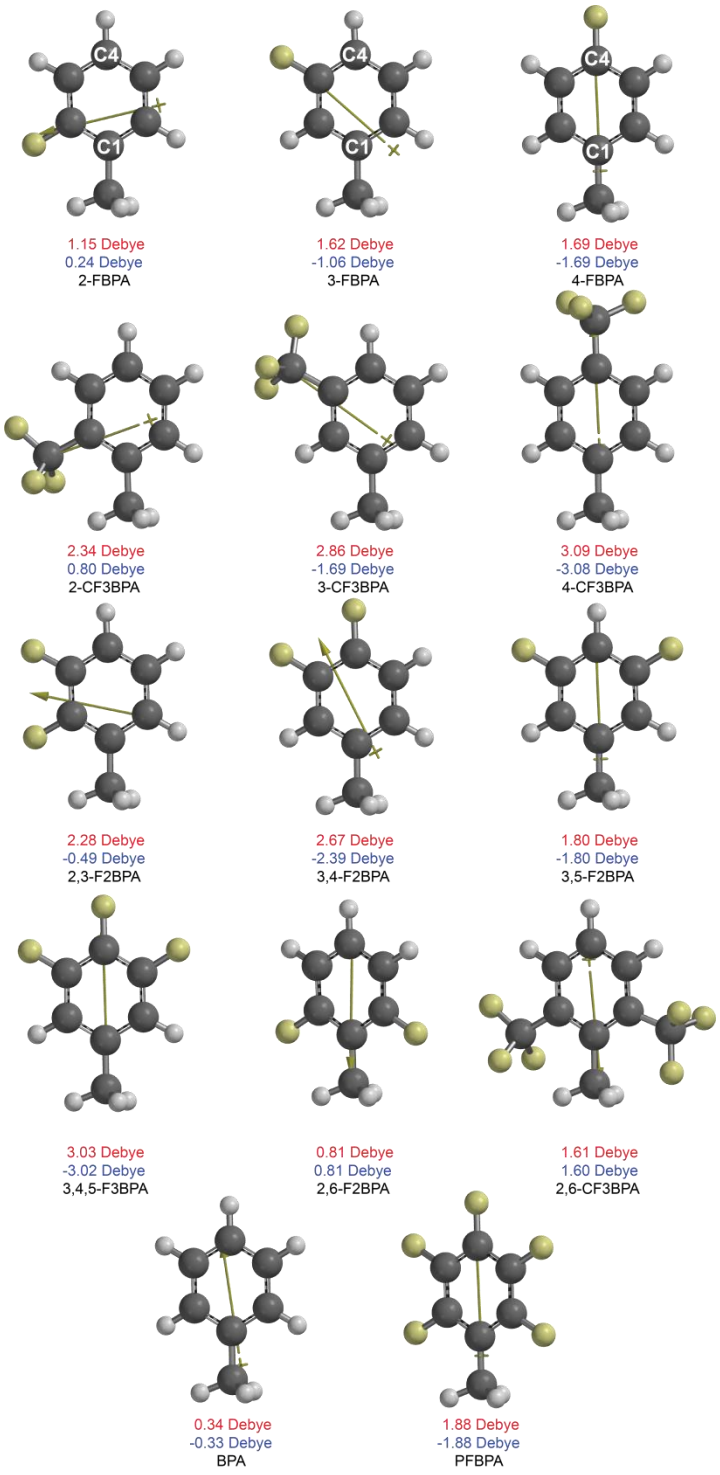

Figure 3.5 Calculated dipole moments for analogous substituted toluene derivatives as calculated from Spartan. Note that the dipole moments in red correspond to the value for the vector shown with each compound. The values in blue correspond to the magnitude of the projection of the dipole moment onto the C1 – C4 axis in the molecule. This axis is explicitly labelled for the first row and follows the sign convention outlined below.

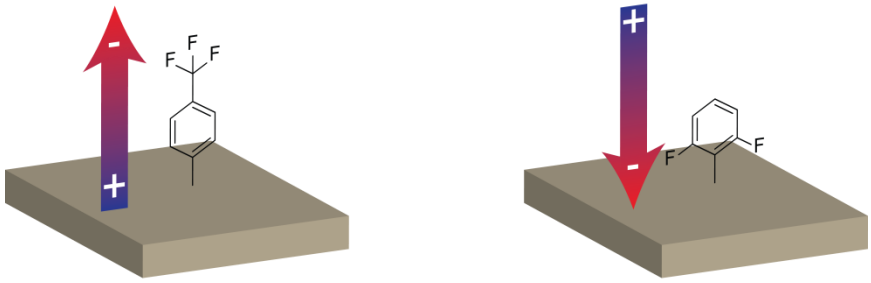

Figure 3.6 Dipole moment convention used for tolyl compounds and phosphonic acids throughout this chapter. Note that the sign convention follows the dipole sign farthest away from the surface. That is the negative end points away from the surface then there is a negative dipole moment and when the positive end points away from the surface, a positive dipole moment is obtained.

These tolyl compounds accentuate the changes in dipole moments that are expected for their phosphonic acid counterparts and serve as a good representation for comparative purposes as all molecules have the same phosphonic acid binding group. This also allows for a quick estimation of which molecules should increase the work function when deposited on the surface and which molecules should aid in decreasing the work function of the ITO substrate. Also, while not only directionality of the dipole was changed, the overall magnitude was altered through the use of fluoro and trifluoromethyl groups.

3.5 ITO Selection and Surface Modification with Benzyl Phosphonic Acids

There are multiple deposition protocols for placing phosphonic acids on the surface, and according to a recent study, the choice of protocol can impact the work function and coverage;[31] thus it was essential to keep modification conditions consistent for all compounds. In an effort to best match what had already been done on IZO and

ITO the modification protocols for prior orientation studies was followed.[49-50] Similarly, as ITO can differ from manufacturer to manufacturer and because roughness does impact both NEXAFS measurements and coverage calculations it was decided that supersmooth ITO from Thin Film Devices would be used rather than the more commonly used ITO from Colorado Concepts. The main difference between these substrates is the RMS roughness values as determined by AFM, which are typically ~ 3 nm for the "rough" ITO and typically ~0.5 – 0.7 nm for the smooth ITO, both over 5 micron square areas, as shown in Figure 3.7. In the case of the smooth ITO, the roughness is below the point at which it impacts measuring alkyl phosphonic acids on ITO.[65] Experimental details for the surface modification protocol can be found in 3.11.2.

3.6 Coverage Analysis of Benzyl Phosphonic Acids on ITO Using XPS

As has been demonstrated both through theoretical calculations[67] and experimentally[31] the coverage of phosphonic acids on the surface of ITO has a relatively strong impact on the work functions that are obtained after modification. Therefore, in order to better understand the role that coverage plays in impacting the orientation of the modifiers on the surface as well as the measured work function it was necessary to quantitatively determine the coverage of the surface modifiers. Sparse coverage or highly dense coverage can aid in explaining differences observed in work function values from what would be expected based on molecular dipoles. Computing these values also allows for the examination of sample to sample variation and will allow for an examination of the role that steric interactions play in the ability of a phosphonic acid to modify a surface.

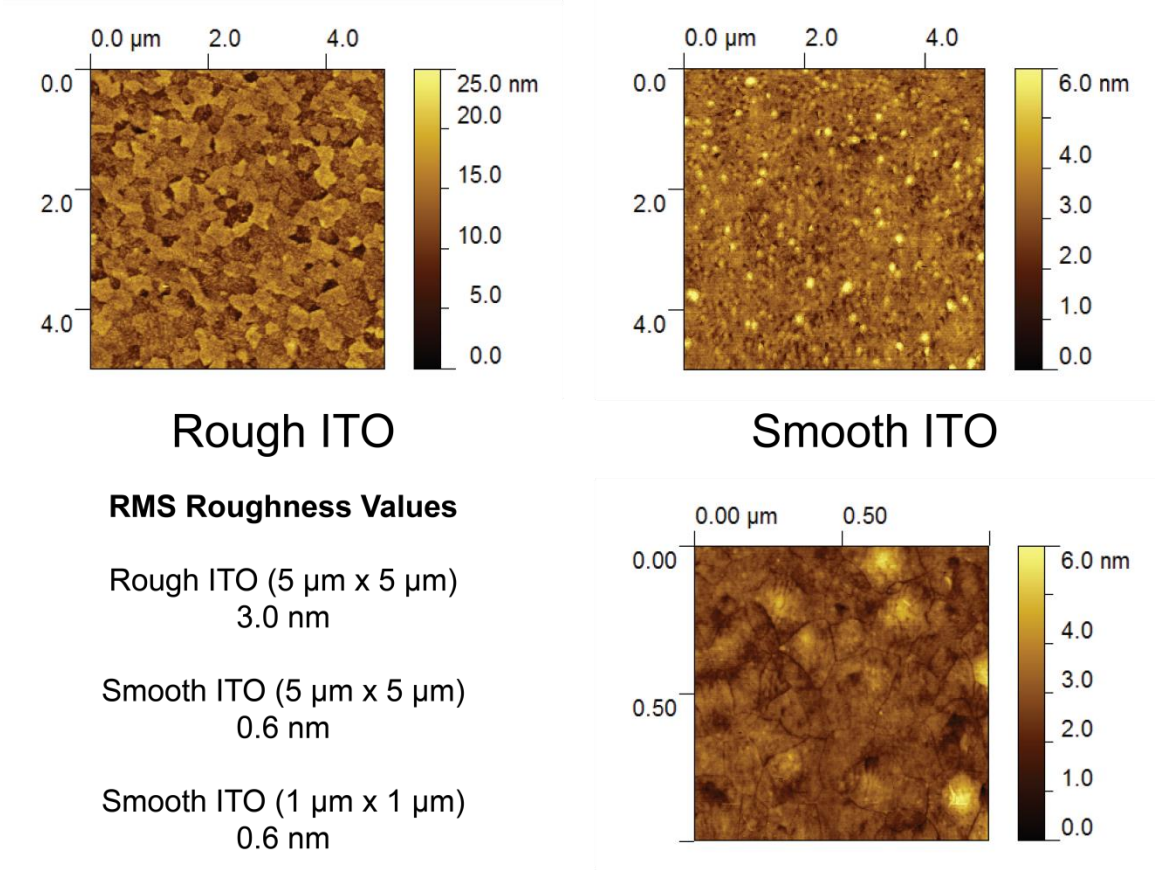

Figure 3.7 Comparison of ITO used in this study (supersmooth ITO) with more commonly used "rough" ITO (Colorado Concepts). The top images are both 5 micron scales and the bottom image is a 1 micron area of the supersmooth ITO obtained directly from the center of the 5 micron image.

3.6.1 Determination of Correction Factor for Experimental Data

When conducting XPS analysis, the X-rays penetrate far deeper than the actual information depth, and in order to obtain quantitative data, this analysis depth (which follows e^{-x}) must be taken into account since it causes signal attenuation with increasing depth. Approximately 95 % of the signal in XPS originates from within a distance of 3 inelastic mean free paths from the surface (3λ).[5, 68] The inelastic mean free path is an

index of how far an ejected electron can travel through a solid element or compound before encountering an inelastic scattering event and losing energy. This means electrons ejected from deeper within the substrate are less likely than those at the surface to be detected and this leads to signal attenuation. In order to quantitatively analyze XPS for coverage this attenuation needs to be accounted for and thus experimental data needs to be corrected. The origin of these correction factors has been previously discussed and was worked on in tandem with Paniagua.[31, 69-70] A summary of how these correction factors are determined can be found in Appendix B.

3.6.2 Calculation of Coverage – Comparing Experimental Data with Surface Models

Based on the previous section and the details provided in Appendix B there is now a correction factor that can be utilized to take into account experimental attenuation. In order to take advantage of this factor it should be possible to compare the experimental data with that of a close-packed complete monolayer of the phosphonic acid in question on ITO. This can be done by comparing experimentally determined XPS atomic ratio values with atomic ratios obtained from theoretical calculations of each individual phosphonic acid when it is geometry-optimized on the surface of an ITO slab.

In order to perform the experimental quantification using the ratio of two elements, it is necessary to first account for several factors that contribute to the overall observed intensity for a given element. These factors are corrected through the use of a sensitivity factor, σ, such that instrument specific parameters, intensity due to the different kinetic energy values at which the observed ionizations occur, and intensity due to the probability of excitation for a given element. Thus, a sensitivity factor such as $\sigma_{\mathrm{In}\ 3d_{3/2}}\,(1041.8\ \mathrm{eV})$ would mean that sensitivity factors for the In $3d_{3/2}$ peak which

occurs at a kinetic energy of 1041.8 eV are taken into account (for the sake of clarity the kinetic energy will be omitted from the following equations). Also, note that if indeed only the In $3d_{3/2}$ peak were to be used for quantification the sensitivity factor would need to be adjusted as it does not account for spin-orbit coupling.

In the case of fluorinated benzyl phosphonic acids on ITO the atomic ratio used to characterize the coverage is that of F/In. These two elements were chosen due to the unique signature from fluorine provided by the phosphonic acid (use of carbon would afford far less reliable results due to the presence of carbonaceous carbon not originating from the phosphonic acid monolayer) and that of indium from the underlying substrate as ITO is mostly indium with typically <10 % tin. Furthermore the sensitivity of these two elements in XPS allows for acquisition of reliable monolayer data. Taking into account sensitivity factors for the raw peak area (A) affords the following ratio of sensitivity corrected areas A^{σ}.

$$\frac{\left(\frac{\boldsymbol{A_{F\ 1s}}}{\boldsymbol{\sigma_{F\ 1s}}}\right)}{\left(\frac{\boldsymbol{A_{In\ 3d}}}{\boldsymbol{\sigma_{In\ 3d}}}\right)} = \frac{\boldsymbol{A^{\sigma}_{F\ 1s}}}{\boldsymbol{A^{\sigma}_{In\ 3d}}} \qquad \text{Equation 3.1}$$

Now that the experimental ratios have been computed it is necessary to determine the theoretical values for the close packed monolayer of the phosphonic acid on ITO. This requires knowledge of the unit cell of ITO used in the DFT calculations, determining the optimized geometry of each phosphonic acid on the surface of ITO and then calculating the footprint of each molecule. These calculations were conducted by Alexander Hyla in Dr. Jean-Luc Brédas' group using the ITO unit cell that is shown in Figure 3.8. The unit cell is based on a bulk In_2O_3 crystalline structure with tin substitutions present in ratios similar to those determined experimentally. The (222)

surface was selected as it best matches the most abundant face from a variety of deposition techniques, and surface free oxygen atoms are hydroxylated.[71] This unit cell volume is comprised of three layers of ITO and each individual layer has dimensions of 1.43 × 2.48 × 0.33 nm (l×w×h) and contains 28 indium atoms and 4 tin atoms.

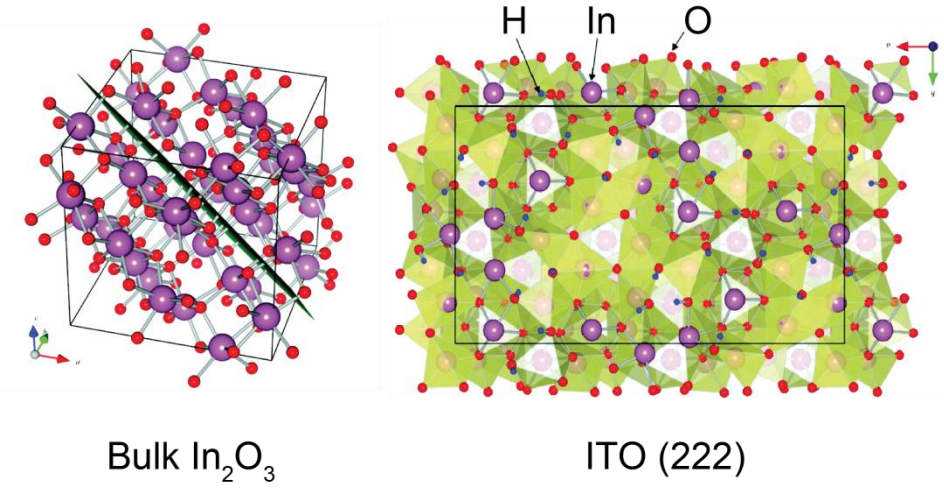

Figure 3.8 (Left) Bulk In_2O_3 unit cell with the (222) plane highlighted. (Right) Top view of hydroxyl terminated ITO (222) surface slab as optimized by DFT level of computation. The unit cell is indicated by the boundary box. Tin substitutions were randomly distributed over cationic positions in the slab. The unshaded polyhedral indicate chemically active surface sites including under-coordinated metal ions and surface hydroxyl groups. Image modified from the literature.[71]

As has been discussed in the previous section, the information depth is a distance of 3λ from the surface. Using the compilation of experimentally determined inelastic mean free paths by Seah[5] it was possible to determine the value of λ for In at the binding energy of the In 3d peak, and thus in a depth of 3λ (8.4 nm) there are 25.3 layers of ITO. Using the footprint of a phosphonic acid molecule (reported for PFBPA as 22.6 $Å^2$)[71] it is possible to determine the number of indium atoms present in the volume beneath the single phosphonic acid molecule to a depth of 3λ (in this instance 45 indium atoms). This means that the ideal F/In ratio is $\frac{5}{45}$ or 0.11. Using the fact that attenuation is

present in the experimental data it is possible to perform the comparison in one of two ways, both of which afford the same result:

- Correct the theoretical data to take into account attenuation, thereby reducing the ratio to match the experimental data, and thus use a multiplicative factor of $\frac{0.95\lambda}{3\lambda} = 0.317$.
- Correct the experimental data to remove the attenuation that is experienced experimentally and bring it in line with the theoretical ratio using a multiplicative factor of $\frac{3\lambda}{0.95\lambda} = 3.16$.

The final $\frac{(F/In)_{EXP}}{(F/In)_{THEORY}} \times 100\ \%$ affords a percentage value compared with that of an ideal monolayer. Note that the assumption is made that the monolayer itself has no attenuation as its length scale is extremely small compared to the bulk ITO information depth.

3.7 Coverage Analysis of Fluorinated Benzyl Phosphonic Acids on ITO

After modification of the smooth ITO surface with phosphonic acids as discussed in 3.11.2, samples were transferred to the XPS instrument for analysis. Multiple sample preparations were completed using the same phosphonic acids to ensure data consistency from batch to batch. Freshly plasma cleaned ITO, detergent solvent cleaned (DSC) ITO, and plasma cleaned and ethanol soaked ITO were examined as reference points; paying particular attention to ensure no fluorine contamination was present on these bare samples. All substrates were also examined in 3 spots to ensure homogeneity of the modification and consistency of the data across the entire surface. A comparison of the normalized XPS data for DSC, DSC/plasma cleaned, DSC/plasma cleaned ethanol soaked, and PFBPA modified ITO are shown in Figure 3.9. It should be noted that the DSC/plasma cleaned, ethanol soaked sample is an ITO sample that is treated in exactly

the same manner as a phosphonic acid modified sample, but without the presence of a phosphonic acid in the modification solution. This reference demonstrates the large amount of adsorbates that deposit on the surface of cleaned ITO from solution when phosphonic acids are not present. Similarly, in the case of a low coverage phosphonic acid these adsorbates would presumably also be present in relatively high quantity compared with an ITO sample having close to a well-packed monolayer.

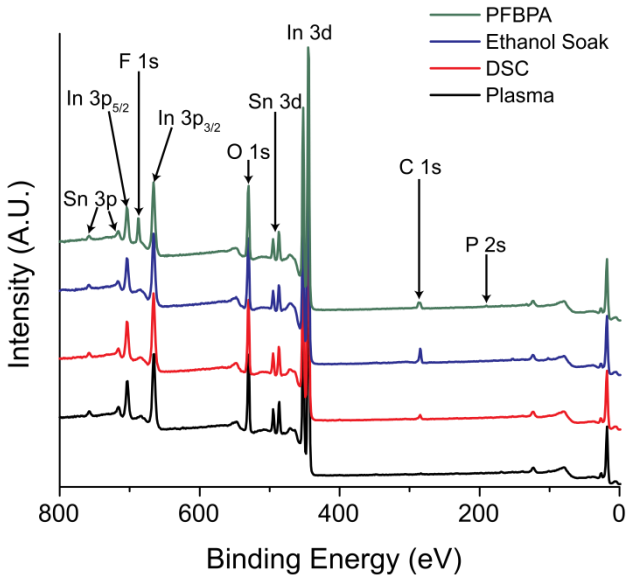

Figure 3.9 Comparison of XPS survey spectra for DSC followed by plasma, DSC, DSC followed by plasma cleaning and immersion in ethanol, and PFBPA modified ITO. The core level peaks have been labelled for convenience. Note the lack of fluorine in the spectra without the phosphonic acid and the drastic changes observed in the carbon peak intensity. Note spectra have been normalized and offset for clarity.

3.7.1 Comparison of Monolayer Purity through C 1s Spectra

Further comparison of survey spectra are not shown, as this type of low resolution spectra was used mainly to confirm the presence of the modifier on the surface (*via* the

presence of fluorine or phosphorus) and to determine that no other surface contaminants are present. High-resolution spectra were used in quantification of atomic peaks by XPS and as previously discussed F 1s and In 3d peaks were chosen for use in coverage calculations (see 3.6.2). In the case of these benzyl phosphonic acids, the C 1s peak can also provide immediate qualitative information regarding the coverage as is demonstrated when comparing the C 1s peak intensities of 2-CF3BPA, 3-CF3BPA, 4-CF3BPA, and 2,6-CF3BPA which are shown in Figure 3.10. The peak at ~293 eV originates from the CF_3 groups bound to the aromatic ring. From the graph below it is possible to deduce that binding of a phosphonic acid is problematic when large groups (such as CF_3) are near the sterically hindered *ortho* positions. This may explain why both 2,6-CF3BPA and 2-CF3BPA have such diminished peaks in this region as substitution at the *ortho* position precludes the formation of a high coverage monolayer. This is particularly true in the case of 2,6-CF3BPA as it has twice the number of trifluoromethyl groups as any of the other three molecules, but also has the smallest peak in this region. Note that it is possible that some of the lack of signal may also originate from the orientation of the molecule on the surface. Depending on the orientation it could cause attenuation of the C 1s peak as electrons excited from the CF_3 groups in 2-CF3BPA or 2,6-CF3BPA have to traverse more of the monolayer than the other molecules. Such attenuation of photoelectrons within a monolayer, however, is more commonly observed in long alkyl chain molecules on the surface.

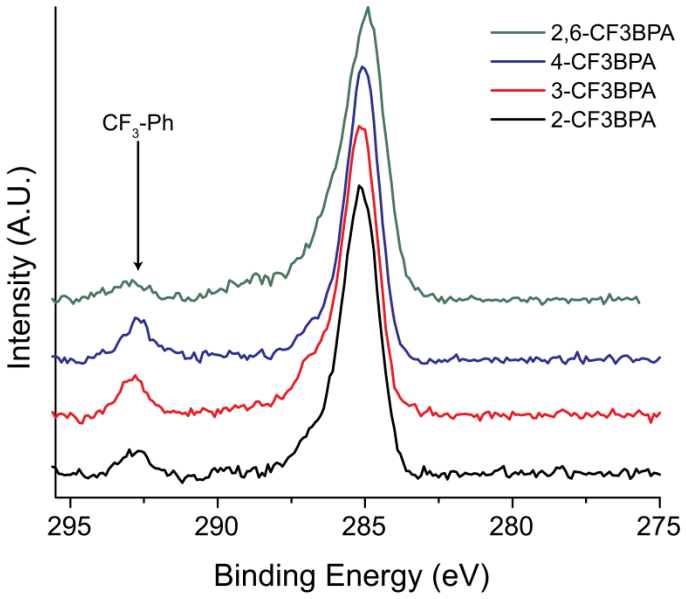

Figure 3.10 Comparison of C 1s peaks for 2-CF3BPA, 3-CF3BPA, and 4-CF3BPA. Spectra have been normalized and offset for clarity. Note the drastic difference in intensity for the CF_3-Ph peak between the 2-CF3BPA and 2,6-CF3BPA compared with both 3-CF3BPA and 4-CF3BPA.

A similar examination of the C 1s spectra for the analogous fluorine-substituted versions of the molecules shows little change in shoulder that originates from the fluorine substitution for 2-FBPA, 3-FBPA, or 4-FBPA. Interestingly, the shoulder in the case of 2,6-F2BPA is distinctly more pronounced than that of its monosubstituted counterparts, which is consistent with what would be expected for a molecule containing more fluorine atoms. Thus, it appears, to a first approximation, that, while the trifluoromethyl groups interfere greatly with the ability of the phosphonic acid to form a high-purity monolayer on the surface, fluorine groups do not have as great an impact on binding when substituted in the *ortho* position.

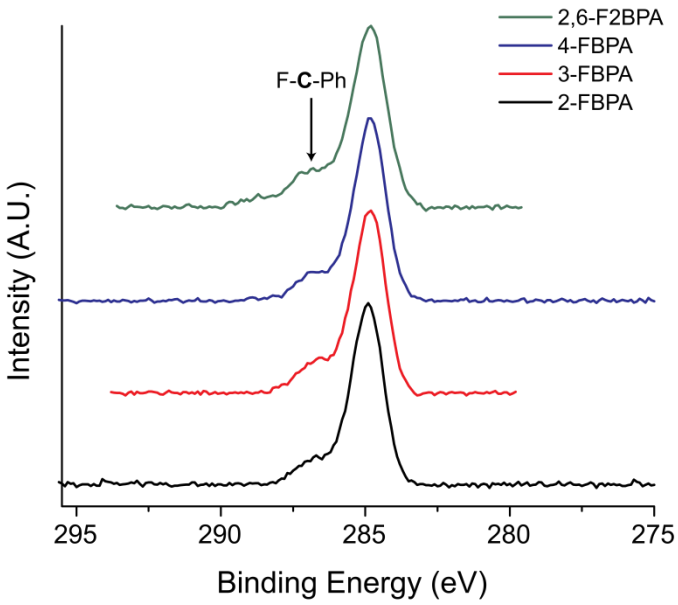

Figure 3.11 Comparison of C 1s peaks for 2-FBPA, 3-FBPA, 4-FBPA, and 2,6-F2BPA. Spectra have been normalized and offset for clarity. As opposed to what was observed in Figure 3.10 similar spectral features are observed for all three of the monosubstituted phosphonic acids.

3.7.2 Monolayer Purity from F/C Atomic Ratios

Examining the F/C atomic ratios through the use of F 1s and C 1s peaks it is possible to gain insight regarding purity of the monolayer. A high-purity monolayer that is well-packed will contain minimal carbonaceous contamination and thus have a F/C ratio that is close to the ratio given by the number of F and C atoms in the free molecule. The lower the purity of the monolayer, and thus the more carbonaceous contaminants that can be present at the surface, the further the experimental ratio will deviate from the ideal ratio. The summary of the experimentally determined atomic ratios and how these values compare with the ideal value for each individual benzyl phosphonic acid is found in Table 3.4. It is in principle possible to use P and C atoms to analyze this ratio, but

because the characteristic phosphorus P 2s or P 2p ionizations have a low cross-section in XPS the ratio is far less reproducible sample to sample and spot to spot.

Table 3.4 Atomic ratio of fluorine to carbon of phosphonic acids on the surface of ITO. Shown are the abbreviation for the molecule, the number of fluorine atoms present in the molecule (since all compounds have 7 carbon atoms), the ideal atomic ratio of F/C in the molecule, the atomic ratio given by F 1s/C 1s, and the ratio of experimental F/C to F/C in the compound expressed as a percentage (Monolayer Purity). Experimental atomic ratios are averaged over 3 spots with the given error as the standard deviation of these spots.

Phosphonic Acid	**# of Fluorine Atoms**	**Molecular F/C**	**XPS F 1s/C 1s**	**Monolayer Purity**
PFBPA	5	0.71	0.58 ± 0.04	82 %
2-FBPA	1	0.14	0.08 ± 0.01	57 %
3-FBPA	1	0.14	0.10 ± 0.01	71 %
4-FBPA	1	0.14	0.10 ± 0.01	71 %
2-CF3BPA	3	0.43	0.27 ± 0.03	63 %
3-CF3BPA	3	0.43	0.27 ± 0.02	63 %
4-CF3BPA	3	0.43	0.32 ± 0.01	74 %
2,3-F2BPA	2	0.29	0.17 ± 0.02	59 %
3,4-F2BPA	2	0.29	0.20 ± 0.01	69 %
3,5-F2BPA	2	0.29	0.22 ± 0.02	76 %
3,4,5-F3BPA	3	0.43	0.32 ± 0.01	74 %
2,6-F2BPA	2	0.29	0.10 ± 0.03	34 %
2,6-CF3BPA	6	0.86	0.16 ± 0.01	19 %

In addition to atomic ratios given, Table 3.4 also provides a percentage value regarding the purity of the monolayer, using the terminology used in the literature.[31] Note that these are **not** coverage values, which will be provided in 3.7.3, but instead are a measure of how much carbonaceous carbon is present on the ITO, or on top of the phosphonic acid monolayer. What can be observed from this data is similar to what was qualitatively discussed in 3.7.1. Benzyl phosphonic acids with substitutions in the 2 and/or 6 position of the ring tend to have a lower monolayer purity and therefore have not reacted completely with the surface to produce a well-packed monolayer. Molecules

such as PFBPA, 4-FBPA, 4-CF3BPA, 3,4-F2BPA, 3,5-F2BPA, 3,4,5-F3BPA all have extremely similar "purity" values between ~ 70 – 80 %. This data indicates that unless there is some steric hindrance that the ability to modify the surface of the ITO is similar regardless of the benzyl phosphonic acid used. There are notable exceptions to this conclusion, the first of which is PFBPA, which has the highest purity value meaning it can pack more readily. The other exceptions to the trend are 2-CF3BPA and 3-CF3BPA, which have higher and lower purity values, respectively, than would be expected when compared with the other molecules in the series. Thus, it appears that a factor such as steric hindrance or molecular orientation is allowing 2-CF3BPA to bind more readily than anticipated and 3-CF3BPA to leave more unmodified sites on the ITO.

3.7.3 Phosphonic Acid Coverage on ITO

Coverage values for the series of fluorinated benzyl phosphonic acids were calculated as discussed in 3.6.2 using the footprint of each phosphonic acid as geometry optimized on the surface of ITO by DFT calculations conducted by Alexander Hyla. Table 3.5 summarizes the molecular footprint used for each phosphonic acid in the coverage calculation, the percent coverage value obtained from the comparison of experimental F/In ratio compared to those calculated for a full monolayer, the ideal absolute coverage value (in molecules/cm^2) from the given footprint, and the experimental absolute coverage as translated from the percent coverage. Figure 3.12 provides a visualization of these differences in molecular footprint of the various molecules relative to one another and Figure 3.13 provides a visualization of the differences of absolute coverage in relationship to the footprint of the surface modifiers.

Table 3.5 Comparison of fluorinated benzyl phosphonic acid coverage values. The molecular footprints given were calculated at the DFT level on surface-bound, geometry optimized phosphonic acids on a slab of ITO. The percent coverage values were obtained from the calculations shown in 3.6.2, and the ideal absolute coverage values obtained using the footprint of the phosphonic acid. The percent coverage values can then be expressed in absolute terms of molecules/cm^2.

Phosphonic Acid	**Molecular Footprint ($Å^2$)**	**Ideal Coverage (10^{14} molecules/cm^2)**	**Experimental % Coverage**	**Experimental Coverage (10^{14} molecules/cm^2)**
PFBPA	22.62	4.42	86 %	3.81
2-FBPA	22.47	4.45	71 %	3.16
3-FBPA	20.57	4.86	78 %	3.80
4-FBPA	20.05	4.99	84 %	4.20
2-CF3BPA	29.04	3.44	78 %	2.69
3-CF3BPA	31.25	3.20	91 %	2.91
4-CF3BPA	24.39	4.10	88 %	3.63
2,3-F2BPA	22.99	4.35	69 %	3.02
3,4-F2BPA	20.56	4.86	78 %	3.80
3,5-F2BPA	21.41	4.67	84 %	3.91
3,4,5-F3BPA	21.65	4.62	83 %	3.85
2,6-F2BPA	20.97	4.77	42 %	2.02
2,6-CF3BPA	35.91	2.78	35 %	0.97

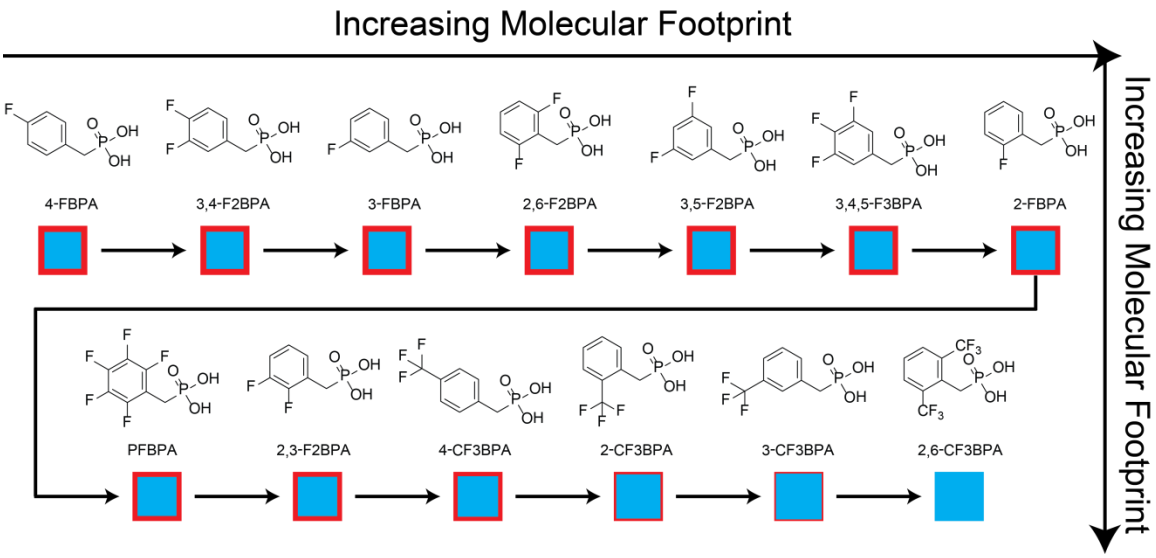

Figure 3.12 Visual comparison of molecular footprint for each phosphonic acid on ITO ordered in increasing size from left to right, top to bottom. The red background box serves as a reference point to the phosphonic acid with the largest footprint, 2,6-CF3BPA and the blue box shows the size of each phosphonic acid in relation to this reference point.

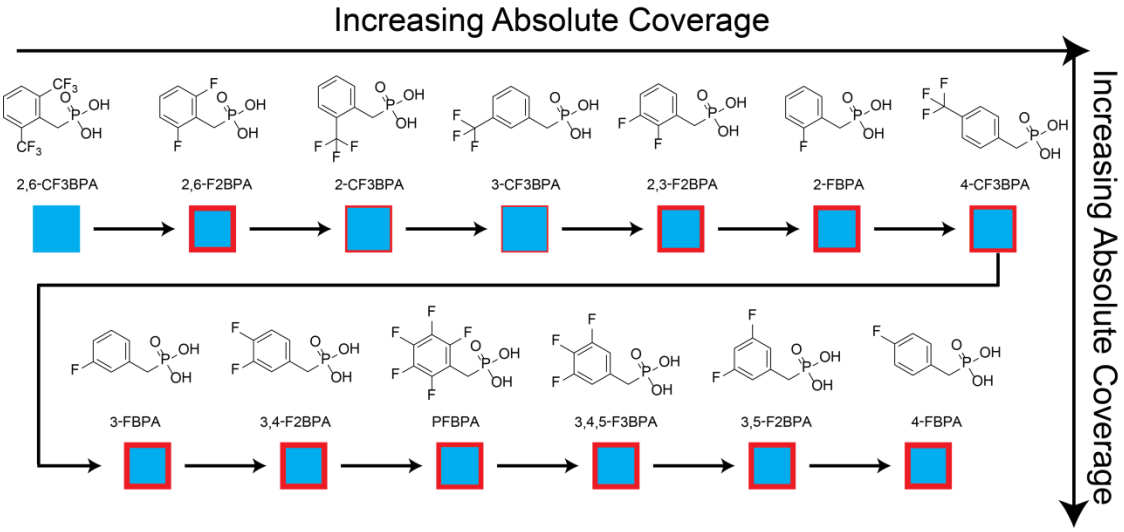

Figure 3.13 Visual comparison of absolute coverage for each phosphonic acid on ITO ordered in increasing coverage from left to right, top to bottom. The molecular footprints from Figure 3.12 to show the relationship between coverage and footprint, with the smallest coverage being 2,6-CF3BPA.

From the above table it becomes evident that, in general, fluorinated benzyl phosphonic acids produce coverage values on the order of ~ 3 – 4 × 10^{14} molecules/cm^2. The coverage value for PFBPA is completely consistent with the value of 85 % reported in the literature for longer modification times .[31] Comparing monosubstituted molecules, there is a clear trend in the absolute coverage (number of molecules per area) observed for the molecules that is not necessarily evident when looking at only percent coverage values. This is because the absolute coverage values take into account the differences in molecular footprint. For instance, consider the case of 3-CF3BPA and 4-CF3BPA. In this comparison 3-CF3BPA has a percent coverage value of 91 % while 4-CF3BPA is 88%, however, looking at absolute coverage the values are 2.91 × 10^{14} and 3.63 × 10^{14} molecules/cm^2, respectively. Thus, while 3-CF3BPA may have a higher overall percent coverage value it actually has a lower absolute coverage due to its larger molecular footprint. This helps better explain why 2-CF3BPA and 3-CF3BPA had similar % purity values from 3.7.2 as both these molecules have very similar absolute coverage values. The graph in Figure 3.14 illustrates the absolute coverage differences for these monosubstituted molecules. The trends between the two types of substituents are strikingly similar with the trifluoromethyl substitution always affording a lower coverage value due to the added bulkiness of this moiety.

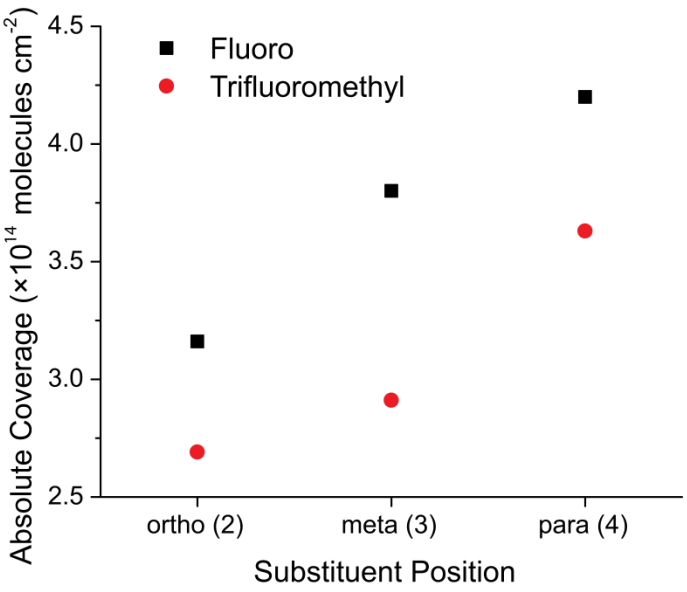

Figure 3.14 Graph comparing the absolute coverage values for monosubstitued fluoro and trifluoromethyl benzyl phosphonic acids as a function of substitution position.

Again, it is evident that substitution in the more sterically hindered 2 and 6 positions leads to a dramatic decrease in the ability of the molecule to form a well-packed monolayer. This is consistent with what was observed in terms of monolayer purity and better explains why those values were so low compared with the other modifiers. It appears that these two modifiers in particular are leaving a large amount of the ITO unmodified and thus allowing for the deposition of a far greater amount of adventitious contaminants on the surface. Comparing the other multiply fluorinated molecules with one another shows that substitution in the 3, 4, or 5 positions affords little impact on the overall coverage. PFBPA has substitution in all 5 positions of the benzene ring, but has a coverage value that is most similar to that of the benzene rings substituted in the 3, 4, and 5 positions rather than those substituted in the 2 and/or 6 positions. Thus, steric bulk and

molecular footprint are interrelated in determining the coverage of a phosphonic acid on ITO.

3.8 Work-Function Modification of ITO with Fluorinated Benzyl Phosphonic Acids

3.8.1 Experimental UPS Results

UPS was used to measure the work function changes of ITO that were induced as a result of the phosphonic acid surface modification. As discussed in 1.4.3 the secondary electron edge (SEE) was used to determine the changes in absolute WF. In addition to the WF, changes in the valence band maximum (VBM) relative to the Fermi level were also evaluated in an effort to better separate the origin of the work function change. For instance, a change in the SEE with a constant VBM indicates that there are changes only to the vacuum level and thus the origin of the WF change is an interface dipole formed by the presence of the surface modifier. If, however, there is both a change in the SEE as well as the VBM then there are contributions both from the interface dipole as in the previous case, as well as from geometry rearrangement at the surface and/or bond dipole, which are observable through shifts in the VBM. The UPS data are summarized in the following figures. Figure 3.15 displays the SEE for work function measurements along with the numerical values of WF and Figure 3.16 shows the VBM along with the accompanying values. Numerical values originate from the average of at least 5 spots measured on each substrate and the error originates from the standard deviation of these multiple spots. The plotted data originate from the spot on each sample that best represents the average numerical value calculated for the WF. Examination of the literature WF values for fluorinated benzyl phosphonic acids provided in Table 3.2 with the experimental values shown in Figure 3.15 indicate good agreement with one another.

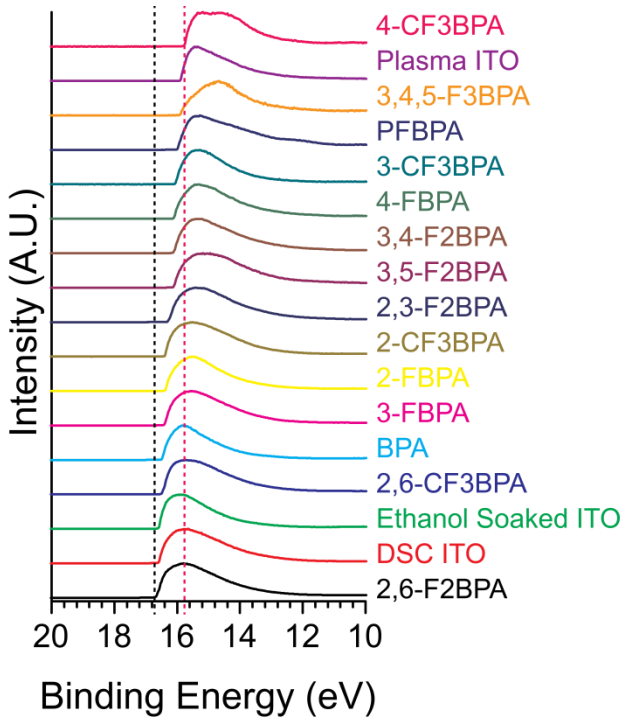

Surface	Work Function (eV)	Standard Deviation (eV)
4-CF3BPA	5.39	0.05
Plasma ITO	5.29	0.06
3,4,5-F3BPA	5.27	0.05
PFBPA	5.22	0.08
3-CF3BPA	5.14	0.05
4-FBPA	5.12	0.06
3,4-F2BPA	5.10	0.01
3,5-F2BPA	5.08	0.08
2,3-F2BPA	4.92	0.02
2-CF3BPA	4.81	0.06
2-FBPA	4.81	0.01
3-FBPA	4.80	0.01
BPA	4.71	0.04
2,6-CF3BPA	4.71	0.02
Ethanol Soaked ITO	4.62	0.02
DSC ITO	4.61	0.02
2,6-F2BPA	4.54	0.01

Figure 3.15 Comparison of experimental UPS data for the modified and control surfaces. Shown at left are the SEE spectra with the corresponding WF value shown in the table to the right. Values are obtained from an average of at least 5 spots on each substrate and standard deviation is the variation in WF from spot to spot. Graphs have been normalized and offset for clarity. Note that the graphs and table are ordered in increasing WF value, bottom to top and the dashed lines represent the extreme values to highlight the differences in SEE values.

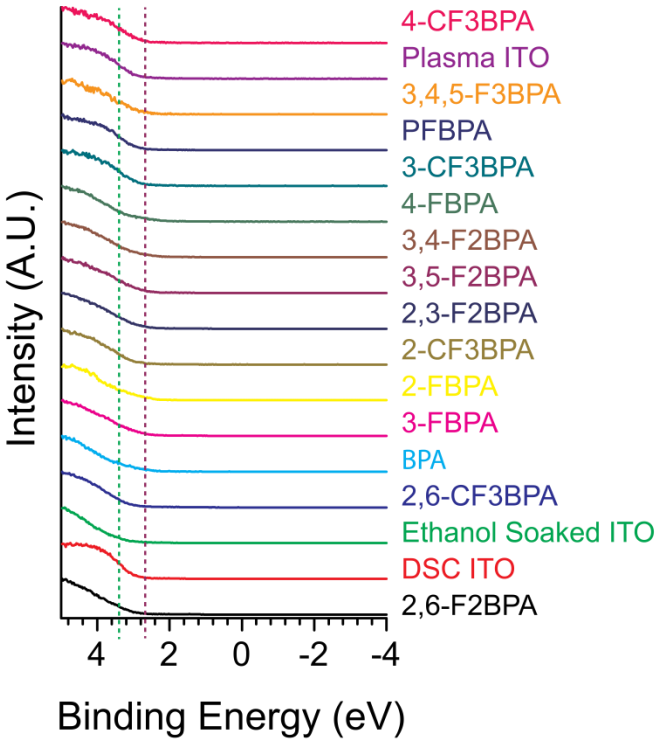

Surface	Valence Band Maximum (eV)	Standard Deviation (eV)
4-CF3BPA	2.77	0.03
Plasma ITO	2.85	0.02
3,4,5-F3BPA	2.75	0.02
PFBPA	2.86	0.03
3-CF3BPA	2.81	0.04
4-FBPA	2.82	0.03
3,4-F2BPA	2.78	0.05
3,5-F2BPA	2.70	0.06
2,3-F2BPA	2.77	0.02
2-CF3BPA	2.93	0.04
2-FBPA	3.02	0.03
3-FBPA	2.74	0.16
BPA	3.02	0.05
2,6-CF3BPA	3.07	0.06
Ethanol Soaked ITO	3.29	0.03
DSC ITO	2.92	0.05
2,6-F2BPA	2.96	0.05

Figure 3.16 Comparison of experimental VBM data for the modified and control surfaces. Shown at the left are the UPS spectra highlighting the VBM region and the corresponding numerical values are provided in the table to the right. Values are obtained from an average of at least 5 spots on each substrate and standard deviation is the variation in WF from spot to spot. Graphs have been normalized, offset and match the ordering of Figure 3.15 for clarity. The dashed lines represent the extreme values of 3,5-F2BPA and ethanol soaked ITO to highlight differences in VBM.

In order to compare the changes in WF and VBM across the samples, a single reference point needs to be chosen, which in the case of phosphonic acid modification means a bare surface. There are three options that could be used (DSC, ethanol soaked, and plasma ITO) and it was determined that DSC ITO would serve as the best reference point. The main reason for this selection of reference surface is that DSC ITO matches the bare surface used in previous work examining benzyl phosphonic acids on ITO.[38] Furthermore, ethanol soaked ITO has more adventitious carbon compared to surfaces that

were soaked with a phosphonic acid modifier and plasma cleaned ITO can have more variations in WF from sample to sample due to the highly active nature of the surface after treatment. Thus, with a reference point chosen it is possible to examine how each modifier impacted the WF and VBM of ITO and then use that information to attribute the portion of the WF change that originates from the formation of an interface dipole due to the presence of the phosphonic acid modifier. Figure 3.17 summarizes all of this information in the form of energy-level diagrams. In this case, the Fermi levels are aligned and the WF changes are shown by changes in vacuum level.

All the modifiers examined, with the exception of 2,6-F2BPA, had the impact of increasing the WF relative to DSC ITO. Plasma cleaning the ITO surface has the impact of both hydroxylating the surface as well as removing adventitious carbon, and thus produces a high WF value. When the sample is soaked in ethanol without any modifier, the surface returns to a state where it is covered with adventitious carbon, which produces a WF lower than what is measured directly after plasma treatment and more similar to that of DSC ITO. This decrease in WF from the deposition of carbonaceous adsorbates on the surface originates from what is known as the pillow effect, where the adsorbates reduce the tailing of the wavefunction out of the substrate.[72] The position of fluorination also has a clear impact on the interface dipole that is formed and is the main origin of the WF changes observed. Changes in the VBM are small by comparison and fall within a range of approximately -0.10 to 0.20 eV for the various phosphonic acids.

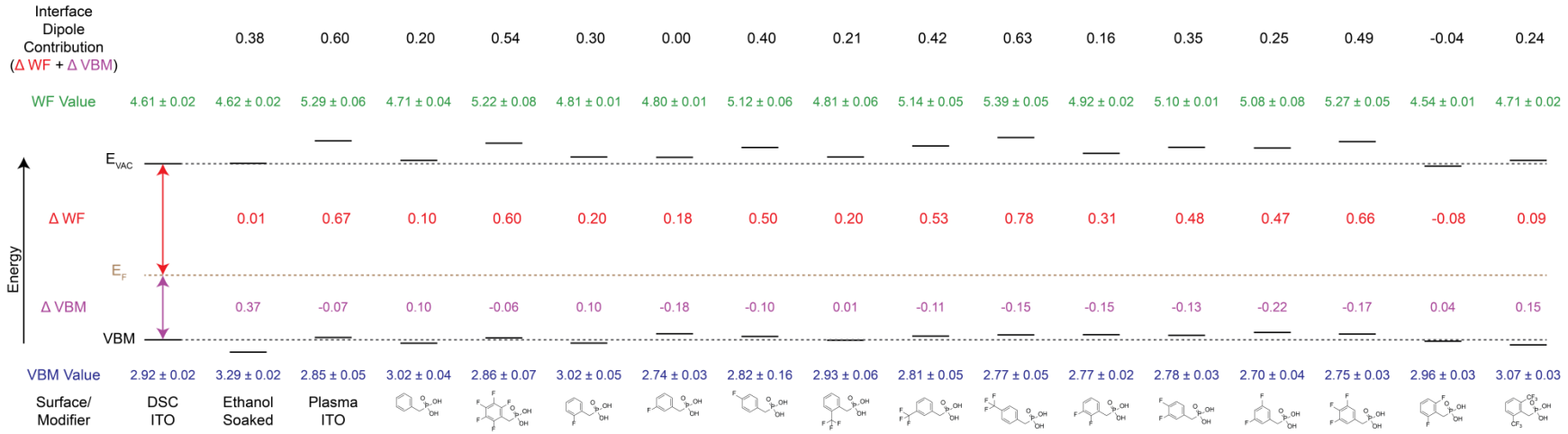

Figure 3.17 Energy-level diagram comparing the WF and VBM of different surfaces and modifiers with respect to DSC ITO. Data shown was collected by UPS. Both ΔWF and ΔVBM show the change occurring relative to DSC ITO. The interface dipole contribution originates from the sum of the change in WF and the change in VBM. Fermi levels are aligned. It should be noted that ITO is a degenerate n-doped semiconductor that has its Fermi level inside of the conduction band within the bulk,[1] however, the electrons that are detected by UPS originate from less than 1 nm below the surface.[5] In this regime, the Fermi level is below that of the conduction band and the conduction band is not shown in this diagram as UPS data does not provide information regarding its position. All values are reported in eV.

3.8.2 Relating Work Function, Interface Dipole, and Coverage

The experimental data shown in the previous section demonstrates the ability of phosphonic acids to alter the WF of ITO over a wide range of values. In order to put the UPS data in better context with the coverage values obtained from XPS analysis in 3.7.3 a 3-dimensional plot was generated to simultaneously examine the impact that the coverage and contribution from the interface dipole have on the final WF value. This plot is shown in Figure 3.18 and shows a general trend that as the WF of ITO increases, there are more molecules present on the surface, and the measured interface dipole becomes larger. This tends to suggest that molecular ordering (as measured by coverage) and interface dipole influence one another, meaning that the formation of a well-packed monolayer leads to the formation of a larger magnitude interface dipole on the surface and thus a larger WF change. In the case of benzyl phosphonic acids this typically means substitutions occur at the para position, which minimizes steric bulk and allows for better overall packing. At lower coverage values (and thus more carbonaceous carbon on the surface as there are larger gaps between phosphonic acid molecules) there is an increase in the VBM, which is consistent with what is seen for the ethanol soaked ITO sample. At higher coverage values, the VBM decreases and the position of the substitution appears to have little impact on VBM shifts as the values are all similar to one another regardless of substitution. This relationship between WF, VBM, and coverage is shown in Figure 3.19.

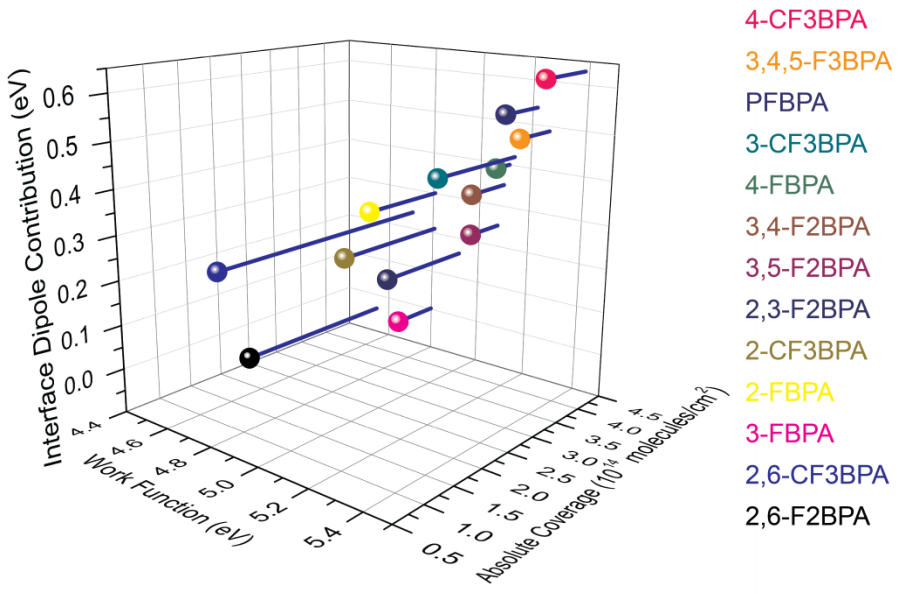

Figure 3.18 3-dimensional plot comparing WF values from UPS (*x*), with absolute coverage (*y*), and the contribution of the interface dipole to the WF change (*z*). Data points are labelled according to colors and are consistent with the color convention for the UPS data shown in 3.8.1.

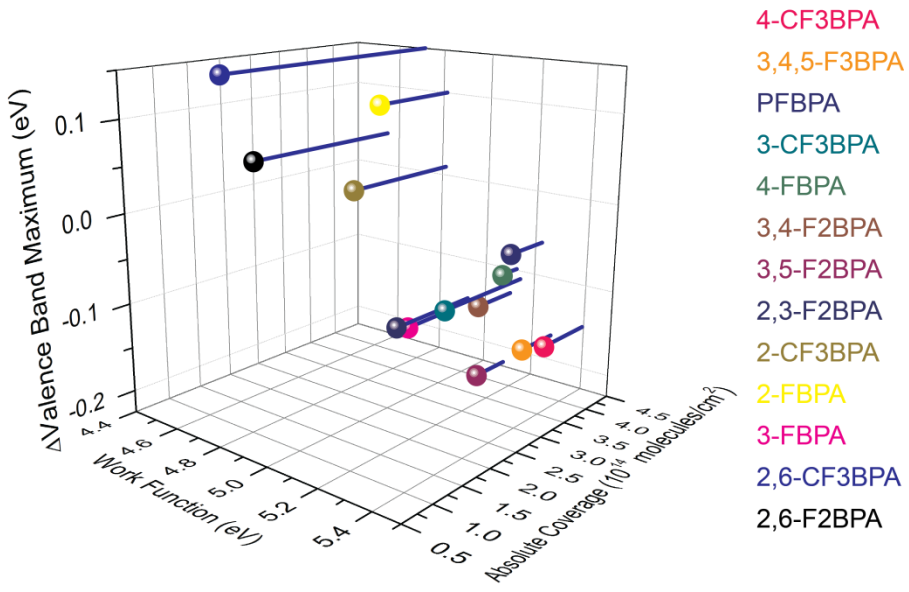

Figure 3.19 3-dimensional plot comparing WF values from UPS (*x*), with absolute coverage (*y*), and the shift in VBM relative to DSC ITO (*z*). Data points are labelled according to colors and are consistent with the color convention for UPS data shown in 3.8.1.

3.8.3 Theoretically Calculated Work Function Changes

DFT calculations were conducted by Alexander Hyla in Dr. Jean-Luc Brédas' group using the same ITO model used for the calculation of coverage discussed in 3.7.3 and for the previous NEXAFS[49-50] and phosphonic acid surface modification joint theoretical and experimental work.[38] This smooth, hydroxylated surface of ITO was examined initially at low coverage values of 2.8×10^{13} molecules/cm^2, which equates to one phosphonic acid per unit cell. This lower coverage value allows for the phosphonic acid to adopt a surface geometry in the absence of intermolecular interactions with other nearby phosphonic acid molecules. In addition, for PFBPA and BPA a higher coverage density of 1.1×10^{14} molecules/cm^2 (this equates to 4 phosphonic acid molecules per unit cell) was also examined to better analyze how intermolecular interactions between modifying molecules impact WF and orientation. The model of ITO used with bound phosphonic acid molecules (in this case BPA) in the four binding sites is shown in Figure 3.20 (for the low coverage case site 1 was consistently used for all modifiers).

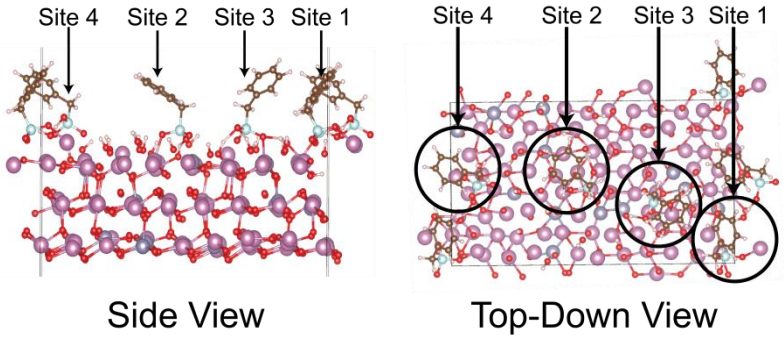

Figure 3.20 ITO unit cell utilized in DFT calculations showing side (left) and top-down (right) views of BPA bound to the surface of the ITO. Shown are the four binding sites that were used in the calculations. Image courtesy of Alexander Hyla.

The modelling that was performed allowed for theoretical work function changes to ITO and dipole moments for surface-bound, geometry optimized phosphonic acids to be calculated. The calculations performed provide a much more realistic picture of what the final molecular dipole of each molecule should be (as projected relative to the surface normal) than the more simplistic calculations that were performed on the tolyl analogues. The calculated WF values after phosphonic acid modification as well as the molecular dipole are provided in Table 3.6, with the experimental values from the previous sections shown for ease of reference.

Table 3.6 DFT level calculations of work function (both calculated WF and WF change relative to that calculated for a bare ITO unit cell) and intrinsic molecular dipole moment of each virtually isolated phosphonic acid in its surface optimized geometry are shown (calculated results courtesy of Alexander Hyla). In this instance coverage values of 2.8×10^{13} molecules/cm^2 were used for the calculations. Shown for reference are the experimentally determined WF values and changes relative to DSC ITO from Figure 3.15. Recall negative dipoles have electron density away from the surface and positive dipoles have electron density closer to the surface.

Modifier	**DFT Calculated WF (eV)**	**ΔWF from Bare ITO from DFT (eV)**	**WF from UPS (eV)**	**ΔWF from DSC ITO (eV)**	**DFT Dipole PA (Debye)**
Bare ITO	3.15	-	-	-	-
DSC ITO	-	-	4.61	-	-
BPA	3.17	0.02	4.71	0.10	0.58
PFBPA	3.43	0.28	5.22	0.60	-1.49
2-FBPA	3.15	0.00	4.81	0.20	1.09
3-FBPA	3.21	0.06	4.80	0.18	0.26
4-FBPA	3.33	0.18	5.12	0.50	-0.76
2-CF3BPA	3.08	-0.07	4.81	0.20	1.66
3-CF3BPA	3.28	0.13	5.14	0.53	-0.18
4-CF3BPA	3.48	0.33	5.39	0.78	-2.17
2,3-F2BPA	3.21	0.06	4.92	0.31	0.52
3,4-F2BPA	3.35	0.20	5.10	0.48	-0.95
3,5-F2BPA	3.35	0.20	5.08	0.47	-1.13
3,4,5-F3BPA	3.48	0.33	5.27	0.66	-2.22
2,6-F2BPA	3.12	-0.03	4.54	-0.08	1.18
2,6-CF3BPA	3.20	0.05	4.71	0.09	0.52

Before beginning the comparison of experimental work function changes with those calculated by theory, it is important to point out the difference in values for bare ITO. From DFT calculations, the bare ITO was found to have a WF of 3.15 eV, which is smaller than the value ~ 4.6 eV typically found experimentally for DSC ITO (depending on how the ITO is prepared there is a range of starting values possible, typically 4 – 5 eV).[73] This discrepancy in absolute value likely originates from limitations in the model of the ITO surface, but does not impact the comparison of the two, however, since when both the experimental and theoretical data are plotted as a function of calculated dipole moment for the phosphonic acid, as shown in Figure 3.21, both sets of data show extremely similar trends. Interestingly, the theoretical modelling best fits the phosphonic acids with some of the lowest coverage values of the 14 molecules, which are 2,6-F2BPA and 2,6-CF3BPA. The molecules with the highest absolute coverage values see the greatest deviation from the theoretical results, such as in the cases of 3,4,5-F3BPA and 4-CF3BPA. This corresponds with recent work showing that the WF calculated greatly depends on the coverage density and binding geometry parameters used.[67]

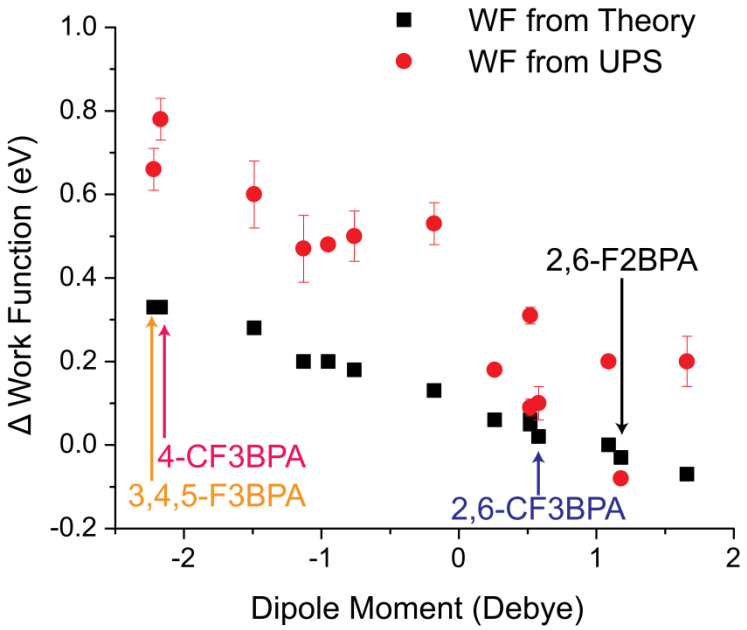

Figure 3.21 Comparison of change in WF values relative to DSC ITO for UPS and bare ITO for DFT, as determined by DFT calculations and by UPS experimental data as a function of calculated dipole moment for each phosphonic acid. The overall trends between experiment and theory are quite good. Error bar for UPS data originates from standard deviation over multiple spots analyzed and highlighted data points correspond to those discussed in the text above.

3.9 Examination of Molecular Ordering of Fluorinated Benzyl Phosphonic Acids

3.9.1 NEXAFS Data Analysis Overview

In an effort to provide an analysis of the molecular ordering of these benzyl phosphonic acids on the surface of ITO, NEXAFS data were collected at the Stanford Synchrotron Radiation Lightsource (SSRL). Data were collected in collaboration with Kristina Knesting and Matthew Gliboff from David Ginger's group at the University of Washington along with Lingzi Sang from Jeanne Pemberton's group at the University of Arizona. Matthew Gliboff conducted all NEXAFS data processing and determined tilt angles from the experimental measurements.

As discussed in 1.4.6, NEXAFS relies on the excitation of core electrons (in the case of the measurements for benzyl phosphonic acids carbon K-shell electrons) to unoccupied molecular orbitals. The incidence angle of the polarized X-ray source was varied between 20° and 90° relative to the surface and changes in the amplitude of these transitions were observed, which were then used to determine the orientation of various transition dipole moments. For these molecules in particular, the transition from C 1s to the C=C π* was observed and this transition occurs at approximately 285 eV. In the case of this excitation, the transition dipole moment is perpendicular to the bond axis and thus normal to the benzene ring.[74] This means that the tilt angle (α) is therefore defined as the angle that forms between the transition dipole moment and the surface normal. This angle is graphically shown in Figure 3.22. It should be noted that PFBPA has much smaller C=C π* features and thus the transition from C 1s to C-F σ* is used instead (occurring at approximately 288 eV). Representative experimental NEXAFS data are shown in Figure 3.23.

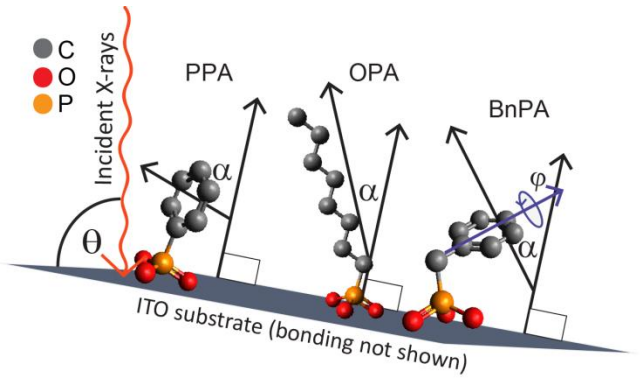

Figure 3.22 Generic phosphonic acids on the surface of ITO. Phenyl, alkyl, and benzyl phosphonic acids are shown to illustrate the differences in how the angle α is measured. Incident X-rays strike the surface at an angle θ. The angle α is formed between the transition dipole moment and the surface normal. In the case of the alkyl phosphonic acid, the transition dipole moment is along the axis of the chain, but in the case of phenyl and benzyl phosphonic acids this dipole is normal to the benzene ring. Thus, the angle reported is that of the benzene ring with respect to the surface normal. Note that benzyl phosphonic acids have an extra degree of rotational freedom (φ) that is not present in phenyl phosphonic acids. Image courtesy of Matthew Gliboff.

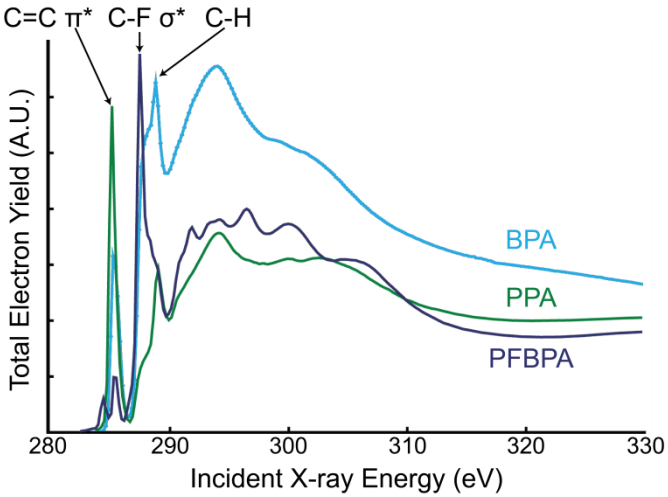

Figure 3.23 Carbon edge NEXAFS TEY spectra for BPA and PFBPA. Phenyl phosphonic acid (PPA) is shown for reference since that tilt angle has been previously determined.[49] All spectra were acquired at an incidence angle of 55°. Note the large decrease in the C=C π* feature for PFBPA relative to BPA and PPA, and the prominent C-F σ* transition. Image courtesy of Matthew Gliboff.

In addition to collecting data at multiple angles, both the total electron yield (TEY) and Auger electron yield (AEY) spectra are collected. The peak areas for the transition of interest (e.g. C=C π* or C-F σ*), $I_v(\theta)$ are then examined as a function of X-ray angle of incidence. It is then possible to fit the data according to Equation 3.2, which is based on the X-ray incidence angle (θ), the tilt angle of the molecule α, and the degree of linear polarization of the beamline at SSRL, which is 0.85.[74-76]

$$I_{\mathrm{v}}(\theta) \propto \frac{0.85}{3}\left(1 + 0.5(3\cos^2(\theta) - 1)(3\cos^2(\alpha) - 1)\right) + \frac{0.15}{2}(1 - \cos^2(\alpha)) \qquad \text{Equation 3.2}$$

Similarly, since the case of PFBPA required the use of C-F σ*transitions, I_p, a slightly altered version of Equation 3.2 is required since the transition occurs in a different plane than that of C=C π*. Thus, to keep the meaning of α consistent Equation 3.3 is used.[74]

$$I_{\mathrm{p}}(\theta) \propto \frac{1.7}{3}\left(1 - 0.25(3\cos^2(\theta) - 1)(3\cos^2(\alpha) - 1)\right) + \frac{0.15}{2}(1 + \cos^2(\alpha)) \qquad \text{Equation 3.3}$$

As both the AEY and TEY spectra are examined, the discrepancy between the resulting calculated angles for α provide a measure of systematic uncertainty in removing the background spectrum of a freshly sputter cleaned ITO sample.

Complete details regarding the analysis of the data can be found in previously published articles[49-50] and their supporting information. The experimental section of this chapter also provides further details regarding the collection of the data.

3.9.2 Tilt Angles from NEXAFS and DFT Calculations

The molecular tilt angles that were obtained from NEXAFS experiments as well as the theoretically calculated tilt angles that were obtained from the DFT level calculations are summarized in Figure 3.24. This figure additionally highlights the magic angle of 54.7°, which is the angle around which it is not possible to distinguish between a surface that is highly ordered having an α of this value and a surface that is composed of random molecular orientations. This loss of dependence on the X-ray angle of incidence can be seen in Equation 3.2 and Equation 3.3 as both have the term $(3\cos^2(\alpha) - 1)$, and as the value of α approaches 54.7° the term goes to zero and thus the intensity is no longer dependent on the X-ray source angle of incidence, θ.[74]

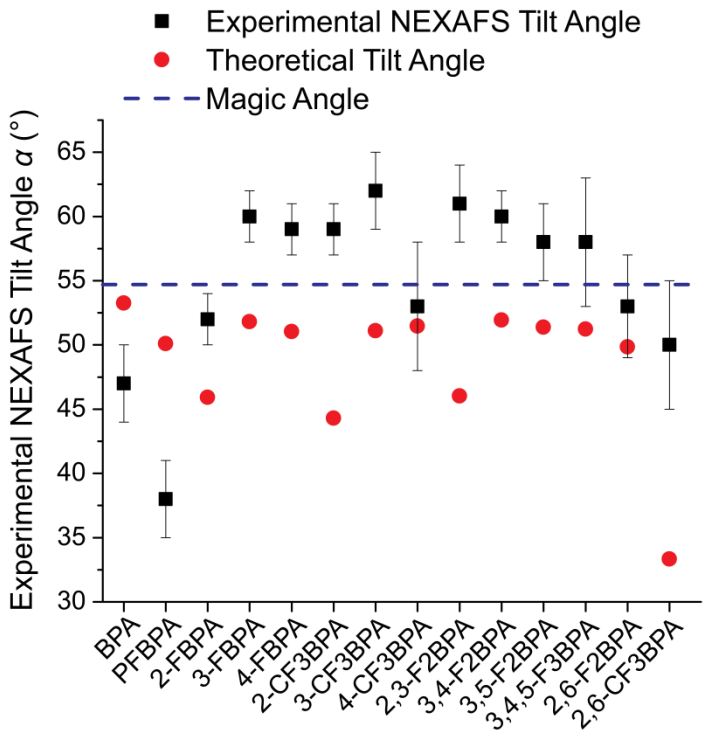

Figure 3.24 Results of the angle α for benzyl phosphonic acids on the surface of ITO as obtained experimentally from NEXAFS data compared with the results calculated at the DFT level of theory. The magic angle (54.7°) is also highlighted since at values of α close to this angle the tilt angle of the molecules is indistinguishable from random orientations. At this tilt angle, the angle of incidence of the source X-ray radiation no longer impacts the intensity of the observed transitions.[74] NEXAFS data courtesy Matthew Gliboff and DFT data courtesy Alexander Hyla.

Unlike previous reports for phosphonic acid tilt angles on IZO[50] and ITO[49] there are, in some cases, large deviations between tilt angles determined by NEXAFS and those obtained from theory. As previously shown in Figure 3.22, benzyl phosphonic acid orientations are complicated by the additional rotational freedom (φ) of the benzene ring about the C1-C4 axis (the twist angle). In nearly all cases (with the exception of BPA and PFBPA), the experimentally determined tilt angle is close to that of the magic angle, which means it is impossible to know whether the molecules are adopting an orientation that is ordered and is the calculated tilt angle, or if they are randomly ordered with

multiple orientations on the surface. These molecules also show a large deviation between the NEXAFS data and the DFT data. Some of that discrepancy is likely due to rotational freedom (φ) that was not present in the studies conducted on phenyl or alkyl phosphonic acids. There are also likely contributions from differences in binding modes (this difference was demonstrated to be on the order of 10° for values of α for phenyl phosphonic acids when examining bidentate vs. tridentate binding) and intermolecular effects, as the experimentally determined packing density for these molecules is an order of magnitude larger than the packing density used for theoretical calculations. Even PFBPA, while having a preferred orientation (as it is removed from the magic angle) experiences a combination of these factors likely leading to the large difference between the calculated tilt angle and NEXAFS data.

As was previously mentioned, both BPA and PFBPA were examined at high and low coverage values as well as at different sites on the surface of the ITO. The tilt angles for this data are summarized in Figure 3.25. It should be noted as was discussed in prior work conducted with phosphonic acids at these binding sites[67] that each site corresponds to different binding modes. At site 1 the phosphonic acid binds in a bidentate fashion to two indium atoms, site 2 contains tridentate binding through a combination of O-In and O-Sn bonds, and both sites 3 and 4 have bidentate binding with phosphoryl hydrogen bonding to the surface hydroxyl groups.[67] Coupling this information with what is shown in Figure 3.25, it appears that tilt angles for BPA are not greatly impacted by coverage, but do see differences based on binding modes. Alternatively, PFBPA tends to see larger differences between low and high coverages in addition to differences based on binding modes. Thus, based on theoretical results it appears that BPA would tend to adopt

bidentate binding to the surface (resembling site 3 at high coverage values) and PFBPA a mixture between bidentate and tridenate binding (resembling sites 2 and 4). These different binding modes, coupled with differences in intermolecular interactions between aryl-aryl and pentafluoroaryl-pentafluoroaryl groups may explain the differences in tilt angles for these two cases.

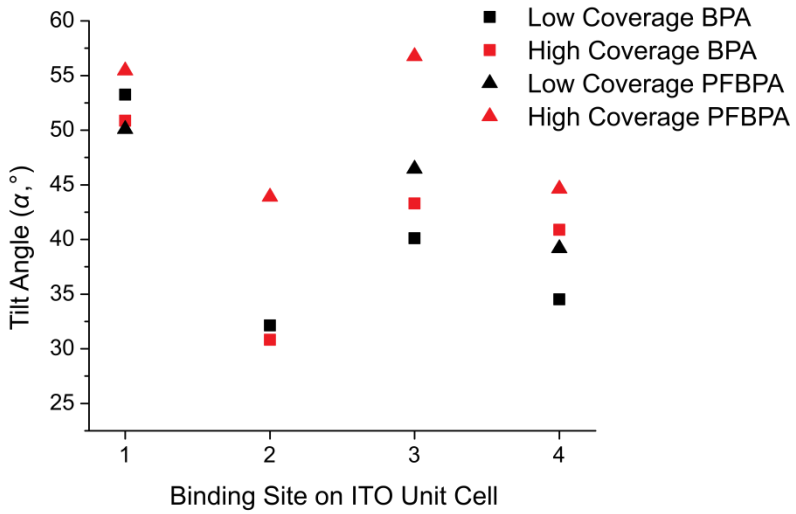

Figure 3.25 Summary of tilt angles obtained from theory for BPA and PFBPA at different sites on the unit cell of ITO and at different coverage concentrations. Data points in black correspond to a coverage of 2.8×10^{13} molecules/cm^2 while those in red correspond to 1.1×10^{14} molecules/cm^2. Binding sites correlate with those shown in Figure 3.20. Data courtesy of Alexander Hyla.

3.10 Conclusions

The overall goal of this chapter was to examine how altering fluorinated substituents of benzyl phosphonic acids on the surface of ITO impacts the work function, coverage, purity of the monolayer, and molecular ordering on the surface. The chapter has shown that the work function of ITO can be drastically varied based on judicious selection of the position of fluorination on the benzene ring. It was also shown that the

work function of ITO is not readily decreased by any of the phosphonic acids discussed within this chapter, and that steric hindrance likely plays a key role in determining the overall ability of a phosphonic acid to form a complete monolayer. In general, however, using the modification conditions described in 3.11.2, the vast majority of benzyl phosphonic acids form a very dense monolayer on the surface of ITO. While it is not a complete monolayer, XPS indicated that the monolayer was 80 – 90 % of an ideal monolayer. The coverage also apparently has an impact on the valence band maximum shift that is observed such that leaving more space open for the deposition of adventitious carbon allows for an increase in the VBM (relative to the Fermi level), which consequently negates some of the work function shift that would be caused by interface dipoles formed by the presence of the phosphonic acid.

DFT calculations corroborated the impact of these modifiers on the surface of ITO as the trends for WF modification of the surface fit well with one another. The calculation of interface dipole moments also demonstrated that molecules with high coverage values also generally had the formation of strong interface dipoles causing the measured changes in WF. From the tilt angle analysis conducted from theory it would appear that fluorinated benzyl phosphonic acids adopt surface conformations that are relatively similar to one another. The experimental results did indicate that most of the measured tilt angles were within a range of approximately 10° from one another, however, due to the nature of NEXAFS, and the angles being so close to the magic angle, it is not possible to determine whether there is ordering on the surface or whether the surface is completely disordered. Complete lack of substitution (BPA) or total fluorination (PFBPA) appear to allow for the formation of favorable intermolecular

interactions that promote the formation of molecular ordering and binding modes appear to be mainly bidentate for BPA and a mixture of bidentate and tridentate for PFBPA based on DFT calculations.

Figure 3.26 summarizes the main experimental findings of this chapter in a 3-dimensional plot comparing work function, absolute coverage, and tilt angle as determined by NEXAFS. The data presented above demonstrates that the position of substitution of a fluorinated benzyl phosphonic acid has an impact on the ability of the modifier to alter the WF of ITO and that the substitution plays a key role in the ability of the phosphonic acid to form a well-packed monolayer (particularly when sterically bulky substituents are present on the molecule). The substitution, however, appears to have little impact on the ordering of these phosphonic acids on ITO. Nearly all the molecules formed monolayers that could not be resolved by NEXAFS analysis, and are likely disordered on the surface. Thus, benzyl phosphonic acids have proven to be far more complex systems than what was previously examined with phenyl and alkyl phosphonic acids.

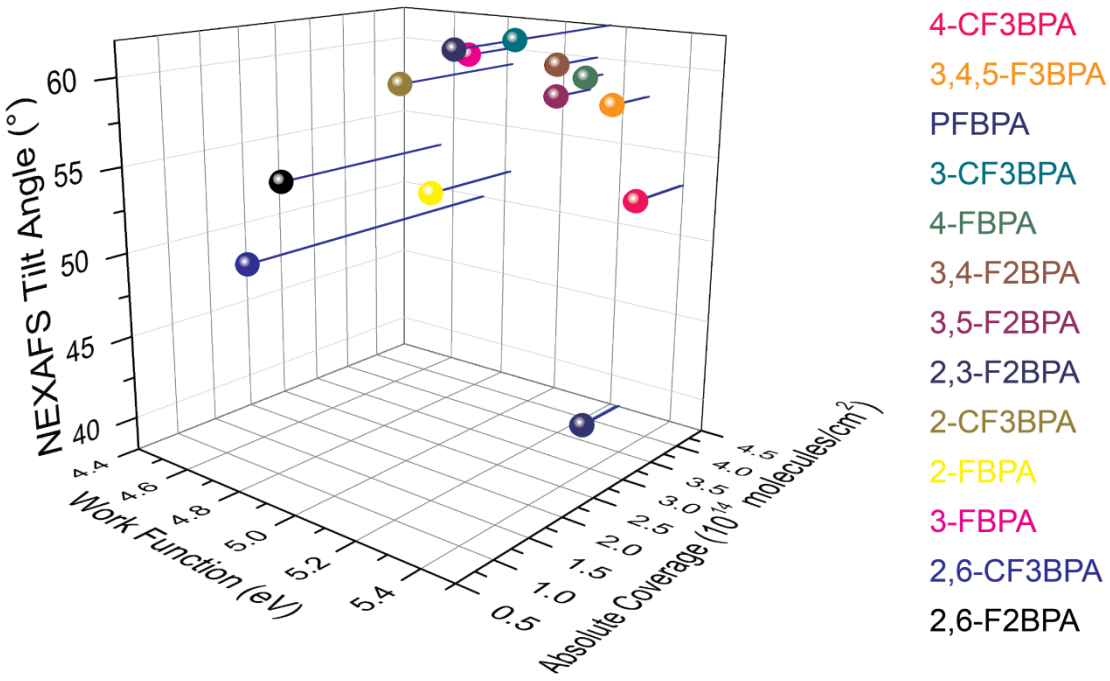

Figure 3.26 3-dimensional plot showing the relationship of experimentally determined values for changes in the WF of ITO (*x*) based on the substitution of the benzene ring, and how this relates to the absolute coverage (*y*) and orientation (*z*) of the modifier on the surface of ITO. Blue drops lines were added to better aid in observing coverage values on the plot.

3.11 Experimental

3.11.1 Materials

All phosphonic acids shown in Figure 3.4 were synthesized as detailed in Chapter 2 of this document with the exceptions of 3,5-F2BPA (synthesized by Peter Hotchkiss) and 3,4,5-F3BPA (synthesized by Guanhua Feng).

3.11.2 ITO Surface Cleaning and Modification

Commercially available ITO substrates (Eagle-XG, Thin Film Devices, Anaheim, CA) were purchased and found to have a surface roughness of 0.7-0.8 nm rms as measured with AFM and shown in Figure 3.7. This low roughness ITO is conducive to

conducting NEXAFS measurements. The ITO was cut into 7.5 mm × 15 mm substrates and sonicated in acetone for 10 min. The substrates were then scrubbed and subsequently sonicated for 10 min with a 5 % solution of Micro-90 detergent in DI water, sonicated in DI water for 10 min, sonicated in ethanol for 10 min, rinsed with ethanol, and dried under a flow of nitrogen. The surfaces were then cleaned with oxygen plasma using either a Plasma-Preen II (100 % Power, Plasmatic Systems, Inc., North Brunswick, NJ) or a Harrick Plasma PDC-32G (100 mL/minute flow of O2, 18 W power at 100 MHz, Pleasantville, NY) plasma cleaner for 5 min. Immediately upon removal from the plasma cleaner the substrates were immersed into a 10 mM solution of the phosphonic acid in ethanol. The surfaces remained immersed in the solution for 48 h at room temperature. Upon removal from solution the surfaces were washed with ethanol, dried under a flow of nitrogen, and annealed under rough vacuum for 2 h at 140 °C. Experimental measurements were all conducted using substrates that had been freshly modified in this manner.

3.11.3 Surface Characterization

3.11.3.1 XPS and UPS

All measurements were conducted in a combined XPS-UPS Kratos Axis Ultra with an average base pressure of 10^{-9} Torr. UPS was acquired prior to acquisition of XPS for all samples. UPS spectra were obtained with a 21.2 eV He (I) excitation and a pass energy of 5 eV using a 27 μm spot size. Each sample was examined in at least 5 spots to ensure consistency over the entire surface and the spectrometer was calibrated using a sputter cleaned silver sample. XPS data were collected with a monochromatic Al Kα source (300 W) using a 400 μm spot size and a pass energy of 160 eV for survey

acquisition and 20 eV for high resolution spectra. Exposure of the surfaces to X-rays was kept to a minimum (ca. 45 min), and spectra were acquired in three spots on each surface. Damage analysis indicated the surface bound phosphonic acids were stable over the timescale of a typical experiment by exposing samples to X-rays for at least 1.5 times the typical acquisition time. All characterizations were performed at normal takeoff angle (0°) and data analyzed using Vision Processing version 2.2.8.

3.11.3.2 NEXAFS

The NEXAFS data were acquired at Stanford Synchrotron Radiation Lightsource (SSRL), at the bending magnet Beam Line 8-2 as has been previously described.[49-50] The slit-to-slit SGM monochromator has an optimal resolution of better than 100 meV in the carbon region, but was operated at a lower resolution of about 200 meV for most measurements in order to maximize throughput while still resolving the features needed for the angular dependence analysis. The toroidal refocusing optics provided a near circular beam cross-section of about 1mm in diameter. The incoming photon flux was recorded from a gold covered wire mesh (gold grid) intercepting a few percent of the beam, via the drain current by a Keithley picoammeter. In order to ensure a proper normalization without artificial structures from contaminants, a fresh layer of gold was evaporated onto the grid before the start of each run. Second order contributions from the beam line monochromator were supressed by a Ti filter, inserted upstream of the gold grid, which strongly absorbs photons above the Ti L-edge at ~ 460 eV. The absolute beam energy was calibrated by measuring the highly oriented pyrolytic graphite (HOPG), assigning the energy of the π^* feature to 285.38 eV. To compensate for small monochromator drifts over the course of the day, the lower energy dip in the gold-grid

absorption spectrum (corresponding to the residual carbon on the optics in the beamline and assumed to be constant) was used to align all spectra to the same absolute calibration during individual runs. The degree of linear polarization is assumed to be 0.85,[76] based on recent measurements on this beamline, though one paper has reported polarization as high as 0.99.[77] Underestimation of the polarization would systematically shift the final result away from the magic angle, 54.7°, by up to 2°. All NEXAFS measurements were conducted at base pressures below 1×10^{-8} Torr. NEXAFS spectra are recorded in two modes simultaneously; total electron yield (TEY), measured as the sample drain current by a Keithley picoammeter, and the Auger electron yield (AEY), measured by a PHI 15-255G double pass cylindrical mirror analyser (CMA) operated in pulse counting mode. The CMA analyzer was set to a pass energy of 200 eV for highest throughput and operated at a fixed kinetic energy of 257 eV, which is part of the broad carbon Auger distribution and chosen specifically to shift contribution from non-NEXAFS features resulting from photoemission peaks in first and second order to before the onset of the C k-edge NEXAFS spectrum (285 eV).

The presence of photoemission peaks from the substrate in raw NEXAFS AEY spectra demonstrates that the thickness of our monolayer samples is on the same order as the escape depth of electrons from substrate excitations or that there are bare patches. Anisotropy of the photoemission peaks is indicative of the former. To remove the substrate background contribution, a bare ITO sample was sputtered under Ar at a pressure of 4×10^{-5} Torr, with a current of 20 mA and a driving voltage of 1 kV for 70 min to remove any carbon contamination. The spectra from this sputter-cleaned substrate were scaled to fit the pre-edge features of each of our sample spectra and subtracted. This

background subtraction is discussed further in a previous paper.[50] For the TEY signal, the background was taken to be a second order polynomial, removed before normalization by the gold-grid signal. The final data processing steps included normalization and averaging between samples for noise reduction. For the AEY data, the sample was normalized to an arbitrary average height of 1.8 in the background past the edge step (320-330 eV). Oscillatory behavior in this range, commonly known as extended x-ray absorption fine structure (EXAFS), was not significant. To minimize error from the background subtraction process, normalization was also performed to the height of the edge step during the peak fitting process for the TEY samples only. After normalization, three spectra for each sample type and angle were averaged together in a three-step process as follows. First, an average spectrum was computed. Second, the individual spectra were scaled and shifted to best match the average. Finally, the modified spectra were averaged together to create the corrected spectrum used for peak fitting and angular dependence studies. We use this process to mitigate any monochromator drift that may be present, which would have resulted in a shift of the spectrum along the energy axis.

Further details regarding the analysis of the NEXAFS data can be found in the supporting information of Gliboff.[50]

3.11.3.3 Tapping Mode AFM

All AFM images were acquired under atmospheric conditions using a commercial Agilent 5600 LS equipped with an AC-AFM controller. The microscope was housed within an acoustic isolation hood. The AFM piezo scanner was calibrated using a 3D reference silicon grating (Veeco, part number 498-000-026) with a 10 μm lateral pitch and a step height of 200 nm. Cantilevers (NSC35/NoAl, Mikromasch, CA) were made

from n-type silicon (phosphorous doped), utilizing cantilevers of 130 ± 5 μm in length, which have a typical probe radius of 10 nm and a typical spring constant of 4.5 N m^{-1}. Image acquisition was performed using PicoView 1.10, and image processing performed using the open source program Gwyddion version 2.20.

Topography images were collected in tapping-mode using a scan speed of 0.5 lines s^{-1}. After approach of the tip to the substrate, the piezo was retracted until the tip was oscillating above the surface and the amplitude set point was then optimized to obtain the best image contrast. Subsequently, the highest possible integral and proportional gains were used to obtain the most accurate representation of the sample. All 1 μm images were flattened using a first order polynomial background and all 5 μm images flattened using a second order polynomial background. Each sample was examined in at least 3 spots to ensure consistency of data over the entire substrate.

3.11.4 Theoretical Calculations

3.11.4.1 Substituted Toluene Compounds

Structures for the substituted toluene analogues of the substituted benzyl phosphonic acids were constructed using Spartan 2010. All structures were initially subjected to geometry optimization using MMFF molecular mechanics. Final geometries and dipole vectors were then calculated using DFT at the B3LYP level of theory using the 6-31G** basis set. Dipole moments obtained in this manner were then projected onto the C1-C4 axis for comparison among the 14 compounds.

3.11.4.2 DFT Phosphonic Acids on ITO Calculations

DFT calculations were conducted as previously described wherein they were carried out to optimize the adsorption geometry of PA molecules on the surface of ITO[49-50]. The theoretical model of the bare ITO surface consisted of a slab of three (In/Sn-O) layers, where the top layer was passivated by hydroxyl groups. First, a low coverage density is used in order to assess the geometry adopted by a PA molecule on the surface in the absence of strong interactions among PA molecules with one phosphonic acid molecule per ITO surface unit cell (24.79×14.32 Å^2), which is equivalent to 2.8×10^{13} molecules/cm^2. In order to evaluate the effect of intermolecular interactions on the variation of the tilt angle in BPA and PFBPA it is then necessary to consider a higher coverage density of 1.1×10^{14} molecules/cm^2, equivalent to four PA molecules in a unit cell as shown in Figure 3.20. As previous work, the Vienna Ab Initio Simulation Package (VASP) was used at the GGA-PBE level of theory with the projector-augmented wave (PAW) method.[49-50, 67] A plane wave cut-off of 300 eV for all elements and a total energy convergence of 10^{-6} eV for the self-consistent iterations were applied in all calculations. The geometry optimizations for the PA-ITO interface systems were performed using a damped molecular dynamics scheme until the forces were 0.04 eV/Å, while the phosphonic acid molecules, the first (In/Sn-O) layer, and all the OH groups on the surface are fully relaxed. All the self-consistent calculations were carried out with the improved tetrahedron method with Blöchl corrections for Brillouin-zone integrations on a $2 \times 2 \times 1$ k-point grid. After optimizing PA/ITO interface geometry, the tilt angle for each phosphonic acid molecule was obtained simply by using the coordinates of their component atoms. Surface roughness was also corrected for as previously described.[50]

Molecular footprints of the phosphonic acids were calculated by using the Cartesian (*x*, *y*, *z*) coordinates of the atoms after convergence of the geometry optimization for the surface bound PA. The range of values in the *x* and *y* directions were then obtained for both the benzyl portion of the molecule and the phosphonic acid potion of the molecule. A rectangle was then formed using the range of values in the *x* and *y* directions, which produced the footprint values used throughout this chapter.

Molecular dipole moments were calculated by taking the optimized phosphonic acid on the ITO surface, removing it from the surface and adding hydrogens to the P-O portion of the phosphonic acid moiety. A geometry optimization was subsequently conducted allowing only the newly added hydrogen atoms to relax (all other atoms were frozen in the original optimized geometry) and the dipole moment was the negative of the dipole correction determined during the final step of the calculation.

3.12 References

[1] Fan, J. C. C.; Goodenough, J. B., X-Ray Photoemission Spectroscopy Studies of Sn-Doped Indium-Oxide Films. *Journal of Applied Physics* **1977,** *48*, 3524-3531.

[2] *Handbook of Transparent Conductors*. Springer: New York, 2010.

[3] Ginley, D. S.; Bright, C., Transparent Conducting Oxides. *MRS Bulletin* **2000,** *25*, 15-18.

[4] Bp Statistical Review of World Energy June 2013. http://www.bp.com/content/dam/bp/pdf/statistical-review/statistical_review_of_world_energy_2013.pdf (accessed 2-20-2014).

[5] Seah, M. P.; Dench, W. A., Quantitative Electron Spectroscopy of Surfaces: A Standard Data Base for Electron Inelastic Mean Free Paths in Solids. *Surface and Interface Analysis* **1979,** *1*, 2-11.

[6] Exarhos, G. J.; Zhou, X. D., Discovery-Based Design of Transparent Conducting Oxide Films. *Thin Solid Films* **2007,** *515*, 7025-7052.

[7] Li, H.; Winget, P.; Brédas, J.-L., Transparent Conducting Oxides of Relevance to Organic Electronics: Electronic Structures of Their Interfaces with Organic Layers. *Chemistry of Materials* **2013,** *26*, 631-646.

[8] Gordon, R. G., Criteria for Choosing Transparent Conductors. *MRS Bulletin* **2000,** *25*, 52-57.

[9] Mizuhashi, M., Electrical Properties of Vacuum-Deposited Indium Oxide and Indium Tin Oxide Films. *Thin Solid Films* **1980,** *70*, 91-100.

[10] Hotchkiss, P. J.; Jones, S. C.; Paniagua, S. A.; Sharma, A.; Kippelen, B.; Armstrong, N. R.; Marder, S. R., The Modification of Indium Tin Oxide with Phosphonic Acids: Mechanism of Binding, Tuning of Surface Properties, and Potential for Use in Organic Electronic Applications. *Accounts of Chemical Research* **2012,** *45*, 337-346.

[11] Queffélec, C.; Petit, M.; Janvier, P.; Knight, D. A.; Bujoli, B., Surface Modification Using Phosphonic Acids and Esters. *Chemical Reviews* **2012**, 3777–3807.

[12] Rigney, M. P.; Funkenbusch, E. F.; Carr, P. W., Physical and Chemical Characterization of Microporous Zirconia. *Journal of Chromatography A* **1990,** *499*, 291-304.

[13] Randon, J.; Blanc, P.; Paterson, R., Modification of Ceramic Membrane Surfaces Using Phosphoric Acid and Alkyl Phosphonic Acids and Its Effects on Ultrafiltration of Bsa Protein. *Journal of Membrane Science* **1995,** *98*, 119-129.

[14] Wieserman, L. F.; Martin, E. S.; Wefers, K.; Novak, J. W., Jr.; Cross, K.; Conroy, C. M. Active Material Useful as a Multipurpose Adsorbent Comprising Metal Oxide/Hydroxide Particles Reacted with One or More Phosphorus-Containing Materials. EP273756A2, 1988.

[15] Wieserman, L. F.; Wefers, K.; Cross, K.; Martin, E. S. Adsorbents from Metal Oxide/Hydroxide Particles Reacted with Phosphorus-Containing Organic Acids. US4994429A, 1991.

[16] Hotchkiss, P. J.; Malicki, M.; Giordano, A. J.; Armstrong, N. R.; Marder, S. R., Characterization of Phosphonic Acid Binding to Zinc Oxide. *Journal of Materials Chemistry* **2011,** *21*, 3107-3112.

[17] Hamberg, I.; Granqvist, C. G., Evaporated Sn-Doped In2o3 Films: Basic Optical Properties and Applications to Energy-Efficient Windows. *Journal of Applied Physics* **1986,** *60*, R123-R160.

[18] Hartnagel, H., *Semiconducting Transparent Thin Films*. Institute of Physics Pub.: 1995.

[19] Klein, A., Electronic Properties of In_2o_3 Surfaces. *Applied Physics Letters* **2000,** *77*, 2009-2011.

[20] Armstrong, N. R.; Veneman, P. A.; Ratcliff, E.; Placencia, D.; Brumbach, M., Oxide Contacts in Organic Photovoltaics: Characterization and Control of near-Surface Composition in Indium−Tin Oxide (Ito) Electrodes. *Accounts of Chemical Research* **2009,** *42*, 1748-1757.

[21] Kim, J. S.; Friend, R. H.; Cacialli, F., Surface Wetting Properties of Treated Indium Tin Oxide Anodes for Polymer Light-Emitting Diodes. *Synthetic Metals* **2000,** *111–112*, 369-372.

[22] Kim, J.-S.; Cacialli, F.; Friend, R., Surface Conditioning of Indium-Tin Oxide Anodes for Organic Light-Emitting Diodes. *Thin Solid Films* **2003,** *445*, 358-366.

[23] Hanson, E. L.; Schwartz, J.; Nickel, B.; Koch, N.; Danisman, M. F., Bonding Self-Assembled, Compact Organophosphonate Monolayers to the Native Oxide Surface of Silicon. *Journal of the American Chemical Society* **2003,** *125*, 16074-16080.

[24] Hotchkiss, P. J. The Design, Synthesis, and Use of Phosphonic Acids for the Surface Modification of Metal Oxides. Ph.D. Thesis, Georgia Institute of Technology, Atlanta, GA, 2008.

[25] Busch, G.; Jaehne, E.; Cai, X.; Oberoi, S.; Adler, H.-J. P., Ultrathin Layers for Adhesion Promotion. *Synthetic Metals* **2003,** *137*, 871-872.

[26] Breen, T. L.; Fryer, P. M.; Nunes, R. W.; Rothwell, M. E., Patterning Indium Tin Oxide and Indium Zinc Oxide Using Microcontact Printing and Wet Etching. *Langmuir* **2001,** *18*, 194-197.

[27] Knesting, K. M.; Hotchkiss, P. J.; MacLeod, B. A.; Marder, S. R.; Ginger, D. S., Spatially Modulating Interfacial Properties of Transparent Conductive Oxides: Patterning Work Function with Phosphonic Acid Self-Assembled Monolayers. *Advanced Materials* **2012,** *24*, 642-646.

[28] Nie, H.-Y.; McIntyre, N. S.; Lau, W. M., Nanolithography of a Full-Coverage Octadecylphosphonic Acid Monolayer Spin Coated on a Si Substrate. *Applied Physics Letters* **2007,** *90*, 203114.

[29] Bulusu, A.; Paniagua, S. A.; MacLeod, B. A.; Sigdel, A. K.; Berry, J. J.; Olson, D. C.; Marder, S. R.; Graham, S., Efficient Modification of Metal Oxide Surfaces with Phosphonic Acids by Spray Coating. *Langmuir* **2013,** *29*, 3935-3942.

[30] Quiñones, R.; Gawalt, E. S., Polystyrene Formation on Monolayer-Modified Nitinol Effectively Controls Corrosion. *Langmuir* **2008,** *24*, 10858-10864.

[31] Paniagua, S. A.; Li, E. L.; Marder, S. R., Adsorption Studies of a Phosphonic Acid on Ito: Film Coverage, Purity, and Induced Electronic Structure Changes. *Physical Chemistry Chemical Physics* **2014,** *16*, 2874-2881.

[32] Appleyard, S. F. J.; Willis, M. R., Electroluminescence: Enhanced Injection Using Ito Electrodes Coated with a Self Assembled Monolayer. *Optical Materials* **1998,** *9*, 120-124.

[33] Appleyard, S. F. J.; Day, S. R.; Pickford, R. D.; Willis, M. R., Organic Electroluminescent Devices: Enhanced Carrier Injection Using Sam Derivatized Ito Electrodes. *Journal of Materials Chemistry* **2000,** *10*, 169-173.

[34] Besbes, S.; Ouada, H. B.; Davenas, J.; Ponsonnet, L.; Jaffrezic, N.; Alcouffe, P., Effect of Surface Treatment and Functionalization on the Ito Properties for Oleds. *Materials Science and Engineering: C* **2006,** *26*, 505-510.

[35] Hanson, E. L.; Guo, J.; Koch, N.; Schwartz, J.; Bernasek, S. L., Advanced Surface Modification of Indium Tin Oxide for Improved Charge Injection in Organic Devices. *Journal of the American Chemical Society* **2005,** *127*, 10058-10062.

[36] Paniagua, S. A.; Hotchkiss, P. J.; Jones, S. C.; Marder, S. R.; Mudalige, A.; Marrikar, F. S.; Pemberton, J. E.; Armstrong, N. R., Phosphonic Acid Modification of Indium-Tin Oxide Electrodes: Combined Xps/Ups/Contact Angle Studies. *Journal of Physical Chemistry C* **2008,** *112*, 7809-7817.

[37] Lacher, S.; Matsuo, Y.; Nakamura, E., Molecular and Supramolecular Control of the Work Function of an Inorganic Electrode with Self-Assembled Monolayer of Umbrella-Shaped Fullerene Derivatives. *Journal of the American Chemical Society* **2011,** *133*, 16997-17004.

[38] Hotchkiss, P. J.; Li, H.; Paramonov, P. B.; Paniagua, S. A.; Jones, S. C.; Armstrong, N. R.; Brédas, J.-L.; Marder, S. R., Modification of the Surface Properties of Indium Tin Oxide with Benzylphosphonic Acids: A Joint Experimental and Theoretical Study. *Advanced Materials* **2009,** *21*, 4496-4501.

[39] MacLeod, B. A.; Horwitz, N. E.; Ratcliff, E. L.; Jenkins, J. L.; Armstrong, N. R.; Giordano, A. J.; Hotchkiss, P. J.; Marder, S. R.; Campbell, C. T.; Ginger, D. S., Built-in Potential in Conjugated Polymer Diodes with Changing Anode Work Function: Interfacial States and Deviation from the Schottky–Mott Limit. *The Journal of Physical Chemistry Letters* **2012,** *3*, 1202-1207.

[40] Bardecker, J. A.; Ma, H.; Kim, T.; Huang, F.; Liu, M. S.; Cheng, Y.-J.; Ting, G.; Jen, A. K. Y., Self-Assembled Electroactive Phosphonic Acids on Ito: Maximizing Hole-Injection in Polymer Light-Emitting Diodes. *Advanced Functional Materials* **2008,** *18*, 3964-3971.

[41] Jee, S. H.; Kim, S. H.; Ko, J. H.; Yoon, Y. S., Study on Work Function Change of Ito Modified by Using a Self-Assembled Monolayer for Organic Based Devices. *Journal of the Korean Physical Society* **2006,** *49*, 2034-2039.

[42] Koh, S. E.; McDonald, K. D.; Holt, D. H.; Dulcey, C. S.; Chaney, J. A.; Pehrsson, P. E., Phenylphosphonic Acid Functionalization of Indium Tin Oxide: Surface Chemistry and Work Functions. *Langmuir* **2006,** *22*, 6249-6255.

[43] Ratcliff, E. L.; Garcia, A.; Paniagua, S. A.; Cowan, S. R.; Giordano, A. J.; Ginley, D. S.; Marder, S. R.; Berry, J. J.; Olson, D. C., Investigating the Influence of Interfacial Contact Properties on Open Circuit Voltages in Organic Photovoltaic Performance: Work Function Versus Selectivity. *Advanced Energy Materials* **2013,** *3*, 647-656.

[44] Sharma, A.; Hotchkiss, P. J.; Marder, S. R.; Kippelen, B., Tailoring the Work Function of Indium Tin Oxide Electrodes in Electrophosphorescent Organic Light-Emitting Diodes. *Journal of Applied Physics* **2009,** *105*, 084507.

[45] Sharma, A.; Haldi, A.; Hotchkiss, P. J.; Marder, S. R.; Kippelen, B., Effect of Phosphonic Acid Surface Modifiers on the Work Function of Indium Tin Oxide and on the Charge Injection Barrier into Organic Single-Layer Diodes. *Journal of Applied Physics* **2009,** *105*, 074511.

[46] Sharma, A.; Haldi, A.; Potscavage Jr, W. J.; Hotchkiss, P. J.; Marder, S. R.; Kippelen, B., Effects of Surface Modification of Indium Tin Oxide Electrodes on the Performance of Molecular Multilayer Organic Photovoltaic Devices. *Journal of Materials Chemistry* **2009,** *19*, 5298-5302.

[47] Sharma, A.; Kippelen, B.; Hotchkiss, P. J.; Marder, S. R., Stabilization of the Work Function of Indium Tin Oxide Using Organic Surface Modifiers in Organic Light-Emitting Diodes. *Applied Physics Letters* **2008,** *93*, 163308.

[48] Wang, H.; Gomez, E. D.; Guan, Z.; Jaye, C.; Toney, M. F.; Fischer, D. A.; Kahn, A.; Loo, Y.-L., Tuning Contact Recombination and Open-Circuit Voltage in Polymer Solar Cells Via Self-Assembled Monolayer Adsorption at the Organic–

Metal Oxide Interface. *The Journal of Physical Chemistry C* **2013,** *117*, 20474-20484.

[49] Gliboff, M.; Li, H.; Knesting, K. M.; Giordano, A. J.; Nordlund, D.; Seidler, G. T.; Brédas, J.-L.; Marder, S. R.; Ginger, D. S., Competing Effects of Fluorination on the Orientation of Aromatic and Aliphatic Phosphonic Acid Monolayers on Indium Tin Oxide. *The Journal of Physical Chemistry C* **2013,** *117*, 15139-15147.

[50] Gliboff, M.; Sang, L. Z.; Knesting, K. M.; Schalnat, M. C.; Mudalige, A.; Ratcliff, E. L.; Li, H.; Sigdel, A. K.; Giordano, A. J.; Berry, J. J.; Nordlund, D.; Seidler, G. T.; Bredas, J. L.; Marder, S. R.; Pemberton, J. E.; Ginger, D. S., Orientation of Phenylphosphonic Acid Self-Assembled Monolayers on a Transparent Conductive Oxide: A Combined Nexafs, Pm-Irras, and Dft Study. *Langmuir* **2013,** *29*, 2166-2174.

[51] Stockhause, S.; Neumann, P.; Schrader, S.; Kant, M.; Brehmer, L., Structural and Optical Properties of Self-Assembled Multilayers Based on Organic Zirconium Bisphosphonates. *Synthetic Metals* **2002,** *127*, 295-298.

[52] Stockhause, S.; Neumann, P.; Kant, M.; Schülke, U.; Schrader, S., Organic/Inorganic Functional Materials for Light-Emitting Devices Based on Conjugated Bisphosphonates. In *Host-Guest-Systems Based on Nanoporous Crystals*, Wiley-VCH Verlag GmbH & Co. KGaA: 2005; pp 197-216.

[53] Ishida, T.; Terada, K.-i.; Hasegawa, K.; Kuwahata, H.; Kusama, K.; Sato, R.; Nakano, M.; Naitoh, Y.; Haga, M.-a., Self-Assembled Monolayer and Multilayer Formation Using Redox-Active Ru Complex with Phosphonic Acids on Silicon Oxide Surface. *Applied Surface Science* **2009,** *255*, 8824-8830.

[54] Gundlach, L.; Szarko, J.; Socaciu-Siebert, L. D.; Neubauer, A.; Ernstorfer, R.; Willig, F., Different Orientations of Large Rigid Organic Chromophores at the Rutile Tio_2 Surface Controlled by Different Binding Geometries of Specific Anchor Groups. *Physical Review B* **2007,** *75*, 125320.

[55] Acton, O.; Dubey, M.; Weidner, T.; O'Malley, K. M.; Kim, T.-W.; Ting, G. G.; Hutchins, D.; Baio, J. E.; Lovejoy, T. C.; Gage, A. H.; Castner, D. G.; Ma, H.; Jen, A. K. Y., Simultaneous Modification of Bottom-Contact Electrode and Dielectric Surfaces for Organic Thin-Film Transistors through Single-Component Spin-Cast Monolayers. *Advanced Functional Materials* **2011,** *21*, 1476-1488.

[56] DelRio, F. W.; Rampulla, D. M.; Jaye, C.; Stan, G.; Gates, R. S.; Fischer, D. A.; Cook, R. F., Structure–Property Relationships for Methyl-Terminated Alkyl Self-Assembled Monolayers. *Chemical Physics Letters* **2011,** *512*, 243-246.

[57] Dubey, M.; Gouzman, I.; Bernasek, S. L.; Schwartz, J., Characterization of Self-Assembled Organic Films Using Differential Charging in X-Ray Photoelectron Spectroscopy. *Langmuir* **2006,** *22*, 4649-4653.

[58] Pellerite, M. J.; Dunbar, T. D.; Boardman, L. D.; Wood, E. J., Effects of Fluorination on Self-Assembled Monolayer Formation from Alkanephosphonic Acids on Aluminum: Kinetics and Structure. *The Journal of Physical Chemistry B* **2003,** *107*, 11726-11736.

[59] Keszthelyi, T.; Pászti, Z.; Rigó, T.; Hakkel, O.; Telegdi, J.; Guczi, L., Investigation of Solid Surfaces Modified by Langmuir−Blodgett Monolayers Using Sum-Frequency Vibrational Spectroscopy and X-Ray Photoelectron Spectroscopy. *The Journal of Physical Chemistry B* **2006,** *110*, 8701-8714.

[60] Hutchins, D. O.; Acton, O.; Weidner, T.; Cernetic, N.; Baio, J. E.; Castner, D. G.; Ma, H.; Jen, A. K. Y., Solid-State Densification of Spun-Cast Self-Assembled Monolayers for Use in Ultra-Thin Hybrid Dielectrics. *Applied Surface Science* **2012,** *261*, 908-915.

[61] Hutchins, D. O.; Weidner, T.; Baio, J.; Polishak, B.; Acton, O.; Cernetic, N.; Ma, H.; Jen, A. K. Y., Effects of Self-Assembled Monolayer Structural Order, Surface Homogeneity and Surface Energy on Pentacene Morphology and Thin Film Transistor Device Performance. *Journal of Materials Chemistry C* **2013,** *1*, 101-113.

[62] Hutchins, D. O.; Acton, O.; Weidner, T.; Cernetic, N.; Baio, J. E.; Ting, G.; Castner, D. G.; Ma, H.; Jen, A. K. Y., Spin Cast Self-Assembled Monolayer Field Effect Transistors. *Organic Electronics* **2012,** *13*, 464-468.

[63] Lin, H.-C.; Polaske, N. W.; Oquendo, L. E.; Gliboff, M.; Knesting, K. M.; Nordlund, D.; Ginger, D. S.; Ratcliff, E. L.; Beam, B. M.; Armstrong, N. R.; McGrath, D. V.; Saavedra, S. S., Electron-Transfer Processes in Zinc Phthalocyanine–Phosphonic Acid Monolayers on Ito: Characterization of Orientation and Charge-Transfer Kinetics by Waveguide Spectroelectrochemistry. *The Journal of Physical Chemistry Letters* **2012,** *3*, 1154-1158.

[64] Dubey, M.; Weidner, T.; Gamble, L. J.; Castner, D. G., Structure and Order of Phosphonic Acid-Based Self-Assembled Monolayers on Si(100). *Langmuir* **2010,** *26*, 14747-14754.

[65] Losego, M. D.; Guske, J. T.; Efremenko, A.; Maria, J.-P.; Franzen, S., Characterizing the Molecular Order of Phosphonic Acid Self-Assembled Monolayers on Indium Tin Oxide Surfaces. *Langmuir* **2011,** *27*, 11883-11888.

[66] Gliboff, M.; Sang, L. Z.; Knesting, K. M.; Schalnat, M. C.; Mudalige, A.; Ratcliff, E. L.; Li, H.; Sigdel, A. K.; Giordano, A. J.; Berry, J. J.; Nordlund, D.; Seidler, G. T.; Bredas, J. L.; Marder, S. R.; Pemberton, J. E.; Ginger, D. S., Orientation of Phenylphosphonic Acid Self-Assembled Mono Layers on a Transparent Conductive Oxide: A Combined Nexafs, Pm-Irras, and Dft Study (Vol 29, Pg 2166, 2013). *Langmuir* **2013,** *29*, 4176-4176.

[67] Li, H.; Paramonov, P.; Bredas, J.-L., Theoretical Study of the Surface Modification of Indium Tin Oxide with Trifluorophenyl Phosphonic Acid Molecules: Impact of Coverage Density and Binding Geometry. *Journal of Materials Chemistry* **2010,** *20*, 2630-2637.

[68] Briggs, D.; Seah, P., *Practical Surface Analysis: Auger and X-Ray Photoelectron Spectroscopy*. Wiley: 1990.

[69] Paniagua, S. A.; Baltazar, J.; Sojoudi, H.; Mohapatra, S. K.; Zhang, S.; Henderson, C. L.; Graham, S.; Barlow, S.; Marder, S. R., Production of Heavily N- and P-Doped Cvd Graphene with Solution-Processed Redox-Active Metal-Organic Species. *Materials Horizons* **2013**, 111-115.

[70] Paniagua-Barrantes, S. Interfacial Engineering of Transparent Conductive Electrodes and Nanoparticles with Phosphonic Acids and Metal-Organic Dopants for Organic Electronic Applications. Ph.D. Thesis, Georgia Institute of Technology, Atlanta, GA, 2013.

[71] Paramonov, P. B.; Paniagua, S. A.; Hotchkiss, P. J.; Jones, S. C.; Armstrong, N. R.; Marder, S. R.; Brédas, J.-L., Theoretical Characterization of the Indium Tin Oxide Surface and of Its Binding Sites for Adsorption of Phosphonic Acid Monolayers. *Chemistry of Materials* **2008,** *20*, 5131-5133.

[72] Brillson, L. J., *Surfaces and Interfaces of Electronic Materials*. Wiley: 2012.

[73] Wu, Q.-H., Progress in Modification of Indium-Tin Oxide/Organic Interfaces for Organic Light-Emitting Diodes. *Critical Reviews in Solid State and Materials Sciences* **2013,** *38*, 318-352.

[74] Stöhr, J., *Nexafs Spectroscopy*. 1st ed.; Springer: Berlin ; New York, 1996.

[75] Wu, C. C.; Wu, C. I.; Sturm, J. C.; Kahn, A., Surface Modification of Indium Tin Oxide by Plasma Treatment: An Effective Method to Improve the Efficiency, Brightness, and Reliability of Organic Light Emitting Devices. *Applied Physics Letters* **1997,** *70*, 1348-1350.

[76] Tirsell, K. G.; Karpenko, V. P., A General Purpose Sub-Kev X-Ray Facility at the Stanford Synchrotron Radiation Laboratory. *Nuclear Instruments and Methods in Physics Research Section A: Accelerators, Spectrometers, Detectors and Associated Equipment* **1990,** *291*, 511-517.

[77] Willey, T. M.; Lee, J. R. I.; Fabbri, J. D.; Wang, D.; Nielsen, M. H.; Randel, J. C.; Schreiner, P. R.; Fokin, A. A.; Tkachenko, B. A.; Fokina, N. A.; Dahl, J. E. P.; Carlson, R. M. K.; Terminello, L. J.; Melosh, N. A.; van Buuren, T., Determining Orientational Structure of Diamondoid Thiols Attached to Silver Using near-Edge X-Ray Absorption Fine Structure Spectroscopy. *Journal of Electron Spectroscopy and related Phenomena* **2009,** *172*, 69-77.

CHAPTER 4

SURFACE MODIFICATION OF ATOMIC LAYER DEPOSITED ZINC OXIDE WITH DIPOLAR PHOPHONIC ACIDS

4.1 Zinc Oxide

Chapter 3 focused on the modification of ITO using phosphonic acids due to the ubiquity with which ITO is used in optoelectronic devices and the large amount of literature focusing on phosphonic acid surface modification that has previously been conducted using ITO. While ITO does have the highest conductivity of commonly used transparent conducting oxides (TCOs), the rising cost of indium, due to its high demand in a wide variety of applications,[1-2] has fueled research into alternative TCOs. Zinc oxide (ZnO) is one such material that has been recently studied as an ITO alternative. There are multiple reasons for this interest: ZnO has a wide band gap (3.4 eV),[3-5] high optical transparency,[6] relatively low cost, and tunable resistivity[2, 7] by selective doping.[5] While ZnO is commonly thought of as a "future material," this is actually more so from the standpoint as a TCO.[3] Research into ZnO dates back many decades[8-9] and it is a very common industrial material used in applications ranging from the rubber industry (as a vulcanization activator) to paints and ceramics.[10]

This chapter focuses on the modification of ZnO, in particular ZnO that has been deposited by atomic layer deposition (ALD), a technique that will be discussed in 4.2. ZnO is of particular interest due to its intrinsically low WF (typically ~ 4 eV)[6] since most organic optoelectronic devices such as organic light-emitting diodes (OLEDs) and

organic photovoltaics (OPVs) require one low WF electrode for electron injection (for instance in OLEDs) or electron collection (in the case of OPVs).[11] Recent technological examples using ZnO have included inverted solar cells, light-emitting diodes, and transistors.[10, 12-13] The ability to tune the WF of ZnO is desirable in order to enhance device performance by minimizing injection/collection barriers. While it is possible to use a variety of anchoring groups on ZnO such as thiols,[14] carboxylic acids,[15] or alkoxysilanes,[16] more recently phosphonic acids have been examined for surface modification of planar ZnO surfaces.[17-21] The goal of this chapter is to take the knowledge acquired from the modification of ITO with phosphonic acids (Chapter 3) and perform a similar analysis using dipolar phosphonic acids on the surface of ZnO. Surfaces will then be characterized to examine the impact these modifiers have on the WF of ZnO, and how that directly compares with the same modifiers on the surface of ITO. In the case of ITO, phosphonic acids that increase the WF were mainly examined (Chapter 3), however, with ZnO it is desirable for some potential applications to lower the WF of the substrate, and thus molecules with molecular dipoles anticipated to decrease the WF were also chosen.

4.1.1 Defects in Zinc Oxide

The control of defects and associated charge carriers is of great importance in applications that take advantage of the intrinsic properties of ZnO. The nominal chemical formula for ZnO is deceptively simplistic as the underlying defects that lead to many of the electrical properties of ZnO have been studied for nearly 50 years.[22] The native structure of ZnO consists of a hexagonal close packed lattice of O^{-2} wherein Zn^{+2} ions occupy half the tetrahedral sites and all octahedral sites are empty. The würtzite ZnO

lattice is shown in Figure 4.1 and it should be noted that ZnO can accommodate intrinsic defects and extrinsic dopants.[22-23]

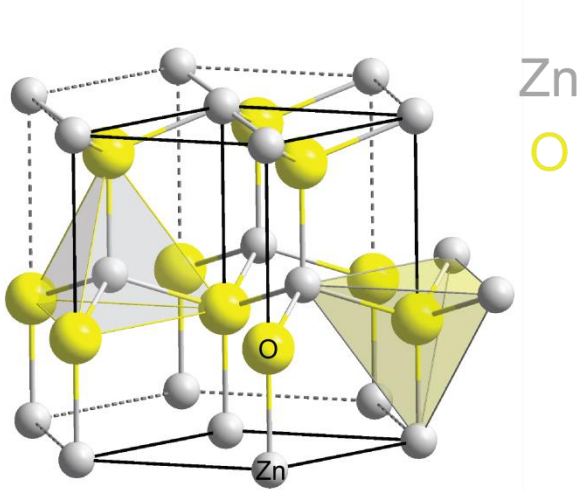

Figure 4.1 Position of Zn and O atoms in the ZnO würtzite crystal lattice. Figure has been adapted.[24]

As previously noted, there is the possibility of both intrinsic and extrinsic defects, which can also occur at the surface as a result the termination of the lattice structure. There are four main types of intrinsic defects that can occur within ZnO, which are zinc vacancies (V_{Zn}), zinc interstitials (Zn_i), oxygen vacancies (V_O), and oxygen interstitials (O_i). The main defects that are typically found within ZnO are zinc interstitials and oxygen vacancies.[22] Figure 4.2 schematically illustrates the energy levels for these intrinsic defect states that occur within the band gap of ZnO where the donor defects are Zn_i and V_O, while the acceptor defects are V_{Zn}. It should be noted that in this notation (developed by Kröger[25] in the early 1970s) X denotes a neutral charge, $'$ and $''$ denote one and two, respectively, positive charges, while $\cdot$ and $\cdot\cdot$ denote one or two negative

charges, respectively. Reactions by which these defects form have been discussed in the literature.[26]

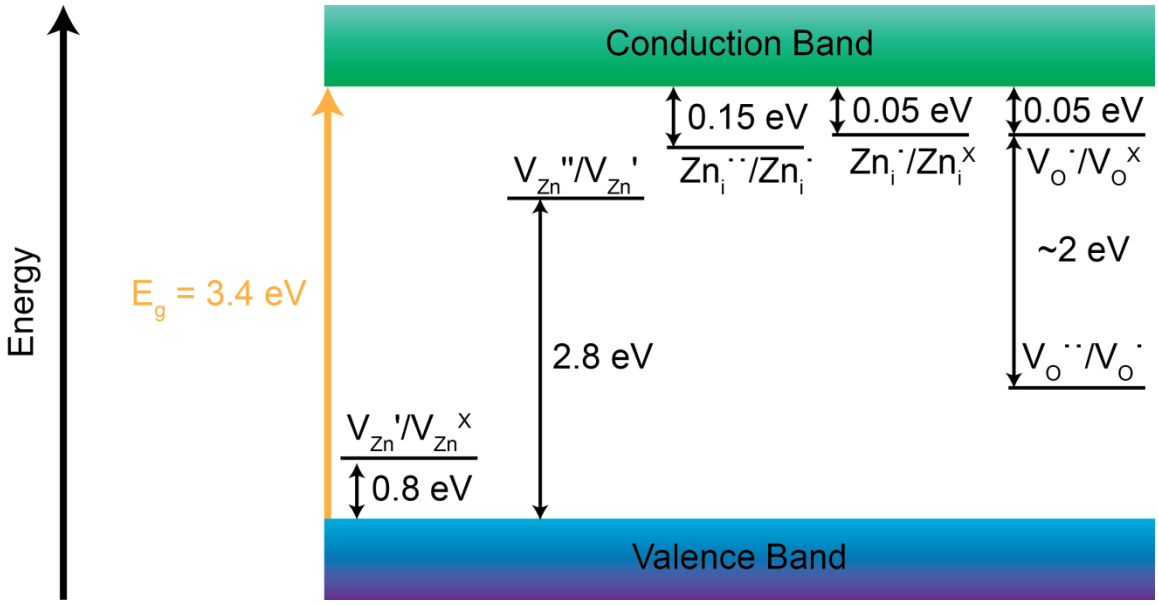

Figure 4.2 Schematic band diagram for energy levels of intrinsic defects present within ZnO. The Zn_i and V_O states are donors and the V_{Zn} states are acceptors. Figure adapted from those found in the literature.[22, 25]

4.2 Atomic Layer Deposition

Atomic layer deposition is a more recent variation on the classical chemical vapor deposition (CVD) where one or more gaseous species react on a heated solid surface resulting in the deposition of a thin film of material on the substrate to be coated.[27-29] The surface has to be sufficiently hot for reactions to proceed rapidly and, thus, achieve acceptable rates of deposition. Ideally the gases used do not react until they impinge on the surface forming a solid film through a heterogeneous reaction (homogeneous reactions can form particulates on the surface and become embedded in the growing film).[30] Atomic layer deposition on the other hand, divides the series of

reactants into separate steps, thereby mitigating the possibility of precursor gases reacting with one another rather than the surface. A typical cycle involves a substrate being exposed to the first reactant gas where a monolayer of material adsorbs to the substrate and excess vapor is removed by vacuum or purging with inert gas. A second reactant is then introduced into the chamber, which reacts with the monolayer of the first material that had just been adsorbed on the substrate. This forms a complete ALD cycle leaving one layer (though typically less than a complete monolayer)[30] of the material to be deposited on the surface. After removal of excess reactant gas from the chamber the cycle is repeated again and again until the desired thickness of material is achieved. The generalized ALD cycle for ZnO is illustrated in Figure 4.3.

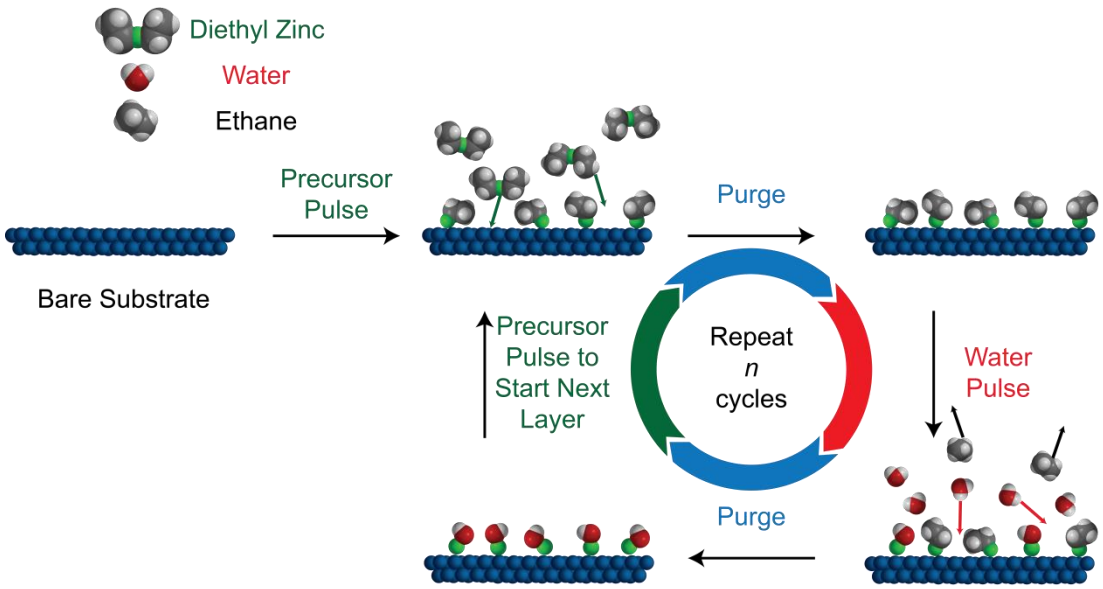

Figure 4.3 Schematic representation of a complete ALD cycle for the deposition of ZnO starting from diethyl zinc and water with ethane gas as a side product. A bare substrate is introduced into the ALD chamber, a precursor gas (diethyl zinc) is subsequently introduced, the chamber is purged. Water is then introduced reacting with the diethyl zinc, the chamber is purged again leaving behind solid zinc oxide. The cycle is then repeated *n* times until the desired thickness is achieved.

ALD has several advantages over more traditional CVD methods. The first of which is that lower temperatures can be used when conducting the deposition, which enables a wider variety of materials to be used (e.g. organics). This decreased temperature comes from the separation of reactant gases, allowing for the selection of more reactive precursor gases to be chosen.[30] The films are also typically defect free as well, since no homogeneous reaction can occur as the gaseous reactants are separated from one another. ALD also affords highly conformal and uniform films since the growth of the film depends on the formation of monolayers on the surface, whereas in the case of CVD the growth is determined by the arrival rate of the reactant gases. Furthermore, it is possible to have highly complex structures covered by ALD as the length of time for any portion of the cycle can be varied.[30] It should be noted, however, that the rate of deposition may be slower than that of a more traditional CVD process as there are multiple precursor pulse/purge/water pulse/purge steps within any one cycle.

4.2.1 Atomic Layer Deposition of Zinc Oxide

As shown in Figure 4.3, the metal-organic precursor for ZnO is diethylzinc, which is used in conjunction with another reactant such as water in order to deposit conformal pinhole-free films on surfaces. The binary reaction for the deposition of ZnO can be written as shown in Equation 4.1, which can be separated into two ALD half-reactions as shown in Equation 3.2 and Equation 4.3.[31] In this case, [S] denotes the substrate, and the * in the equations denotes which portion of the reaction is serving as the active site for nucleation and growth of the ZnO. Typically, deposition of ALD by ZnO takes place in the range of ~ 100 °C to 250 °C.[30, 32]

$$Zn(CH_2CH_3)_2 + H_2O \rightarrow ZnO + 2C_2H_6 \qquad \text{Equation 4.1}$$

$$[S]{:}OH^* + Zn(CH_2CH_3)_2 \rightarrow [S]{:}OZn(CH_2CH_3)^* + C_2H_6 \quad \text{Equation 4.2}$$

$$[S]{:}OZn(CH_2CH_3)_2{}^* + H_2O \rightarrow [S]{:}OZnOH^* + C_2H_6 \quad \text{Equation 4.3}$$

4.3 Literature Precedent Regarding Phosphonic Acid Modification of ZnO

There is not an abundance of literature regarding the use of phosphonic acids for modifying the surface of ZnO, but there are some examples where such modifications were conducted and the substrates subsequently analyzed. Table 4.1 provides a summary of the various phosphonic acids that have been used to modify the surface of ZnO along with the characterization methods used to prove the modification was successful (and with the WF values if measured). As can be seen there have been many different types of ZnO modified, with only several reports specifically using ALD ZnO as the substrate.[21, 33] Furthermore, there is a surprising lack of analysis regarding the WF of the surface after modification with the main results coming from DFT calculations[34] and UPS results conducted by collaborators at the University of Arizona.[33, 35] Other studies have focused on the modification of ZnO to examine competition between phosphonic acids and other surface modifiers (e.g. thiols and carboxylic acids),[19-20, 36-37] or for use in device architectures such as OPVs.[38-40] It should also be noted that several of the studies have mentioned the ability of surface modifiers such as phosphonic acids or carboxylic acids to etch the surface of ZnO,[21] forming zinc phosphonate salts.[41] This problem of surface etching is one that will be discussed further in 4.5.2.

Table 4.1 Summary of phosphonic acids that have been used to modify the surface of ZnO either experimentally or through theoretical calculations as noted. Values for WF are noted when available. Abbreviations for techniques not previously used in this thesis are as follows: transmission electron microscopy (TEM), Fourier transform infrared spectroscopy (FTIR), diffuse reflectance infrared Fourier transform spectroscopy (DRIFT), phosphorus magic angle spinning nuclear magnetic resonance spectroscopy (^{31}P MAS NMR), dynamic light scattering (DLS), thermogravimetric analysis (TGA), quartz crystal microbalance (QCM), scanning electron microscopy (SEM).

Phosphonic Acid	ZnO Substrate	Characterization	Reference
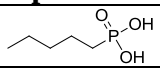	polycrystalline zinc	XPS contact angle scanning KP	17
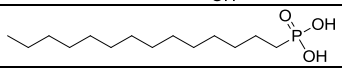			
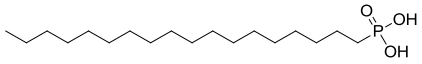	ZnO nanocrystals	TEM FTIR	41
	ZnO nanoparticles	DRIFT ^{31}P MAS NMR DLS TGA	42
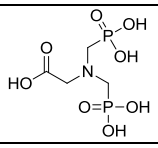	Co/ZnO core/shell particles	FTIR TGA	36
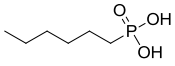	Polycrystalline ZnO thin film (0001)	XPS contact angle QCM comparison with thiol	19
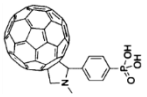	ZnO nanoparticles on ITO	AFM SEM	38
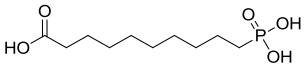	ZnO wafers (000$\bar{1}$)	contact angle AFM FTIR XPS	20
	ZnO nanowires		
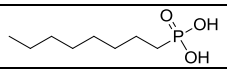	RF magnetron sputter deposited ZnO	XPS IRRAS AFM contact angle	18
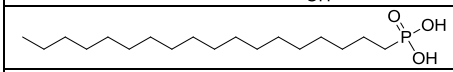			
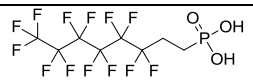			
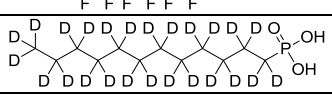			
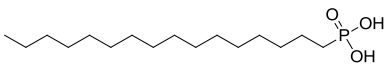	single-crystal ZnO (10$\bar{1}$0)	AFM FTIR XPS comparison with	37

Phosphonic Acid	ZnO Substrate	Characterization	Reference
		thiol, carboxylic acid, and amine	
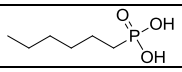	Al-Doped ZnO nanoparticles on ITO	conductive AFM contact angle	39-40
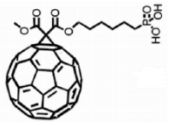			
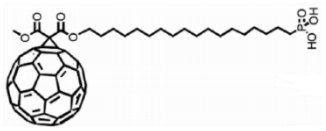			
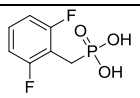	polar ZnO (0002) theoretical slab	DFT calculations	34
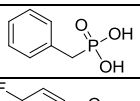			
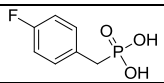			
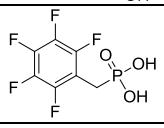			
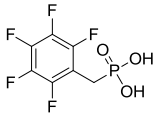	ALD ZnO	XPS UPS (WF ~ 4.4 – 4.6 eV)	21
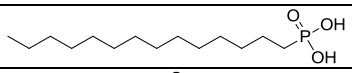	ZnO nanorods	XPS FTIR SEM DFT calculations	43
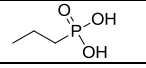			
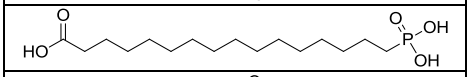			43-44
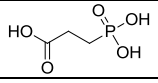			
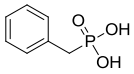	ALD ZnO	XPS UPS (WF = 3.6 eV)	33
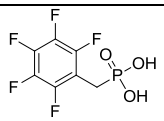		XPS UPS (WF = 4.0 eV)	
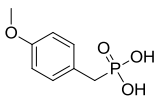		XPS UPS (WF = 4.1 eV)	
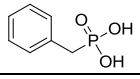	gallium-doped ZnO	XPS DFT	35

Phosphonic Acid	ZnO Substrate	Characterization	Reference
		UPS (WF = 3.91 eV)	
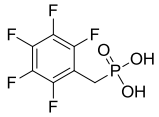		XPS DFT UPS (WF = 4.41 eV)	
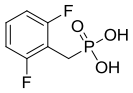		XPS DFT UPS (WF = 3.70 eV)	
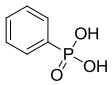		XPS DFT UPS (WF = 3.71 eV)	
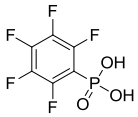		XPS DFT UPS (WF = 4.86 eV)	

4.4 Selection of Phosphonic Acids for Modification of ALD ZnO

Phosphonic acids similar to those used in Chapter 3 were chosen for study on the surface of ZnO and ITO. Figure 4.4 summarizes the structures of the chosen molecules and associated abbreviations. The molecule 2,6-F2BPA was initially chosen as an example in which the molecular dipole is opposite that of phosphonic acids designed to increase the WF. In Chapter 3 this was the main compound that led to a slight decrease in the WF of ITO. 2,6-CF3BPA was also chosen as a stronger analogue to 2,6-F2BPA and to determine if these two molecules previously examined on ITO behave in a similar manner on ZnO. DABPA was chosen as it has π-conjugated donor and π-acceptor moieties which should lead to an even larger intrinsic dipole moment with the negative end pointed toward the surface. Other phosphonic acids were chosen based on intrinsic dipoles that should either increase or decrease the WF of the substrate. In all cases (with the exception of MeOBPA) there is also the presence of a heteroatom such as F or N

which allows for the modification of the surface to be more readily observed in spectral data acquired by XPS analysis.

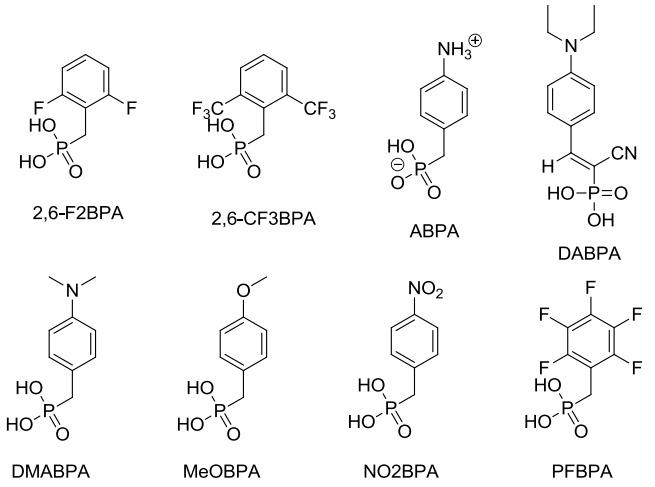

Figure 4.4 Phosphonic acids chosen for the modification of ZnO and ITO. The focus was on the use of phosphonic acids containing molecular dipoles that would be anticipated to create a decrease in the WF of the surface (2,6-F2BPA, 2,6-CF3BPA, ABPA, DABPA, DMABPA, MeOBPA) along with molecules that would also increase the WF as a control (NO2BPA and PFBPA).

4.5 Comparison of Phosphonic Acid Modification Conditions for ZnO

4.5.1 Comparison of Immersion Conditions

4.5.1.1 XPS Analysis – Comparison of Immersion Protocols

From a practical standpoint, an analysis of the literature references shown in Table 4.1 for the modification of ZnO indicate that there are numerous methods for surface modification that can be used. Thus, an initial analysis to determine whether or not the choice in modification technique has an impact on the ability to form a high quality monolayer of phosphonic acids on ZnO needed to be examined. Five different modification techniques were chosen, which are summarized in Table 4.2. These

techniques were drawn from the literature technique used to modify the surface of RF-magnetron sputter deposited ZnO (method 1),[18] a technique commonly used for the preparation of phosphonic acid monolayers for use in device studies (method 2),[45] the modification technique that is commonly used in the Marder group for the modification of metal oxides with phosphonic acids (method 3),[46] and recent results conducted using high temperature modification of ITO with phosphonic acids (methods 4 and 5).[47-48]

Table 4.2 Summary of modification methods used to treat ALD ZnO. The triethylamine (TEA) wash after modification is commonly used to remove any unbound/physisorbed phosphonic acid molecules from the surface of the substrate

Modification Method	Summary of Method
1	Tethering by aggregation (1 mM, ethanol), bake at 140 °C overnight, TEA wash
2	2 hour immersion (1 mM, 2:1 chloroform:ethanol), bake at 120 °C 30 min, no subsequent washing
3	Overnight immersion (10 mM, ethanol) bake at 140 °C overnight, TEA wash
4	Oxygen plasma clean, immersion 5 h at 80 °C (10 mM, ethanol), TEA wash
5	No oxygen plasma cleaning, immersion 5 h at 80 °C (10 mM, ethanol) TEA wash

In order to conduct this comparison of techniques, the fluorinated phosphonic acids were chosen for analysis (2,6-F2BPA and 2,6-CF3BPA) so that the F 1s peak could be used for analysis of monolayer quality. A comparison of monolayer quality based on the F 1s/C 1s ratios as well as F 1s/Zn 3p is provided in Figure 4.5. Based on results with ITO, it was found that a full monolayer with either of these surface modifiers was not formed. It should therefore not be unexpected that a similar situation would also occur in the case of ZnO, and the experimental F/C ratios far removed from the ideal F/C ratio corroborate this supposition, and indeed, the monolayer "quality" on ZnO is low. It

should be noted, however, that etching was observed for methods 4 and 5 using both phosphonic acid modifiers. The ZnO was almost completely removed in both cases and the underlying glass substrate exposed based on XPS analysis that revealed a large decrease in Zn peaks and the presence of the Na 1s peak (Figure 4.6). Interestingly, no single modification method worked best for both phosphonic acid materials. In the case of 2,6-F2BPA, tethering by aggregation afforded the highest overall quality of monolayer, while in the case of 2,6-CF3BPA both modification methods 2 and 3 afforded similar results based on the error bar of the analysis. Analysis of F/Zn ratios to obtain relative coverage also indicated that this was similar regardless of the modification method chosen. It should be noted that in contrast to ITO, absolute coverage values are not used for comparison as the experimental surface and theoretically modelled surface[34, 49] differ from one another in terms of roughness. While the ITO surface used was extremely smooth (as shown in the AFM comparison in Figure 4.7), the surface of ALD ZnO was found to be granular in nature with a calculated surface roughness of 2-3 nm over a 5 μm × 5 μm area. This granular nature means that the overall surface area accessible to the phosphonic acids is higher than would be expected based on the modelled surface. Thus, a comparison of experimental F/Zn ratios always afforded values higher than the theoretical F/Zn ratio (even after appropriate corrections). Thus, only relative atomic ratios were used for comparison purposes.

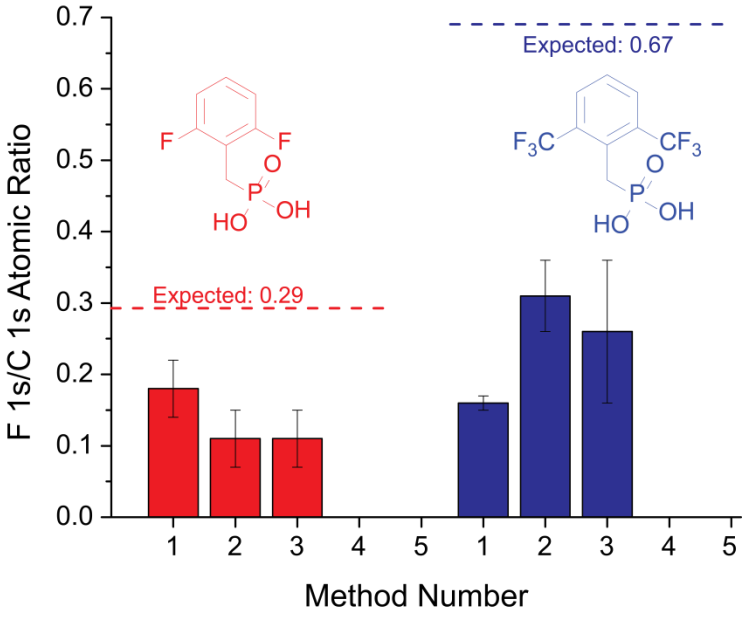

Figure 4.5 Comparison of F 1s/C 1s atomic ratios for the modification methods outlined in Table 4.2 for 2,6-F2BPA and 2,6-CF3BPA. Methods 4 and 5 do not have atomic ratios given as the method etched away ZnO from the underlying substrate leaving glass behind. The expected ratios originate from the F/C ratio found in the individual molecules.

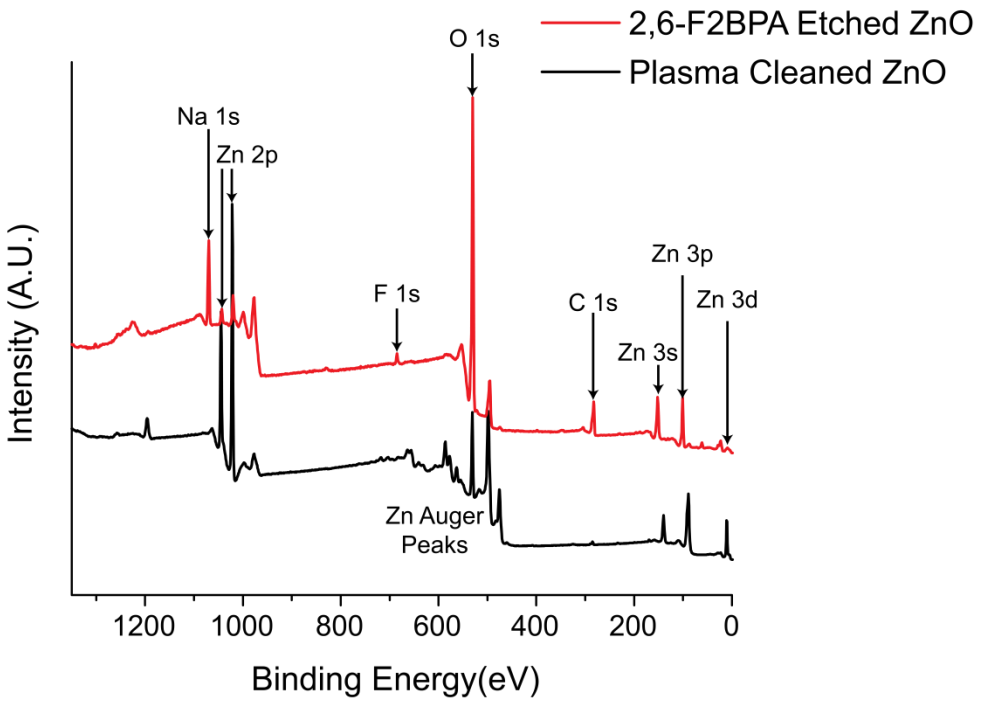

Figure 4.6 XPS survey spectra for freshly plasma cleaned ZnO and the surface after 2,6-F2BPA had etched away the majority of ZnO. Data for this comparison was acquired using modification technique 4 and while there are small peaks left for Zn (and loss of Zn Auger peaks) the vast majority has been etched away leaving behind a small amount of phosphonic acid (evidenced by F 1s peak) and exposing the underlying glass substrate (Na 1s peak). Spectra have been normalized and offset for clarity.

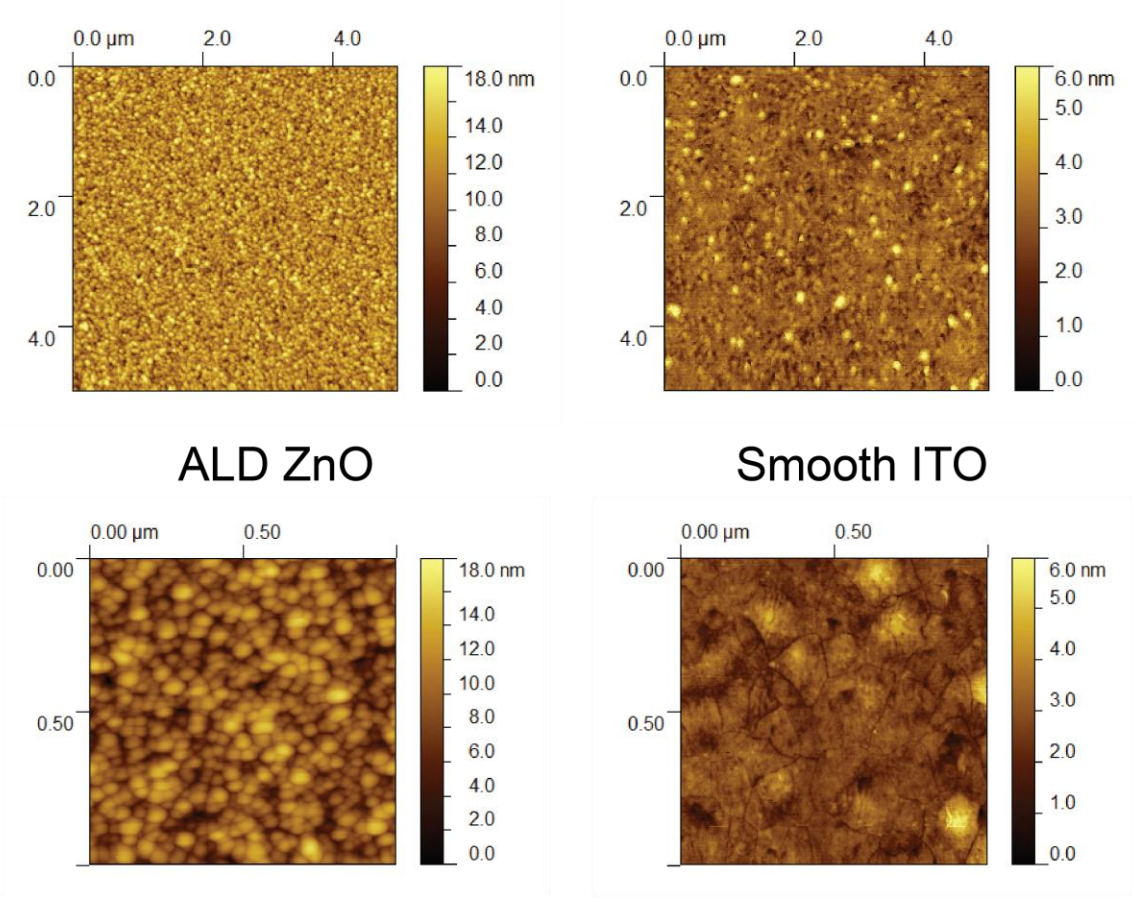

RMS Roughness Values

ALD ZnO (5 µm x 5 µm) 2.2 nm	Smooth ITO (5 µm x 5 µm) 0.6 nm
ALD ZnO (1 µm x 1 µm) 2.3 nm	Smooth ITO (1 µm x 1 µm) 0.6 nm

Figure 4.7 Comparison of tapping-mode AFM images of ALD ZnO (left) and smooth ITO (right). In both cases 5 µm × 5 µm images are shown at the top and 1 µm × 1 µm are shown at the bottom with values for RMS roughness also provided. Note the differences in the height scales between the two substrates, which was necessary so as to not obscure all of the topographic features present on the ITO samples.

4.5.1.2 Kelvin Probe Analysis

4.5.1.2.1 Kelvin Probe - Comparison of Pre- and Post-Modification Conditions

As there was not a clear trend among the two phosphonic acids examined in 4.5.1.1 an examination of whether or not the pre- or post-modification treatments had an impact on altering the WF of the substrate needed to be conducted. WF was measured by KP rather than UPS as there was a large sample space that needed to be examined, and KP is more suited for such a high-throughput study. A summary of the change in WF relative to the bare ALD ZnO substrate is shown in Figure 4.8. The results indicate that neither plasma pre-treatment nor TEA post-treatment washing has a significant impact on the WF change (< 0.1 eV). It should be noted that over the course of the various experiments conducted in order to acquire data for this chapter, DABPA proved to be an extremely variable surface modifier in terms of impact on the WF having either a significant decrease in WF (as seen in Figure 4.8) or affording only a slight decrease from bare ZnO (as seen when discussing the data in 4.6). Overall, this analysis indicates that plasma cleaning of ZnO is not detrimental to the resulting WF change and that the substrate can withstand a base rinse using TEA in order to remove any unbound phosphonic acid molecules from the surface after treatment. When conducting this study, both 2,6-F2BPA and ABPA etched the surface of ZnO producing a substrate similar to what was seen in Figure 4.6, i.e. mainly glass and no longer conductive.

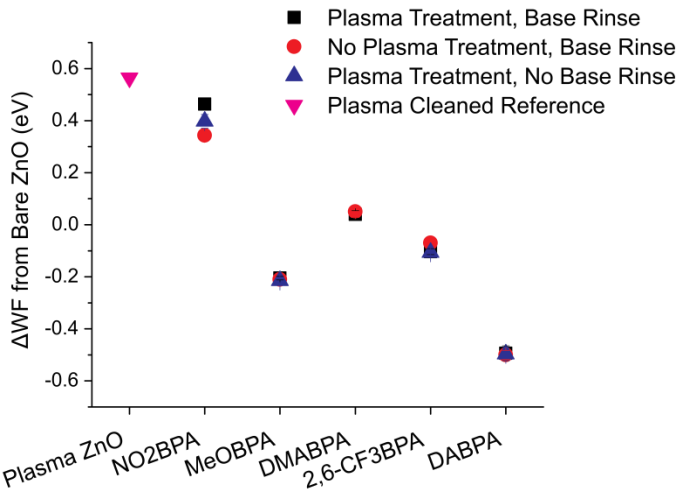

Figure 4.8 Comparison of KP data showing WF changes relative to a bare ZnO substrate after modification. In this instance, method 3 from Table 4.2 was used for the modification meaning that the substrates were soaked in 10 mM phosphonic acid solutions overnight (either with or without a plasma pre-treatment) and then subsequently either washed with TEA or not post-modification. WF values are the average of at least 5 spots on each substrate. An HOPG substrate was referenced and measured multiple times over the course of data collection to ensure instrumental consistency over the time scale of the experiment.

4.5.1.2.2 Kelvin Probe - Comparison of Concentration and Modification Time

As both of the previous sets of experiments shown in 4.5.1.1 and 4.5.1.2.1 revealed instances where the phosphonic acid modifier etched away the ZnO from the surface, it was important to examine the role that modification time and concentration of phosphonic acid solution play in determining when phosphonic acids will etch ZnO as well as how this impacts the overall WF change. Drawing on the information previously gleaned, concentrations of 1 mM and 10 mM phosphonic acid solutions were chosen to be examined at intervals of 24 and 48 hours (essentially choosing some of the extreme cases, low/high concentration and short/long modification time, from Table 4.2 and the protocol used in Chapter 3) to determine what conditions would allow for maximal WF

change without substantial etching. WF was again monitored by KP and the summary of the results are provided in Figure 4.9. The following phosphonic acid modifiers were examined, 2,6-F2BPA, MeOBPA, and DABPA. Based on these results, it appears that high concentration and extended modification time lead to etched surfaces in the case of 2,6-F2BPA, as WF measurements could not be obtained for surfaces treated with 10 mM solutions (regardless of immersion time). There is also likely etching present in the case of MeOBPA and DABPA, evidenced by the large variation in the duplicate high-concentration, long modification time samples. Also note that the decrease in the WF for both DABPA and MeOBPA is less than what was observed in Figure 4.8, and is representative of the variability observed for WF lowering modifiers on ZnO. Etching analysis will be discussed further in 4.5.2.

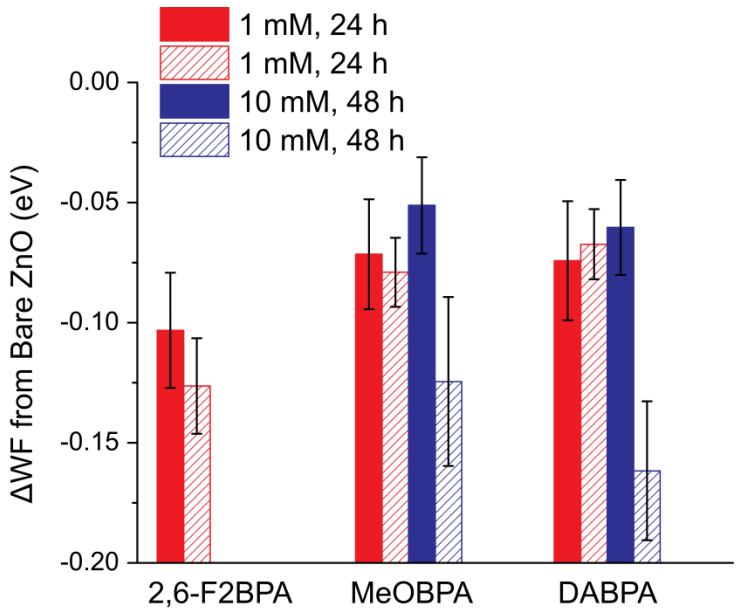

Figure 4.9 Comparison of three phosphonic acid modifiers examined under low/high concentration (1/10 mM) and short/long modification times (24/48 h). In the case of the 10 mM, 48 h modification for 2,6-F2BPA complete etching of ZnO was observed. Duplicate samples were analyzed to demonstrate the variability observed in WF changes, particularly at higher concentrations/longer modification times.

4.5.1.3 IRRAS Analysis of PFBPA and DABPA on ALD ZnO

IRRAS analysis was also conducted using DABPA and PFBPA. These two molecules were chosen because PFBPA has been previously examined on the surface of ITO by IRRAS[48] and it was anticipated that the cyano functionality would be easy to track on the ZnO modified surface. Unfortunately, the cyano vibrational modes observed in the powder occur at approximately 2200 cm^{-1}, which overlaps with carbon dioxide and, even after extensive purging, the signal from the modifier was too weak and still obscured. Thus, the phosphonic acid fingerprint region was examined and a comparison between the transmission IR of the PFBPA and DABPA powder with the IRRAS of the phosphonic acids on ZnO are shown in Figure 4.10. The transmission IR of PFBPA and associated IRRAS spectra are consistent with one another as well as what was observed for octadecylphosphonic acid.[18] Thus, it appears that the molecule binds in a tridentate manner (there is no peak corresponding to that assigned to P=O for the powder). It should be pointed out that other binding modes cannot be completely excluded due to the broad nature of the feature at ~1015 cm^{-1} as small features from P-O(H) stretches may be obscured by the intensity of this peak. The IRRAS of DABPA, however, indicates that this modifier binds in a mixture of bidentate and tridentate modes as there is still a peak present for P=O.

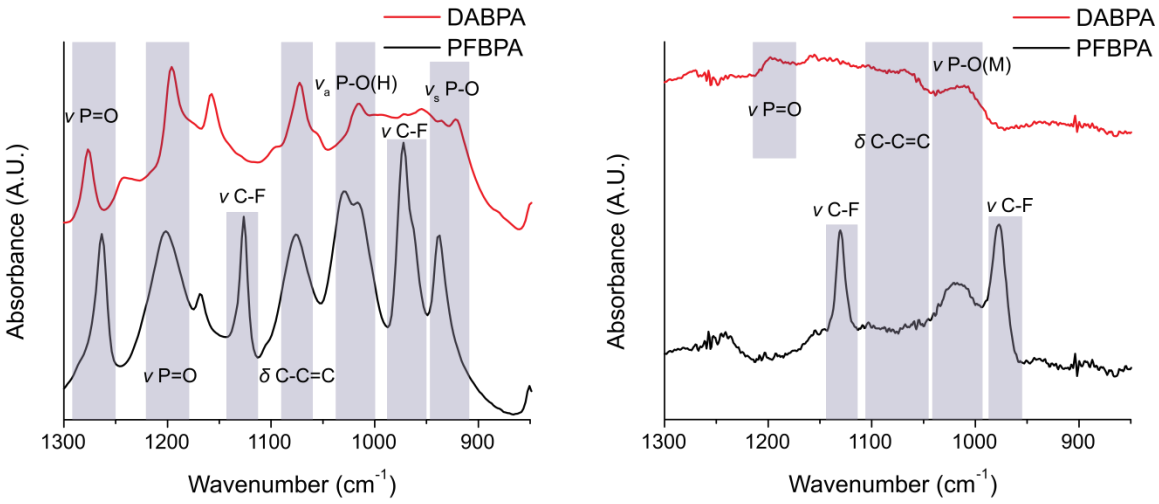

Figure 4.10 Comparison of transmission IR of PFBPA and DABPA powders (left) with the IRRAS data collected for ALD ZnO deposited on a gold surface for enhanced reflectivity and modified with either PFBPA or DABPA (right). Spectral features are highlighted and labelled in both cases.

4.5.2 Examination of ZnO Etching by Phosphonic Acids

4.5.2.1 Tracking ZnO Etching by AFM Analysis

Previous analysis of phosphonic acids on RF-Magnetron Deposited ZnO with alkyl phosphonic acids did not indicate issues with etching.[18] In that case, however, 300 nm of ZnO was used as the substrate, whereas in this study only 30 nm of ALD ZnO was used as that would more closely mimic a thickness used within a device. Thus, it appears that, at this thickness, etching, which may not have been readily apparent using alkylphosphonic acids and a thicker layer of ZnO, appeared to be a problematic issue based on the previous studies discussed in 4.5.1. Thus, in order to better observe the extent of etching that was being caused by each phosphonic acid, four of the surface modifiers from Figure 4.4 (PFBPA, DABPA, MeOBPA, and 2,6-F2BPA) along with 3,4,5-F3BPA and 4-CF3BPA from Chapter 3 were examined. The additional phosphonic

acids from Chapter 3 were chosen as they afforded the largest increase in WF on ITO and based on the presumption that the inductive electron withdrawing effects of the fluorinated substituents lead to more acidic phosphonic acids (which will be examined in 4.5.2.2). The surface of ZnO was then modified for a period of 24 hours using solution concentrations of 10 mM. If surfaces saw significant etching, the experiment was repeated using a lower concentration of 1 mM. The results from the AFM analysis of these surfaces are provided in Figure 4.11 and Figure 4.12. The summary of RMS roughness values (averaged over at least 3 spots on each surface and measured at 1 μm × 1 μm and 5 μm × 5 μm spot sizes) are provided in Table 4.3.

The AFM data indicates that modifiers such as DABPA, 2,6-F2BPA, and 3,4,5-F3BPA at 10 mM concentrations significantly etch the ZnO, leaving behind surfaces that are more reminiscent of the underlying glass than the granular structure of ZnO. Neither DABPA nor 3,4,5-F3BPA etch as severely as 2,6-F2BPA as evidenced by roughness values in Table 4.3 The other surface modifiers at 10 mM concentrations do not show signs of etching that can be readily detected by AFM and closely match that of the bare ZnO surface. When lower concentrations of 2,6-F2BPA and 3,4,5-F3BPA are used to modify the surface of ZnO, the etching problem appears to be mitigated affording ZnO surfaces that resemble those of an untreated substrate, which is consistent with what has been observed when conducting KP measurements and fits with the measured roughness values as well. This observation of etching may explain some of the large variability that was observed for changes in WF by other measurements (such as KP and UPS) as depending on the modification conditions used, drastic changes to the underlying ZnO may be taking place which either enhance or diminish the ability of the phosphonic acid

molecular dipole to tune the WF of the ZnO substrate. It is also very likely that such morphological changes lead to changes in how the phosphonic acid binds to the substrate. This, in turn, can lead to changes in the orientation of the molecular dipole at the surface of the substrate and again lead to variability in WF changes. In an effort to correlate etching ability with the acidity of the phosphonic acid, pK_a measurements were conducted on a series of phosphonic acid molecules and the results are discussed in the next section.

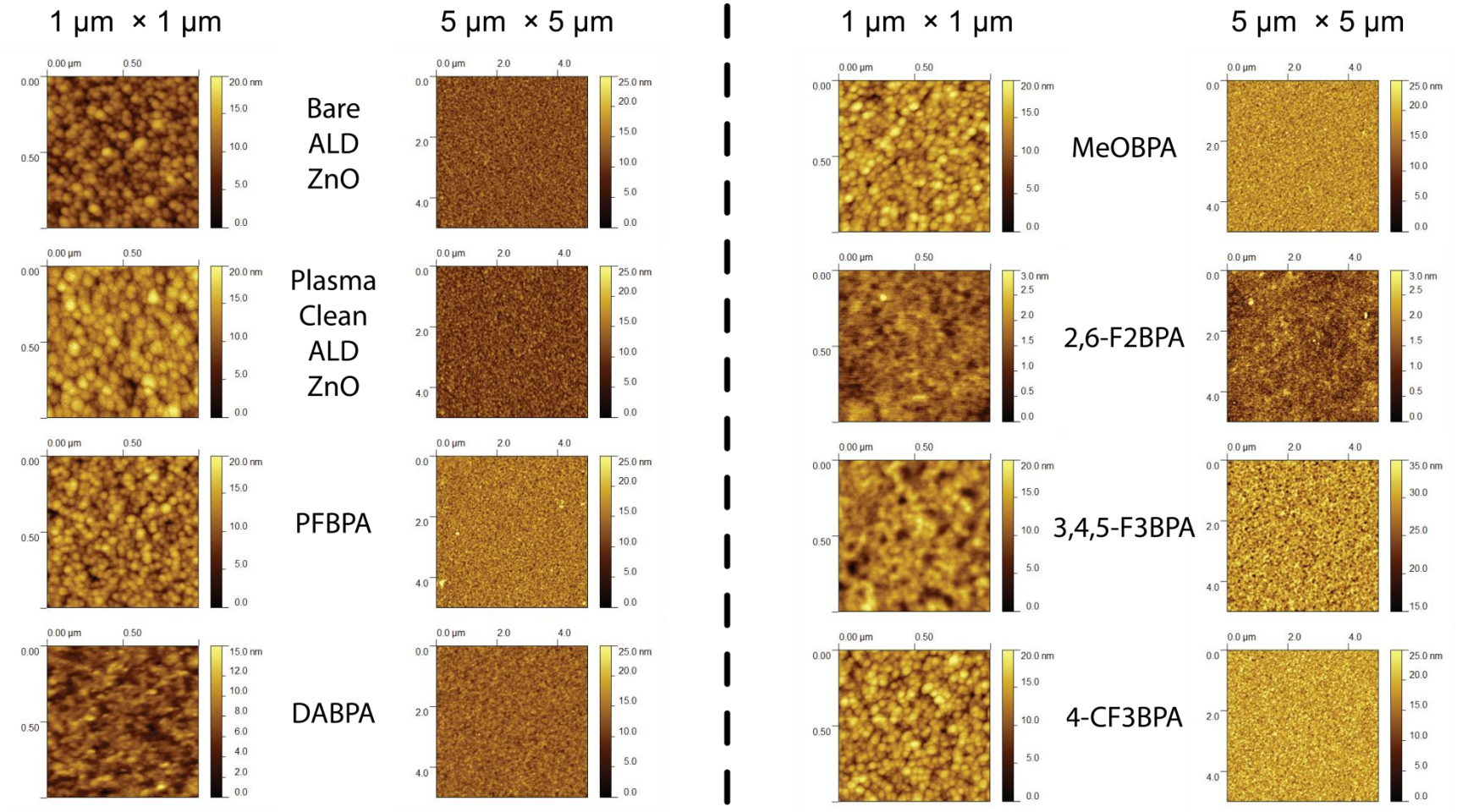

Figure 4.11 Comparison of AFM images at spot sizes of 1 μm × 1 μm and 5 μm × 5 μm for bare, plasma cleaned, and 10 mM phosphonic acid modified ALD ZnO. When possible, vertical scales were attempted to be maintained constant within a given image size (1 μm or 5 μm).

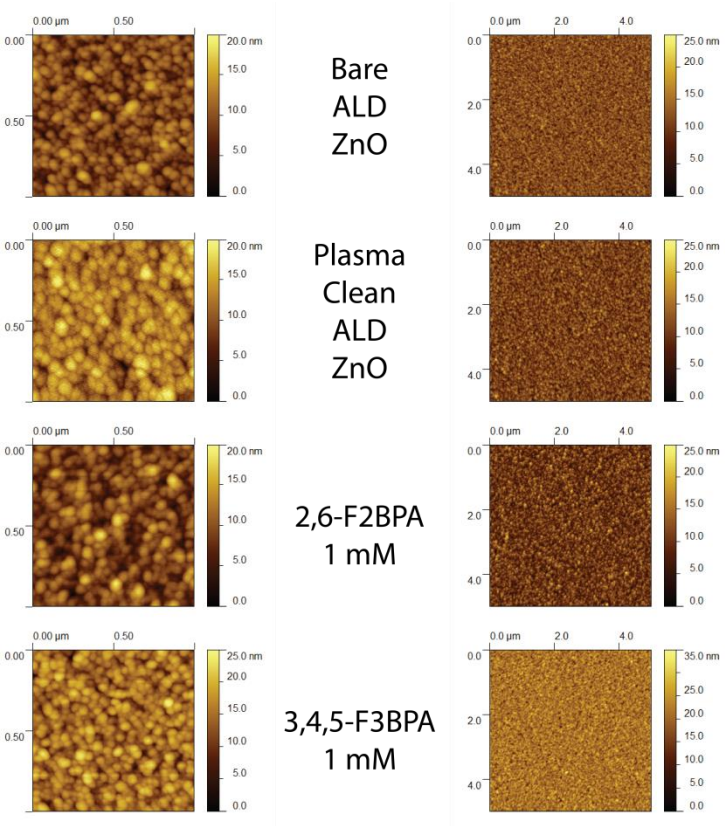

Figure 4.12 Comparison of AFM images of spot sizes 1 μm × 1 μm (left) and 5 μm × 5 μm (right) for bare, plasma cleaned, and 1 mM phosphonic acid modified ALD ZnO. When possible, vertical scales were attempted to be maintained constant within a given image size (1 μm or 5 μm) and with those images shown in Figure 4.11.[32]

Table 4.3 Comparison of RMS roughness values for ZnO modified with the phosphonic acids shown. Concentrations of 1 mM and/or 10 mM are shown depending on the extent of etching observed. In some cases, the RMS roughness value showed minimal changes, while the topography had clearly been altered from that of the bare substrate. Instances where the ZnO experienced severe etching have extremely low roughness values. Standard deviation originates from averaging the RMS values over a t least 3 spots.

ZnO Surface Treatment	**RMS Roughness 1 μm × 1 μm (nm)**	**RMS Roughness 5 μm × 5 μm (nm)**	**RMS Roughness 1 μm × 1 μm (nm)**	**RMS Roughness 5 μm × 5 μm (nm)**
Bare	2.30 ± 0.03	2.24 ± 0.06	-	
Plasma Cleaned	2.44 ± 0.13	2.54 ± 0.21		
Phosphonic Acid Modifier	**1 mM**		**10 mM**	
PFBPA	-	-	2.57 ± 0.13	2.61 ± 0.04
DABPA	-	-	1.86 ± 0.13	1.94 ± 0.07
MeOBPA	-	-	2.47 ± 0.08	2.56 ± 0.13
2,6-F2BPA	2.68 ± 0.15	2.62 ± 0.06	0.34 ± 0.02	0.43 ± 0.06
3,4,5-F3BPA	3.00 ±0.10	3.15 ± 0.02	2.63 ±0.19	2.73 ±0.04
4-CF3BPA	-	-	2.70 ± 0.14	2.77 ± 0.06

4.5.2.2 Correlation between ZnO Etching and Acidity of Phosphonic Acids (pK_a measurements)

In an attempt to correlate etching with the acidity of the phosphonic acid being used for modification, it was necessary to examine pK_a values (in the case of phosphonic acids pK_{a1} and pK_{a2}) for the phosphonic acids examined. There are some literature examples of pK_a measurements that have been conducted to measure the pK_a values of phenyl and benzyl phosphonic acids. The phenyl substituted phosphonic acid pK_a measurements are summarized in Table 4.4 for some electron-donating and electron-withdrawing substituents. Benzyl phosphonic acid pK_a values found in the literature are summarized in Table 4.5. Analysis of the literature indicated that unlike in benzoic acids (where substituent and position have a larger impact on acidity),[50] the pK_a values found for phenyl and benzyl phosphonic acids substitution by various substituents has little

impact on the overall acidity of the molecule when compared within the same solvent. Furthermore, the position of the substitution has even less of an impact on the pK_a values.

Table 4.4 Summary of substituted phenyl phosphonic acid pK_a values found in the literature. Values were determined either in pure water or in a mixture of 50:50 ethanol:water (unless otherwise noted). Various references provided[51-53] have more compounds reported than those provided in this table.

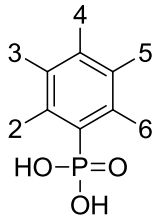

Position, Substituent, and Reference	pK_{a1} ($ArPO_3H_2$)		pK_{a2} ($ArPO_3H^-$)	
	In H_2O	In 50:50 ethanol:H_2O	In H_2O	In 50:50 ethanol:H_2O
2,3,4,5,6-H[51-53]	1.83 1.80	3.15	7.07 7.50	8.26
2-F[52]	1.64	2.84	6.80	7.99
3-F[54]	1.53	-	7.16	-
2-Cl[52]	1.63	2.94	6.98	8.21
3-Cl[51]	1.55	2.83	6.65	7.94
4-Cl[51]	1.66	2.93	6.75	7.99
2-Br[52]	1.64	2.91	7.00	8.22
3-Br[51]	1.54	2.85	6.69	7.96
4-Br[51]	1.60	2.88	6.83	8.01
2-I[52]	1.74	3.06	7.06	8.40
2-CH_3O[54]	2.21	-	8.21	-
3-CH_3O[54]	1.74	-	7.42	-
4-CH_3O[54]	2.00	-	7.65	-
2-NO_2[54]	1.28	-	7.05	-
3-NO_2[54]	1.20	-	6.69	-
4-NO_2[54]	1.19	-	6.67	-
2,3,4,5,6-H[a 55]	-	4.53 ± 0.08	-	9.97 ± 0.06
3,4,5-F3PPA[a 55]	-	3.76 ± 0.07	-	9.16 ± 0.05

[a] Measurement performed in 75:25 ethanol:H_2O under inert atmosphere. Standard deviation originated from 3 measurements

Table 4.5 Summary of substituted benzyl phosphonic acid pK_a values found in the literature. Values were determined either in pure water or in methanol.

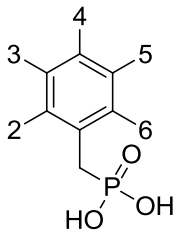

Position and Substituent	pK_{a1} ($ArCH_2PO_3H_2$)		pK_{a2} ($ArCH_2PO_3H^-$)	
	In H_2O	In Methanol	In H_2O	In Methanol
2,3,4,5,6-H	2.03[56] 2.69[57] 2.30[58]	6.20[59]	7.51[56] 7.62[57] 7.55[58]	13.9[59]
4-NO_2	-	5.60[59]	-	13.2[59]
4-CH_3O	-	6.27[59]	-	13.9[59]

To confirm that such minimal impact was also the case for the various phosphonic acids used to modify the surface of ZnO, pK_a measurements were conducted as previously reported,[55] using a solvent system of 75:25 ethanol:H_2O as that ratio best matched the pure ethanol used during the modification of ZnO. All measurements were conducted under nitrogen, and a summary of the pK_a values are provided in Table 4.6. As anticipated, there were not drastic changes in pK_a among the various phosphonic acid modifiers examined. There is also not a clear correlation between the acidity of the modifier and its ability to etch the ZnO substrate. For instance, the most acidic molecule examined (3,4,5-F3BPA, pK_{a1} = 4.17) significantly etched ZnO while PFBPA with a similar acidity (pK_{a1} = 4.37) did not show a tendency to etch ZnO. Further still, the slightly less acidic 2,6-F2BPA (pK_{a1} = 4.44) severely etched the ZnO surface under a variety of modification conditions. Thus, it is likely that another factor in addition to acidity plays a role in determining whether a phosphonic acid will etch ZnO, such as the

solubility of zinc-phosphonate complexes in ethanol. This may explain why there is not a direct correlation between etching and acidity.

Table 4.6 Summary of pK_a values experimentally determined for phosphonic acids used to modify the surface of ALD ZnO. All measurements were conducted in a solvent system of 75:25 ethanol:H_2O under inert atmosphere. All measurements were conducted at 20 °C using a standardized solution of NaOH at least 3 times with the average and standard deviation reported for both pK_{a1} and pK_{a2}.

Phosphonic Acid Modifier	pK_{a1}	pK_{a2}
PFBPA	4.37 ± 0.20	10.69 ± 0.19
4-CF3BPA	4.56 ± 0.11	10.55 ± 0.05
3,4,5-F3BPA	4.17 ± 0.09	10.15 ± 0.09
2,6-F2BPA	4.44 ± 0.05	10.66 ± 0.08

4.6 Comparison of Work Function Changes from Phosphonic Acid Modification on ZnO and ITO (Kelvin Probe and UPS)

Due to the reproducibility issues observed for obtaining WF values, and etching issues encountered with ZnO, a direct comparison between ALD ZnO and a metal oxide for which phosphonic acid modification is known to be highly reliable/reproducible was needed. To this end, a set of phosphonic acid molecules was chosen including PFBPA, MeOBPA, and DABPA (2,6-F2BPA was not used for this comparison due to its severe etching of ZnO, which was known to not occur for ITO, likely making a comparison impossible). This comparison also afforded the opportunity to examine how UPS data compared to KP data for samples of both ZnO and ITO. A summary of the experimentally determined WF values obtained by UPS can be found in Figure 4.13. Figure 4.13 also shows the same set of surfaces that were also measured by KP analysis

prior to UPS measurements and WF values were obtained by referencing to a freshly cleaved HOPG surface with a WF of 4.5 eV.

As can be seen from the UPS data, both the surface modification of ZnO and ITO tracked well with one another with ZnO WF values consistently lower than that of ITO due to its lower starting WF value. Interestingly, however, neither of the molecules anticipated to decrease the WF of the substrate did so in the case of ZnO or ITO with both seeing an increase in WF of ~ 0.2 eV from the starting WF value. An examination of the WF values obtained by KP analysis also shows that the same trend tracks for both ZnO and ITO. The absolute values of WF in the case of the bare and plasma cleaned substrates are quite different between KP analysis and UPS, however, likely owing to the fact that KP can be completed more readily upon cleaning than UPS. Thus, the WF is higher as less time has passed and fewer contaminants have been able to be deposited on the surface of the substrate, which tends to lower the WF. The values for the modified substrates, however, are quite similar between the two techniques typically within ~0.2 eV of one another, which is what has been observed in the literature when comparing the techniques.[60-61] Thus, it appears from this comparison that the modifiers such as MeOBPA and DABPA do not have a tendency to decrease the WF of the metal oxide substrate (relative to the bare ZnO surface) and inconsistencies in the data observed with ZnO likely originate with issues of etching of the ZnO substrate.

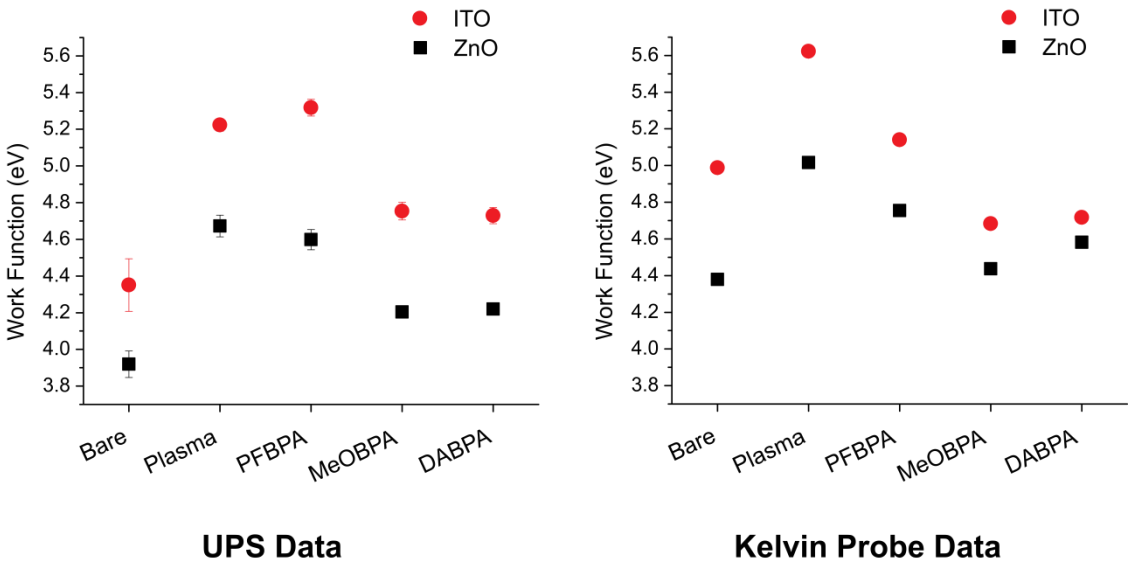

Figure 4.13 Comparison of WF values for phosphonic acid modified ITO and ZnO. All surfaces were modified using 10 mM solutions of phosphonic acid overnight, followed by a bake at 140 °C and a rinse with a solution of 5 % TEA in ethanol. Etching was not observed for these surfaces of ZnO. UPS data (left) is the average over 7 spots on each surface and KP data (right) originates from the average of 5 spots on each surface. The same surfaces were used during the measurements, first measuring with KP then by UPS.

4.7 Spin Coating of Phosphonic Acid Surface Modifiers on ZnO

Due to the ability to etch ZnO, an alternative method for the deposition of phosphonic acids on this metal oxide needed to be investigated. To that end, recent work with collaborators from the National Renewable Energy Laboratory (NREL) has indicated success with spin coating phosphonic acids (4-CF3BPA and 2,6-F2BPA) onto the surface of ZnO (in this case sol-gel deposited ZnO substrates).[62] To determine the viability of this method for producing more reliable WF modifications of ZnO, PFBPA, MeOBPA, DABPA, and 2,6-F2BPA were spin coated onto the surface of ALD ZnO and XPS/UPS measurements obtained. Note that, in an effort to reproduce results from NREL, UV-Ozone cleaning of ZnO was performed *in lieu* of oxygen plasma cleaning. Relatively similar starting WF values, however, are obtained for both plasma and UV-

ozone cleaned ZnO. In order to attain these layers of phosphonic acid, a 10 mM ethanolic solution of the phosphonic acid is spin-coated at 2000 rpm for 1 min onto a freshly cleaned ZnO surface and subsequently annealed at 120 °C for 2 minutes. No subsequent washing was performed. A comparison of the WF values obtained using this technique is provided in Table 4.7. As can be seen, no drastic decreases in WF were observed for spin-coated phosphonic acids on ZnO and the only decrease from 2,6-F2BPA was on the order of what is typically observed for ITO surface modification (in terms of ΔWF). The benefit of this method, however, is that it mitigates etching of the underlying ZnO substrate. However, as there is no subsequent washing step after the spin-coating and annealing there is far more than a monolayer of material deposited on the surface as evidenced by AFM (Figure 4.14). As can be seen in the AFM comparison before and after spin-coating, a thick film (~4 nm based on AFM) is deposited onto the surface. This was corroborated by XPS analysis noting the attenuation of Auger signals originating from the underlying Zn substrate (Figure 4.15). Subsequent washing of the surface with a solution of TEA in an attempt to remove the majority of the physisorbed layers produced highly irregular WF values deviating greatly from spot to spot (values ranging from 3.3 to 3.9 eV). Also, there was still a film of approximately 1 nm thickness (based on AFM imaging) of the 2,6-F2BPA on the surface of ITO and it was not as homogeneous as the bare or unwashed sample.

Table 4.7 Comparison of UPS data for spin-coated phosphonic acid layers on ZnO. Values are the average of 7 spots on each surface. Plasma cleaned ZnO is shown for reference.

Surface	Work Function (eV)	Δ Work Function (eV) from Bare ZnO
Bare ZnO	3.91 ± 0.02	-
Plasma ZnO	4.67 ± 0.06	+0.76
UV-Ozone ZnO	4.30 ± 0.03	+0.39
PFBPA	4.46 ± 0.12	+0.55
MeOBPA	4.03 ± 0.05	+0.12
DABPA	4.40 ± 0.02	+0.49
2,6-F2BPA	3.81 ± 0.07	-0.10

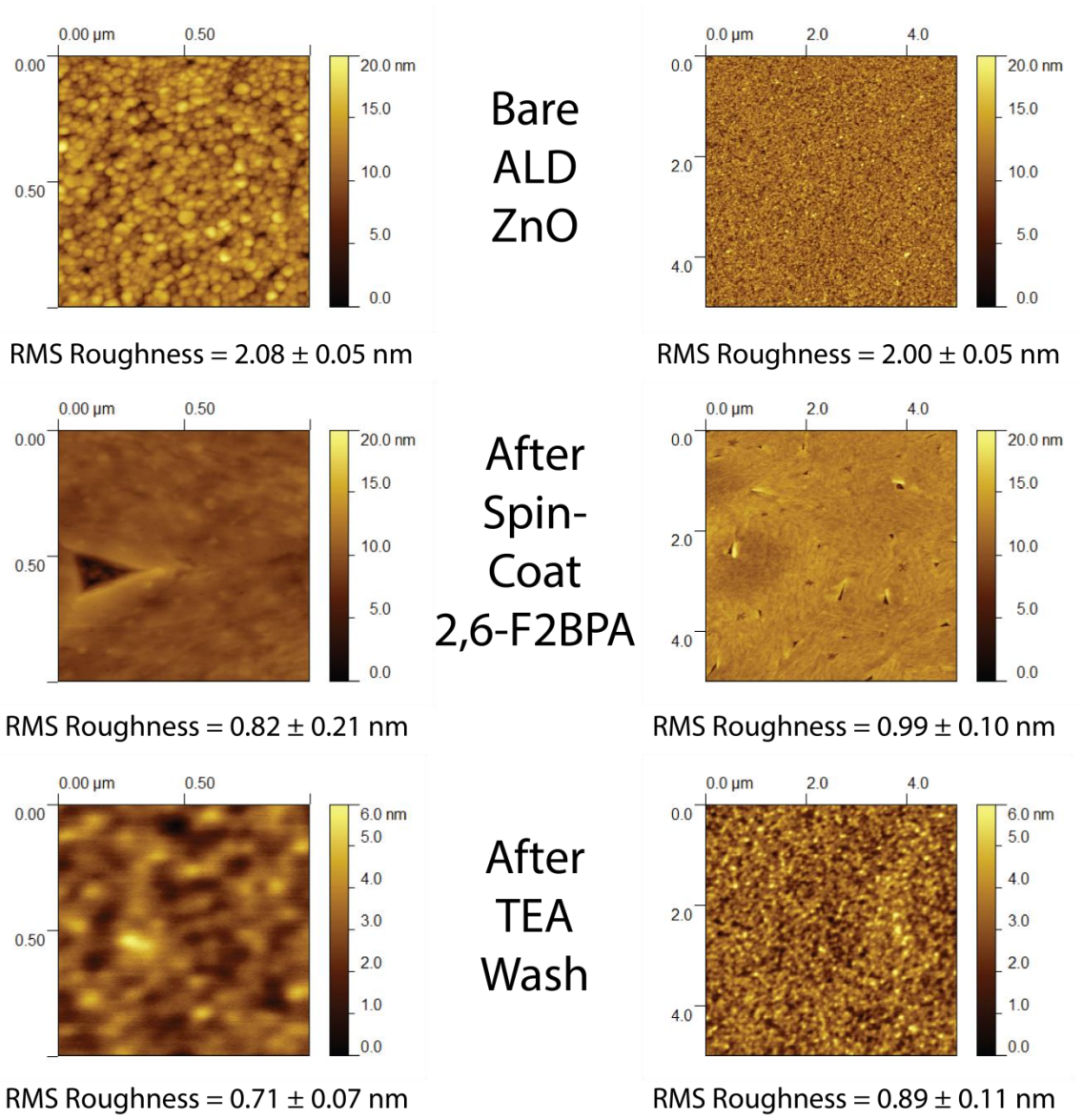

Figure 4.14 AFM comparison of ZnO before (top) and after (center) spin-coating a 10 mM solution of 2,6-F2BPA on the surface. Subsequent washing with an ethanolic solution of TEA does seem to remove the multilayers (bottom), but affords irregular WF values. Scan sizes of 1 μm × 1 μm (left) and 5 μm × 5 μm (right) were obtained and the RMS roughness values (averaged over 3 spots on each surface) are also provided.

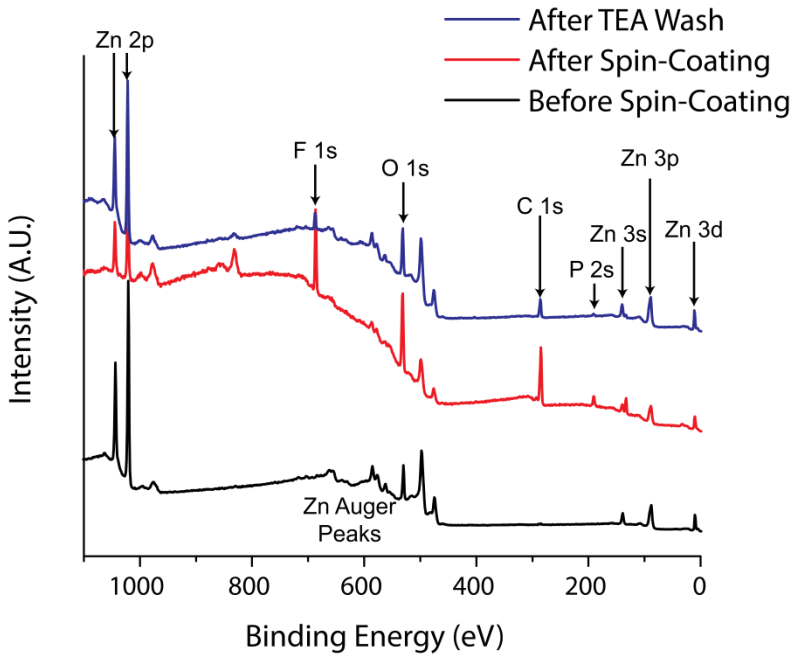

Figure 4.15 XPS survey comparison of ZnO before and after spin-coating 2,6-F2BPA as well as after washing with a solution of TEA. Note the near loss of Zn Auger peaks after the spin coating stop and the presence of the large P2s peak, which then decreases after the TEA wash, but is still far more apparent than in a typical monolayer of phosphonic acid.

Overall, spin-coating of phosphonic acids on the surfaces of substrates appears to be promising, but a closer examination of deposition techniques is required and a direct comparison with ITO is also needed to prove the viability of the technique. Furthermore, careful studies would have to be conducted in order to determine the efficacy of such a thick layer of essentially insulating material in devices. This is by far the most straightforward way that has thus far been reported of depositing phosphonic acids on the surface of a metal oxide, but it also has the potential to have issues with reproducibility given the nature of spin-coating. Other methods discussed in the literature and in this thesis rely solely on the chemisorption of the phosphonic acid on the surface of the metal oxide, while this method relies greatly on the physisorption of such material with a small

amount possibly chemisorbed at the surface. A more thorough exploration of washing protocols may yield a good set of conditions to produce reliable WF modifications with this method while minimizing the amount of material adsorbed onto the surface.

4.8 Conclusions

Surface modification of ALD ZnO with phosphonic acids has proven to be less reliable compared to ITO in terms of affording reproducible WF changes. It is possible to increase the WF of ZnO with phosphonic acids in a manner similar to that of ITO. Similarly to ITO, decreasing the WF of ZnO also proved to be more challenging than simply selecting a phosphonic acid modifier with a molecular dipole in the direction opposite to materials that increase WF. While more potential for decreases by phosphonic acid were obtained than in the case of ITO (as shown in Chapter 3), reproducing such WF decreases from batch to batch proved difficult. This variability likely originates from the tendency of phosphonic acids to etch away the ZnO substrate in some cases removing nearly all the ZnO to leave only the underlying glass substrate behind. Based on the comparison of experimentally determined pK_a values of the phosphonic acid and AFM/XPS data of which modifiers have a tendency to etch the ZnO substrate no clear correlation was observed between acidity and propensity to etch. At higher modification temperatures (~75 °C), ZnO does not withstand phosphonic acid solutions regardless of the modifier chosen, which lends credence to the hypothesis that an interplay between acidity and the solvation of zinc-phosphonate complexes is what determines etching of the underlying substrate.

Based on the numerous modification conditions that were examined, it appears that lower concentration phosphonic acid modification solutions are preferable to the 10

mM concentration that is typically used in such surface treatments. Even for phosphonic acids that readily etch the ALD ZnO surface, there is far less of a tendency to do so at the lower concentration. Spin-coating of phosphonic acids onto the surface of ZnO appears to be a promising technique allowing for extremely fast modification times and WF changes similar to those measured for immersion by KP and UPS. Further studies, however, are required to examine this technique in more detail and to optimize the deposition and subsequent washing conditions. When a reliable modification technique that does not etch the ZnO surface is used (such as the dopants discussed in Chapter 5) ALD ZnO proves to be an excellent metal oxide with which to work, having bare substrates that are extremely consistent from batch to batch both in terms of morphology and intrinsic surface properties (such as WF). Overall, modification of ALD ZnO with phosphonic acids must be done with a greater degree of care than other metal oxides, with deposition conditions potentially varying from molecule to molecule based on how it interacts with the ZnO surface.

4.9 Experimental

4.9.1 Materials

All phosphonic acids used in this chapter were synthesized as detailed in Chapter 2 of this thesis.

4.9.2 ITO and ALD ZnO Film Preparation and Cleaning

ZnO substrates were prepared by cleaning 1 in. × 1 in. glass microscope slides in the same manner as reported for ITO (substrates are scrubbed and subsequently sonicated for 10 min with a 5 % solution of Micro-90 detergent in DI water, sonicated in DI water for 10 min, sonicated in ethanol for 10 min, rinsed with ethanol, and dried under a flow of

nitrogen) followed by either oxygen plasma cleaning. Immediately after oxygen plasma samples were loaded into the atomic layer deposition system (Cambridge NanoTech, Savannah 100) and 30 nm of ZnO was deposited. When ready for use, these surfaces were rinsed with ethanol, and dried under a flow of nitrogen.

Commercially available ITO substrates (Eagle-XG, Thin Film Devices, Anaheim, CA) were purchased and found to have a surface roughness of 0.7-0.8 nm rms as measured with AFM. The ITO was cut into square substrates which were then scrubbed and subsequently sonicated for 10 min with a 5 % solution of Micro-90 detergent in DI water, sonicated in DI water for 10 min, sonicated in ethanol for 10 min, rinsed with ethanol, and dried under a flow of nitrogen to afford DSC ITO samples. Plasma treated ITO surfaces were treated using oxygen plasma with a Plasma-Preen II (100 % Power, Plasmatic Systems, Inc., North Brunswick, NJ) for 5 min.

4.9.3 ALD ZnO Phosphonic Acid Modification

In the case of ZnO substrates that were modified by immersion, freshly prepared and cleaned ZnO substrates were placed in the modification solution (concentration and modification time varied according to the text above). Upon removal surfaces were typically rinsed with a 5 % solution of triethylamine (TEA) in ethanol (note that rinsing was used rather than sonication as sonication appeared to be too harsh and potential film delamination could be observed), washed with ethanol, and dried under a flow of nitrogen. In the case of spin-coated surfaces, the freshly cleaned ZnO substrates were treated with UV-Ozone for 3 minutes and a 10 mM phosphonic acid solution was spun immediately on the substrate at 2000 rpm for 1 min. This was followed by a short annealing protocol conducted at 120 °C for 2 minutes.

4.9.4 Surface Characterization

4.9.4.1 XPS and UPS Measurements

All measurements were conducted in a combined XPS-UPS Kratos Axis Ultra with an average base pressure of 10^{-9} Torr. UPS was acquired prior to acquisition of XPS for all samples. UPS spectra were obtained with a 21.2 eV He (I) excitation and a pass energy of 5 eV using a 27 μm spot size. Each sample was examined in at least 7 spots to ensure consistency over the entire surface and the spectrometer was calibrated using a sputter cleaned silver sample. XPS data were collected with a monochromatic Al Kα source (300 W) using a 400 μm spot size and a pass energy of 160 eV for survey acquisition and 20 eV for high resolution spectra. Exposure of the surfaces to X-rays was kept to a minimum (ca. 45 min), and spectra were acquired in three spots on each surface. Most characterizations were performed at normal takeoff angle (0°). Data was analyzed using Vision Processing version 2.2.8.

4.9.4.2 Kelvin Probe

Kelvin Probe analysis (Besocke Delta Phi) of surfaces was conducted in air with a probe diameter of approximately 3 mm. Samples analyzed by KP were cut to be 1 in. × 1 in. so that 5 data points could be collected on each surface. Average values and standard deviations were generated from these multiple spots. Highly ordered pyrolytic graphite, freshly cleaved using the Scotch tape method, was used (typical WF of 4.5 eV) at the beginning and end of each set of measurements as well as periodically every 2 – 4 samples analyzed to account for any instrumental drift.

4.9.4.3 IR Analysis

IR analysis was conducted using a dry-air purged Digilab FTS-600 FT-IR instrument equipped with an MCT detector. In the case of powder samples, a KBr pellet was used and 32 scans were collected for each spectrum at a resolution of 2 cm^{-1}, referencing a transmission spectrum of a pure KBr pellet. In the case of IRRAS measurements, a grazing-angle accessory (80° angle of incidence, Pike) was used. A Perkin-Elmer gold grid polarizer was used to produce p-polarized light and data was collected at a resolution of 2 cm^{-1} with a mirror speed of 1.28 cm/s. 10,000 scans were collected for each surface measurement and referenced to a bare ALD ZnO substrate.

4.9.4.4 Tapping Mode AFM

All AFM images were acquired under atmospheric conditions using a commercial Agilent 5600 LS equipped with an AC-AFM controller. The microscope was housed within an acoustic isolation hood. The AFM piezo scanner was calibrated using a 3D reference silicon grating (Veeco, part number 498-000-026) with a 10 μm lateral pitch and a step height of 200 nm. Cantilevers (NSC35/NoAl, Mikromasch, CA) were made from n-type silicon (phosphorus doped), utilizing cantilevers of 130 ± 5 μm in length, which have a typical probe radius of 10 nm and a typical spring constant of 4.5 N m^{-1}. Image acquisition was performed using PicoView 1.10, and image processing performed using the open source program Gwyddion version 2.20.

Topography images were collected in tapping-mode using a scan speed of 0.5 lines s^{-1}. After approach of the tip to the substrate, the piezo was retracted until the tip was oscillating above the surface and the amplitude set point was then optimized to obtain the best image contrast. Subsequently, the highest possible integral and

proportional gains were used to obtain the most accurate representation of the sample. All 1 μm images were flattened using a first order polynomial background and all 5 μm images flattened using a second order polynomial background. Each sample was examined in at least 3 spots to ensure consistency of data over the entire substrate.

4.9.5 Determination of pK_a Values

Titrations of the acids were conducted in a manner similar to that reported previously for phenylphosphonic acid.[63] The pK_a values of various phosphonic acids have been measured several times in the literature,[51-52, 54, 63-64] and this particular method was chosen due to the use of a solvent mixture containing a high ethanol content, which is similar to the conditions used for the modification of the ITO and ZnO substrates. All titrations were performed at an ambient temperature of 20 °C and made with a Thermo Orion 420A+ pH meter equipped with a VWR sympHony glass electrode (filled with saturated solutions of KCl in either deionized water or methanol) calibrated against pH 4, 7, and 10 buffer solutions (Hach Company). A standardized solution of 0.10 M NaOH in a mixture of 75:25 ethanol:water (v:v) served as the titrant. Solutions of the phosphonic acid for titration were dissolved in the same ethanol:water mixture at a concentration of 0.01 M. All solutions were degassed by sparging with nitrogen prior to use and all titrations were performed under a flow of nitrogen.

4.10 References

[1] Zhou, Y.; Cheun, H.; Choi, S.; Potscavage, W. J.; Fuentes-Hernandez, C.; Kippelen, B., Indium Tin Oxide-Free and Metal-Free Semitransparent Organic Solar Cells. *Applied Physics Letters* **2010,** *97*, 153304.

[2] Grzegorz, L.; Marek, G.; Elzbieta, G.; Pavlo, S.; Vladyslav, C.; Dmytro, V., Zno Films Grown by Atomic Layer Deposition for Organic Electronics. *Semiconductor Science and Technology* **2012,** *27*, 074006.

[3] Jagadish, C.; Pearton, S. J., *Zinc Oxide Bulk, Thin Films and Nanostructures: Processing, Properties, and Applications*. Elsevier Science: 2011.

[4] Anderson, J.; Chris, G. V. d. W., Fundamentals of Zinc Oxide as a Semiconductor. *Reports on Progress in Physics* **2009,** *72*, 126501.

[5] Özgür, Ü.; Alivov, Y. I.; Liu, C.; Teke, A.; Reshchikov, M. A.; Doğan, S.; Avrutin, V.; Cho, S.-J.; Morkoç, H., A Comprehensive Review of Zno Materials and Devices. *Journal of Applied Physics* **2005,** *98*, 041301.

[6] *Handbook of Transparent Conductors*. Springer: New York, 2010.

[7] Guziewicz, E.; Godlewski, M.; Wachnicki, L.; Krajewski, T. A.; Luka, G.; Gieraltowska, S.; Jakiela, R.; Stonert, A.; Lisowski, W.; Krawczyk, M.; Sobczak, J. W.; Jablonski, A., Ald Grown Zinc Oxide with Controllable Electrical Properties. *Semiconductor Science and Technology* **2012,** *27*, 074011.

[8] Morkoç, H.; Özgür, Ü., *Zinc Oxide: Fundamentals, Materials and Device Technology*. Wiley: 2008.

[9] Bunn, C. W., The Lattice-Dimensions of Zinc Oxide. *Proceedings of the Physical Society* **1935,** *47*, 835.

[10] *Zinc Oxide - a Material for Micro- and Optoelectronic Applications*. Springer: Dordrecht, 2005.

[11] Zhou, Y. H.; Fuentes-Hernandez, C.; Shim, J.; Meyer, J.; Giordano, A. J.; Li, H.; Winget, P.; Papadopoulos, T.; Cheun, H.; Kim, J.; Fenoll, M.; Dindar, A.; Haske, W.; Najafabadi, E.; Khan, T. M.; Sojoudi, H.; Barlow, S.; Graham, S.; Bredas, J. L.; Marder, S. R.; Kahn, A.; Kippelen, B., A Universal Method to Produce Low-Work Function Electrodes for Organic Electronics. *Science* **2012,** *336*, 327-332.

[12] Hsu, J. W. P.; Lloyd, M. T., Organic/Inorganic Hybrids for Solar Energy Generation. *MRS Bulletin* **2010,** *35*, 422-428.

[13] Wöll, C., The Chemistry and Physics of Zinc Oxide Surfaces. *Progress in Surface Science* **2007,** *82*, 55-120.

[14] Nogues, C.; Lang, P., Self-Assembled Alkanethiol Monolayers on a Zn Substrate: Structure and Organization. *Langmuir* **2007,** *23*, 8385-8391.

[15] Yip, H.-L.; Hau, S. K.; Baek, N. S.; Jen, A. K. Y., Self-Assembled Monolayer Modified Zno/Metal Bilayer Cathodes for Polymer/Fullerene Bulk-Heterojunction Solar Cells. *Applied Physics Letters* **2008,** *92*, 193313.

[16] Allen, C. G.; Baker, D. J.; Albin, J. M.; Oertli, H. E.; Gillaspie, D. T.; Olson, D. C.; Furtak, T. E.; Collins, R. T., Surface Modification of Zno Using Triethoxysilane-Based Molecules. *Langmuir* **2008,** *24*, 13393-13398.

[17] Sinapi, F.; Forget, L.; Delhalle, J.; Mekhalif, Z., Formation and Characterization of Thin Films of H(Ch2)Xpo(Oh)2 on Polycrystalline Zinc Substrates. *Surface and Interface Analysis* **2002,** *34*, 148-154.

[18] Hotchkiss, P. J.; Malicki, M.; Giordano, A. J.; Armstrong, N. R.; Marder, S. R., Characterization of Phosphonic Acid Binding to Zinc Oxide. *Journal of Materials Chemistry* **2011,** *21*, 3107-3112.

[19] Perkins, C. L., Molecular Anchors for Self-Assembled Monolayers on Zno: A Direct Comparison of the Thiol and Phosphonic Acid Moieties. *The Journal of Physical Chemistry C* **2009,** *113*, 18276-18286.

[20] Zhang, B.; Kong, T.; Xu, W.; Su, R.; Gao, Y.; Cheng, G., Surface Functionalization of Zinc Oxide by Carboxyalkylphosphonic Acid Self-Assembled Monolayers. *Langmuir* **2010,** *26*, 4514-4522.

[21] Bulusu, A.; Paniagua, S. A.; MacLeod, B. A.; Sigdel, A. K.; Berry, J. J.; Olson, D. C.; Marder, S. R.; Graham, S., Efficient Modification of Metal Oxide Surfaces with Phosphonic Acids by Spray Coating. *Langmuir* **2013,** *29*, 3935-3942.

[22] Schmidt-Mende, L.; MacManus-Driscoll, J. L., Zno – Nanostructures, Defects, and Devices. *Materials Today* **2007,** *10*, 40-48.

[23] McCluskey, M. D.; Jokela, S. J., Defects in Zno. *Journal of Applied Physics* **2009,** *106*, 071101.

[24] Wurtzite Polyhedra. https://upload.wikimedia.org/wikipedia/commons/8/8e/Wurtzite_polyhedra.png (accessed 3-22-2014).

[25] Kröger, F. A., *The Chemistry of Imperfect Crystals: Preparation, Purification, Crystal Growth and Phase Theory*. North-Holland Pub. Co.: 1973.

[26] Han, J.; Mantas, P. Q.; Senos, A. M. R., Grain Growth in Mn-Doped Zno. *Journal of the European Ceramic Society* **2000,** *20*, 2753-2758.

[27] Pierson, H. O., *Handbook of Chemical Vapor Deposition, 2nd Edition: Principles, Technology and Applications*. Elsevier Science: 1999.

[28] Sherman, A., *Chemical Vapor Deposition for Microelectronics: Principles, Technology, and Applications*. Noyes Publications: 1987.

[29] Sudarshan, E. J. H. P. T. S., *Surface Engineering Series Volume 2: Chemical Vapor Deposition*. ASM International: 2000.

[30] Kääriäinen, T.; Cameron, D.; Kääriäinen, M. L.; Sherman, A., *Atomic Layer Deposition: Principles, Characteristics, and Nanotechnology Applicatons*. Wiley: 2013.

[31] King, D. M.; Liang, X.; Carney, C. S.; Hakim, L. F.; Li, P.; Weimer, A. W., Atomic Layer Deposition of Uv-Absorbing Zno Films on Sio2 and Tio2 Nanoparticles Using a Fluidized Bed Reactor. *Advanced Functional Materials* **2008,** *18*, 607-615.

[32] Ferguson, J. D.; Weimer, A. W.; George, S. M., Surface Chemistry and Infrared Absorbance Changes During Zno Atomic Layer Deposition on Zro2 and Batio3 Particles. *Journal of Vacuum Science & Technology A* **2005,** *23*, 118-125.

[33] Macech, M. R. Electrical, Structural, and Compositional Characterization of Interlayer Material and New Active Layers in Organic Solar Cells. University of Arizona, Arizona, 2012.

[34] Wood, C.; Li, H.; Winget, P.; Brédas, J.-L., Binding Modes of Fluorinated Benzylphosphonic Acids on the Polar Zno Surface and Impact on Work Function. *The Journal of Physical Chemistry C* **2012,** *116*, 19125-19133.

[35] Li, H.; Ratcliff, E. L.; Sigdel, A. K.; Giordano, A. J.; Marder, S. R.; Berry, J. J.; Brédas, J.-L., Modification of the Gallium-Doped Zinc Oxide Surface with Self-Assembled Monolayers of Phosphonic Acids: A Joint Theoretical and Experimental Study. *Advanced Functional Materials* **2014**, Early View.

[36] Wei, T.; Jin, C. Q.; Zhong, W.; Liu, J.-M., High Permittivity Polymer Embedded with Co⁄Zno Core/Shell Nanoparticles Modified by Organophosphorus Acid. *Applied Physics Letters* **2007,** *91*, 222907.

[37] Chen, J.; Ruther, R. E.; Tan, Y.; Bishop, L. M.; Hamers, R. J., Molecular Adsorption on Zno(10$\bar{1}$0) Single-Crystal Surfaces: Morphology and Charge Transfer. *Langmuir* **2012,** *28*, 10437-10445.

[38] Hau, S. K.; Cheng, Y.-J.; Yip, H.-L.; Zhang, Y.; Ma, H.; Jen, A. K. Y., Effect of Chemical Modification of Fullerene-Based Self-Assembled Monolayers on the Performance of Inverted Polymer Solar Cells. *ACS Applied Materials & Interfaces* **2010,** *2*, 1892-1902.

[39] Stubhan, T.; Litzov, I.; Li, N.; Wang, H. Q.; Krantz, J.; Machui, F.; Steidl, M.; Oh, H.; Matt, G. J.; Brabec, C. J. In *Low-Temperature Solution-Processed Metal Oxide Buffer Layers Fulfilling Large Area Production Requirements*, 2012; pp 84770J-84770J-6.

[40] Stubhan, T.; Salinas, M.; Ebel, A.; Krebs, F. C.; Hirsch, A.; Halik, M.; Brabec, C. J., Increasing the Fill Factor of Inverted P3ht:Pcbm Solar Cells through Surface Modification of Al-Doped Zno Via Phosphonic Acid-Anchored C60 Sams. *Advanced Energy Materials* **2012,** *2*, 532-535.

[41] Chen, Y.; Kim, M.; Lian, G.; Johnson, M. B.; Peng, X., Side Reactions in Controlling the Quality, Yield, and Stability of High Quality Colloidal Nanocrystals. *Journal of the American Chemical Society* **2005,** *127*, 13331-13337.

[42] Demir, M. M.; Koynov, K.; Akbey, Ü.; Bubeck, C.; Park, I.; Lieberwirth, I.; Wegner, G., Optical Properties of Composites of Pmma and Surface-Modified Zincite Nanoparticles. *Macromolecules* **2007,** *40*, 1089-1100.

[43] Smecca, E.; Motta, A.; Fragalà, M. E.; Aleeva, Y.; Condorelli, G. G., Spectroscopic and Theoretical Study of the Grafting Modes of Phosphonic Acids on Zno Nanorods. *The Journal of Physical Chemistry C* **2013,** *117*, 5364-5372.

[44] Di Mauro, A.; Smecca, E.; D'Urso, A.; Condorelli, G. G.; Fragalà, M. E., Tetra-Anionic Porphyrin Loading onto Zno Nanoneedles: A Hybrid Covalent/Non Covalent Approach. *Materials Chemistry and Physics* **2014,** *143*, 977-982.

[45] Sharma, A.; Kippelen, B.; Hotchkiss, P. J.; Marder, S. R., Stabilization of the Work Function of Indium Tin Oxide Using Organic Surface Modifiers in Organic Light-Emitting Diodes. *Applied Physics Letters* **2008,** *93*, 163308.

[46] Hotchkiss, P. J. The Design, Synthesis, and Use of Phosphonic Acids for the Surface Modification of Metal Oxides. Ph.D. Thesis, Georgia Institute of Technology, Atlanta, GA, 2008.

[47] Paniagua, S. A.; Li, E. L.; Marder, S. R., Adsorption Studies of a Phosphonic Acid on Ito: Film Coverage, Purity, and Induced Electronic Structure Changes. *Physical Chemistry Chemical Physics* **2014,** *16*, 2874-2881.

[48] Paniagua-Barrantes, S. Interfacial Engineering of Transparent Conductive Electrodes and Nanoparticles with Phosphonic Acids and Metal-Organic Dopants for Organic Electronic Applications. Ph.D. Thesis, Georgia Institute of Technology, Atlanta, GA, 2013.

[49] Li, H.; Schirra, L. K.; Shim, J.; Cheun, H.; Kippelen, B.; Monti, O. L. A.; Bredas, J.-L., Zinc Oxide as a Model Transparent Conducting Oxide: A Theoretical and Experimental Study of the Impact of Hydroxylation, Vacancies, Interstitials, and Extrinsic Doping on the Electronic Properties of the Polar Zno (0002) Surface. *Chemistry of Materials* **2012,** *24*, 3044-3055.

[50] Hollingsworth, C. A.; Seybold, P. G.; Hadad, C. M., Substituent Effects on the Electronic Structure and Pka of Benzoic Acid. *International Journal of Quantum Chemistry* **2002,** *90*, 1396-1403.

[51] Jaffé, H. H.; Freedman, L. D.; Doak, G. O., The Acid Dissociation Constants of Aromatic Phosphonic Acids. I. Meta and Para Substituted Compounds1. *Journal of the American Chemical Society* **1953,** *75*, 2209-2211.

[52] Jaffé, H. H.; Freedman, L. D.; Doak, G. O., The Acid Dissociation Constants of Aromatic Phosphonic Acids. Ii. Compounds with Ortho Substituents. *Journal of the American Chemical Society* **1954,** *76*, 1548-1552.

[53] Gulinski, J.; Maciejewska, U.; Stewart, R., The Effects of High Concentrations of Aqueous Tetramethylammonium Chloride and Other Salts on the Dissociation of Phenylphosphonic Acid and on the Enolization of Acetone. *Journal of Solution Chemistry* **1988,** *17*, 297-304.

[54] Nagarajan, K.; Shelly, K. P.; Perkins, R. R.; Stewart, R., Arylphosphonic Acids. I. Substituent Effects on Their First and Second Dissociations. *Canadian Journal of Chemistry* **1987,** *65*, 1729-1733.

[55] Gliboff, M.; Li, H.; Knesting, K. M.; Giordano, A. J.; Nordlund, D.; Seidler, G. T.; Brédas, J.-L.; Marder, S. R.; Ginger, D. S., Competing Effects of Fluorination on the Orientation of Aromatic and Aliphatic Phosphonic Acid Monolayers on Indium Tin Oxide. *The Journal of Physical Chemistry C* **2013,** *117*, 15139-15147.

[56] Boehmer, V.; Vogt, W.; Chafaa, S.; Meullemeestre, J.; Schwing, M.-J.; Vierling, F., (O-Hydroxyphenyl)Methylphosphonic Acids: Synthesis and Potentiometric Determinations of Their Pka Values. *Helvetica Chimica Acta* **1993,** *76*, 139 - 149.

[57] Alimarin; Fadeewa, *Acta Chimica Academiae Scientiarum Hungaricae* **1962,** *32*, 171,172.

[58] Chavane, *Annales de Chimie (Cachan, France)* **1949,** *12*, 372-379.

[59] Calvo, K. C.; Westheimer, F. H., Mechanism of the Conant-Swan Fragmentation and the Formation of Monomeric Metaphosphate Ion. *Journal of the American Chemical Society* **1984,** *106*, 4205-4210.

[60] Beerbom, M. M.; Lagel, B.; Cascio, A. J.; Doran, B. V.; Schlaf, R., Direct Comparison of Photoemission Spectroscopy and in Situ Kelvin Probe Work Function Measurements on Indium Tin Oxide Films. *Journal of Electron Spectroscopy and related Phenomena* **2006,** *152*, 12-17.

[61] Kim, J. S.; Lagel, B.; Moons, E.; Johansson, N.; Baikie, I. D.; Salaneck, W. R.; Friend, R. H.; Cacialli, F., Kelvin Probe and Ultraviolet Photoemission Measurements of Indium Tin Oxide Work Function: A Comparison. *Synthetic Metals* **2000,** *111*, 311-314.

[62] Cowan, S. R.; Schulz, P.; Giordano, A. J.; Garcia, A.; MacLeod, B. A.; Marder, S. R.; Kahn, A.; Ginley, D. S.; Ratcliff, E. L.; Olson, D. C., Chemically Controlled Reversible and Irreversible Extraction Barriers Via Stable Interface Modification of Zinc Oxide Electron Collection Layer in Polycarbazole-Based Organic Solar Cells. *Advanced Functional Materials* **2014**, Accepted.

[63] Peppard, D. F.; Mason, G. W.; Andrejasich, C. M., Variation of the Pka of (X)(Y)Po(Oh) with X and Y in 75 and 95 Per Cent Ethanol. *Journal of Inorganic and Nuclear Chemistry* **1965,** *27*, 697-709.

[64] Franz, R. D., Comparisons of Pka and Log P Values of Some Carboxylic and Phosphonic Acids: Synthesis and Measurement. *Aaps Pharmsci* **2001,** *3*, 1-13.

CHAPTER 5

SURFACE MODIFICATION OF METALS AND METAL OXIDES USING REDOX-ACTIVE ORGANIC AND METAL-ORGANIC COMPOUNDS TO ALTER WORK FUNCTION

5.1 Redox Active Dopants to Tailor Work Function

Thus far, this thesis has focused on the use of phosphonic acids to modify surfaces, relying on the dipole of the tail group, reinforced or opposed by the bond dipole to alter the work function of ITO (Chapter 3) and ZnO (Chapter 4). Specifically, Chapters 3 and 4 demonstrated that the WF of both ITO and ZnO can be readily increased through phosphonic acid modification. Decreasing the WF, however, proved to be more challenging than anticipated and only minor decreases were observed with molecules such as 2,6-F2BPA likely due to opposing dipole effects (tail vs. bond dipole). The technique of phosphonic acid modification is also limited to the surfaces of metal oxides and thus cannot be readily applied to other metallic substrates such as gold or silver. Therefore, in order to investigate methods to increase and decrease the WF of both metals and metal oxides, modifiers other than phosphonic acids need to be investigated.

5.1.1 Doping of Inorganic and Organic Materials

Doping allows for control over the electrical properties of a semiconductor by introducing impurities into an otherwise extremely pure material. These impurities vary the resistivity inherent within the material depending on the types and concentrations of

the dopants.[1] One of the classic examples of doping is silicon which can be doped to form both n-type and p-type silicon. In the case of n-type silicon a donor material (such as phosphorus) is introduced into the lattice, which donates an electron into the conduction band. In the case of p-type silicon, an acceptor material (such as boron) is used. In the case of boron, its substitution in the lattice requires that an extra electron be donated from the surrounding silicon and accepted by the boron to form four covalent bonds, thereby creating a positively charged hole in the valence band of silicon. Generalized band diagrams for these types of doping, along with intrinsic silicon are shown schematically in Figure 5.1. Fortuitously, the terminology n- and p-type fits the description of the carrier type produced by the doping (e.g. negative electrons or positive holes)[1] given that the term was coined when it was observed that placing a metal whisker against a p-type material forms a Schottky barrier diode and a positive bias was required for the production of current (alternatively an n-type material requires a negative bias).[2-3]

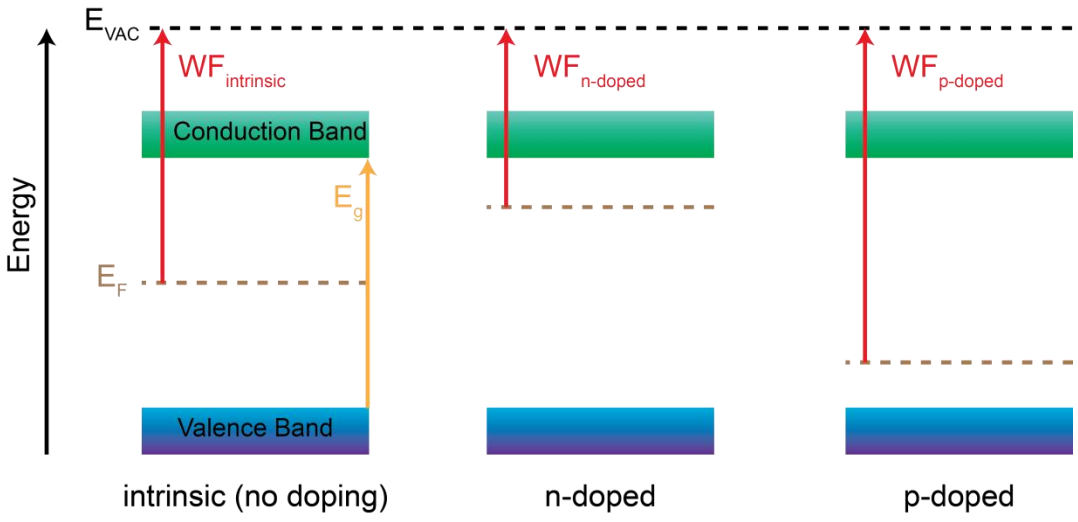

Figure 5.1 Schematic band diagram of doping in a semiconductor, showing the case of an intrinsic semiconductor (e.g. silicon) without any impurities (undoped, left), with donor impurities (n-doped, e.g. phosphorus, center), and with acceptor impurities (p-doped, e.g. boron, right). Image adapted from Sze.[4]

The concept of doping also plays an increasingly important role in organic electronics applications as well, allowing for changes in both conductivity and barriers to carrier collection/injection.[5] Both inorganic materials and small molecules can be used to accomplish doping in organic devices. Organic small molecules are a good choice due to their larger size making diffusion within the device structure less likely compared with the smaller, potentially more mobile metal ions.[6-7] The choice of a chemical dopant is an important one, and is dictated by multiple factors. The first factor that needs to be considered is the type of doping, n- or p-type, that is required for the application and whether the chosen dopant can influence materials with a given electron affinity or ionization energy, respectively. The dopant should also be stable, not able to migrate, and it is desirable that it be processible from either solution or vapor in order to maximize compatibility with different processing conditions.[5, 8-9] There are multiple review articles that discuss doping of metal-organic and organic-organic interfaces to better align energy levels.[10-13]

5.1.2 Doping of Inorganic Surfaces by Adsorption

As discussed in the previous section, it is possible to dope materials such as silicon by introducing deliberate impurities into the lattice. Another technique to alter the work function of substrates, however, is by adsorption of redox-active materials to the surface of a substrate, thereby altering its work function to better align with an organic overlayer. Before continuing it is important to disambiguate what is meant by adsorption in the context of this chapter. The previous chapters focused on adsorption of modifiers to the surface through the formation of a covalent linkage (for instance a phosphorus-oxygen-metal bond formation). Adsorption discussed in this chapter is far

more general in that materials are physisorbed or electrostatically bound to the surface. As will be discussed, this gives dopants an advantage over a more substrate specific surface modifier because they are not reliant on specific chemistry between the surface and the adsorbate (e.g. thiol to gold or phosphonic acid to metal oxide bonding) and increases the number of surfaces that can be modified in this manner. A true "dopant" on a surface is a material that causes an electron transfer event between the substrate and itself thereby either donating electrons to (n-type) or accepting electrons from (p-type) the substrate. As will be shown, however, many "dopants" on surfaces cause a combination of effects that reinforce one another; assuming integral electron transfer from/to the dopant, these effects include: shifts in the Fermi level relative to the band edges, and the formation of an interface dipole that also leads to a change in WF.

Materials that are commonly used to p-dope surfaces, thereby increasing their WF, are strong acceptor molecules with tetrafluoro-tetracyanoquinodimethane (F_4-TCNQ) being one of the more widely used materials for this purpose (Figure 5.2). One of the earlier studies probing F_4-TCNQ to increase WF, consequently decreasing hole injection barriers, was reported by Koch where it was shown that when F_4-TCNQ was deposited on the surface of gold (by vapor deposition) a WF increase of 0.35 eV was observed by UPS.[14] UPS combined with XPS measurements of thin (5 Å) and thick (60 Å) films showed that in thick films both the anion form of F_4-TCNQ and the neutral species were present, but in thinner films mainly the anion form was observed, indicating an electron transfer from the gold to the dopant.[14] It was later demonstrated that at sub-monolayer coverages, a network of ordered F_4-TCNQ anions form on the surface of gold.[15] Further studies were then conducted using F_4-TCNQ on copper, showing a 0.6

eV WF increase.[16-17] The nature of the WF modification was further clarified, compared to the previous study, by combining experimental data with theoretical calculations to show that the origin of the WF change comes from multiple factors including electron transfer and molecular geometric distortions.[16] More recently, ZnO treated with F_4-TCNQ has been shown to see a WF increase up to 2.8 eV, with the origin of this change coming not from electron transfer, but rather from band bending and the formation of an interface dipole (partial electron transfer equivalent to *ca*. 0.02 electrons/molecule).[18] It should be noted that F_4-TCNQ can be used to change the WF of graphene[19] and silver [20] surfaces. Thus, while the mechanism of action of this molecule is different depending on whether metal or metal oxides surfaces are used, a WF increase still occurs. This dopant in particular, however, is relatively volatile,[21] can interdiffuse within organic films,[22] and is soluble in a limited range of solvents.[23-24]

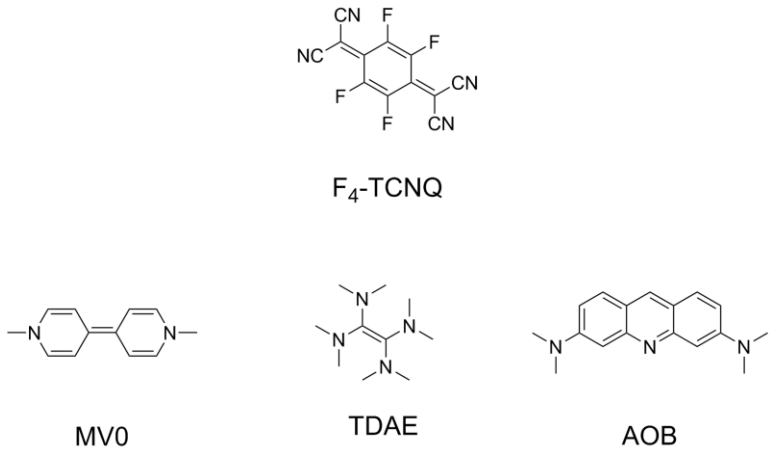

Figure 5.2 Examples of p- (top) and n- (bottom) dopants that have been used to treat the surfaces of various types of substrates including metals, metal oxides, and graphene. Also provided are the abbreviations used throughout the text.

Materials that can serve to lower the WF of multiple substrates by n-doping have also been examined. The structures of some of these materials are shown in Figure 5.2 and include tetrakis(dimethylamino)ethylene (TDAE) as well as neutral methyl viologen (MV0). Both compounds were initially examined on gold surfaces with a reduction in the WF of gold by 2.2 eV being found in the case of MV0[25] and 1.3 eV in the case of TDAE.[26] Both studies of the thermally evaporated dopant on gold used a combination of photoelectron spectroscopy techniques coupled with theoretical calculations to conclude that electron transfer from the dopant to the gold surface was taking place, which formed a large interface dipole thus leading to the observed WF reduction.[25] Another modifier that has been thermally deposited on gold is acridine orange base (AOB) with an observed WF change of -1.7 eV for an inhomogeneous layer < 1 nm and -1.9 eV for complete coverage.[27] As in the case of the previous two modifiers the change in WF was attributable to electron transfer leading to the formation of a large interface dipole. While it was claimed that such modifiers should have a similar impact to the WF of other substrates[27] it appears that only TDAE was also examined on another substrate, namely ITO.[28] In this case, a WF reduction of 0.9 eV was observed for a thermally evaporated monolayer, attributable to a electron transfer event that then leads to the formation of an interface dipole.[28] The authors noted that there was a slight increase in WF (0.2 eV) upon exposure to air for several minutes. The results of these studies are summarized in Table 5.1.

Table 5.1 Summary of WF modification by various n-dopant materials thermally evaporated on gold and/or ITO. The substrate used, along with the WF value of the substrate before and after treatment are noted as well as the overall change in WF.

Modifier	Substrate	Bare Substrate WF (eV)	WF After Dopant Evaporation (eV)	ΔWF (eV)	Reference
MV0	Gold	5.5	3.3	-2.2	[25]
TDAE	ITO	4.6	3.7	-0.9	[28]
	Gold	5.2	3.9	-1.3	[26]
AOB	Gold (incomplete layer)	5.2	3.5	-1.7	[27]
	(complete layer)	5.2	3.3	-1.9	[27]

5.1.3 Redox-Active Metal-Organic Compounds for Doping

Recently, both p- and n-dopants have been examined in the Marder group, and the structures of the metal-organic materials are provided in Figure 5.3. Molybdenum tris[1,2-bis(trifluoromethyl)ethane-1,2-dithiolene] ($Mo(tfd)_3$) was examined since F_4-TCNQ is a volatile material that has a tendency to diffuse within an organic layer.[21, 29] This particular material was chosen for several reasons, the first of which was because of its larger size, which aids in mitigating diffusion through the doped material. In comparison with F_4-TCNQ, which has an electron affinity (EA) of 5.25 eV,[30-31] $Mo(tfd)_3$ is an even more powerful oxidant with an EA of 5.6 eV,[32-34] is less volatile, and is also more readily used as a solution oxidant due to its good solubility, which can be tuned based on the substituents placed on the dithiolene moieties.

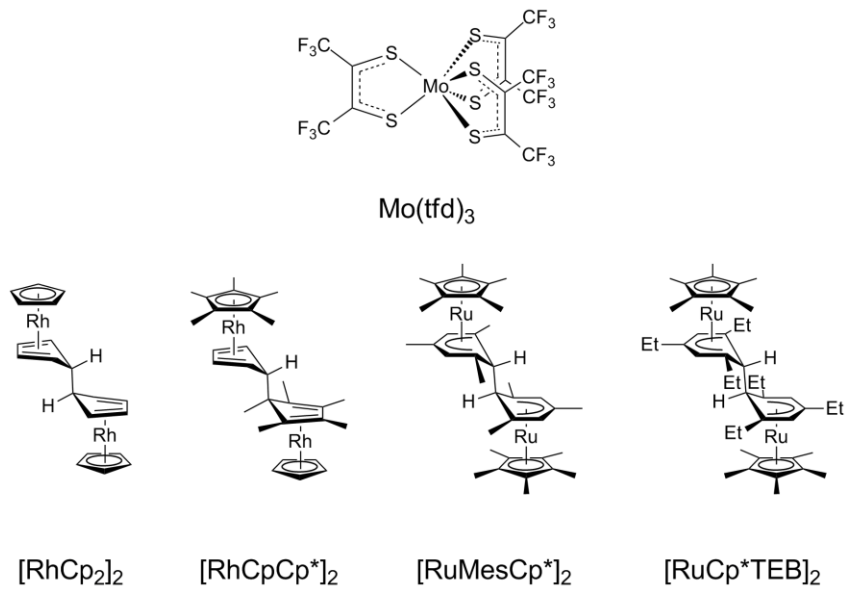

Figure 5.3 Redox-active metal-organic species recently examined by the Marder group for p- (top) and n-doping (bottom).[8-9, 33-34]

In the case of n-dopants, the ability to dope low electron affinity (EA) materials yet for the dopant itself to be relatively stable for handling are two criteria that are simultaneously difficult to satisfy.[5] In order to circumvent this problem and form essentially air-stable dopants, it is possible to couple electron transfer chemistry to chemical reactions. The organometallic sandwich compounds shown in Figure 5.3 are such an example, being relatively air-stable solids, but are also "masked" forms of strongly reducing monomers, capable of doping materials with EA as lows as *ca*. 3 eV.[8-9] As discussed in 5.1.2 the n-dopants used were all processed by vapor deposition, so the ability to process such materials from solution would be extremely useful. The mechanism behind how these dimers dissociate to form a monomer that readily acts as a donor material has also been investigated, with two distinct mechanisms possible, which are summarized in Figure 5.4.[35] In one mechanism, the dimer form of the material can dissociate to form two 19 electron monomers, which both readily give up an electron to

an acceptor thereby forming two monomer cations. It is also possible for electron transfer from the dimer to the acceptor to occur first, followed by dissociation of the dimer cation to form a 19 electron monomer (which subsequently also transfers an electron to an acceptor) and a monomer cation, once again resulting in the formation of two monomer cations. Regardless of the mechanism, the thermodynamics of doping will be influenced by both the $[M^+/M]$ redox potential and the free energy of dissociation of the central C-C bond of the dimer.

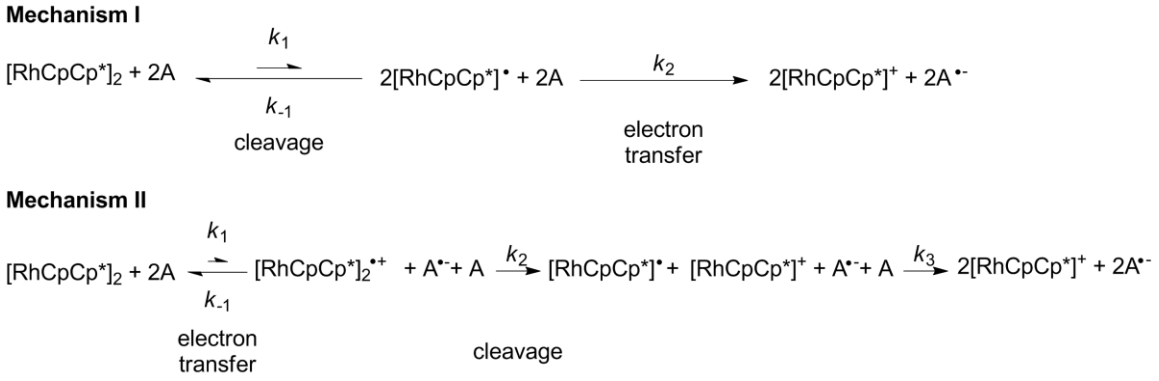

Figure 5.4 The two mechanisms by which electron transfer occurs using $[RhCpCp^*]_2$ as an example. The first step can either be the dissociation of the dimer (mechanism I) or electron transfer from the dimer to the acceptor (mechanism II). Mechanisms adapted from Guo.[8, 35]

It is important to note that materials such as those shown in Figure 5.3 have recently been investigated for their ability to dope surfaces by adsorption. In particular, graphene was treated with a molybdenum p-dopant and $[RhCpCp^*]_2$ as an n-dopant.[36] Unlike the methods discussed in 5.1.2, solution processing was used instead of vacuum deposition; the graphene surface was soaked in a dilute solution of the dopant for short amounts of time. This straightforward solution processing methodology still produced

drastic changes in the WF of graphene, showing an increase for the p-dopant of 0.2 – 0.7 eV depending on the treatment conditions and a WF decrease of 1.3 eV in the case of the n-dopant (using treatment time of a few seconds).[36] The ability to produce such drastic WF changes by solution soaking without the need to vapor deposit the material is highly attractive for device fabrication as it could potentially increase throughput and decrease fabrication complexity.

5.2 Selection of Dopants for Treatment of ITO, ZnO, and Gold

As shown in 5.1.2 work has already been done to indicate that dopants do have a significant impact on the surfaces of metals and metal oxides in terms of tuning work function. The p- and n-dopants that were subsequently discussed in 5.1.3 are more strongly oxidizing or reducing, respectively, compared with what has already been examined in the literature. Since it had already been shown that these materials are effective dopants of organic semiconductors,[8-9, 33-35] and influence the work function of graphene,[37] two questions were raised. The first question was whether or not these metal-organic dopants would have an impact on the work function of metal and/or metal oxide surfaces. Then, if such metal-organic species do influence the work function, how do they compare with other compounds reported in the literature. That is, does the oxidizing or reducing strength of the dopant have an impact on the work function modification of the substrate? In order to investigate these questions, a series of metal-organic molecules were chosen from the work discussed in 5.1.3 along with several materials that had previously shown work function tuning ability as discussed in 5.1.2. A summary of the materials chosen for this study along with their abbreviations used throughout the text are provided in Figure 5.5.

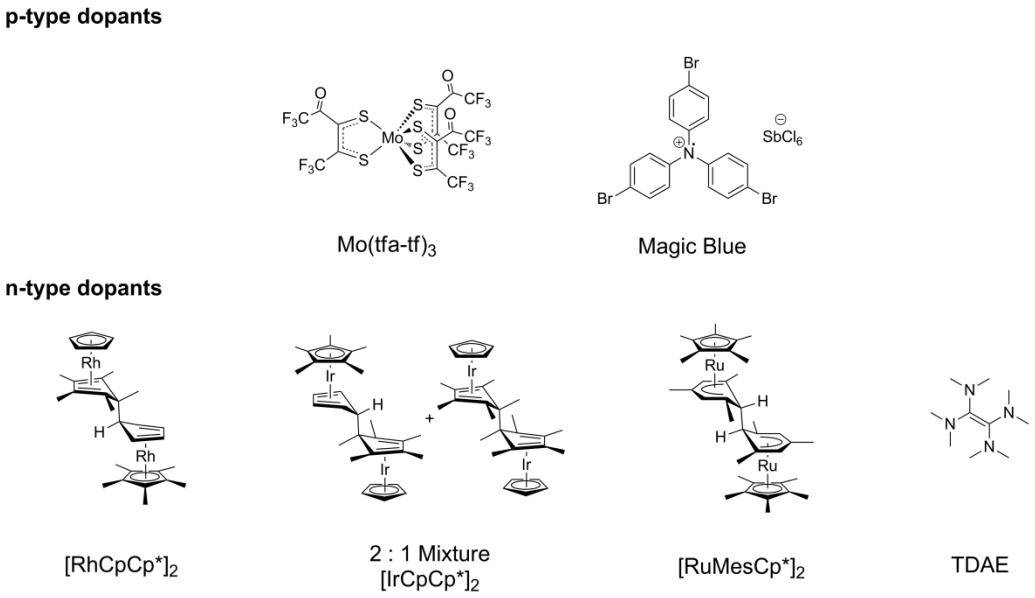

Figure 5.5 Summary of p- and n-dopants that were used in the treatment of ITO, ZnO, and gold surfaces. Abbreviations for these materials are also provided.

A comparison of redox potentials for some of the materials shown in Figure 5.3 and Figure 5.5 are provided in Figure 5.6. It should first be noted that in the case of the dimer materials both the oxidation of the dimer, generalized as $[M]_2$, and the oxidation of its monomer, $[M^+/M]$, are noted. For these materials, in order to represent the effective redox potential for the $[M^+ / \frac{1}{2} M_2]$ couples, $E_{eff}[M^+ / \frac{1}{2} M_2]$, this can be done according to the following equation using electrochemical potentials for the reduction of the monomer cation to the monomer and estimates of ΔG_{diss} based on DFT calculations.[38]

$$E_{eff}\left(M^+/\frac{1}{2}M_2\right) = E(M^+/M) + \left(\frac{1}{2F}\right)\Delta G_{diss}(M_2) \qquad \text{Equation 5.1}$$

Thus, the dimer materials have similar effective dopant strength (assuming thermodynamic completion and no hindrance based on kinetic considerations) that are all larger than for materials such as MV0 and TDAE. In the case of the p-dopants, while

there is still variation, the materials are relatively close to one another in terms of their first reduction potential.

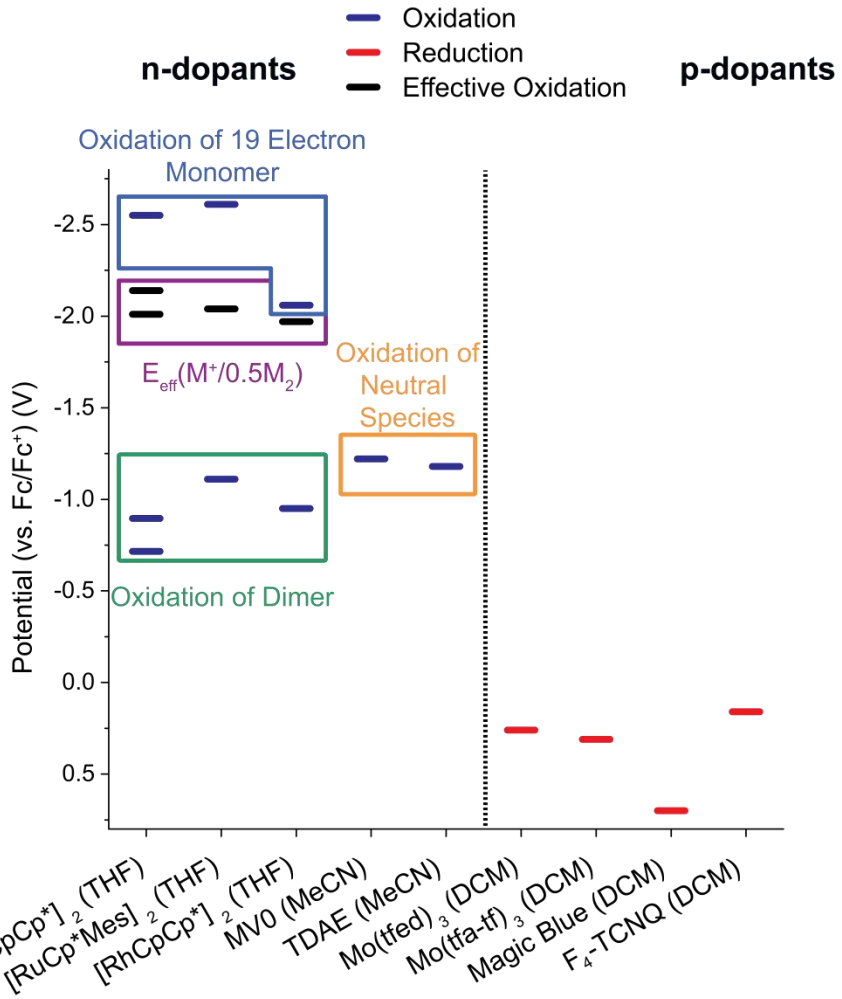

Figure 5.6 Electrochemical potentials for materials investigated in this chapter as well as for materials previously used in the literature to treat surfaces. The solvent in which the electrochemical data was collected is noted. In the case of the n-type dimer materials, the oxidation of the dimer $[M]_2$ and the more reactive monomer $[M^+/M]$ are shown. Also shown is the thermodynamic estimate of doping strength, $E_{eff}(M^+/0.5M_2)$, as afforded from Equation 3.3 based on electrochemical data and DFT calculations (two values are reported for $[IrCpCp^*]_2$ as the dominant isomer and the minor isomer afford slightly different values for both dimer oxidation and effective oxidation.[38] In the case of p-type materials, only first reduction potentials are reported. All potentials reported are *vs.* the ferrocenium/ferrocene (Fc^+/Fc) couple. References for data are as follows: $[RuMesCp^*]_2$,[8, 35] $[RhCpCp^*]_2$,[35] MV0,[39] TDAE,[40-41] $Mo(tfd)_3$,[33] $Mo(tfa\text{-}tf)_3$,[42] Magic Blue,[43] F_4-TCNQ.[33, 44]

5.3 n-Doping of Metals and Metal Oxides with Metal-Organic Species

5.3.1 Surface Treatment

Surfaces of smooth ITO, atomic layer deposition (ALD) ZnO, and gold were obtained. After appropriate cleaning steps, as detailed in the experimental section of this chapter (5.6), samples were transferred into a nitrogen filled glove box. Even though the dimers and monomer cations are air stable, the low WF surface (ITO, gold, ZnO) after modification is air sensitive (5.3.3.3), which is why sample treatment took place inside the glove box using anhydrous, oxygen-free toluene. Toluene was chosen for these studies since the dimers have good solubility in it, and it is possible to easily purify toluene to obtain anhydrous, oxygen-free solvent. After surfaces were immersed in dilute solutions of the dimers in toluene for short amounts of time (60 s, or 1 h), they were rinsed to remove any material that was physisorbed to the surface. Samples were then taken for XPS/UPS for analysis using a nitrogen filled transfer arm, which allowed for sample transport without exposure to air. It is important to note that for each experiment collection of XPS/UPS data occurred using the bare substrate. This substrate would then be transferred into the glove box for treatment (it was noted the glove box antechamber pump-fill cycles introduced contaminants on clean surfaces so samples were brought into the box inside of the transfer arm), and after modification that same sample would then be measured by XPS/UPS.

5.3.2 XPS Analysis

5.3.2.1 XPS Analysis of ITO Treated with $[IrCpCp^*]_2$

As described in 5.3.1 ITO surfaces were treated with $[IrCpCp^*]_2$ by immersion in dilute toluene solutions (typically 2 mM) for both 60s and 1 h. Even with such short modification times, drastic changes in the WF were observed as will be discussed later in 5.3.3. XPS analysis of surfaces after treatment indicated the presence of Ir, and a comparison of the survey spectra and high-resolution Ir 4f region for both freshly cleaned ITO and ITO treated with $[IrCpCp^*]_2$ are shown in Figure 5.7 and Figure 5.8, respectively. It should be noted that the Ir 4f peak was chosen as the peak by which modification of the surface would be tracked as it has a higher ionization cross section than the Ir 4p, Ir 4d, and Ir 4s peaks, which is of particular importance when looking at a monolayer or less of material. It should also be noted that while Ir 4d peaks could be observed, their proximity to peaks originating from C 1s can make quantification more difficult.

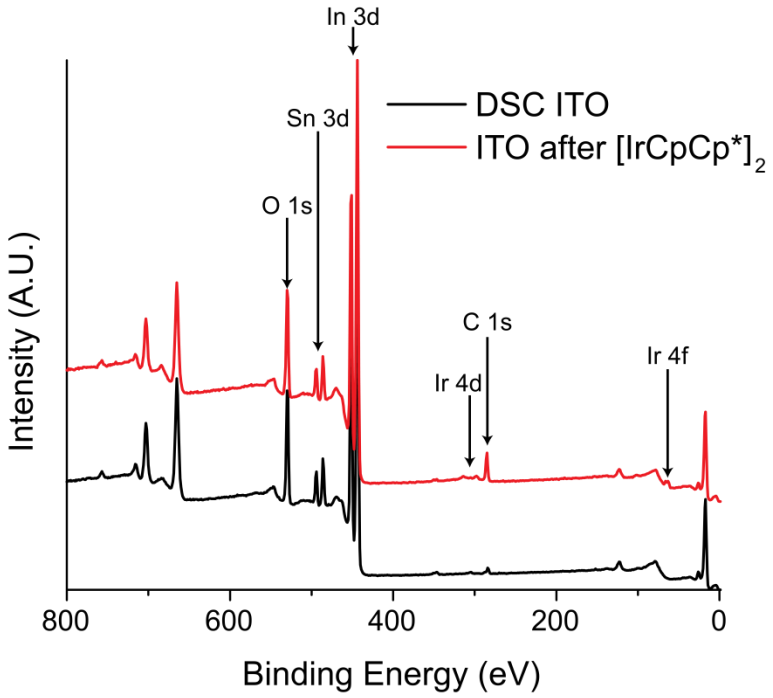

Figure 5.7 Comparison of survey spectra obtained by XPS. Spectra shown are for an ITO sample that was initially detergent solvent cleaned and subsequently immersed in a 2 mM solution of $[IrCpCp^*]_2$ in anhydrous toluene for 1 h. Important core ionizations are labeled. Spectra have been normalized and offset for clarity.

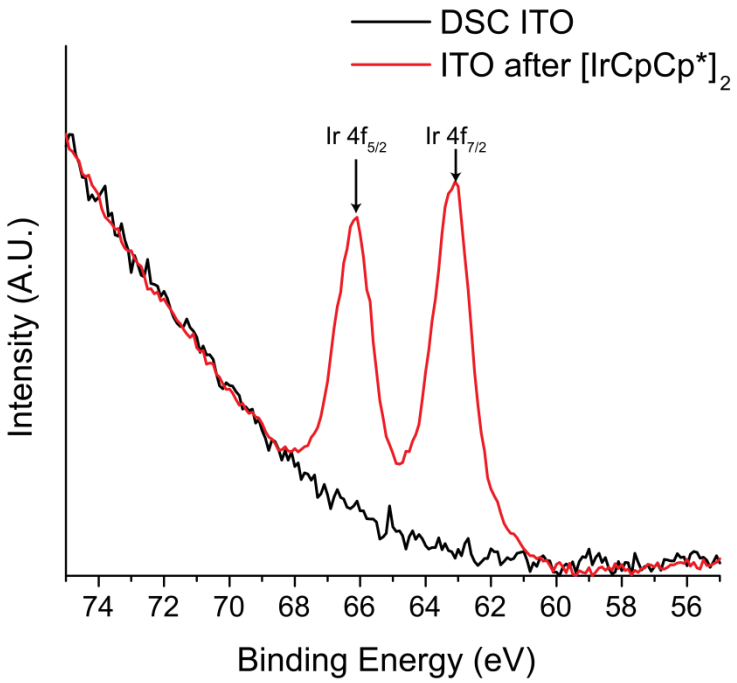

Figure 5.8 Comparison of high-resolution spectra obtained by XPS in the region where Ir 4f ionizations typically occur. These high resolution spectra correspond to the same sample used to obtain Figure 5.7. Note that there is no Ir present on the surface of ITO prior to treatment with $[IrCpCp^*]_2$. Spectra have been normalized.

As previously reported, dimers such as those being investigated can react with acceptors to form 2 monomer cations.[8, 35, 37] In the dimer form, the Ir in the metal-organic complex exists as Ir (I). However, the Ir in the monomer cation is Ir (III). In order to probe whether the dimer or monomer cation form of the complex was present on ITO after treatment with the dimer solution, high-resolution XPS analysis was conducted. Figure 5.9 shows a comparison of ITO that was treated with $[IrCpCp^*]_2$ for either 60 s or 1 h as well as a thick, drop-cast film of the dimer on top of ITO. The data shows that the drop-cast film is mainly Ir (I), meaning that essentially only dimer is present. There is a small shoulder originating from Ir (III), which is likely due to the small amount of the film that was able to interact with the surface, and thus form a monomer cation. In the

case of the ITO that was immersed in a solution of the dimer, there appears to be only Ir (III) present on the surface, which is consistent with the formation of a cationic monomer on the surface of ITO. It should be noted that the peak positions for Ir (I) and Ir (III) are consistent with other Ir (I) and Ir (III) complexes found in the NIST spectral database.[45]

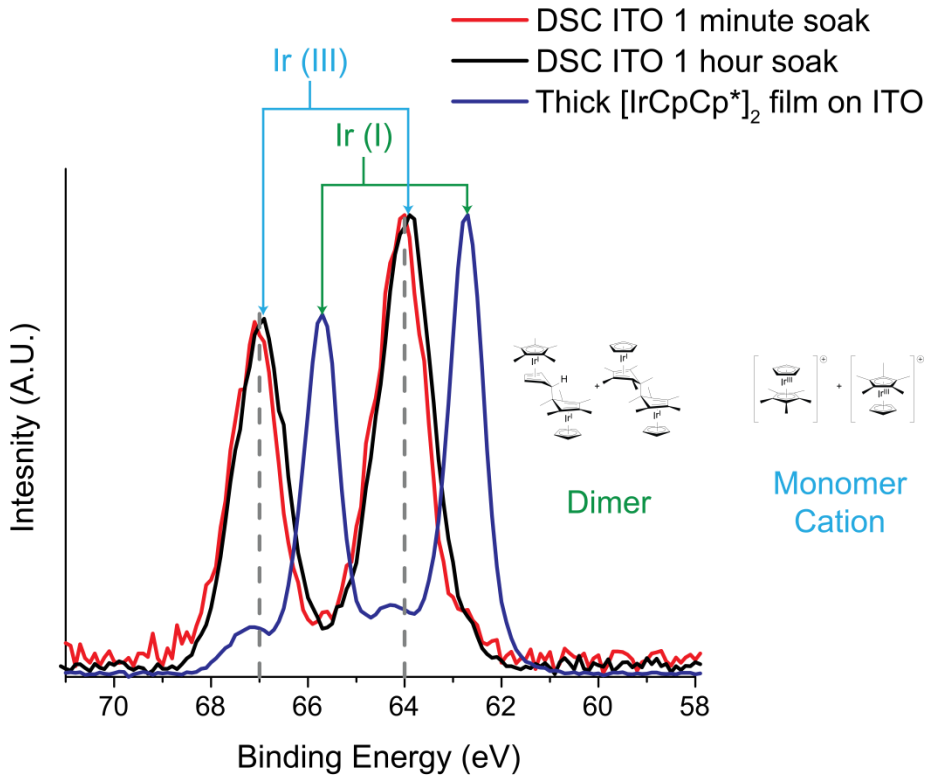

Figure 5.9 XPS high-resolution Ir 4f spectra (shown are the Ir $4f_{5/2}$ and $4f_{7/2}$ peaks) comparing DSC ITO that was treated for either 60 s or 1 h with a 2 mM solution of $[IrCpCp^*]_2$ in anhydrous toluene. Also shown is a DSC ITO sample onto which was drop-cast a thick film of $[IrCpCp^*]_2$ from a concentrated solution in anhydrous toluene. There is good agreement between the high binding energy shoulders present in the thick film, correspond with what is observed for the solution soaked samples, thereby indicating the presence of monomer cation on the surface after treatment. The structure of $[IrCpCp^*]_2$ and its monomer cation form are also shown, and the labeled oxidation states color coded to correspond with the structures shown (inset). Spectra have been normalized.

Since it is evident that monomer cations are present on the surface of ITO after treatment in solutions of the dimers, attempts were made to examine if it could be determined by XPS where the donated electrons were in the ITO substrate. There are several possibilities as to where the electrons could be located after donation including: localization on In sites, localization on Sn sites, delocalized within In states close to/in the conduction band, or conversion of surface hydroxyl groups to negatively charged oxygen groups with the concomitant loss of molecular hydrogen. As indium is the main component in ITO, it would be anticipated to be the most likely recipient of electrons transferred from $[IrCpCp^*]_2$. If reduction of ITO by the dopant does take place, it should be possible to observe the change in oxidation state based on XPS analysis, with the reduced form of In expected to move toward lower binding energy. Unfortunately, however, examination of the In 3d peak before and after treatment did not show any significant shifts (e.g any shifts beyond what can be observed in variation of peak position from spot to spot on the same sample). Attempts were also made using angle-resolved XPS to enhance the surface sensitivity of the technique (by minimizing the amount of bulk ITO that is probed during the analysis) by acquiring data at an incidence angle of 70°, but this data also did not provide any reliable peak shifts. It should also be noted that an examination of Sn 3d peaks in a similar manner showed no evidence of shifts in position. Thus, while there clearly is an electron being transferred from the monomer to the surface, there are two possibilities as to why this core-level shift cannot be observed. One possibility is the electron transfer may be extremely delocalized and thus In atoms at the surface are seeing partial electron transfer leading to only subtle shifts in the spectra smaller than the instrumental error. Another possibility is that even

at a take-off angle of 70° there is still too much bulk ITO being probed, which is masking the reduced form of In (which exists directly at the surface) from being readily observed. In lieu of XPS data showing electron transfer data, UPS will have to be used, specifically looking at shifts in VBM as discussed in 5.3.3.

In order to probe how much of the monomer cation was present on the surface after treatment, XPS analysis was used to calculate the coverage of the modifier in the same manner as that used for phosphonic acids on ITO (3.6). In order to use an Ir/In ratio (analogous to F/In ratios used for phosphonic acids) to calculate coverage, the density of the monomer in a close-packed arrangement needed to be determined. This would thus allow a theoretical Ir/In ratio for an ideal monolayer to be obtained, and subsequently be compared with the experimentally determined ratio. Note this assumes a vertical cation orientation relative to the surface normal. Based on a Spartan model of the monomer cation, the radius of the monomer was determined to be 4.487 Å (the average distance from the centroid of the molecule to outer hydrogen atoms in the Cp* ring plus the Van der Waals radius of hydrogen) meaning that the area of molecule would be 63.25 $Å^2$. However, when the close-packing of the molecule is considered, the direct molecular footprint underestimates the area taken up by one molecule as there is empty space between molecules. Figure 5.10 illustrates this packing arrangement of the monomers, and shows the unoccupied space as well as the more representative area (which includes this empty space) as bounded by the parallelogram. This area is thus calculated to be 69.8 $Å^2$. Again, using the model of ITO developed by the Bredas group[46] (3.6) and a sample information depth of 3λ (8.4 nm) it can be determined that for every Ir atom there are 139 In atoms present in the volume bounded by the monomer cation footprint and

sample information depth. Correcting the theoretical Ir/In ratio to compare with the experimental Ir/In data affords the coverage values summarized in Table 5.2 for DSC ITO after 60 s and 1 h of dopant treatment and plasma cleaned ITO after 60 s of dopant treatment. Note XPS data was collected on three distinct spots and percent coverage reported is the average of the three spots. The variation in spot to spot percent coverage as determined by the standard deviation was less than ± 9 % in all cases. Based on this data it appears that the dopants produce monolayer to sub-monolayer coverage depending on the modification conditions and surface pre-treatment used.

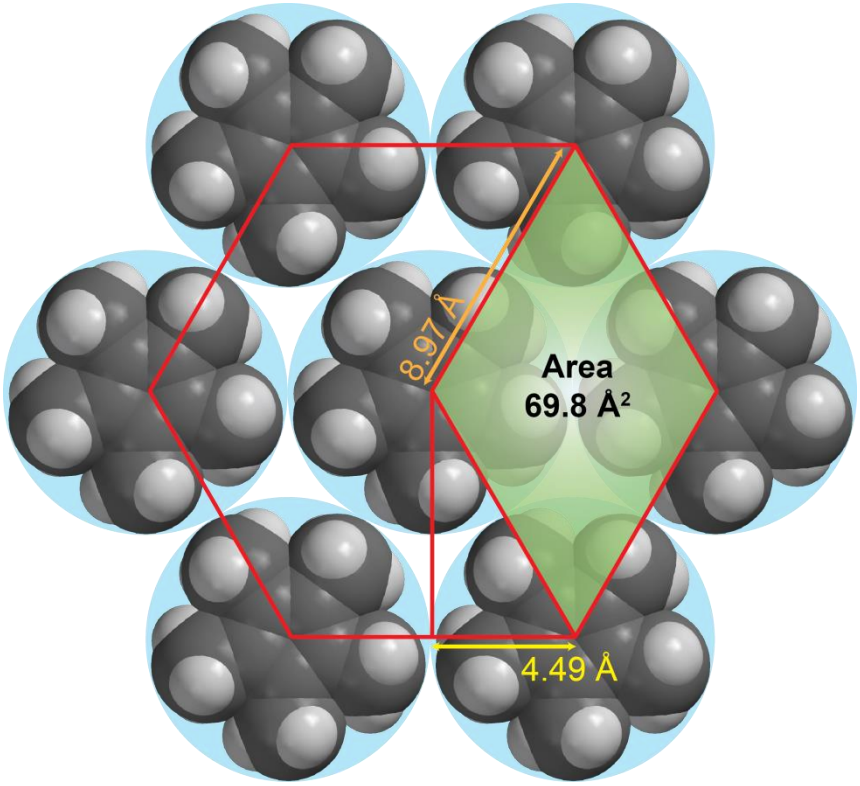

Figure 5.10 Monomer cation of $[IrCpCp^*]_2$ as a space-filling model in a close-packed geometry (represented by the red line). The radius of the molecule is shown in yellow and the centroid-to-centroid distance is shown in peach. The area formed by the light green shaded rhombus best represents the molecular footprint, taking into account the hexagonal packing that is shown.

Table 5.2 Comparison of $[IrCpCp^*]^+$ coverage on either plasma or detergent solvent cleaned ITO treated with a 2 mM solution of $[IrCpCp^*]_2$ under the conditions shown. The coverage values are expressed in both percent coverage (percent of an ideal monolayer) and absolute coverage (molecules/cm^2). Coverage values obtained from a comparison of Ir/In atomic ratios obtained from XPS data with Ir/In ratio obtained from a theoretical slab of ITO.

ITO Cleaning	**$[IrCpCp^*]_2$ Treatment Conditions**	**Molecular Footprint ($Å^2$)**	**Ideal Coverage (10^{14} molecules/cm^2)**	**Experimental % Coverage**	**Experimental Coverage (10^{14} molecules/cm^2)**
DSC	2 mM, 60 s	69.8	1.43	73 %	1.04
DSC	2 mM, 1 h			92 %	1.32
Plasma	2 mM, 60 s			93 %	1.33

5.3.2.2 XPS Analysis of ITO Treated with $[RuMesCp^*]_2$ and $[RhCpCp^*]_2$

A similar analysis to that discussed in 5.3.2.1 was conducted for ITO treated with the two other dimers in order to confirm modification of the surface as well as calculate coverage of the monomer cation that subsequently forms after treatment in the solution of dimer. Using DSC ITO, substrates were soaked in a 2 mM solution of $[RuMesCp^*]_2$ or $[RhCpCp^*]_2$ for 60 s or 10 s, respectively. Survey spectra comparing DSC ITO and DSC ITO after treatment with the Ru and Rh dimers are shown in Figure 5.11. High-resolution spectra showing the Ru 3d and Rh 3d peaks are shown in Figure 5.12. In the case of the Rh dopant, both Rh (III) and Rh (I) were observed on the surface, which is consistent with the report of monolayer to sub-monolayer coverage of the dopant on graphene.[37] In the case of the Ru dopant, however, no oxidation state change occurs between the dimer form and the monomer cation form. Thus, it is not possible to explicitly state that the monomer cation form is on the surface, but based on observations and the comparable WF modifications (5.3.3) found with the different dimers, it is assumed that the monomer cation for the Ru dopant also formed on ITO.

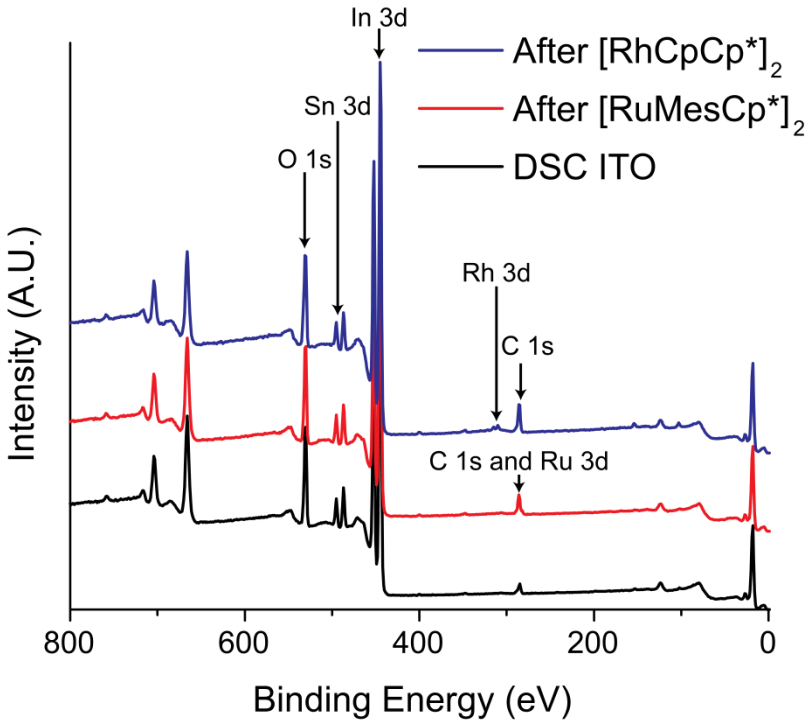

Figure 5.11 XPS survey spectra for DSC ITO and ITO after treatment in 2 mM solutions of $[RuMesCp^*]_2$ and $[RhCpCp^*]_2$ for 60 s or 10 s, respectively. Note in the case of the Ru dopant, the Ru 3d peak occurs in the same area as the peak originating from C 1s. Also note that in the case of the Rh dopant, there are peaks originating from Si 2s and Si 2p (~150 and 100 eV, respectively). These peaks originate from contamination due to the antechamber of the glovebox (silicon oil) and was how (as mentioned previously) it was determined substrates should not be directly exposed to the antechamber of a glove box.

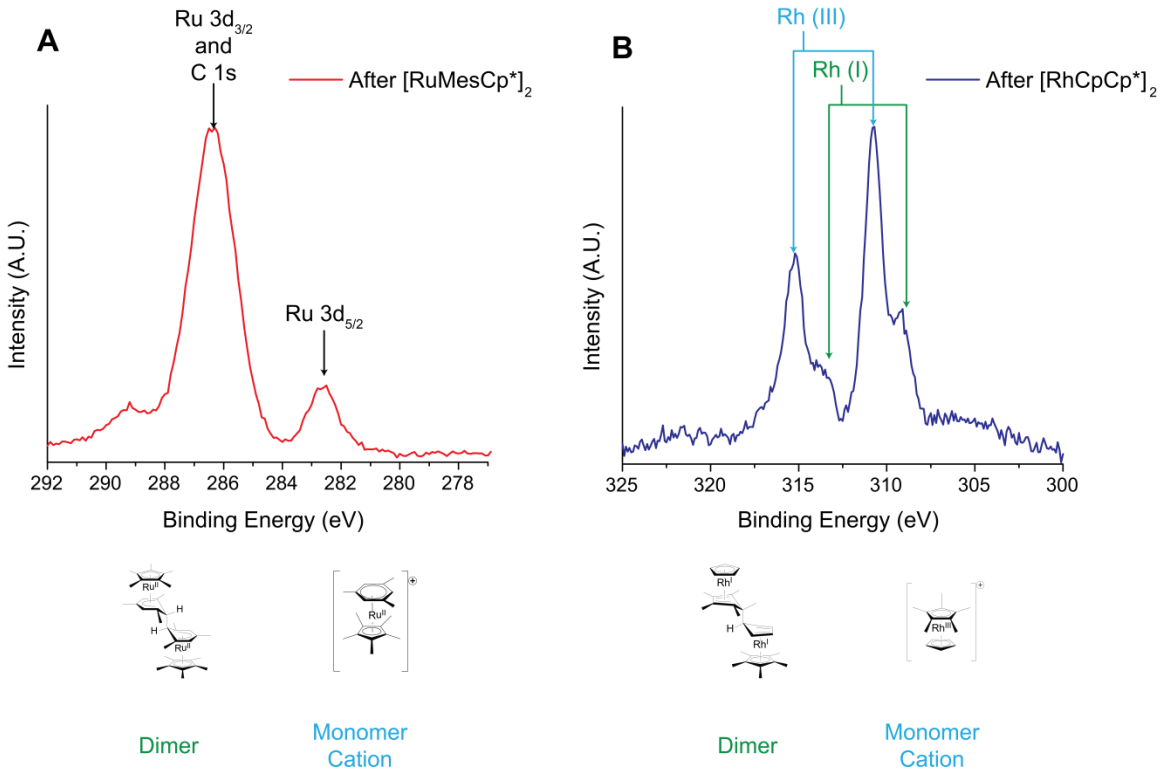

Figure 5.12 High resolution spectra acquired by XPS after DSC ITO was treated with the Ru (**A**) and Rh (**B**) dimers. The respective dimer and monomer cations are shown below the spectral data for each dopant. In the case of the Ru dopant, no oxidation state change occurs when going from the dimer to the cation form. Also it should be noted that only the Ru $3d_{5/2}$ peak is visible since the Ru $3d_{3/2}$ peak overlaps with the C 1s peak. In the case of the Rh dimer, both the dimer as Rh (I) and the cation as Rh (III) are present on the surface, which is consistent with what was observed with this dopant on graphene.[37]

Calculation of coverage for the Ru and Rh dopants on the surface of ITO was also conducted in a manner similar to that discussed in the previous section for $[IrCpCp^*]^+$ on ITO. The coverage data for these two dopants is summarized in Table 5.3 with a similarly prepared ITO sample treated with $[IrCpCp^*]_2$ shown for reference. As can be seen, the coverage values for the Ir and Rh dopants are relatively similar, while the Ru dopant is much lower. This change in coverage is likely due to the difference in structure of the Ru dopant from the other materials tested, namely the presence of a mesitylene

group rather than a cyclopentadiene. While this group does not vastly change the molecular footprint of the vertically standing molecule, there is a delicate balance of factors affecting the orientation of organometallic sandwich compounds with respect to inorganic surface layers and thus it is possible to have the molecule laying on the surface such that the Cp and Cp* rings are parallel to the surface normal rather than the assumed perpendicular orientation.[47] This would then lead to a lower overall packing density. It should be noted that because of the presence of more than just the monomer cation (e.g. the presence of the shoulder from the Rh (I) dimer), the Rh coverage is likely overestimated slightly. In all cases, however, less than a monolayer of material was deposited on the surface. It should also be noted that for the Rh dimer on graphene, a similar coverage was observed (75 % of a monolayer).[37]

Table 5.3 Comparison of coverage values for DSC ITO treated with 2 mM solutions of $[IrCpCp^*]_2$, $[RuMesCp^*]_2$, and $[RhCpCp^*]_2$ for 60 s. The coverage values are expressed in both percent coverage (percent of an ideal monolayer) and absolute coverage (molecules/cm^2). Coverage values obtained from a comparison of M/In (where M = Ir, Ru, or Rh) atomic ratios obtained from XPS data with M/In ratio obtained from a theoretical slab of ITO.

Dopant	**Molecular Footprint ($Å^2$)**	**Theory M/In Ratio**	**Ideal Coverage (10^{14} molecules/cm^2)**	**Experimental % Coverage**	**Experimental Coverage (10^{14} molecules/cm^2)**
$[IrCpCp^*]_2$	69.8	1/139	1.43	73 %	1.04
$[RuMesCp^*]_2$	71.1	1/153	1.41	30 %	0.42
$[RhCpCp^*]_2$	71.0	1/151	1.41	94 %	1.32

5.3.2.3 XPS Analysis of Au and ALD ZnO Treated with $[IrCpCp^*]_2$

The $[IrCpCp^*]_2$ dimer was also used to treat surfaces of atomic layer deposition (ALD) ZnO and gold in order to examine the impact one of the dopants had on another

metal oxide as well as a metal. Both gold and ZnO surfaces were treated in the same manner as the ITO substrates (with the exception of the initial surface cleaning as noted in the experimental section, 5.6). A comparison of survey spectra before and after modification for these surfaces is shown in Figure 5.13. As can be seen, both surfaces were successfully modified with the dimer as observed by the presence of Ir peaks in the spectra after treatment. High-resolution Ir 4f spectra are also shown in Figure 5.13. Coverage values for these surfaces, however, could not be readily calculated. In the case of ZnO (as discussed in 4.5.1), the ALD ZnO surface is granular in nature (Figure 4.7). Thus, while the theoretically calculated surface matches that of the favored orientation of the polycrystalline ALD ZnO film (the (0002) plane), it does not take into account the geometry of the surface (partially exposed spheres) and thus the experimental surface has more surface area that can be accessed by modifiers than the calculated surface. This means that the theoretical Ir/Zn ratio would be underestimated compared with the experimental surface and apparent coverage values would have limited utility. In the case of the Au surfaces, the experimental values for the Ir/Au are overestimated due to the fact that the Ir ionizations (both the Ir 4d and Ir 4f) overlap with the onset of the analogous gold peaks (Au 4d and Au 4f) and in the shake ups of other peaks (C 1s for Ir 4d and Au 5p for Ir 4f). This means that the integrated values will be overestimated and thus comparing an experimental Ir/Au ratio to that calculated from a theoretical model affords data that is not reliable. In both cases, however, there appears to be only the Ir (III) oxidation state present on the surface, which, based on the ITO data, is indicative of a monolayer or less of the monomer cation on the surface of either ZnO or Au.

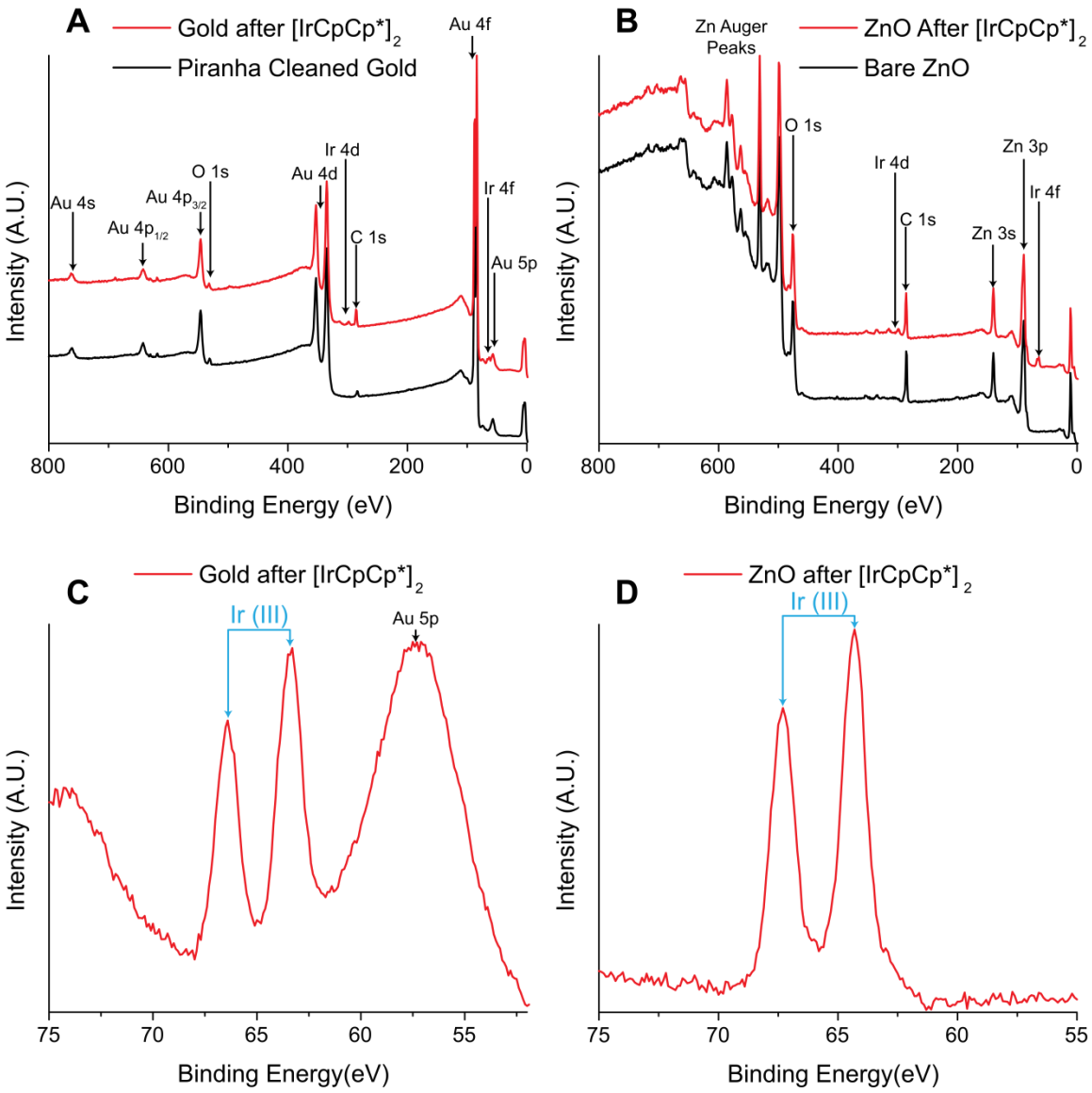

Figure 5.13 Comparison of survey and high-resolution Ir 4f spectra from XPS analysis for Au (**A** and **C**) and ZnO (**B** and **D**) after treatment with $[IrCpCp^*]_2$ (2 mM in anhydrous toluene for 60 s). In the case of the Au substrate the Ir 4f peak occurs at the tail of the Au 5p and the onset of the Au 4f peak making reliable quantification difficult. For both the Au and ZnO treated surfaces, the Ir present appears to originate only from the Ir (III) oxidation state, indicating the presence of monomer cation on the surface. Survey spectra have been normalized, offset, and core ionizations labeled for clarity.

5.3.3 UPS Analysis of ITO, ZnO, and Au Treated with n-Dopants

5.3.3.1 Work Function Modification by n-Dopants

In order to examine the impact the surface modifiers have on the WF of the substrate (ITO, ZnO, or Au) UPS was used to examine shifts in the secondary electron edge and obtain WF values before and after modification. A summary of these WF values for different modification conditions and different substrates is shown graphically in Figure 5.14. In all cases, the bare substrate was measured prior to modification, the sample was treated, and the same sample was then examined again after modification. All UPS analysis was conducted prior to XPS analysis and each data point is the average of at least 7 spots measured on each surface with the error bar originating from the spot to spot standard deviation. The measured values are also summarized in Table 5.4 along with the change in WF after treatment of the surface with the dopant.

Table 5.4 Summary of experimental UPS data shown in Figure 5.14 along with the change in WF after modification.

Substrate	Cleaning Protocol	Immersion Time	Dopant	WF before Modification (eV)	WF after Modification (eV)	ΔWF (eV)
ITO	DSC	10 s	Rh	4.57 ± 0.06	3.67 ± 0.07	-1.00
	DSC	60 s	Ru	4.53 ± 0.04	3.46 ± 0.07	-1.07
	DSC	60 s	Ir	4.63 ± 0.04	3.29 ± 0.08	-1.34
	Plasma	60 s	Ir	5.29 ± 0.06	3.69 ± 0.03	-1.60
	DSC	1 h	Ir	4.78 ± 0.04	3.45 ± 0.06	-1.33
ZnO	Solvent Rinse	60 s	Ir	3.90 ± 0.02	3.40 ± 0.04	-0.50
		1 h	Ir	3.88 ± 0.04	3.30 ± 0.10	-0.58
Gold	Piranha	60 s	Ir	5.22 ± 0.03	3.35 ± 0.03	-1.87

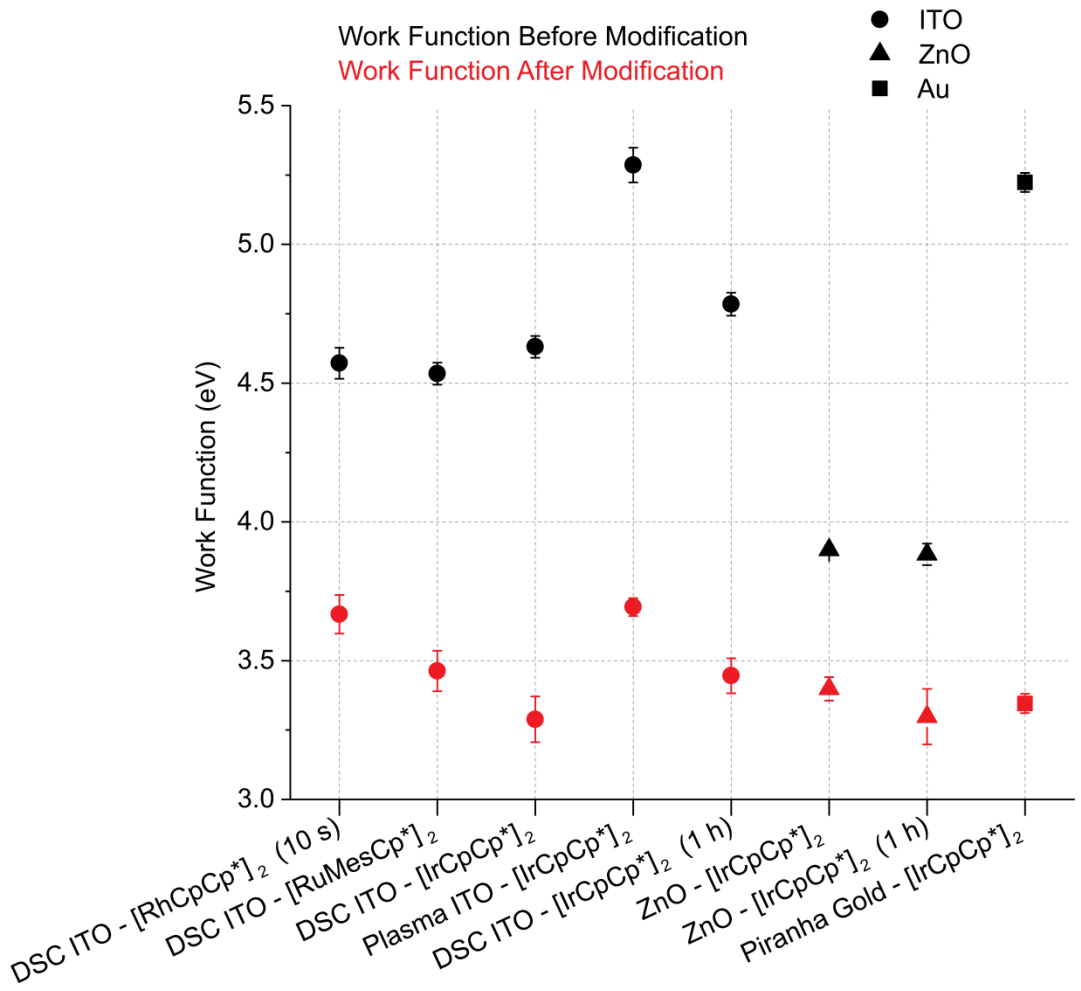

Figure 5.14 Comparison of WF values for ITO, ZnO, and gold with the noted n-dopants. All samples were treated for 60 s in the solution of the dopant unless otherwise noted on the graph. Cleaning protocols included detergent solvent cleaning or plasma cleaning for ITO, rinsing with ethanol for ZnO, and piranha cleaning for the gold surface. Substrates were examined in a minimum of 7 spots to ensure consistency of the data over the whole surface. Red data points indicate a measurement after modification and black data points indicate measurements prior to modification. Different shapes correspond to different substrate types as shown in the legend.

The data shows that all three surfaces showed substantial decreases in WF after treatment with the Ir dimer. The largest shifts were observed for plasma-cleaned ITO and piranha-cleaned gold (-1.60 and -1.87 eV, respectively) which demonstrates that even

high WF materials can see significant reduction in WF. In the case of ITO, all three n-dopants showed similar WF reductions on the order of 1.0 to 1.3 eV from the bare substrate, which is to be expected based on the similarity of the calculated effective redox potentials as shown in Figure 5.6. It appears that the Ir dopant has a larger impact on the WF compared with its Rh and Ru counterparts. It is, however, important to point out that factors such as coverage (in the case of the Ru dopant), which can impact the number of electrons transferred and therefore the magnitude of the interface dipole, and modification time (in the case of the Rh dopant) also likely influence the ability of the material to cause a change in the WF. Thus, a more thorough, direct comparison between the three materials would be needed in order to draw reliable conclusions regarding the origin of this difference in WF reduction. In the case of the Ir dopant, it appears that while modification time did have an impact on the coverage of the monomer cation (as shown for ITO) it does not influence the change in WF. This trend regarding treatment time is consistent for both ZnO and ITO. It appears that the use of $[IrCpCp^*]_2$ and similar dimers affords a reliable method by which to reduce the WF of metals and metal oxides without the need for vapor deposition of the dopant.

While it is possible to compare the WF values obtained above with those reported in the literature (summarized in Table 5.1), such a comparison must be done with the caveat that the dimer materials were deposited from solution soaking and materials such as TDAE, MVO, and AOB were vacuum deposited. Thus, in order to have a direct comparison both TDAE and $[IrCpCp^*]_2$ were used to treat the surface of DSC ITO using 2 mM solutions in anhydrous toluene for 60 s. An ITO sample was also soaked overnight in a 10 M solution of NaOH to examine what changes happen in the presence of base in

an attempt to mimic what would happen if the dimers or TDAE are reacting with hydroxyl groups on the surface of ITO. The WF values before and after treatment are summarized in Table 5.5. The data shows that TDAE does decrease the WF of ITO as expected, but not to as large an extent as that of the Ir dimer treated surface. It should also be noted that the final WF value obtained for the TDAE treated ITO is similar to that reported in the literature of 3.7 eV for vapor deposition. In the case of the base-treated surface, there is essentially no change between the surface before NaOH treatment, and the surface after treatment with the base.

Table 5.5 Comparison of WF values before and after treatment of DSC ITO with $[IrCpCp^*]_2$ (2 mM, 60 s), TDAE (2 mM 60 s), and NaOH (10 M, overnight). Error bar originates from standard deviation over 7 spots on each surface.

Modifier	**WF Before Treatment (eV)**	**WF After Treatment (eV)**	**ΔWF (eV)**
$[IrCpCp^*]_2$	4.63 ± 0.04	3.29 ± 0.08	-1.34
TDAE	4.57 ± 0.06	3.87 ± 0.06	-0.70
NaOH	4.28 ± 0.02	4.23 ± 0.03	+0.05

5.3.3.2 Interface Dipole Contribution from Monomer Cation Species on the Surface

Now that the WF modification had been confirmed and demonstrated to be a reliable and substantial reduction in WF compared with bare surfaces for both metals and metal oxides, it was necessary to use UPS to examine the interface dipole contribution to the WF shift. Examination of shifts in the VBM is a way to distinguish between changes to the Fermi level relative to the band structure from changes in the Fermi level due to the presence of an interface dipole. Figure 5.15 summarizes the VBM values before and after treatment of ITO and ZnO. Table 5.6 then takes the values shown in Figure 5.15 along with the ΔWF values from Table 5.4 to afford the interface dipole contribution

(ΔWF + ΔVBM). This table shows that the majority of the change in WF originates from the formation of an interface dipole once the monomer cation is on the surface of the substrate and that only a small contribution comes from movement of the VBM relative to the Fermi level. Thus, the cationic monomers are likely electrostatically bound to the surface of the substrate, which forms an interface dipole and leads to an observed decrease in the WF. This observation is consistent with what has been observed in the literature for MV0[25] and TDAE[26, 28] where n-dopants lead to the formation of cationic species on the surface and thus an interface dipole with the positive pole pointing away from the surface.

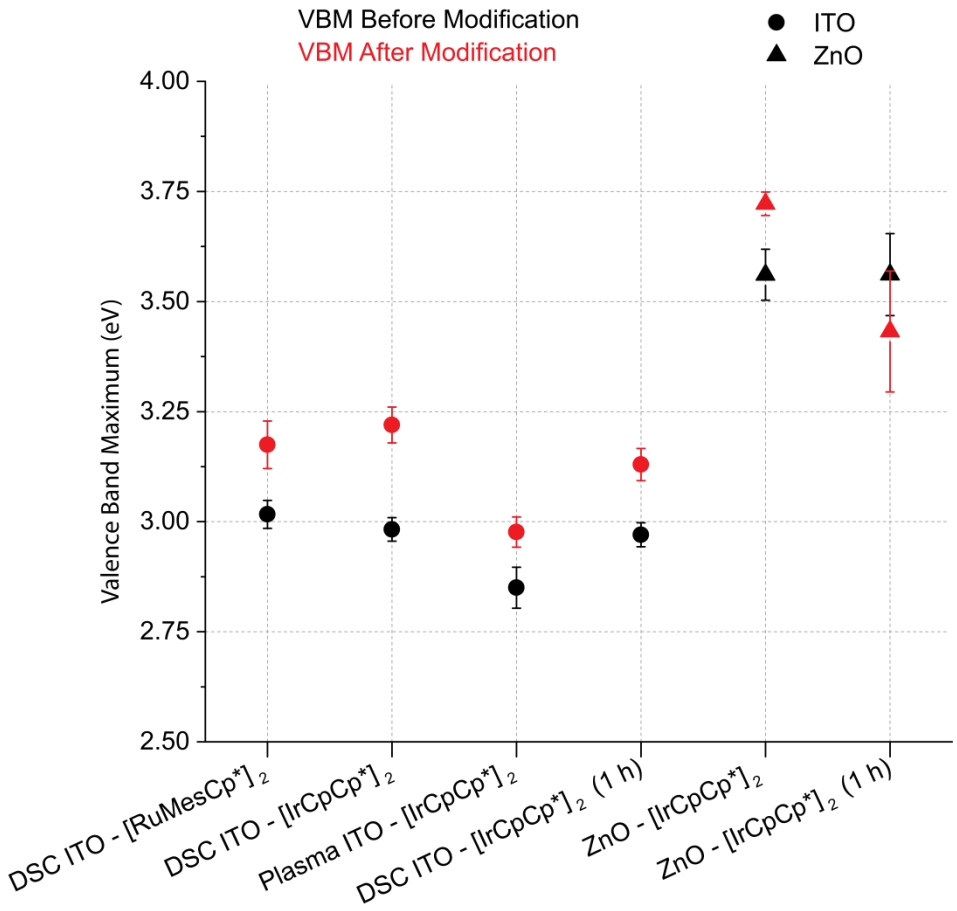

Figure 5.15 Valence band maximum values for ITO and ZnO surfaces before and after treatment under the noted modification conditions. Values shown are with respect to the Fermi level. As gold is a metal it has no clear VBM, only a Fermi level step, and thus no shift was observed.

Table 5.6 Summary of VBM values shown in Figure 5.15 to obtain changes in VBM (ΔVBM) along with changes in WF (ΔWF), which afford the interface dipole contribution to the shift in WF (ΔWF + ΔVBM).

Surface	VBM Before (eV)	VBM After (eV)	ΔVBM (eV)	ΔWF (eV)	Interface Dipole Contribution (eV)
DSC ITO $[RuMesCp^*]_2$ (60 s)	3.02 ± 0.03	3.17 ± 0.05	+0.15	-1.07	-0.92
DSC ITO $[IrCpCp^*]_2$ (60 s)	2.98 ± 0.03	3.22 ± 0.04	+0.24	-1.34	-1.1
Plasma ITO $[IrCpCp^*]_2$ (60 s)	2.85 ± 0.05	2.98 ±0.03	+0.13	-1.60	-1.47
DSC ITO $[IrCpCp^*]_2$ (1 h)	2.97 ± 0.03	3.13 ± 0.04	+0.16	-1.33	-1.17
ZnO $[IrCpCp^*]_2$ (60 s)	3.56 ± 0.06	3.72 ± 0.03	+0.16	-0.50	-0.34
ZnO $[IrCpCp^*]_2$ (1 h)	3.56 ± 0.09	3.43 ± 0.14	-0.13	-0.58	-0.71

5.3.3.3 Work Function Stability in Air after Modification

Since n-dopants such as TDAE, MV0, or the 19-electron monomer species of the dimers are unstable in air, readily oxidizing due to the presence of oxygen and water, it is important to determine whether, after the surface modification has taken place (under inert atmosphere), the shift in WF remains upon exposure to air. In order to probe this question, both surfaces of ITO and ZnO treated with $[IrCpCp^*]_2$ were exposed to air for various amounts of time and the WF examined after each exposure. In order to obtain this data, the as prepared samples were removed from UHV and brought up to atmosphere under a blanket of nitrogen. The sample was then exposed to air for the

given amount of time and then immediately returned to UHV for analysis. The same substrate in each case was tracked throughout the air exposure process. The data tracking changes in WF with air exposure are shown in Figure 5.16 and indicate that the initial large change in WF occurs within the first minutes of air exposure, regardless of substrate, and that the WF increases by about half the value of the initial decrease (~ 0.5 eV for ITO and ~ 0.3 eV for ZnO) within this short amount of time. After that point, the WF stabilizes at around 4 eV for both surfaces. The same ITO sample shown in Figure 5.16 was also examined after a total of 12 days of air exposure and a WF of 3.90 ± 0.09 eV was obtained. A similarly prepared ITO sample was also examined after 30 days of storage within a glove box (typically ~ 1 ppm O_2) and there was also an observed increase in WF from an initial value after treatment of 3.3 eV to 3.7 eV, which is on the order of the change observed for the 5 min of air exposure. TDAE treated ITO has also been reported to undergo changes in WF after exposure to air.[28] It is important to note that in all these cases for ITO, the final WF value is still well below that of DSC ITO, but in the case of ZnO, where the initial starting WF is much lower, the final WF after air exposure stabilizes around the starting value. A comparison of the XPS Ir 4f peaks for these samples (Figure 5.17) shows a very small shift to lower binding energy values of ~0.2 eV. When compared to the dimer form, however, the Ir species still exist as monomer cations and are stable on the surface at long exposure times, which is to be expected based on the chemical stability of the 18-electron monomer cations (for instance $IrCpCp^{*+}PF_6^-$ is completely stable in air).

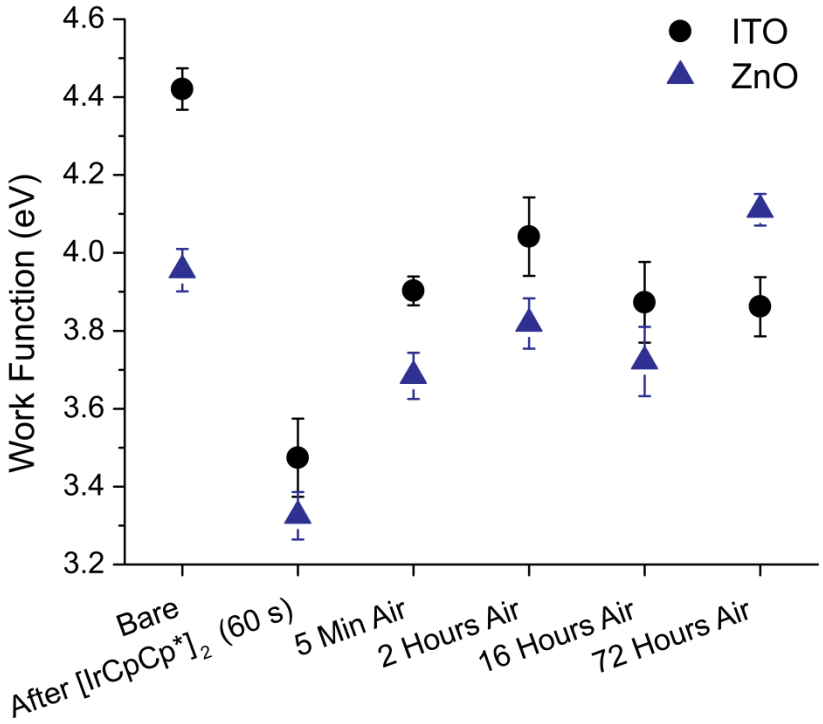

Figure 5.16 Summary of WF shifts for ITO and ZnO surfaces that were treated with $[IrCpCp^*]_2$ and subsequently exposed to atmosphere for 5 min, 2 h, 16 h, and 72 h. WF was tracked *via* UPS analysis and when samples were not being exposed to atmosphere the substrates were stored under vacuum. Each data point originates from the average and standard deviation of 7 spots on the surface.

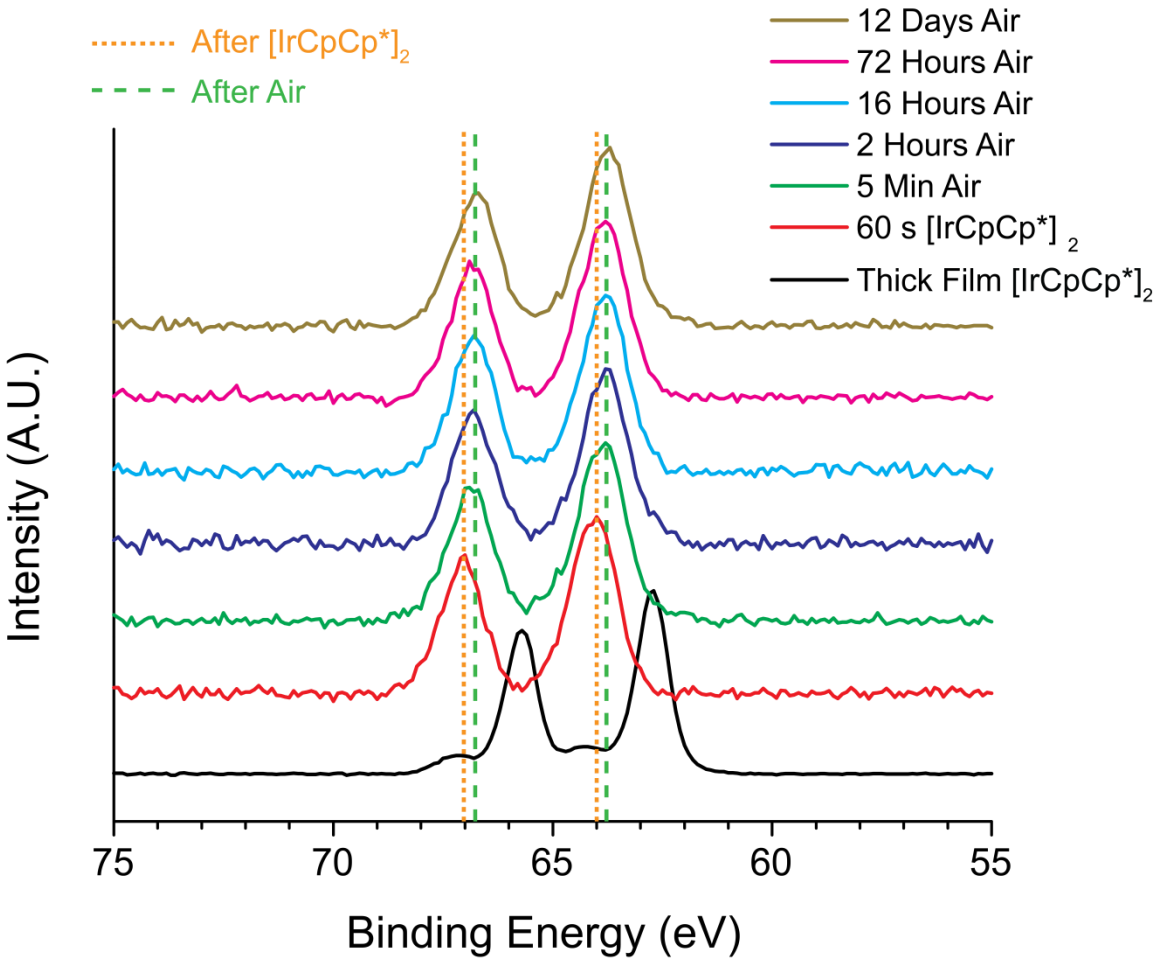

Figure 5.17 Comparison of Ir 4f peaks for a drop-cast film of the dimer on ITO, a solution soaked sample of ITO immediately after treatment without exposure to air, and after varying amounts of time exposed to atmospheric conditions. The vertical dashed lines serve as guides to show the subtle difference in binding energy observed for the Ir 4f peak position after treatment and after air exposure. Graphs have been normalized and vertically offset for clarity.

5.3.4 Summary of Results for n-Dopants

Overall, it has been shown that the various dimers examined above have the ability to greatly reduce the WF of metals (Au) and metal oxides (ITO and ZnO) with typical WF values after treatment (irrespective of surface type or dopant chosen) of ~3.3 – 3.6 eV. It is also evident that the source of this reduction in WF is the deposition of a

sub-monolayer of monomer cations on the surface of the substrate, presumably compensated by negative charges within the ITO, which leads to the formation of an interface dipole and a concomitant reduction in WF. While it was demonstrated that the oxidation to the 18-electron monomer cations, it could not be readily determined where the electrons transferred from the dopants are localized within the substrate. However, based on no apparent shifts in In or Sn core levels by XPS, and the small shifts in the VBM observed by UPS, it can be speculated that the electrons transferred are delocalized within the substrate. There is an increase in WF upon exposure to air within the first 5 minutes, but the WF appears to stabilize after this point at around 4 eV for many days of atmospheric exposure and, at least in the case of ITO, the WF after air exposure is still below that of DSC ITO.

5.4 p-Doping of Metals and Metal Oxides with Organic and Metal-Organic Species

5.4.1 Surface Treatment

ITO was used to examine the effects of the p-dopants, Magic Blue and Mo(tfa-tf)$_3$. In the case of Mo(tfa-tf)$_3$ toluene could again be used as the solvent, but for Magic Blue, which is insoluble in toluene, anhydrous dichloromethane (DCM) was used. As Magic Blue is a commercially available material (making it more readily available) it was possible to examine how concentration and immersion time impact the measured WF after treatment. Furthermore, due to the nature of these p-dopants they are not as readily susceptible to atmospheric exposure, and this was demonstrated by conducting modification of ITO with Magic Blue under atmospheric conditions as well as under inert atmosphere (as shown in 5.4.4). The resulting WF values were extremely similar to one another. It should be noted that while UPS is a technique that is suitable when exact WF

values are desired, KP values (when properly referenced to a substrate such as highly ordered pyrolitic graphite, HOPG) were found to provide good estimates of WF values. The sample throughput rate for KP, however, is substantially higher, which is why KP was used for a large number of samples when optimizing modification conditions. These observations of KP *vs.* UPS are consistent with those found in the literature when comparing the two techniques.[48-49] It should be noted that the vast majority of this work was conducted in collaboration with Devin Friend from the University of Florida.

5.4.2 Optimization of ITO Modification Conditions for p-type Materials

Since it was possible to test a wider range of modification conditions (due to the readily available nature of Magic Blue, and the ease with which KP can be conducted) a survey of various modification conditions was examined prior to conducting a more thorough XPS/UPS analysis of the surfaces. It should be noted that to ensure consistency among the various modification conditions, samples were prepared inside a glove box and kept under inert atmosphere until immediately before KP measurements (in the case of testing temperature dependence, samples were prepared outside the glove box as boiling DCM was needed). Variables such as concentration, modification time, and temperature were all examined in order to determine which set of conditions led to the most drastic WF change for ITO before and after treatment. Figure 5.18 summarizes the results of testing different modification conditions using concentrations of 0.5 mM, 2 mM, and 8.7 mM (the maximum concentration soluble in DCM) Magic Blue in DCM.

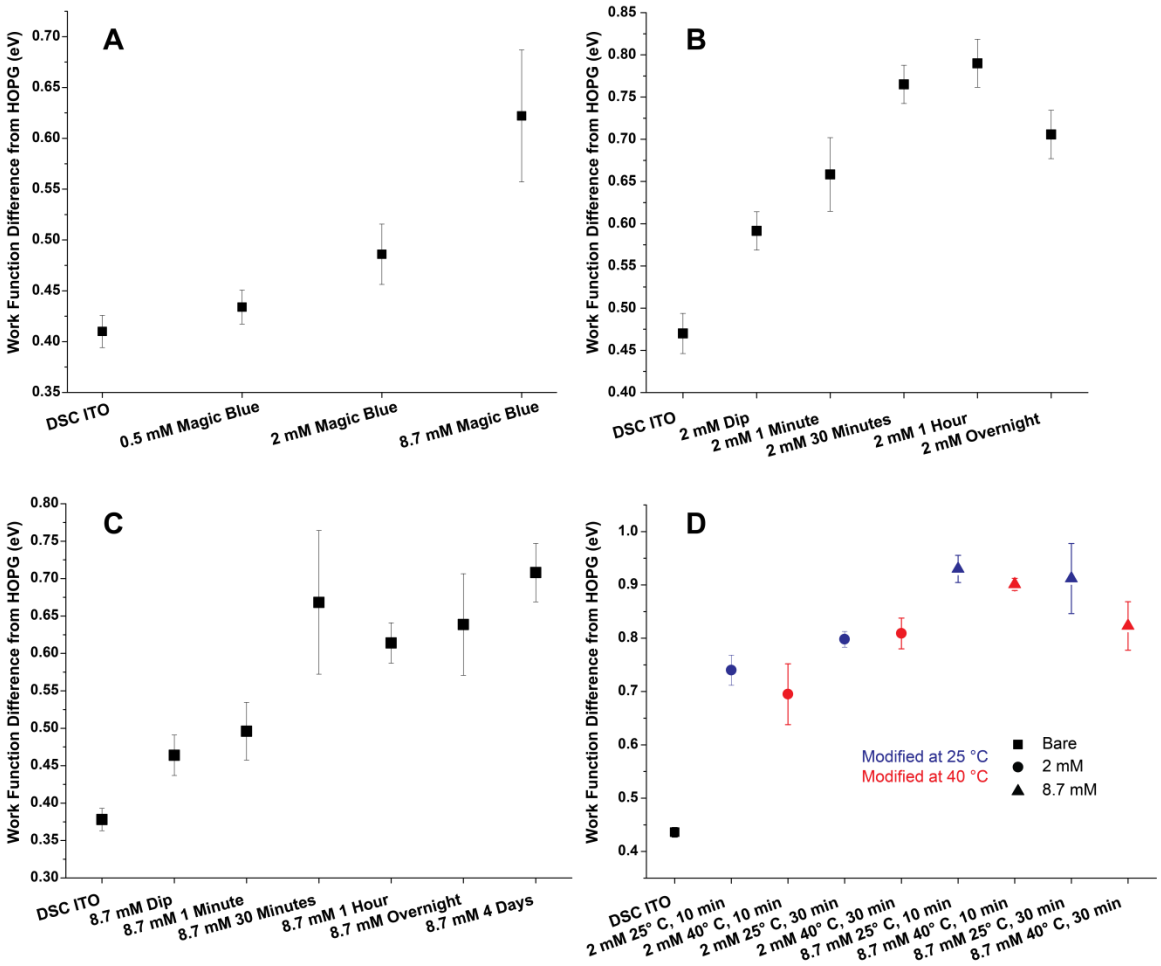

Figure 5.18 Comparison of WF values obtained from different modification conditions of ITO using solutions of Magic Blue in DCM. All data was collected using KP, with the error bar originating from the average of at least 5 spots on each surface. All data is referenced to freshly cleaved HOPG surfaces and show WF changes relative to that reference point. Modification conditions examined include different concentrations (**A**) all treated for 10 min, different modification times using 2 mM (**B**) and 8.7 mM (**C**) solutions of Magic Blue in DCM, and examining the impact of concentration, time, and modification temperature (**D**) with samples modified at 25 °C in blue and those modified at 40 °C in red. A freshly DSC ITO sample is provided for each set of measurements. Samples in (**D**) were prepared outside of the glove box.

The data shown in Figure 5.18 indicate that both solution concentration and modification time impact the ability to increase the WF of ITO. There are, however, diminishing returns on modifying substrates for longer than an hour as the WF change

begins to decrease beyond this point. Similarly, there was no clear advantage to modifying surfaces at elevated temperatures compared with room temperature. Figure 5.18D does show that when directly comparing the two concentrations, the more concentrated solution of Magic Blue affords an increase in WF. From this set of experiments, it was concluded that optimal modification conditions for Magic Blue on ITO was to treat the surface using a high concentration for approximately 1 hour. These trends were further validated with UPS as shown in 5.4.4.

In the case of $Mo(tfa\text{-}tf)_3$, both immersion time and solvent were examined to determine if there was an influence on the final WF value and also to see how this particular dopant compares with Magic Blue. The data shown in Figure 5.19 summarizes the comparison of modifying the surface of ITO with $Mo(tfa\text{-}tf)_3$ using 2 mM solutions in either toluene or DCM for modification times of 60 s, 1 hour, and overnight. While there is an increase in the WF relative to the freshly cleaned ITO substrate, neither solvent nor modification time appear to have a very large impact on the final WF after modification with differences between the smallest and largest WF shift on the order of ~ 0.1 eV. These WF shifts of at most 0.3 eV are relatively consistent with what was reported for this compound when treating graphene surfaces, where the largest WF increase reported was 0.5 eV.[37] Since the WF changes with Magic Blue (upwards of ~ 0.5 eV) were larger, the remainder of studies focused on the use of this dopant.

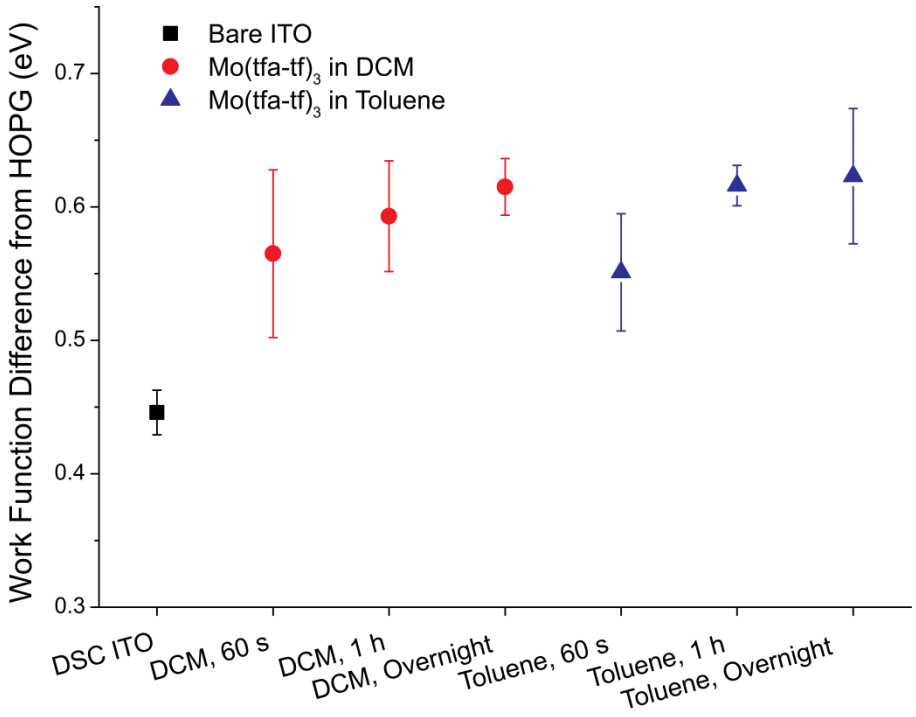

Figure 5.19 Summary of KP data for 2 mM solutions of Mo(tfa-tf)$_3$ in solutions of toluene or DCM for varying amounts of time. Data originates from the average of at least 5 spots on each surface with the error bar from the standard deviation of these measurements. Values shown are relative to freshly cleaved HOPG and all samples were kept under inert atmosphere until just before measurement by KP.

5.4.3 XPS Analysis of Surfaces Treated with Magic Blue

In order to confirm that the surface was modified with Magic Blue, XPS analysis was conducted comparing both 2 and 8.7 mM concentrations along with a thick film of the salt drop-cast on top of ITO. A comparison of the survey spectra is shown in Figure 5.20. Based on the results from the n-dopants it would be anticipated that an interface dipole would be formed after Magic Blue accepts an electron from the surface. Thus, the amine-containing portion of the salt would become a neutral amine and be readily washed away from the surface while the $SbCl_6^-$ would remain, electrostatically bound to

the surface. XPS, however, indicated that both Br and Cl were present on the surface after modification. An examination of the Sb 3d peak is not possible as it overlaps with the O 1s peak from the ITO substrate, making the two indistinguishable from one another (and Sb 3p peaks were weak in the thick film and overlap with Sn 3p and In 3s/Sn Auger peaks). While not easily visible in the survey spectra of the ITO soaked samples, N was detected on the surface of ITO after treatment, but with large spot-to-spot variations due to its weak intensity. Quantification of the spectra is further complicated by large differences in Cl/Br ratios from sample to sample making it unclear if there is a preference of either the amine or Sb portions of the salt to remain on the surface, or if there is simply a dependence regarding how well the surface has been washed after treatment. Thus, in the case of this dopant, the XPS data was treated as a qualitative indication that the surface had been modified to corroborate KP and UPS data. Similar to the case for the n-dopants, no shifts in In or Sn peak positions were observed to indicate that the substrate donated electrons to the dopant. A representative comparison showing the high-resolution In $3d_{5/2}$ peak is provided in Figure 5.21.

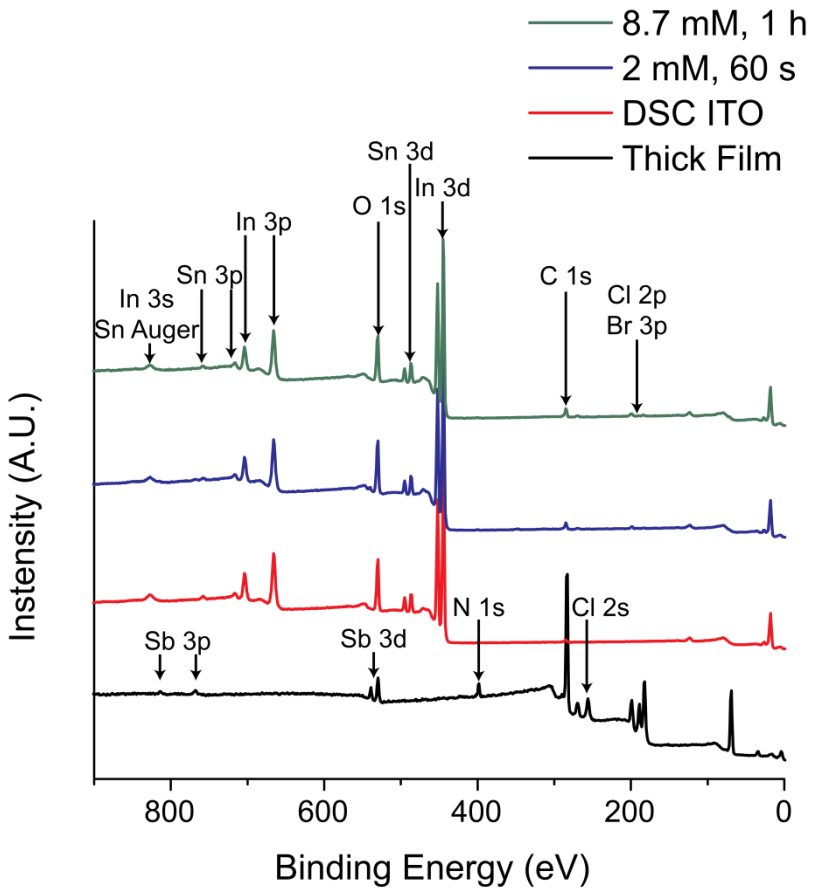

Figure 5.20 Comparison of survey spectra for a thick film of Magic Blue drop-cast on the surface of ITO, a DSC ITO sample, and ITO after treatment with low and high concentrations of Magic Blue for either 60 s or 1 h. Spectra have been normalized, offset, and important ionizations labeled for clarity.

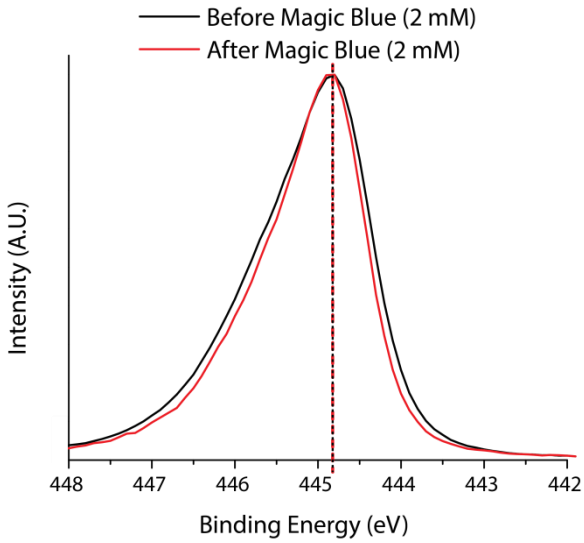

Figure 5.21 Comparison of high-resolution XPS data for the In $3d_{5/2}$ peaks of surfaces before and after modification with Magic Blue. The color coded dashed lines indicate the position of the peak, which does not change after modification with Magic Blue.

5.4.4 UPS Analysis of Surfaces Treated with Magic Blue

In order to confirm the KP data and provide absolute WF values, UPS analysis was conducted using the two extreme cases of modification, namely a short modification at low concentration (2 mM for 60 s) and a high concentration for a longer period of time (8.7 mM for 1 h). The secondary electron edge of the UPS spectra are shown in Figure 5.22, with a freshly DSC ITO surface for comparison and a table summarizing the numerical WF values. There is a significant difference between the two modification conditions, which corresponds with the trend observed from the KP data. While the WF increase of ~ 0.6 eV is large, it is not as large as what was observed for WF shifts on ITO using phosphonic acid surface modifiers as discussed in Chapter 3.

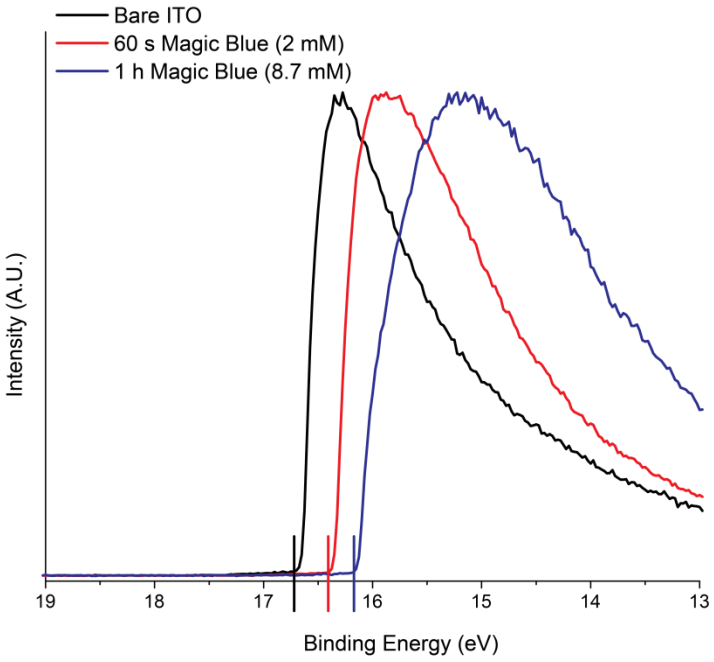

	2 mM, 60 s WF (eV)	8.7 mM, 1 h WF (eV)
Before Magic Blue	4.48 ± 0.06	4.44 ± 0.09
After Magic Blue	4.82 ± 0.04	5.00 ± 0.08
ΔWF	+0.34	+0.56

Figure 5.22 Comparison of WF for DSC ITO treated with solutions of Magic Blue in DCM at either 2 mM for 60 s or 8.7 mM for 1 h (left). The numerical values obtained from the average of 7 spots on each surface are also provided (right) with the error bar originating from the standard deviation among these spots. Note the trend to observe a higher WF value for the more concentrated solution at longer modification times. Spectra have been normalized and the onset of the secondary electron edge is denoted by the color coded vertical line intersecting the *x*-axis.

A comparison of the VBM values before and after treatment was also examined. The values, along with the calculated interface dipole contribution are summarized in Table 5.7. As can be seen, in the case of the more concentrated modification solution there was a large shift in the VBM after modification, with only a small shift for the less concentrated modification conditions. Thus, while there is clearly a contribution to the shift in WF originating from the formation of an interface dipole, there also appears to be evidence for electron transfer leading to shifting of the Fermi level relative to the band structure (in this case meaning the Fermi level shifts without the position of the valence band or conduction band changing) as being a larger contributing factor to the WF shift.

This is in contrast to what was observed in n-doping where movement of the Fermi level with respect to the band structure was minimal compared with the contribution originating from the interface dipole. This observation may be explained because the density of states in ITO falls off strongly below the Fermi level, so a relatively small number of holes from dopants can cause a large shift in the Fermi, while at the same time there exist a limited number of sites available to donors and thus the interface dipole dominates in the case of the n-dopants. Similar to the n-dopants, looking at the XPS data does not show a shift in the In peaks. The inference that both electron transfer and interface dipole play roles in the WF change is similar to what was observed in the case of $Mo(tfa\text{-}tf)_3$ on graphene, where the interface dipole was a smaller overall component of the change in WF.[37]

Table 5.7 Summary of VBM values for the UPS data of ITO treated with Magic Blue shown in Figure 5.22. The VBM before and after surface modification are provided along with the changes in VBM (ΔVBM) changes in WF (ΔWF), and the interface dipole contribution to the shift in WF (ΔWF + ΔVBM).

Surface	**VBM Before (eV)**	**VBM After (eV)**	**ΔVBM (eV)**	**ΔWF (eV)**	**Interface Dipole Contribution (eV)**
2 mM, 60 s	2.96 ± 0.08	2.89 ± 0.03	-0.07	+0.34	+0.27
8.7 mM, 1 h	3.00 ± 0.08	2.56 ± 0.07	-0.44	+0.56	+0.12

As alluded to in 5.4.1 a direct comparison of treating ITO with Magic Blue under atmospheric conditions and under inert atmosphere was conducted using otherwise identical modification conditions, and the results of the changes in WF examined by UPS. Table 5.8 summarizes the shifts in WF that were observed from this comparison, which shows that the two preparation conditions produced nearly identical results and

that the modified surface is stable in atmosphere for at least a few hours (KP studies indicated similar stability overnight, but this was not confirmed by UPS). Thus, while the overall shifts in WF may not be as large as with dipolar phosphonic acids, the protocol is in many ways more straightforward, requiring shorter time and fewer steps after surface treatment, which may be advantageous for high-throughput processing.

Table 5.8 Summary of UPS results showing changes in WF before and after modification, comparing ITO treated with a 2 mM solution of Magic Blue in DCM for 60 s carried out under either inert atmosphere or ambient air.

Surface	**WF Before (eV)**	**WF After (eV)**	**ΔWF (eV)**
2 mM, 60 s **Inert**	4.56 ± 0.14	4.91 ± 0.04	+0.35
2 mM, 60 s **Ambient**	4.48 ± 0.06	4.82 ± 0.04	+0.34

5.4.5 Summary of Results for p-Dopants

Electron accepting p-dopants, when used to treat the surface of a metal oxide such as ITO, have the ability to alter the WF of the surface. An examination of varying modification conditions demonstrated for Magic Blue that solution concentration and immersion time do have an impact on the overall WF measured after modification, but that for $Mo(tfa\text{-}tf)_3$ similar variables such as solvent or immersion time result in nearly identical WF changes, relative to DSC ITO. XPS confirmed the presence of Magic Blue on the surface after modification, however, further studies would be required in order to determine which portion of the salt more favors adsorption to the surface after modification, and at what coverage does it adsorb. UPS VBM shifts indicate that more

than just an interface dipole is responsible for the WF modification after treatment suggesting the possibility of electron transfer from the ITO surface to the p-dopant. Overall, the largest increase in WF observed with this set of materials was ~ 0.6 eV relative to the bare surface; that modification does not have to be performed in a glove box and surfaces after modification are stable for at least several hours in air.

5.5 Conclusions

The goal of this chapter was to examine means other than phosphonic acid modification for tuning the WF of a surface, particularly for decreasing the WF of metal oxides, which is something that has been shown to be difficult to do when utilizing phosphonic acids (Chapters 3 and 4). The purpose of the chapter was to also examine not only if it was possible to modify the WF of multiple surfaces (metals and metal oxides) with one modifier, but also provide some information as to what drives the WF modification. It was shown that redox active n-type dimer materials $[IrCpCp^*]_2$, $[RuMesCp^*]_2$, and $[RhCpCp^*]_2$ do have the ability to greatly decrease the WF of both metals and metal oxides. The WF reduction originates from the deposition of a sub-monolayer of monomer cations on the surface of the substrate after the dimer dissociates and donates an electron to the surface (though there was no direct experimental evidence as to which material on the surface accepted the electron, but it is posited that it is distributed throughout the top layers of the substrate). These cations (and the presumably negatively charged surface) lead to the formation of a large interface dipole, which, based on UPS data, is the main source for the WF decrease. The largest WF decreases observed were ~ -1.6, -0.6, and -1.9 eV using $[IrCpCp^*]_2$ on ITO, ZnO, and gold, respectively.

The use of redox active p-dopants also have an impact on the WF of metal oxides such as ITO, which was demonstrated through the use of two metal-organic species. Unlike in the case of the n-dopants, where changes in WF were observed within minutes of atmospheric exposure (though reaching a steady state that lasts for periods of at least 12 days in air), these p-doped interfaces are stable such that processing with a material like Magic Blue can be conducted in air. Analogous to the n-dopants, it can be inferred that the p-dopants also experience electron transfer, in this case serving as an electron acceptor from the substrate though experimental XPS could not confirm this hypothesis. Analogous to the n-dopants, the formation of an interface dipole after modification is part of the reason for the WF change, but unlike in the n-dopant case it is not the majority contribution leading to changes in WF possibly due to differences in terms of density of states. The largest WF increase observed for ITO after treatment was ~ 0.6 eV using Magic Blue.

As expected, based on the similar effective redox potentials for the dimers, similar WF values were attained after treatment. When the dimers were compared with a material such as TDAE, however, noticeable differences in WF changes were observed. In the case of p-dopants, a difference in reduction potential did appear to have a larger influence on the material's ability to increase the WF as both Magic Blue and $Mo(tfa\text{-}tf)_3$, which have different reduction potentials afforded relatively different WF changes.

Overall, the redox active materials examined in this chapter along with other surface modifiers such as phosphonic acids, thiols, and carboxylic acids provide the opportunity to have a wide variety of materials available for WF tuning. Redox active dopants are attractive from the standpoint that they are more surface agnostic than other

modifiers which have specific chemical reactions that occur between the substrate and binding group. The tradeoff may come in the overall stability of the surface after modification as covalently bound modifiers are extremely stable on the surface. In order to address this issue of stability further investigations of the n- and p-doped surfaces after modification and subsequent processing would still need to be explored.

5.6 Experimental

5.6.1 Materials

Magic Blue and TDAE were purchased from Sigma-Aldrich. Magic Blue was used without further purification, while TDAE was distilled and sparged with nitrogen prior to transfer into the glove box. Toluene and dichloromethane (VWR) were dried by distillation over calcium hydride and subsequently freeze-pump-thawed 3 times in order to remove oxygen prior to transferring into the glove box. The synthesis of $[RhCpCp^*]_2$,[35] $[RuMesCp^*]_2$,[35] $[IrCpCp^*]_2$,[50] and $Mo(tfa\text{-}tf)_3$[37] have been previously reported and was conducted by Swagat Mohapatra, Jared Delcamp, and Yadong Zhang. The reducing power of the monomers and the oxidative stability of the dimers was examined through cyclic voltammetry analysis measured in THF, 0.1 M *n*-Bu_4NPF_6, at a scan rate of 100 mV/sec, with ferrocene as an internal standard.

5.6.2 Surface Preparation, Cleaning, and Modification

Commercially available ITO substrates (Eagle-XG, Thin Film Devices, Anaheim, CA) were purchased and found to have a surface roughness of 0.7-0.8 nm rms as measured with AFM. The ITO was cut into 15 mm × 15 mm substrates which were then scrubbed and subsequently sonicated for 10 min with a 5 % solution of Micro-90 detergent in DI water, sonicated in DI water for 10 min, sonicated in ethanol for 10 min,

rinsed with ethanol, and dried under a flow of nitrogen to afford DSC ITO samples. Plasma treated ITO surfaces were treated using oxygen plasma with a Plasma-Preen II (100 % Power, Plasmatic Systems, Inc., North Brunswick, NJ) for 5 min.

ZnO substrates were prepared by cleaning 1 in. × 1 in. glass microscope slides in the same manner as reported for ITO followed by oxygen plasma cleaning. Immediately after oxygen plasma samples were loaded into the atomic layer deposition system (Cambridge NanoTech, Savannah 100) and 30 nm of ZnO was deposited. These larger surfaces were then cut into 15 mm × 15 mm prior to use, rinsed with ethanol, and dried under a flow of nitrogen.

Commercially available Glass:Ti:Gold slides (EMF Corporation, Ithaca, NY) were cut into 15 mm × 15 mm surfaces. These surfaces were sonicated for 10 min in ethanol, rinsed with ethanol, and dried under a flow of nitrogen. Surfaces were then cleaned by immersion in a Piranha solution for 30 minutes (3:1 sulfuric acid:30 % hydrogen peroxide), rinsing with DI water followed by immersion in DI water for 20 minutes, washing with water, followed by ethanol, and drying under a flow of nitrogen.

In all cases, samples were immediately transferred to the XPS/UPS for analysis upon completion of the cleaning protocol. After analysis of the substrate, surfaces were transferred to a nitrogen filled glove box (< 0.1 ppm water and < 0.5 ppm oxygen) using a Kratos air-sensitive transporter 39-322 that couples with the transfer chamber of the Kratos Axis Ultra^{DLD} XPS/UPS under a positive pressure of nitrogen. After entry into the glove box samples were then treated with the solutions of n- and p-dopants as noted in the text (typically 2 mM except for Magic Blue which used concentrations of 0.5, 2, and 8.7 mM in solutions of either toluene or, in the case of Magic Blue,

dichloromethane). Samples were then rinsed three times with fresh solvent (toluene or dichloromethane), dried with a flow of nitrogen, and transferred under inert atmosphere to either the XPS/UPS or Kelvin Probe for analysis. In the case of Magic Blue samples that were prepared in atmosphere, all processing protocols were the same except for conducting the modification outside of the glove box. In the case of thick films for $[IrCpCp^*]_2$ and Magic Blue concentrated solutions in either toluene or dichloromethane were made and then drop-cast on the surface of ITO.

5.6.3 Surface Characterization

5.6.3.1 XPS and UPS Measurements

All measurements were conducted in a combined XPS-UPS Kratos Axis Ultra with an average base pressure of 10^{-9} Torr. UPS was acquired prior to acquisition of XPS for all samples. UPS spectra were obtained with a 21.2 eV He (I) excitation and a pass energy of 5 eV using a 27 μm spot size. Each sample was examined in at least 7 spots to ensure consistency over the entire surface and the spectrometer was calibrated using a sputter cleaned silver sample. XPS data were collected with a monochromatic Al Kα source (300 W) using a 400 μm spot size and a pass energy of 160 eV for survey acquisition and 20 eV for high resolution spectra. Exposure of the surfaces to X-rays was kept to a minimum (ca. 45 min), and spectra were acquired in three spots on each surface. Most characterizations were performed at normal takeoff angle (0°) except when noted for angle resolved analysis which was conducted at a takeoff angle of 70°. XPS data for drop-cast films of the dopants required the use of charge neutralization and UPS data could not be directly collected on such thick films. Data was analyzed using Vision Processing version 2.2.8.

5.6.3.2 Kelvin Probe

Kelvin Probe analysis (Besocke Delta Phi) of surfaces was conducted in air with a probe diameter of approximately 3 mm. Samples analyzed by KP were cut to be 1 in. × 1 in. so that 5 data points could be collected on each surface. Average values and standard deviations were generated from these multiple spots. Highly ordered pyrolytic graphite, freshly cleaved using the Scotch tape method, was used (typical WF of 4.5 eV) at the beginning and end of each set of measurements as well as periodically every 2 – 4 samples analyzed to account for any instrumental drift.

5.7 References

[1] Sze, S. M.; Ng, K. K., *Physics of Semiconductor Devices*. 3rd ed.; Wiley-Interscience: Hoboken, N.J., 2007.

[2] Riordan, M.; Hoddeson, L., The Origins of the Pn Junction. *Spectrum, IEEE* **1997,** *34*, 46-51.

[3] Ohl, R. S., Light-Sensitive Electric Device. Google Patents: 1946.

[4] Birchall, J. M.; Haszeldine, R. N., Polyfluoroarenes .1. Pentafluorophenol. *Journal of the Chemical Society* **1959**, 13-17.

[5] Walzer, K.; Maennig, B.; Pfeiffer, M.; Leo, K., Highly Efficient Organic Devices Based on Electrically Doped Transport Layers. *Chemical Reviews* **2007,** *107*, 1233-1271.

[6] Parthasarathy, G.; Shen, C.; Kahn, A.; Forrest, S. R., Lithium Doping of Semiconducting Organic Charge Transport Materials. *Journal of Applied Physics* **2001,** *89*, 4986-4992.

[7] Kido, J.; Matsumoto, T., Bright Organic Electroluminescent Devices Having a Metal-Doped Electron-Injecting Layer. *Applied Physics Letters* **1998,** *73*, 2866-2868.

[8] Guo, S.; Kim, S. B.; Mohapatra, S. K.; Qi, Y.; Sajoto, T.; Kahn, A.; Marder, S. R.; Barlow, S., N-Doping of Organic Electronic Materials Using Air-Stable Organometallics. *Advanced Materials* **2012,** *24*, 699-703.

[9] Qi, Y.; Mohapatra, S. K.; Bok Kim, S.; Barlow, S.; Marder, S. R.; Kahn, A., Solution Doping of Organic Semiconductors Using Air-Stable N-Dopants. *Applied Physics Letters* **2012,** *100*, 083305.

[10] Braun, S.; Salaneck, W. R.; Fahlman, M., Energy-Level Alignment at Organic/Metal and Organic/Organic Interfaces. *Advanced Materials* **2009,** *21*, 1450-1472.

[11] Weiying, G.; Antoine, K., Electrical Doping: The Impact on Interfaces of Π -Conjugated Molecular Films. *Journal of Physics: Condensed Matter* **2003,** *15*, S2757.

[12] Ishii, H.; Sugiyama, K.; Ito, E.; Seki, K., Energy Level Alignment and Interfacial Electronic Structures at Organic/Metal and Organic/Organic Interfaces. *Advanced Materials* **1999,** *11*, 605-625.

[13] Rana, O.; Srivastava, R.; Chauhan, G.; Zulfequar, M.; Husain, M.; Srivastava, P. C.; Kamalasanan, M. N., Modification of Metal–Organic Interface Using F4-Tcnq for Enhanced Hole Injection Properties in Optoelectronic Devices. *physica status solidi (a)* **2012,** *209*, 2539-2545.

[14] Koch, N.; Duhm, S.; Rabe, J. P.; Vollmer, A.; Johnson, R. L., Optimized Hole Injection with Strong Electron Acceptors at Organic-Metal Interfaces. *Physical Review Letters* **2005,** *95*, 237601.

[15] Faraggi, M. N.; Jiang, N.; Gonzalez-Lakunza, N.; Langner, A.; Stepanow, S.; Kern, K.; Arnau, A., Bonding and Charge Transfer in Metal–Organic Coordination Networks on Au(111) with Strong Acceptor Molecules. *The Journal of Physical Chemistry C* **2012,** *116*, 24558-24565.

[16] Romaner, L.; Heimel, G.; Brédas, J.-L.; Gerlach, A.; Schreiber, F.; Johnson, R. L.; Zegenhagen, J.; Duhm, S.; Koch, N.; Zojer, E., Impact of Bidirectional Charge Transfer and Molecular Distortions on the Electronic Structure of a Metal-Organic Interface. *Physical Review Letters* **2007,** *99*, 256801.

[17] Frisch, J.; Glowatzki, H.; Janietz, S.; Koch, N., Solution-Based Metal Electrode Modification for Improved Charge Injection in Polymer Field-Effect Transistors. *Organic Electronics* **2009,** *10*, 1459-1465.

[18] Schlesinger, R.; Xu, Y.; Hofmann, O. T.; Winkler, S.; Frisch, J.; Niederhausen, J.; Vollmer, A.; Blumstengel, S.; Henneberger, F.; Rinke, P.; Scheffler, M.; Koch, N., Controlling the Work Function of Zno and the Energy-Level Alignment at the Interface to Organic Semiconductors with a Molecular Electron Acceptor. *Physical Review B* **2013,** *87*, 155311.

[19] Chen, W.; Chen, S.; Qi, D. C.; Gao, X. Y.; Wee, A. T. S., Surface Transfer P-Type Doping of Epitaxial Graphene. *Journal of the American Chemical Society* **2007,** *129*, 10418-10422.

[20] Rangger, G. M.; Hofmann, O. T.; Romaner, L.; Heimel, G.; Bröker, B.; Blum, R.-P.; Johnson, R. L.; Koch, N.; Zojer, E., F4tcnq on Cu, Ag, and Au as Prototypical Example for a Strong Organic Acceptor on Coinage Metals. *Physical Review B* **2009,** *79*, 165306.

[21] Drechsel, J.; Pfeiffer, M.; Zhou, X.; Nollau, A.; Leo, K., Organic Mip-Diodes by P-Doping of Amorphous Wide-Gap Semiconductors: Cv and Impedance Spectroscopy. *Synthetic Metals* **2002,** *127*, 201-205.

[22] Duhm, S.; Salzmann, I.; Bröker, B.; Glowatzki, H.; Johnson, R. L.; Koch, N., Interdiffusion of Molecular Acceptors through Organic Layers to Metal Substrates Mimics Doping-Related Energy Level Shifts. *Applied Physics Letters* **2009,** *95*, 093305.

[23] Nakamura, T.; Azumi, R.; Tachibana, H.; Matsumoto, M., Electroabsorption of Cetylthiotetrathiafulvalene / Fluoro-Containing 7,7,8,8-Tetracyanoquinodimethane Systems in Langmuir-Blodgett Films. *Synthetic Metals* **1997,** *86*, 1819-1820.

[24] V. Jourdain, I.; Fourmigue, M.; Guyon, F.; Amaudrut, J., Syntheses and Electrochemical Characterization of Heteroleptic Cyclopentadienyl-Dithiolene D2 Tungsten Complexes. Structures and Magnetic Properties of Charge-Transfer Salts [Dagger]. *Journal of the Chemical Society, Dalton Transactions* **1998**, 483-488.

[25] Broker, B.; Blum, R. P.; Frisch, J.; Vollmer, A.; Hofmann, O. T.; Rieger, R.; Mullen, K.; Rabe, J. P.; Zojer, E.; Koch, N., Gold Work Function Reduction by 2.2 Ev with an Air-Stable Molecular Donor Layer. *Applied Physics Letters* **2008,** *93*, 243303.

[26] Lindell, L.; Unge, M.; Osikowicz, W.; Stafstrom, S.; Salaneck, W. R.; Crispin, X.; de Jong, M. P., Integer Charge Transfer at the Tetrakis(Dimethylamino)Ethylene/Au Interface. *Applied Physics Letters* **2008,** *92*, 163302.

[27] Li, F.; Zhou, Y.; Zhang, F.; Liu, X.; Zhan, Y.; Fahlman, M., Tuning Work Function of Noble Metals as Promising Cathodes in Organic Electronic Devices. *Chemistry of Materials* **2009,** *21*, 2798-2802.

[28] Osikowicz, W.; Crispin, X.; Tengstedt, C.; Lindell, L.; Kugler, T.; Salaneck, W. R., Transparent Low-Work-Function Indium Tin Oxide Electrode Obtained by

Molecular Scale Interface Engineering. *Applied Physics Letters* **2004,** *85*, 1616-1618.

[29] Gao, Z. Q.; Mi, B. X.; Xu, G. Z.; Wan, Y. Q.; Gong, M. L.; Cheah, K. W.; Chen, C. H., An Organic P-Type Dopant with High Thermal Stability for an Organic Semiconductor. *Chemical Communications* **2008**, 117-119.

[30] Gao, W.; Kahn, A., Controlled P Doping of the Hole-Transport Molecular Material N,N′-Diphenyl-N,N′-Bis(1-Naphthyl)-1,1′-Biphenyl-4,4′-Diamine with Tetrafluorotetracyanoquinodimethane. *Journal of Applied Physics* **2003,** *94*, 359-366.

[31] Yim, K.-H.; Whiting, G. L.; Murphy, C. E.; Halls, J. J. M.; Burroughes, J. H.; Friend, R. H.; Kim, J.-S., Controlling Electrical Properties of Conjugated Polymers Via a Solution-Based P-Type Doping. *Advanced Materials* **2008,** *20*, 3319-3324.

[32] Davison, A.; Edelstein, N.; Holm, R. H.; Maki, A. H., Synthetic and Electron Spin Resonance Studies of Six-Coordinate Complexes Related by Electron-Transfer Reactions. *Journal of the American Chemical Society* **1964,** *86*, 2799-2805.

[33] Qi, Y.; Sajoto, T.; Barlow, S.; Kim, E.-G.; Brédas, J.-L.; Marder, S. R.; Kahn, A., Use of a High Electron-Affinity Molybdenum Dithiolene Complex to P-Dope Hole-Transport Layers. *Journal of the American Chemical Society* **2009,** *131*, 12530-12531.

[34] Qi, Y.; Sajoto, T.; Kröger, M.; Kandabarow, A. M.; Park, W.; Barlow, S.; Kim, E.-G.; Wielunski, L.; Feldman, L. C.; Bartynski, R. A.; Brédas, J.-L.; Marder, S. R.; Kahn, A., A Molybdenum Dithiolene Complex as P-Dopant for Hole-Transport Materials: A Multitechnique Experimental and Theoretical Investigation. *Chemistry of Materials* **2009,** *22*, 524-531.

[35] Guo, S.; Mohapatra, S. K.; Romanov, A.; Timofeeva, T. V.; Hardcastle, K. I.; Yesudas, K.; Risko, C.; Brédas, J.-L.; Marder, S. R.; Barlow, S., N-Doping of Organic Electronic Materials Using Air-Stable Organometallics: A Mechanistic Study of Reduction by Dimeric Sandwich Compounds. *Chemistry – A European Journal* **2012,** *18*, 14760-14772.

[36] Paniagua, S. A.; Li, E. L.; Marder, S. R., Adsorption Studies of a Phosphonic Acid on Ito: Film Coverage, Purity, and Induced Electronic Structure Changes. *Physical Chemistry Chemical Physics* **2014,** *16*, 2874-2881.

[37] Paniagua, S. A.; Baltazar, J.; Sojoudi, H.; Mohapatra, S. K.; Zhang, S.; Henderson, C. L.; Graham, S.; Barlow, S.; Marder, S. R., Production of Heavily N- and P-Doped Cvd Graphene with Solution-Processed Redox-Active Metal-Organic Species. *Materials Horizons* **2013**, 111-115.

[38] Mohapatra, S. K.; Fonari, A.; Risko, C.; Moudgil, K. Y.; Delcamp, J. H.; Timofeeva, T. V.; Brédas, J.-L.; Marder, S. R.; Barlow, S., Dimers of Nineteen-Electron Sandwich Compounds as Reductants: A Crystallographic and Quantum-Chemical Investigation. **2014**.

[39] Bockman, T. M.; Kochi, J. K., Isolation and Oxidation-Reduction of Methylviologen Cation Radicals. Novel Disproportionation in Charge-Transfer Salts by X-Ray Crystallography. *The Journal of Organic Chemistry* **1990,** *55*, 4127-4135.

[40] Garnier, J.; Kennedy, A. R.; Berlouis, L. E. A.; Turner, A. T.; Murphy, J. A., Structure and Reactivity in Neutral Organic Electron Donors Derived from 4-Dimethylaminopyridine. *Beilstein Journal of Organic Chemistry* **2010,** *6*, 73.

[41] Burkholder, C.; Dolbier, W. R.; Médebielle, M., Tetrakis(Dimethylamino)Ethylene as a Useful Reductant of Some Bromodifluoromethyl Heterocycles. Application to the Synthesis of New Gem-Difluorinated Heteroarylated Compounds. *The Journal of Organic Chemistry* **1998,** *63*, 5385-5394.

[42] Mohapatra, S., Unpublished Data.

[43] Connelly, N. G.; Geiger, W. E., Chemical Redox Agents for Organometallic Chemistry. *Chemical Reviews* **1996,** *96*, 877-910.

[44] Kato, S.-i.; Diederich, F., Non-Planar Push-Pull Chromophores. *Chemical Communications* **2010,** *46*, 1994-2006.

[45] Kramida, A.; Ralchenko, Y.; Reader, J.; Team, N. A., Nist Atomic Spectra Database (Version 5.0). http://physics.nist.gov/asd, 2012.

[46] Paramonov, P. B.; Paniagua, S. A.; Hotchkiss, P. J.; Jones, S. C.; Armstrong, N. R.; Marder, S. R.; Brédas, J.-L., Theoretical Characterization of the Indium Tin Oxide Surface and of Its Binding Sites for Adsorption of Phosphonic Acid Monolayers. *Chemistry of Materials* **2008,** *20*, 5131-5133.

[47] Evans, J. S. O.; Barlow, S.; Wong, H.-V.; O'Hare, D., In Situ X-Ray Diffraction Evidence of Guest Molecule Reorientation During an Intercalation Reaction. *Advanced Materials* **1995,** *7*, 163-166.

[48] Kim, J. S.; Friend, R. H.; Cacialli, F., Surface Wetting Properties of Treated Indium Tin Oxide Anodes for Polymer Light-Emitting Diodes. *Synthetic Metals* **2000,** *111–112*, 369-372.

[49] Beerbom, M. M.; Lagel, B.; Cascio, A. J.; Doran, B. V.; Schlaf, R., Direct Comparison of Photoemission Spectroscopy and in Situ Kelvin Probe Work Function Measurements on Indium Tin Oxide Films. *Journal of Electron Spectroscopy and related Phenomena* **2006,** *152*, 12-17.

[50] Mohapatra, S. K.; Romanov, A.; Angles, G.; Timofeeva, T. V.; Barlow, S.; Marder, S. R., Synthesis and Characterization of Nonamethylrhodocenium and Iridocenium Hexafluorophosphate Salts. *Journal of Organometallic Chemistry* **2012,** *706–707*, 140-143.

CHAPTER 6

CONCLUSIONS AND OUTLOOK

This thesis has focused on the use of two distinct, but related methods for surface modification to tune the electronic properties of transparent conducting oxides, particularly ITO and ZnO. One method is based on the chemisorption of phosphonic acids to the surface of the substrate (Chapters 3 and 4), which, by virtue of the dipole inherent within the molecule, induces a dipole at the interface of the substrate thereby altering the WF of the material that is being modified. In the other approach in which dopants are used to treat these TCOs (Chapter 5), an interface dipole is formed from the electrostatic adsorption of charged species on the substrate, presumably by electron transfer taking place between the dopant and the TCO surface. In both cases (based on XPS measurements of modified ITO) a sub-monolayer of material at the surface can be responsible for drastic WF changes. Phosphonic acids can increase the WF of ITO to 5.4 eV (starting from ~ 4.5 eV) and that of ZnO to 4.5 eV (starting from ~ 3.9 eV), and in the case of metal-organic dopants, can decrease the WF of both ITO and ZnO to approximately 3.3 eV.

Chapter 2 discussed the synthesis of various surface modifiers, in particular phosphonic acids, and is representative of the wide variety of functionalities that can be placed on a surface through the incorporation of a phosphonic acid binding group. The summary of literature phosphonic acids provided in Chapters 3 and 4 that have been used to modify the surfaces of ITO and ZnO show (coupled with the synthetic section of this thesis, Chapter 2) that materials from simple alkyl tails to more complicated fullerene and

perylene diimide molecules can be made typically in a straightforward manner and on relatively large scales. In an effort to better illustrate both the variety of phosphonic acids that have been used as well as the surfaces which have been modified in this manner data from molecules synthesized in the Marder group and subsequently used by various collaborators (Georgia Tech, the University of Arizona, the University of Washington, National Renewable Energy Laboratory, and Princeton) has been summarized in Figure 6.1 (with the dashed lines representing the WF of the bare substrate). The data for this figure originates from a variety of measurement techniques including KP, UPS, and LIXPS. For the sake of clarity, for a single metal oxide where multiple measurement techniques were used the most representative value is shown, but typically from technique to technique small deviations in WF were measured (usually less than 0.3 eV). Thus, this shows that not only can phosphonic acids tune the WF of a wide variety of substrates, but can do so in a manner that is reproducible in many independent laboratories.

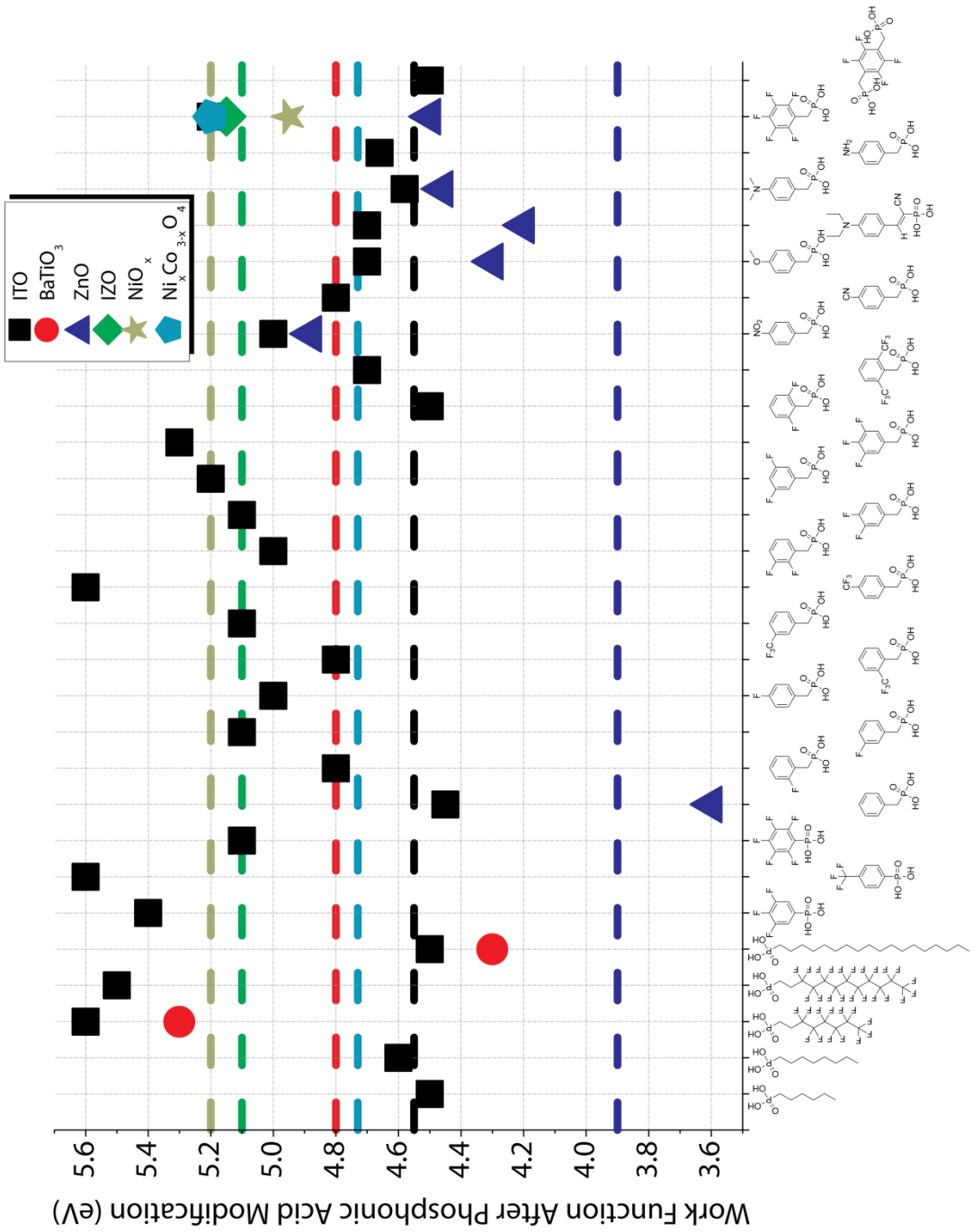

Figure 6.1 Compilation of work function data for phosphonic acids synthesized in the Marder group and used at a variety of institutions for the modification of multiple metal oxide surfaces. Data presented is a compilation of KP, UPS, and LIXPS WF measurements with the most representative value shown for phosphonic acids on a given metal oxide measured using multiple techniques. The data shown here originates from a variety of sources including this thesis, unpublished results by this author, and published sources as well.[1-10] Note that the dashed lines represent the WF of the bare substrate.

In the case of phosphonic acids on ITO, it appears that ordering is a factor that needs to be considered for optimizing modification conditions on this substrate. As was shown in Chapter 3, nearly all the benzyl phosphonic acids examined afforded molecular orientations that (based on NEXAFS measurements) could not be readily determined, and are thus likely a mixture of orientations leading to disordered surfaces. It would be interesting to follow up on recently published work demonstrating that phosphonic acids afford higher quality monolayers when deposited under high-temperature modification conditions,[11] and conduct studies using NEXAFS and PM-IRRAS to compare with results discussed in Chapter 3. It is likely that the enhanced quality of the monolayers formed at high temperatures originates from better overall packing, which presumably originates from more ordering at the surface. Being able to provide empirical evidence that such well-ordered monolayers form would be beneficial to the scientific community as it would provide a set of modification conditions for phosphonic acids on ITO that would be easy to reproduce from laboratory to laboratory (on a time scale of several hours). Such information would also be able to better inform the design of future benzyl phosphonic acids in such a way that additional substituents/steric bulk could be used to enhance the orientation of the interface dipole, potentially leading to even larger changes in WF.

While ITO appears to have questions related to molecular orientation, it appears that the stability of the underlying ZnO when conducting phosphonic acid modification needs further examination. As shown in Chapter 4, the ZnO substrate is readily etched by phosphonic acid surface modifiers and in many cases reproducible WF values were much more difficult to attain for this metal oxide in comparison with ITO. To further

probe the ZnO stability to phosphonic acid modification, a direct comparison using phosphonic acids which show a propensity to etch the surface of ALD ZnO (for instance 2,6-F2BPA and 3,4,5-F3BPA) should be tested on ZnO deposited by multiple techniques (such as ALD, RF-Magnetron, and sol-gel deposited) thereby examining whether the roughness of the ZnO surface or the preferred orientation impacts the etching effects of the phosphonic acid (the exposed crystal face has been shown to be a factor in etching under acidic and basic conditions)[12-14] as no direct correlation between acidity and etching ability was found in Chapter 4. Furthermore, it would be important to re-examine some of the alkyl phosphonic acids previously deposited on RF-Magnetron prepared ZnO[15] (where etching of the ZnO was not observed) on ALD ZnO looking not only at etching, but also IRRAS to examine if any differences in the predominately exposed crystal face (in this case 001[16] and 0002,[17] respectively) leads to differences in binding. One other important comparison that should be conducted in the future is to further probe the possibility of spin-coating phosphonic acids on ZnO. Based on current results differences exist between WF values obtained for the same benzyl phosphonic (2,6-F2BPA) acid spin-coated on ALD ZnO (3.8 eV) and sol-gel deposited ZnO (3.4 eV).[18] It remains to be determined if these differences are attributable to the differences in reactivity of ALD ZnO and sol-gel ZnO.

Generally, being able to tune the WF of substrates either up or down in energy is an interesting scientific endeavor in its own right, when put in the context of organic optoelectronic devices, the significance of surface modification of metal oxides is readily highlighted. Interest in this field has been rapidly increasing over the last several decades[19] due to the potential for high-throughput manufacturing of flexible, lightweight,

and low-cost devices such as light-emitting diodes, photovoltaics, and transistors. There are multiple factors that determine overall efficiency within devices, such as the properties of electrodes and organic active layers, but also of crucial importance is the interface between these two disparate materials. Having the ability to compatibilize the inorganic electrode with the organic overlayer (both physically and electronically) aids in minimizing the barriers to injection/collection of carriers within organic optoelectronic devices. In the case of phosphonic acids on ITO[3, 6, 20-22] (and to some extent ZnO as well)[18] exploration of the utility of these surface modifiers has already begun, with these modifiers being found to simultaneously enhance wetting of the active layer on the ITO substrate and to minimize energetic barriers to the movement of carriers into or out of the device.

In the case of the doping approach, some of the surfaces modified this way that had previously been examined in the literature (Chapter 5), have been found to decrease electron injection barriers in devices such as OLEDs.[23] For n- and p-dopants used in this thesis, however, no device studies have been performed, and is the next step to take in the examination of these particular modifiers. For instance, making simple electron-only sandwich device structures consisting of a top electrode and electron transport material deposited on top of either ITO [M^+]/ITO (where [M^+] is the monomer cation deposited on the surface from the solution of the dimers investigated in Chapter 5; [IrCpCp*]$_2$, [RuMesCp*]$_2$, and [RhCpCp*]$_2$) in a manner similar to that used to investigate TDAE on ITO[23] would allow for a determination of electron injection efficiency from the ITO. The electron transporting layer could be varied so that materials having electron affinities greater than or less than the WF of the surface after modification could be examined.

Furthermore, it would be important to compare the dimers with other methods of lowering the WF of ITO such as TDAE, or polytheylenimine ethoxylated (PEIE), which is a polymer material processed from aqueous solutions that has recently been demonstrated to decrease the WF of a variety of substrates.[24] Verification that the monomer cations present on the surface (as confirmed by XPS analysis in Chapter 5) do reduce the electron injection barrier and are not detrimental to the flow of electrons into the device would validate the usefulness of the technique beyond the spectroscopic studies conducted thus far.

Assuming the dopants do indeed decrease the barrier to electron injection, as would be expected from the WFs of the modified surfaces, and produce results similar to the TDAE and PEIE control devices, several more questions can then be addressed. This can include examination of the ITO substrate after the device preparation by removing the top electrode and active layer to see if a layer of monomer cations is still present, or if there was migration of these charged species into the active layer. Investigation of whether the dimer treated ITO surface observes any differences in long term stability under applied current, or if there are differences in device performance based on processing conditions (i.e. does the low WF surface remain after treatment with a variety of solvents) could also be conducted. Another interesting question to test would be to see how much air exposure of the dimer treated ITO impacts overall device performance to probe the influence the WF increase after air exposure has on the device. The question of air exposure can also be coupled with testing whether or not it is possible to perform the surface modification in ambient conditions rather than inside of a glove box since both the starting dimer and resultant monomer cation are relatively air-stable, and would thus

test if the WF of ~ 4 eV is still achieved (similar to the WF for glove box modified then air exposed ITO).

Interestingly, this thesis has afforded insight that phosphonic acid modification and doping of surfaces should not be treated as mutually exclusive means of modifying a substrate, but rather as methods that should complement one another depending on the needs of the application. As was demonstrated when examining ITO using these two techniques (Chapters 3 and 5) phosphonic acids have the advantage of being able to increase the WF more so than the p-dopants examined to date, and alternatively, n-dopants can decrease the WF of ITO to a much greater extent than the phosphonic acids examined so far. The reason for these differences may come from the nature of the modifier coupled with the density of states in ITO. In the case of phosphonic acids, WF decreases may not be as readily possible to achieve because of the bond dipole that forms. When modifiers that increase the WF are deposited on the surface of ITO, the bond dipole and molecular dipole are typically additive, thereby leading to large changes in WF. When the modifiers have a molecular dipole designed to decrease the WF, however, the bond dipole opposes the molecular dipole, thus negating some of its magnitude and making WF decreases harder to achieve. In the case of the dopants, the ability to tune the WF is likely related to the density of states as ITO is a n-doped semiconductor that has its Fermi level inside of the conduction band[25] in the bulk and right below the conduction band at the surface. Thus, it is relatively easy to have a large number of electrons be accepted by the ITO and allow for a large number of monomer cations to electrostatically bind to the surface of the substrate leading to a large interface dipole. For p-dopants, however, the density of states likely falls off rather sharply below

the Fermi level and so ITO cannot readily donate a large number of electrons to the dopant, which means that relatively few anionic species can be electrostatically bound to the surface, and that any electrons ITO does donate can greatly change the position of the Fermi level. This hypothesis is corroborated by the UPS data from Chapter 5, which demonstrated that in the case of p-dopants a shift in the VBM (meaning a Fermi level shift relative to the band structure) has more of an impact on the WF than the interface dipole. It would be interesting to examine the same n- and p-dopants on a surface such as $NiO_{1+\delta}$, which is p-type by virtue of its defects, meaning that if the previous hypothesis is true, the impact of n- and p-dopants would be reversed, and a WF increase would be more readily accessible than a WF decrease. Moreover, the bond dipole and molecular dipole oppose one another in the case of phosphonic acids designed to decrease the WF on ZnO and ITO; this is not necessarily the case for all oxides, where different binding modes and surface chemistries might give rise to opposite bond dipoles.

Overall, this thesis sought to examine methods by which the WF of a variety of surfaces (in particular ITO and ZnO) can be modified. In the case of phosphonic acids on ITO, the goal was to provide a systematic study demonstrating the relationship that exists between the molecular dipole, the coverage of the modifier on the surface, and the molecular orientation once bound to the substrate. A clear relationship was demonstrated between molecular dipole and coverage; however, analysis of the orientation of the molecules on the surface was complicated due to rotational degrees of freedom present within benzylphosphonic acids. It was then demonstrated that the modification of ZnO is less straightforward compared to its ITO counterpart, with issues of etching and variable results consequently being present for this metal oxide. Progress was made, however, to

indicate that phosphonic acid modification of ZnO benefits from lower concentration and shorter modification times in order to mitigate etching of the underlying substrate. The study also demonstrated that, just like on ITO, decreasing the WF with these types of modifiers is more problematic than originally anticipated and that both ITO and ZnO see similar shifts in WF (relative to their respective bare WF values) when the same phosphonic acids are used to treat the substrates. While this thesis has demonstrated the versatility of two related methods for altering the WF of metals and metal oxides, more work is still required to examine the limits of the techniques shown, determine how generally applicable these methods are to other substrates (particularly in the case of the dopants) and determine the real utility of the materials for use in device architectures. It is the hope of this author that the work provided herein can be utilized in future device studies as both methods discussed are straightforward ways by which to increase or decrease the WF of ITO, ZnO, and likely other substrates as well.

6.1 References

[1] Schulmeyer, T.; Paniagua, S. A.; Veneman, P. A.; Jones, S. C.; Hotchkiss, P. J.; Mudalige, A.; Pemberton, J. E.; Marder, S. R.; Armstrong, N. R., Modification of Batio3 Thin Films: Adjustment of the Effective Surface Work Function. *Journal of Materials Chemistry* **2007,** *17*, 4563-4570.

[2] Paniagua, S. A.; Hotchkiss, P. J.; Jones, S. C.; Marder, S. R.; Mudalige, A.; Marrikar, F. S.; Pemberton, J. E.; Armstrong, N. R., Phosphonic Acid Modification of Indium-Tin Oxide Electrodes: Combined Xps/Ups/Contact Angle Studies. *Journal of Physical Chemistry C* **2008,** *112*, 7809-7817.

[3] Sharma, A.; Kippelen, B.; Hotchkiss, P. J.; Marder, S. R., Stabilization of the Work Function of Indium Tin Oxide Using Organic Surface Modifiers in Organic Light-Emitting Diodes. *Applied Physics Letters* **2008,** *93*, 163308.

[4] Hotchkiss, P. J. The Design, Synthesis, and Use of Phosphonic Acids for the Surface Modification of Metal Oxides. Ph.D. Thesis, Georgia Institute of Technology, Atlanta, GA, 2008.

[5] Hotchkiss, P. J.; Jones, S. C.; Paniagua, S. A.; Sharma, A.; Kippelen, B.; Armstrong, N. R.; Marder, S. R., The Modification of Indium Tin Oxide with Phosphonic Acids: Mechanism of Binding, Tuning of Surface Properties, and Potential for Use in Organic Electronic Applications. *Accounts of Chemical Research* **2012,** *45*, 337-346.

[6] Knesting, K. M.; Hotchkiss, P. J.; MacLeod, B. A.; Marder, S. R.; Ginger, D. S., Spatially Modulating Interfacial Properties of Transparent Conductive Oxides: Patterning Work Function with Phosphonic Acid Self-Assembled Monolayers. *Advanced Materials* **2012,** *24*, 642-646.

[7] MacLeod, B. A.; Horwitz, N. E.; Ratcliff, E. L.; Jenkins, J. L.; Armstrong, N. R.; Giordano, A. J.; Hotchkiss, P. J.; Marder, S. R.; Campbell, C. T.; Ginger, D. S., Built-in Potential in Conjugated Polymer Diodes with Changing Anode Work Function: Interfacial States and Deviation from the Schottky–Mott Limit. *The Journal of Physical Chemistry Letters* **2012,** *3*, 1202-1207.

[8] Bulusu, A.; Paniagua, S. A.; MacLeod, B. A.; Sigdel, A. K.; Berry, J. J.; Olson, D. C.; Marder, S. R.; Graham, S., Efficient Modification of Metal Oxide Surfaces with Phosphonic Acids by Spray Coating. *Langmuir* **2013,** *29*, 3935-3942.

[9] Macech, M. R. Electrical, Structural, and Compositional Characterization of Interlayer Material and New Active Layers in Organic Solar Cells. University of Arizona, Arizona, 2012.

[10] Ndione, P. F.; Garcia, A.; Widjonarko, N. E.; Sigdel, A. K.; Steirer, K. X.; Olson, D. C.; Parilla, P. A.; Ginley, D. S.; Armstong, N. R.; Richards, R. E.; Ratcliff, E. L.; Berry, J. J., Highly-Tunable Nickel Cobalt Oxide as a Low-Temperature P-Type Contact in Organic Photovoltaic Devices. *Advanced Energy Materials* **2013,** *3*, 524-531.

[11] Paniagua, S. A.; Li, E. L.; Marder, S. R., Adsorption Studies of a Phosphonic Acid on Ito: Film Coverage, Purity, and Induced Electronic Structure Changes. *Physical Chemistry Chemical Physics* **2014,** *16*, 2874-2881.

[12] Palacios-Lidón, E.; Pickup, D. F.; Johnson, P. S.; Ruther, R. E.; Tena-Zaera, R.; Hamers, R. J.; Colchero, J.; Himpsel, F. J.; Ortega, J. E.; Rogero, C., Face-Selective Etching of Zno During Attachment of Dyes. *The Journal of Physical Chemistry C* **2013,** *117*, 18414-18422.

[13] Nicholas, N. J.; Ducker, W.; Franks, G. V., Differential Etching of Zno Native Planes under Basic Conditions. *Langmuir* **2012,** *28*, 5633-5641.

[14] Hüpkes, J.; Owen, J. I.; Pust, S. E.; Bunte , E., Chemical Etching of Zinc Oxide for Thin-Film Silicon Solar Cells. *ChemPhysChem* **2012,** *13*, 66-73.

[15] Hotchkiss, P. J.; Malicki, M.; Giordano, A. J.; Armstrong, N. R.; Marder, S. R., Characterization of Phosphonic Acid Binding to Zinc Oxide. *Journal of Materials Chemistry* **2011,** *21*, 3107-3112.

[16] van de Pol, F. C. M.; Blom, F. R.; Popma, T. J. A., R.F. Planar Magnetron Sputtered Zno Films I: Structural Properties. *Thin Solid Films* **1991,** *204*, 349-364.

[17] Li, H.; Schirra, L. K.; Shim, J.; Cheun, H.; Kippelen, B.; Monti, O. L. A.; Bredas, J.-L., Zinc Oxide as a Model Transparent Conducting Oxide: A Theoretical and Experimental Study of the Impact of Hydroxylation, Vacancies, Interstitials, and

Extrinsic Doping on the Electronic Properties of the Polar Zno (0002) Surface. *Chemistry of Materials* **2012,** *24*, 3044-3055.

[18] Cowan, S. R.; Schulz, P.; Giordano, A. J.; Garcia, A.; MacLeod, B. A.; Marder, S. R.; Kahn, A.; Ginley, D. S.; Ratcliff, E. L.; Olson, D. C., Chemically Controlled Reversible and Irreversible Extraction Barriers Via Stable Interface Modification of Zinc Oxide Electron Collection Layer in Polycarbazole-Based Organic Solar Cells. *Advanced Functional Materials* **2014**, Accepted.

[19] Martins, R.; Fortunato, E.; Barquinha, P.; Pereira, L., *Transparent Oxide Electronics: From Materials to Devices*. Wiley: 2012.

[20] Sharma, A.; Haldi, A.; Hotchkiss, P. J.; Marder, S. R.; Kippelen, B., Effect of Phosphonic Acid Surface Modifiers on the Work Function of Indium Tin Oxide and on the Charge Injection Barrier into Organic Single-Layer Diodes. *Journal of Applied Physics* **2009,** *105*, 074511.

[21] Sharma, A.; Haldi, A.; Potscavage Jr, W. J.; Hotchkiss, P. J.; Marder, S. R.; Kippelen, B., Effects of Surface Modification of Indium Tin Oxide Electrodes on the Performance of Molecular Multilayer Organic Photovoltaic Devices. *Journal of Materials Chemistry* **2009,** *19*, 5298-5302.

[22] Sharma, A.; Hotchkiss, P. J.; Marder, S. R.; Kippelen, B., Tailoring the Work Function of Indium Tin Oxide Electrodes in Electrophosphorescent Organic Light-Emitting Diodes. *Journal of Applied Physics* **2009,** *105*, 084507.

[23] Osikowicz, W.; Crispin, X.; Tengstedt, C.; Lindell, L.; Kugler, T.; Salaneck, W. R., Transparent Low-Work-Function Indium Tin Oxide Electrode Obtained by Molecular Scale Interface Engineering. *Applied Physics Letters* **2004,** *85*, 1616-1618.

[24] Zhou, Y. H.; Fuentes-Hernandez, C.; Shim, J.; Meyer, J.; Giordano, A. J.; Li, H.; Winget, P.; Papadopoulos, T.; Cheun, H.; Kim, J.; Fenoll, M.; Dindar, A.; Haske, W.; Najafabadi, E.; Khan, T. M.; Sojoudi, H.; Barlow, S.; Graham, S.; Bredas, J. L.; Marder, S. R.; Kahn, A.; Kippelen, B., A Universal Method to Produce Low-Work Function Electrodes for Organic Electronics. *Science* **2012,** *336*, 327-332.

[25] Fan, J. C. C.; Goodenough, J. B., X-Ray Photoemission Spectroscopy Studies of Sn-Doped Indium-Oxide Films. *Journal of Applied Physics* **1977,** *48*, 3524-3531.

APPENDIX A

SURFACE MODIFICATION FOR MONOLAYER THERMOCHCEMICAL NANOLITHOGRAPHY

A.1 Overview of Thermochemical Nanolithography

Having the ability to control the patterning of a surface on the nanometer scale is an interesting challenge due to the number of fields to which the patterning of the surface can be applied. This could include, but is not limited to, areas of chemistry[1], biochemistry[2-5], electronics[6], data storage[7-10], and inorganic chemistry.[11-13] There are several methods that have currently been developed for generating patterned surfaces at this time that are based on the use of scanning probe microscopy, particularly the atomic force microscope (AFM).[14-17] Many of the methods that have been used are based on the principle of deforming the surface wherein topographical changes to the surface are exploited by removing material from the surface for subsequent deposition in the negative region, performing crosslinking at the surface, or using the buildup of polymer caused by the depression of the AFM tip into the surface.[7] Dip-pen nanolithography (DPN) is also a promising method for the patterning of surfaces due to its ability to place molecules on the surface in a positive writing mode.[18] Another interesting method that exists is to utilize an electrical bias applied through an AFM (AFM-assisted electrostatic lithography) tip in order to cause changes in the *z* direction of the polymer.[6, 19] It is even possible to simply utilize the surface contact of the AFM tip to remove material from the surface by mechanically plowing through the surface and this can be combined with heating for thermomechanical nanolithography.[20-22] As with all nanoscale methods,

inherent issues remain with the overall speed and in some cases the parallelization of the process.

Research in the Marder group (in collaboration with Elisa Riedo's and Jennifer Curtis' groups) has also focused on the use of AFM techniques to perform surface patterning by incorporating the ability to heat an AFM tip with chemical reactions (namely deprotections) that occur at higher temperatures. This method has been termed thermochemical nanolithography (TCNL) and has resulted in several publications both completed and in progress.[23-26] This particular system was chosen since it has the ability to truly control surface changes at the nanometer scale (currently demonstrated down to 12 nm), can have writing speeds that are fast (ideally on the order of centimeters per second), does not require physically deforming the surface in order for the modification to occur, and can function under a variety of environmental conditions which would enhance its overall versatility in a wide variety of research settings. The methodology used relies on utilizing resistively heated AFM tips, which solves the problem of dip-pen nanolithography which is limited by mass transfer, since TCNL is limited only by heat transfer and generally it is accepted that heat transfer can occur on a scale much faster than mass transfer. Modeling of such heat transfer has currently been examined for the tips used during the process.[27] This heating of the surface is truly only half of the method since the other half of patterning the surface relies on the ability to perform chemical reactions selectively on the surface. In cases that have been studied in the group thus far, this has included the deprotection of a reactive group within a patterned region. This exposes a chemically reactive group, which can be utilized for further selective chemistry or selective deposition at the surface. Much of the work that has been conducted thus far

has focused on the use of polymers for the patterning of surfaces, the general scheme of which is shown in Figure A.1. Recent examples of TCNL have demonstrated the ability to form gradients on the surface of a substrate, enabling extremely complex patterns as shown in Figure A.2, as well as parallelization of the protocol.

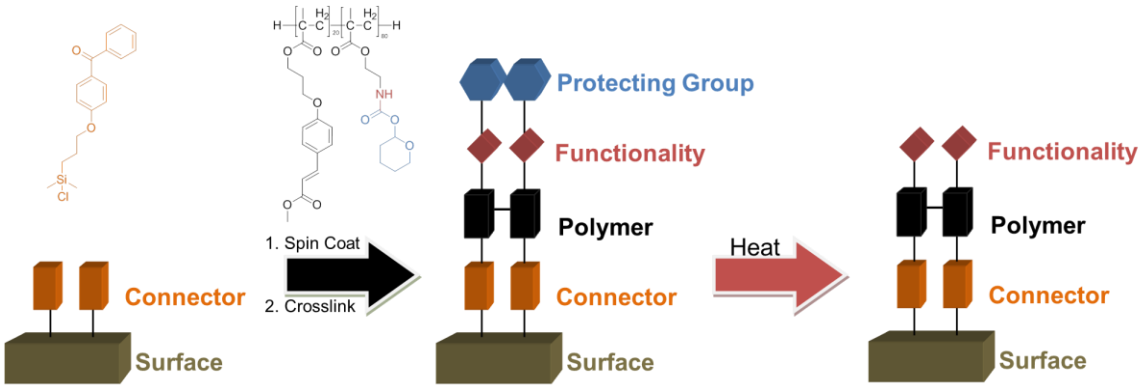

Figure A.1 Schematic representation of thermochemical nanolithography using a polymer containing a THP carbamate protecting group. The resistively heated AFM tip serves to perform the desired chemical deprotection, which exposes the desired functionality on the surface (in this case a primary amine) so that other materials (such as nanoparticles, small molecules, cells, etc.) can be attached at these newly formed binding sites. Note that the use of the chlorosilane benzophenone is to form a covalent linkage between the surface and the polymer layer to avoid delamination in subsequent processing steps.

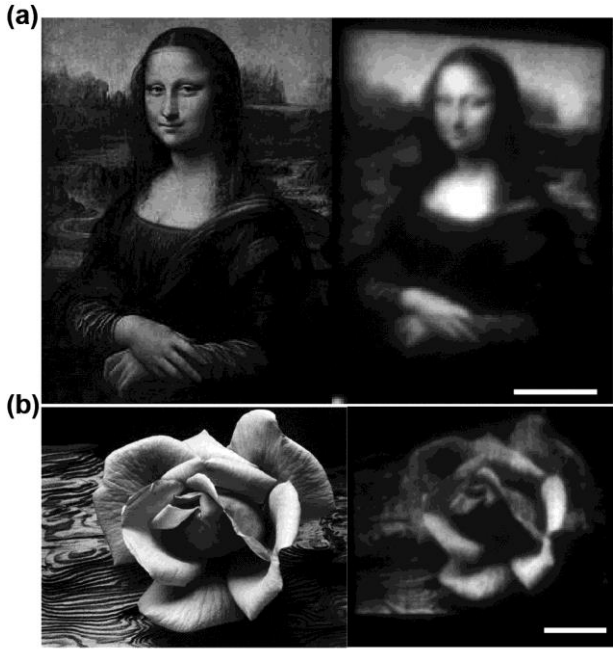

Figure A.2 Complex patterns generated using TCNL in the case of (a) (left) the original image of the Mona Lisa is shown with the experimental rendition (right) of the same image reproduced at a size of ~32 μm through the use of TCNL and subsequent binding of NHS-DyLight 633 to the surface. (b) (Left) Original image by Ansel Adams entitled "Rose and Driftwood" and the TCNL reproduction of the image (right). In both cases the scale bar is 10 μm. Image has been reproduced from the literature.[25]

A.2 Selection of Protecting Group for Monolayer Based TCNL

While the polymer based system has clearly been proven to work, some issues such as non-specific binding of materials to the polymer surface have remained. Thus, in an effort to provide for the same functionality on the surface, while minimizing the problems inherent to the use of a polymer, monolayers were chosen to be examined for TCNL applications. There exists literature precedence for the use of monolayers for patterning *via* other SPM techniques such as electrochemical deprotection.[28] This methodology involved the use of a α,α-dimethyl-3,5-dimethoxybenzyloxycarbonyl (DDZ) protecting group. The molecule in question as well as the overall scheme of the

electrochemical deprotection is outlined in Figure A.3. It should be noted that the DDZ protecting group has been used as a photocleavable amine-protecting group in the literature[29] as well as a photobase generator in lithography (deep UV absorption).[30] Another interesting point to note about the structure shown in Figure A.3 is that it has been previously reported in the literature,[31] and the proposed mechanism for deprotection (determined through irradiation in solution and in solid state)[30] is the same as that shown in Figure A.3.

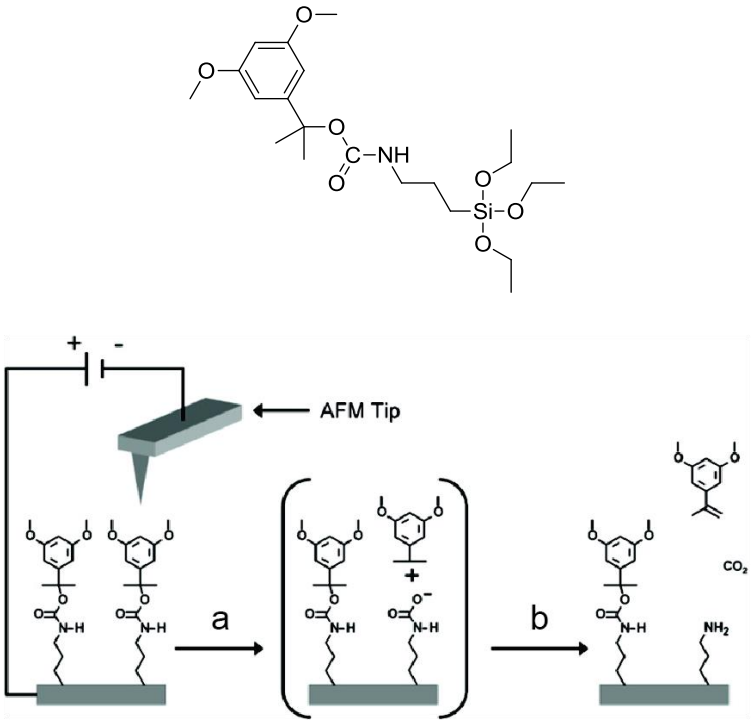

Figure A.3 Structure of monolayer for surface modification (top) and schematic of surface deprotection through the use of an AFM tip and applied bias (bottom). The molecule undergoes a heterolytic bond cleaveage (a) followed by the release of carbon dioxide and 3,5-dimethoxy-α-methylstyrene (b), which yields a primary amine. Image modified from the literature. [28]

A.3 Thermal Deprotection of the DDZ Protecting Group

The structure of the silane surface modifier and the expected products from a thermal decomposition are summarized in Figure A.4. The characterization of other carbamate based materials has been discussed previously in the literature and indicates that there are several possibilities for the thermal decomposition of the material.[32-35] After synthesis, pyrolysis of the material through thermogravimetric analysis coupled with mass spectrometry (TGA-MS) was used to demonstrate the production of CO_2 gas upon heating, which would be indicative of the deprotection event taking place (Figure A.5). The deprotection event was also confirmed by ^{1}H and ^{13}C NMR examining varying temperatures between 130 °C and 200 °C, at which point the deprotection was observed with the simultaneous formation of the expected alcohol and alkene side products from Figure A.4.

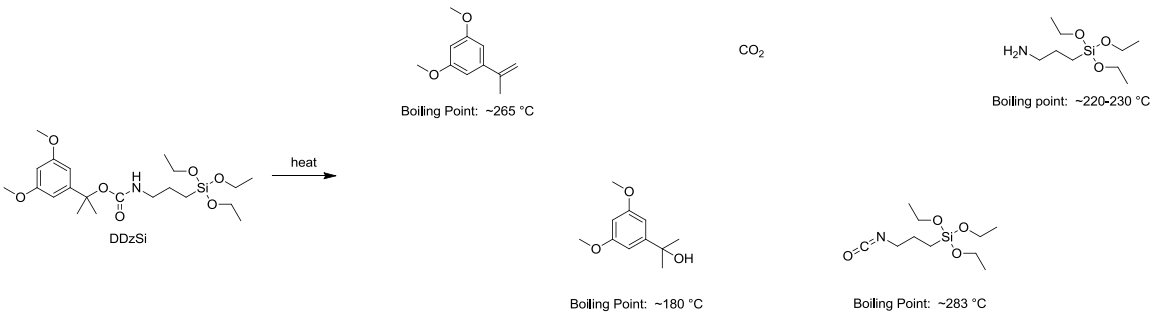

Figure A.4 Structure of silane utilized throughout the monolayer TCNL studies (DDzSi) along with the expected products from a thermal decomposition of the material.

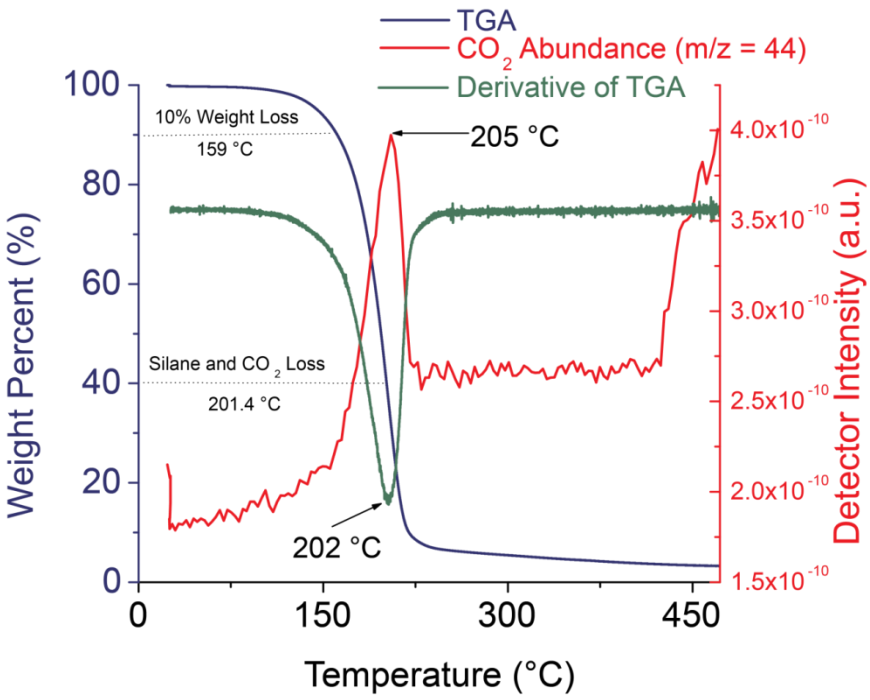

Figure A.5 TGA under inert atmosphere (blue trace) of DDzSi overlaid with the derivative TGA graph (green trace). The detector intensity of the mass spectrometer (red trace) is for CO_2 and corresponds well with the derivative TGA.

A.4 ^{1}H NMR Analysis of DDz Deprotection *via* Heating

As another method to corroborate the TGA data and show the formation of the decomposition products as a function of time, an experiment was setup wherein approximately 100 mg of the DDz Si was heated in the bulk. This was done without any solvent in a Claisen flask while monitoring the temperature of both the oil bath as well as the temperature within the flask. Four data points were collected at internal flask temperatures of 130, 153, 170, and 200 °C allowing each to remain at temperature for approximately 8-10 minutes. The comparison of the ^{1}H NMR spectra for these compounds can be seen in Figure A.6.

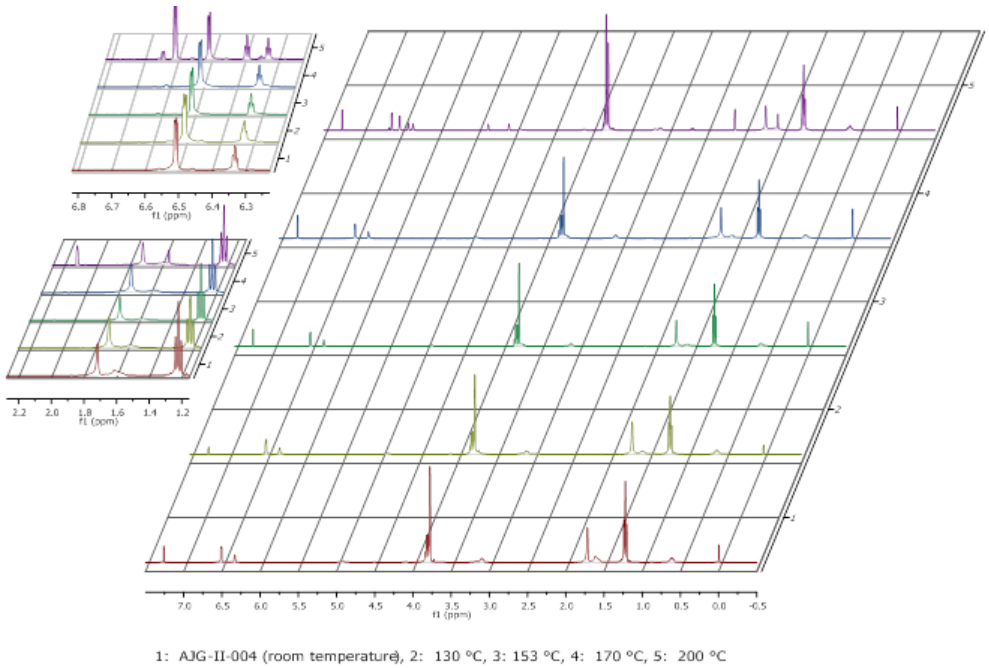

Figure A.6 Comparison of ^{1}H NMR spectra for heating of DDz Si at various temperatures as indicated below the figure. Note the inset shows the aromatic region of the spectrum (top) and the alkyl region (bottom). All spectra were obtained on a Varian 400 MHz NMR in $CDCl_3$ utilizing the residual solvent peak for reference at 7.26 ppm.

The most apparent information obtained from this spectrum is that there is very little difference between the room temperature spectrum and those obtained at 130, 153, and 170 °C. Yet, at 200 °C there is a marked difference apparent in both the aromatic and aliphatic regions of the spectrum. Of particular note is the appearance of two new sets of aromatic peaks, a doublet at 6.61 and a triplet at 6.40 ppm as well as a doublet at 6.65 and triplet at 6.35 ppm. An enlargement of this region for the 200 °C sample is provided in Figure A.7. Note that there is the presence of three distinct sets of peaks which correspond to three different molecules. Also note that these molecules appear to be in a 1:1:0.13 ratio (based on the aromatic doublet) of DDz protected silane:alkene:starting alcohol. Therefore, two distinct conclusions can be drawn from this information. The first being that the deprotection appears to be successful based on

this data since the expected alkene decomposition product was successfully trapped. The data also indicates that there is a slight amount of the reaction going to reform the starting isocyanate as evidenced by the formation of the initial alcohol. Various literature reports have examined the thermal decomposition of carbamates and have indicated that one of the possible results when this decomposition occurs can be the formation of the starting isocyanate.

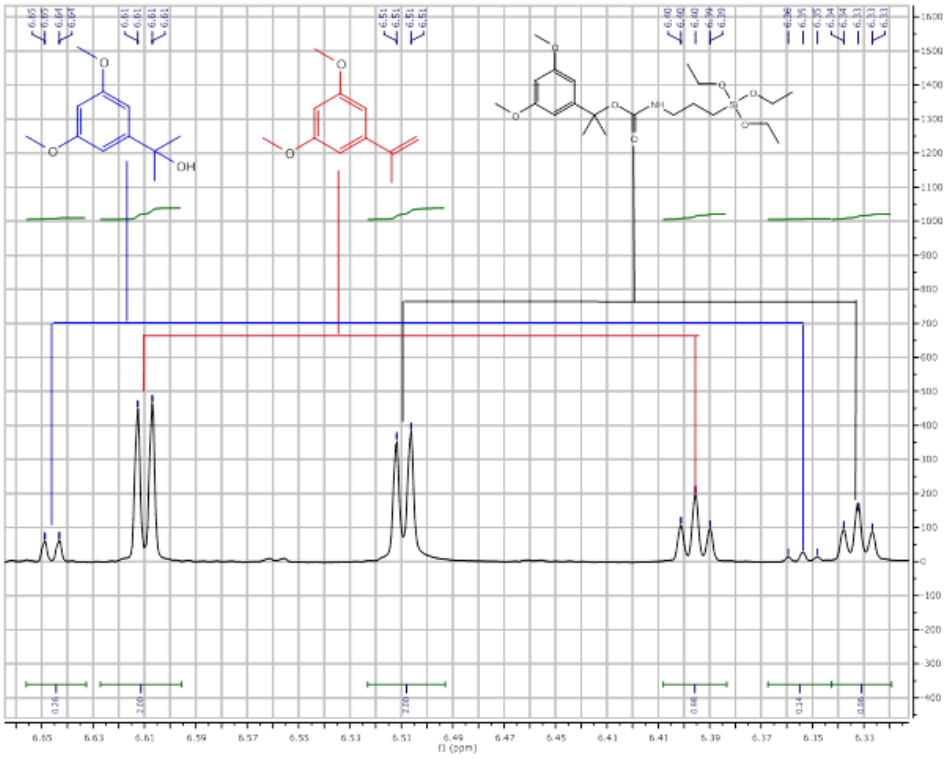

Figure A.7 Enlarged aromatic ^{1}H region for 200 °C DDz Si sample.

Further examination of the ^{1}H NMR spectra provides insight into the pyrolysis of the sample. In Figure A.8 the major changes between the silane at room temperature and after heating to 200 °C can be readily seen. As previously noted, the presence of the alkene product cannot be disputed as it matches what has been previously reported in the

literature.[36] The shifts that are highlighted and correspond to the starting alcohol is based on spectra that was collected of the starting material in CDCl3. Unfortunately, due to overlap with the starting material the peak at 1.7 cannot be resolved, but the peak at approximately 1.5 ppm is readily observed. The most interesting item to note from these overlaid spectra is the presence of a triplet at approximately 2.7 ppm. This peak is consistent with a literature report for the silane amine.[33]

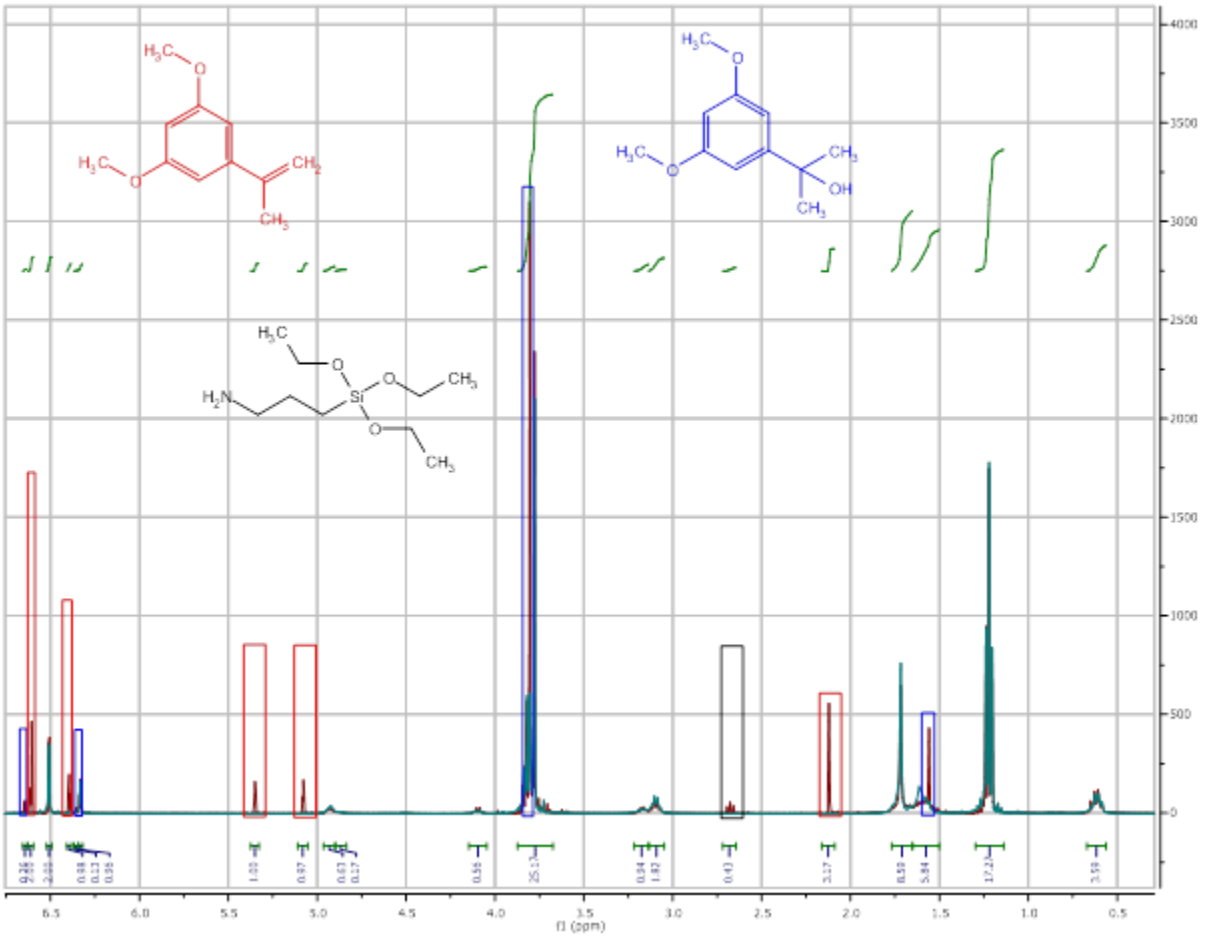

Figure A.8 Overlay of ^{1}H NMR spectra of DDz Si at room temperature (blue) and heated to 200 °C (red). The peaks of interest are highlighted with the color corresponding to the molecule provided in the image.

A.5 ^{13}C NMR Analysis of DDz Deprotection *via* Heating

In a manner similar to that conducted for the monitoring of heating by 1H NMR, 13C NMR was also used to monitor the bulk heating for the thermal deprotection of the DDz protecting group. The comparison of the ^{13}C spectra before and after heating at 200 °C for 8-10 minutes are shown in Figure A.9 along with color-coded peak assignments. Overall, this data corroborates what was observed for the ^{1}H NMR data. Also of note is the presence of some peaks for the starting alcohol, the desired amine, and the starting isocyanate as well. It should be noted that not all peaks are present for these molecules, likely due to concentration issues and that the peak present for the isocyanate is not enough direct evidence without repeating the experiment and ensuring that the reaction goes to completion. Otherwise, the data supports the previous analysis and thus there is evidence for the formation of all expected products from the pyrolysis reaction.

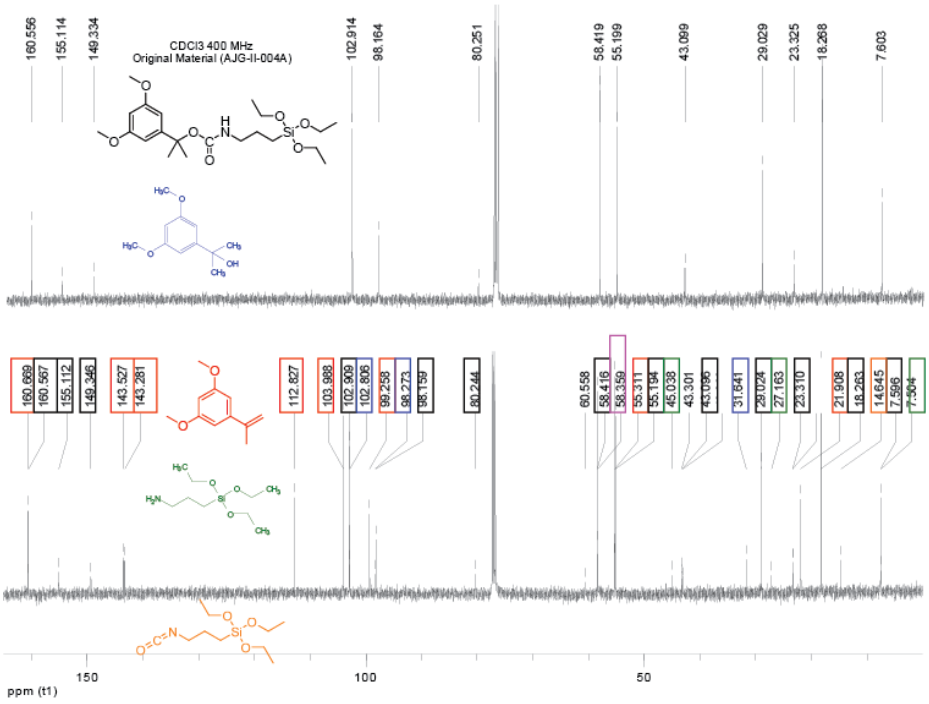

Figure A.9 ^{13}C NMR comparison of DDz Si at room temperature (top) and after heating to 200 °C for 8-10 minutes. The peak assignments are based on literature values for the molecules in question.

A.6 Analysis of Surface Bound DDz Deprotection

A.6.1 IRRAS Analysis

The IR spectrum for the DDz Si had been collected (by KBr pellet), which matched the literature report.[28] In order to perform the grazing angle IR experiment the blank reference (Glass:Ti:Au:SiO_x) was used as a background and 2000 scans were collected. A comparison of these two sets of data can be found in Figure A.10. The data indicates successful modification of the surface as well. Note that the carbonyl and aromatic stretches are readily observed (although it appears that the carbonyl has a slight shoulder). Also Si-O bonds are observed on the surface as well, similar to those observed

in the bulk. What is somewhat concerning, however, is the absence/low signal from the C-H stretching. It would be expected as there are both methylene and methyl groups within the molecule that these stretches should be readily apparent, and have been observed for the modification of surfaces with phosphonic acids. Yet, in this spectrum, the low intensity could indicate a low coverage on the surface, which would be corroborated by the relatively low intensity of the other signals within the spectrum (for instance the intensity of the carbonyl is 9.84×10^{-4} which is rather low even for a "monolayer"). Another possible explanation for the absence of these spectral features could be contamination of the unmodified surface. The carbonaceous contamination on the surface could have been enough to cancel any C-H stretching that had been observed and give rise to the collected data. In either case, it appears that the surface is not well covered and that subsequent experiments should involve the hydroxylation of the surface prior to the modification. This should enhance the ability of the silane to bind, resulting in increased coverage, and should provide for better analysis in the future from both IRRAS and XPS.

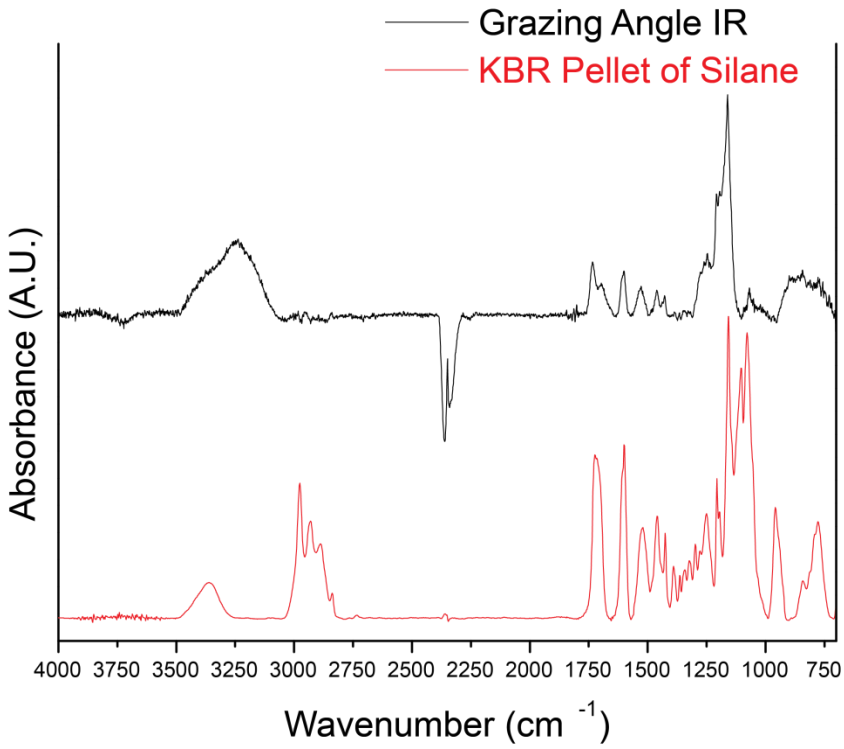

Figure A.10 Comparison of KBr pellet of DDz Si and IRRAS spectrum of the modified Glass:Ti:Au:SiOx:Silane surface. Note that the IRRAS spectrum was obtained utilizing 2000 scans, reference to an unmodified substrate, water was subtracted from the spectrum, and the baseline corrected.

A.6.2 Surface Deprotection and Binding

The silane was examined in the bulk on glass slides through the use of multiple methods including contact angle, XPS, IRRAS and UV-Vis spectroscopy. In the case of analysis by UV-Vis, fluorescein isothiocyante (FITC) was bound to the surface after deprotection and the intensity monitored as a function of time in a 200 °C oven. As a control, surfaces were also modified with aminopropyl triethoxy silane (APTES) since this would mimic the surface after a complete deprotection event. A summary of the experimental scheme and experimental UV-Vis evidence is shown in Figure A.11. The data showed the inability of FITC to bind to the surface of a DDzSi modified sample that

had not been heated. Upon heating at 200 °C for 10 minutes, however, the characteristic absorption of FITC was observed, which decreased with increasing amount of time at high temperature. The APTES control sample shows absorbance that also decreased with increasing time at 200 °C. Contact angle was in good agreement with the UV-Vis data and showed hydrophobic (DDz protected) surfaces becoming more hydrophilic after heating and returning to hydrophobic after treatment with FITC. IRRAS corroborated the deprotection event as evidenced by the disappearance of the carbonyl peak from the DDz protecting group upon heating. Through this combination of techniques it appeared that the DDz group was able to thermally cleave at approximately 200 °C when bound to the surface.

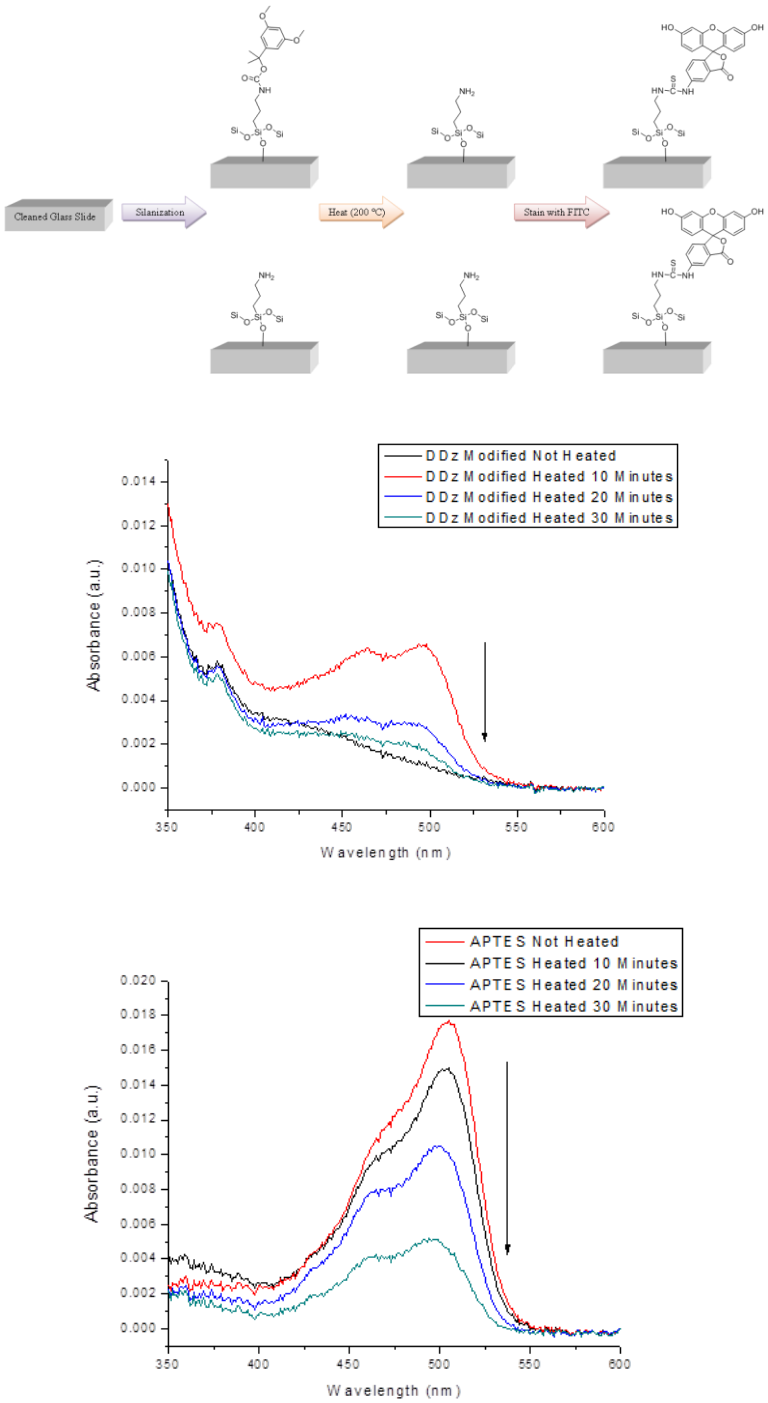

Figure A.11 (Top) Experimental scheme for examining the deprotection of DDzSi on the surface of a glass slide. APTES modified surface served as the control, and the structure of FITC after attachment to the surface bound amine is shown. (center) Absorbance as a function of the amount of time DDzSi modified and FITC treated slides were heated. Note the lack of signal without heating and the decrease with extended heating. (Bottom, right) Absorbance of APTES modified and FITC treated slides as a control.

A.7 Attempts at TCNL Patterning of DDz Si

Based on the evidence shown in A.3 the DDzSi molecule appeared to be a good candidate for patterning with a thermal cantilever. Patterning and indirectly observing the chemical deprotection (through lateral force microscopy (LFM) or staining with a fluorescent dye) proved to be challenging. Initial results (Figure A.12) were promising and a pattern of triangles made at varying heater temperatures became readily visible in the LFM, but appeared to spread with increasing tip temperature. Further attempts at patterning were highly variable in terms of results, going from images similar to that in Figure A.12 to not being able to observe any measurable signs of successful patterning. Another promising example was patterning the surface to selectively bind a protein, streptavidin. AFM contact and tapping mode images along with the programmed patterns are shown in Figure A.13. While a friction change was noted, no change in the phase image was observed and thus it is unclear if the desired deprotection and binding took place.

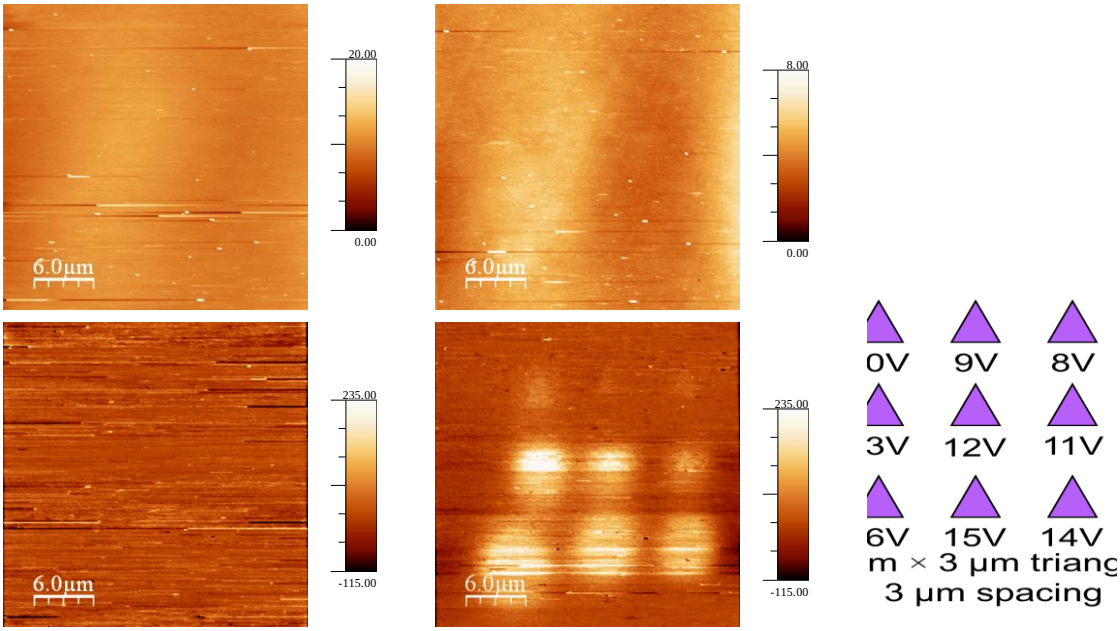

Figure A.12 Topography and phase images before (left) and after (right) patterning using the template shown at right. Note that triangles appear to form at lower voltages and at higher voltages, but is more spread out after patterning at higher voltages. The scales are in nm for topography and mV for friction.

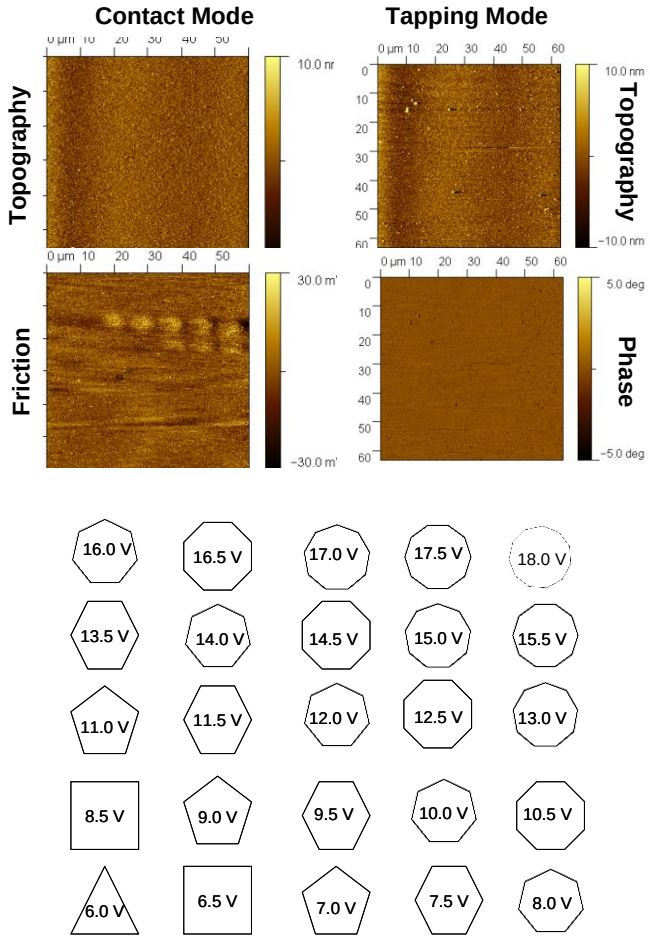

Figure A.13 (Top) Contact and tapping mode AFM images after patterning of a DDzSi modified silica sample with streptavidin. Shapes are visible in the friction image above approximately 14 V, which may be indicative of the onset of deprotection. The phase image, however, does not corroborate the friction image if streptavidin had bound to the patterned areas. (Bottom) Desired patterns programmed to vary tip temperature at the surface.

Due to the variable nature of the patterning electrochemical deprotection with an AFM tip as reported in the literature[28] was attempted and verified through the use of a fluorescent dye. Multiple substrates on which to deposit the silane were attempted such as glass, silica and silicon, but no exceptionally conclusive evidence was obtained that pointed to localized chemical deprotection by TCNL. Thus, while the material appears to work well in the bulk, it does not appear to work as well when selectively heated with the

AFM tip. This could be due to multiple factors such as physical desorption of the modifier due to the heat combined with the mechanical force of the cantilever on the surface or the thermal conductivity of the substrate. At this time it is unclear if monolayer TCNL is a viable alternative to polymer based methods.

A.8 Conclusions

This chapter demonstrated that thermal deprotection of the DDz protecting group is possible at approximately 200 °C based on analysis by TGA-MS with additional NMR analysis. When bound to the surface, which was confirmed by XPS analysis, and heated in the bulk the protecting group appears to cleave. Indirectly, this cleavage was demonstrated through the heating and subsequent binding of a fluorescently labelled dye with corroborating evidence originating from contact angle analysis, IRRAS, and UV-Vis. However, attempts to pattern the protected amine and selectively form primary amine sites on the surface of the substrate proved to be problematic and it is currently unclear whether an actual deprotection event is taking place due to localized heating with the AFM cantilever. There are several possible explanations for this difficulty. It is possible that the combination of heat and force from the AFM cantilever is causing the monolayer to cleave off the surface rather than deprotecting, it is also possible that the physical contact between the cantilever and the surface is desorbing the molecule while patterning. It is also possible that the selection of substrate (both glass and silicon wafers were used) greatly impacts the ability of the surface to either dissipate or confine heat. Overall, there is some promise in the basic principle of the technique based on bulk studies, however the problems that arose when attempting to pattern the substrate cannot

be understated and further research (potentially even with a different protecting group) is needed in order to better determine the viability of monolayer based TCNL.

A.9 Experimental

A.9.1 Materials

Synthesis of the DDz silane was conducted as discussed in Chapter 2. FITC was purchased from Sigma Aldrich and used without further purification.

A.9.2 Surface Treatment

Under inert atmosphere, freshly Piranha cleaned glass, silicon, or silica substrates were immersed in a 10 mM solution of the silane in anhydrous toluene. Typically in the case of DDzSi the reaction was allowed to occur overnight. In the case of APTES the surface was allowed to modify for several hours. In both cases upon removal from solution the surface was washed with toluene and immediately used in subsequent steps.

A.9.3 IRRAS

IRRAS spectroscopy was conducted in the same manner as reported in Chapter 4.

A.9.4 TGA-MS

TGA-MS was carried out using a TA Q500 TGA coupled to a quadrapole mass spectrometer. Samples were loaded into a TGA pan (Seiko 2.0mm Al pans, P/N SSC000E030) and allowed to purge under nitrogen for approximately 30 minutes prior to the start of the run. Samples were heated at a constant ramp rate from room temperature to the desired temperature. Multiple runs were conducted in order to ensure consistency of the data collected.

A.9.5 AFM Patterning

An Agilent 5600 LS AFM or Nanoscope Multimode IV (Veeco) equipped with a thermal cantilever was utilized in order to achieve chemical patterning. Patterning was done in collaboration with Debin Wang and Keith Carroll. The thermal cantilever is placed in series with a reference resistor (2 kΩ) biased with an applied voltage as shown in the text. Imaging was either conducted using the same thermal cantilever or an NSC-35NoAl (cantilever C) from MikroMasch.

A.10 References

[1] Gotsmann, B.; Duerig, U.; Frommer, J.; Hawker, C. J., Exploiting Chemical Switching in a Diels-Alder Polymer for Nanoscale Probe Lithography and Data Storage. *Advanced Functional Materials* **2006,** *16*, 1499-1505.

[2] Ginger, D. S.; Zhang, H.; Mirkin, C. A., The Evolution of Dip-Pen Nanolithography. *Angewandte Chemie-International Edition* **2004,** *43*, 30-45.

[3] Salaita, K.; Wang, Y. H.; Mirkin, C. A., Applications of Dip-Pen Nanolithography. *Nature Nanotechnology* **2007,** *2*, 145-155.

[4] Chung, S. W.; Ginger, D. S.; Morales, M. W.; Zhang, Z. F.; Chandrasekhar, V.; Ratner, M. A.; Mirkin, C. A., Top-Down Meets Bottom-Up: Dip-Pen Nanolithography and DNA-Directed Assembly of Nanoscale Electrical Circuits. *Small* **2005,** *1*, 64-69.

[5] Lim, J. H.; Ginger, D. S.; Lee, K. B.; Heo, J.; Nam, J. M.; Mirkin, C. A., Direct-Write Dip-Pen Nanolithography of Proteins on Modified Silicon Oxide Surfaces. *Angewandte Chemie-International Edition* **2003,** *42*, 2309-2312.

[6] Lyuksyutov, S. F.; Vaia, R. A.; Paramonov, P. B.; Juhl, S.; Waterhouse, L.; Ralich, R. M.; Sigalov, G.; Sancaktar, E., Electrostatic Nanolithography in Polymers Using Atomic Force Microscopy. *Nature Materials* **2003,** *2*, 468-472.

[7] Vettiger, P.; Despont, M.; Drechsler, U.; Durig, U.; Haberle, W.; Lutwyche, M. I.; Rothuizen, H. E.; Stutz, R.; Widmer, R.; Binnig, G. K., The "Millipede" - More Than One Thousand Tips for Future Afm Data Storage. *Ibm Journal of Research and Development* **2000,** *44*, 323-340.

[8] Vettiger, P.; Cross, G.; Despont, M.; Drechsler, U.; Durig, U.; Gotsmann, B.; Haberle, W.; Lantz, M. A.; Rothuizen, H. E.; Stutz, R.; Binnig, G. K., The "Millipede" - Nanotechnology Entering Data Storage. *Ieee Transactions on Nanotechnology* **2002,** *1*, 39-55.

[9] Eleftheriou, E.; Antonakopoulos, T.; Binnig, G. K.; Cherubini, G.; Despont, M.; Dholakia, A.; Durig, U.; Lantz, M. A.; Pozidis, H.; Rothuizen, H. E.; Vettiger, P., Millipede - a Mems-Based Scanning-Probe Data-Storage System. *IEEE Transactions on Magnetics* **2003,** *39*, 938-945.

[10] Terris, B. D.; Thomson, T., Nanofabricated and Self-Assembled Magnetic Structures as Data Storage Media. *Journal of Physics D-Applied Physics* **2005,** *38*, R199-R222.

[11] Lieber, C. M.; Liu, J.; Sheehan, P. E., Understanding and Manipulating Inorganic Materials with Scanning Probe Microscopes. *Angewandte Chemie-International Edition in English* **1996,** *35*, 687-704.

[12] Nelson, B. A.; King, W. P.; Laracuente, A. R.; Sheehan, P. E.; Whitman, L. J., Direct Deposition of Continuous Metal Nanostructures by Thermal Dip-Pen Nanolithography. *Applied Physics Letters* **2006,** *88*, 033104.

[13] Sheehan, P. E.; Whitman, L. J.; King, W. P.; Nelson, B. A., Nanoscale Deposition of Solid Inks Via Thermal Dip Pen Nanolithography. *Applied Physics Letters* **2004,** *85*, 1589-1591.

[14] Bottomley, L. A., Scanning Probe Microscopy. *Analytical Chemistry* **1998,** *70*, 425r-475r.

[15] Nyffenegger, R. M.; Penner, R. M., Nanometer-Scale Surface Modification Using the Scanning Probe Microscope: Progress since 1991. *Chemical Reviews* **1997,** *97*, 1195-1230.

[16] Poggi, M. A.; Gadsby, E. D.; Bottomley, L. A.; King, W. P.; Oroudjev, E.; Hansma, H., Scanning Probe Microscopy. *Analytical Chemistry* **2004,** *76*, 3429-3443.

[17] Garcia, R.; Martinez, R. V.; Martinez, J., Nano-Chemistry and Scanning Probe Nanolithographies. *Chemical Society Reviews* **2006,** *35*, 29-38.

[18] Piner, R. D.; Zhu, J.; Xu, F.; Hong, S. H.; Mirkin, C. A., "Dip-Pen" Nanolithography. *Science* **1999,** *283*, 661-663.

[19] Lyuksyutov, S. F.; Paramonov, P. B.; Juhl, S.; Vaia, R. A., Amplitude-Modulated Electrostatic Nanolithography in Polymers Based on Atomic Force Microscopy. *Applied Physics Letters* **2003,** *83*, 4405-4407.

[20] Sohn, L. L.; Willett, R. L., Fabrication of Nanostructures Using Atomic-Force-Microscope-Based Lithography. *Applied Physics Letters* **1995,** *67*, 1552-1554.

[21] Hu, S.; Hamidi, A.; Altmeyer, S.; Koster, T.; Spangenberg, B.; Kurz, H., Fabrication of Silicon and Metal Nanowires and Dots Using Mechanical Atomic Force Lithography. *Journal of Vacuum Science & Technology B* **1998,** *16*, 2822-2824.

[22] Xie, X. N.; Chung, H. J.; Sow, C. H.; Wee, A. T. S., Nanoscale Materials Patterning and Engineering by Atomic Force Microscopy Nanolithography. *Materials Science & Engineering R-Reports* **2006,** *54*, 1-48.

[23] Szoszkiewicz, R.; Okada, T.; Jones, S. C.; Li, T. D.; King, W. P.; Marder, S. R.; Riedo, E., High-Speed, Sub-15 Nm Feature Size Thermochemical Nanolithography. *Nano Letters* **2007,** *7*, 1064-1069.

[24] Wang, D. B.; Szoszkiewicz, R.; Lucas, M.; Riedo, E.; Okada, T.; Jones, S. C.; Marder, S. R.; Lee, J.; King, W. P., Local Wettability Modification by Thermochemical Nanolithography with Write-Read-Overwrite Capability. *Applied Physics Letters* **2007,** *91*, -.

[25] Carroll, K. M.; Giordano, A. J.; Wang, D.; Kodali, V. K.; Scrimgeour, J.; King, W. P.; Marder, S. R.; Riedo, E.; Curtis, J. E., Fabricating Nanoscale Chemical Gradients with Thermochemical Nanolithography. *Langmuir* **2013,** *29*, 8675-8682.

[26] Carroll, K. M.; Lu, X.; Kim, S.; Gao, Y.; Kim, H.-J.; Somnath, S.; Polloni, L.; Sordan, R.; King, W. P.; Curtis, J. E.; Riedo, E., Parallelization of Thermochemical Nanolithography. *Nanoscale* **2014,** *6*, 1299-1304.

[27] King, W. P.; Goodson, K. E., Thermomechanical Formation of Nanoscale Polymer Indents with a Heated Silicon Tip. *Journal of Heat Transfer-Transactions of the Asme* **2007,** *129*, 1600-1604.

[28] Fresco, Z. M.; Suez, I.; Backer, S. A.; Frechet, J. M. J., Afm-Induced Amine Deprotection: Triggering Localized Bond Cleavage by Application of Tip/Substrate Voltage Bias for the Surface Self-Assembly of Nanosized Dendritic Objects. *Journal of the American Chemical Society* **2004,** *126*, 8374-8375.

[29] Birr, C.; Stahnke, G.; Lang, P.; Lochinge.W, Alpha,Alpha-Dimethyl-3,5-Dimethoxybenzyloxycarbonyl (Ddz) Residue, an N-Protecting Group Labile toward Weak Acids and Irradiation. *Annalen Der Chemie-Justus Liebig* **1972,** *763*, 162-172.

[30] Cameron, J. F.; Frechet, J. M. J., Base Catalysis in Imaging Materials. 1. Design and Synthesis of Novel Light-Sensitive Urethanes as Photoprecursors of Amines. *The Journal of Organic Chemistry* **1990,** *55*, 5919-5922.

[31] Jennane, J.; Boutros, T.; Giasson, R., Photolithography of Self-Assembled Monolayers: Optimization of Protecting Groups by an Electroanalytical Method. *Canadian Journal of Chemistry-Revue Canadienne De Chimie* **1996,** *74*, 2509-2517.

[32] Dyer, E.; Wright, G. C., Thermal Degradation of Alkyl N-Phenylcarbamates. *Journal of the American Chemical Society* **1959,** *81*, 2138-2143.

[33] Kovyazin, V. A.; Nikitin, A. V.; Kopylov, V. M.; Sokol'skaya, I. B., Reaction of Organosilicon Amines with Dicarboxylic Anhydrides. *Russian Journal of General Chemistry* **2003,** *73*, 1072-1076.

[34] Dyer, E.; Newborn, G. E., Thermal Degradation of Carbamates of Methylenebis-(4-Phenyl Isocyanate). *Journal of the American Chemical Society* **1958,** *80*, 5495-5498.

[35] Dyer, E.; Read, R. E., Thermal Degradation of O-1-Hexadecyl N-1-Naphthylcarbamates and Related Compounds. *Journal of Organic Chemistry* **1961,** *26*, 4388-&.

[36] Lau, S. Y. W.; Hughes, G.; O'Shea, P. D.; Davies, I. W., Magnesiation of Electron-Rich Aryl Bromides and Their Use in Nickel-Catalyzed Cross-Coupling Reactions. *Organic Letters* **2007,** *9*, 2239-2242.

APPENDIX B

COVERAGE ANALYSIS – DETERMINATION OF CORRECTION FACTOR FOR EXPERIMENTAL DATA

As discussed in Chapter 3, when conducting XPS analysis, the X-rays penetrate far deeper than the actual information depth, and in order to obtain quantitative data, this analysis depth (which follows e^{-x}) must be taken into account since it causes signal attenuation with increasing depth. Approximately 95 % of the signal in XPS originates from within a distance of 3 inelastic mean free paths from the surface (3λ).[1-2] Graphically, it is possible to observe that 95 % of the signal intensity originates from within a distance of 3λ from the surface as shown in Figure B.1.

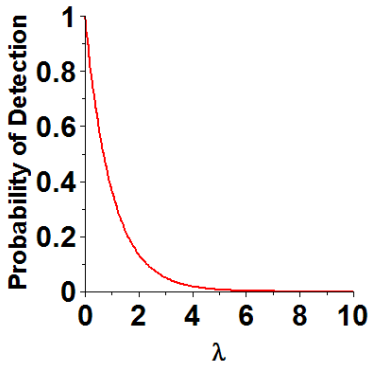

Figure B.1 Graph showing the probability of detection of an electron in XPS analysis as a function of analysis depth in units of inelastic mean free paths (λ).

The inelastic mean free path is the distance an electron can travel in a given medium before losing energy. In order to better understand where this generalization comes from; take the generic case where there is an ITO substrate being analyzed by XPS. The signal

intensity from the substrate, $I_{\text{substrate}}$, will decay with increasing depth. This signal decay of detected electrons originating from a depth *t* in the substrate is expressed as[1]

$$I^{t}_{\text{decay}} = I^{\infty}_{\text{substrate}} e^{-\left(\frac{t}{\lambda(E_{\text{substrate}})\cdot\cos\theta}\right)} \qquad \text{Equation B.1}$$

where $I^{\infty}_{\text{substrate}}$is the signal intensity that would be present had no signal decay occurred, I^{t}_{decay} is then the experimentally detected signal that intrinsically has scattering and signal decay, *t* is the distance from the surface, $\lambda(E_{\text{substrate}})$ is the inelastic mean free path at the kinetic energy for the substrate peak of interest (in this case the In 3d line), and $\cos\theta$ is the angle of analysis relative to the surface normal. If a takeoff angle of 0° is used, the expression in Equation B.1 can be simplified to

$$I^{t}_{decay} = I^{\infty}_{\text{substrate}} e^{-\left(\frac{t}{\lambda}\right)}. \qquad \text{Equation B.2}$$

Alternatively, if there is no decay present then this case would be represented as

$$I^{\infty}_{no\ decay} = I^{\infty}_{\text{substrate}}. \qquad \text{Equation B.3}$$

If both Equation B.2 and Equation B.3 are evaluated over a distance (*t*) of 0 to 3λ this means that

$$I^{t}_{decay} = \lambda \cdot I^{\infty}_{\text{substrate}} \left[-e^{-\left(\frac{t}{\lambda}\right)}\right]\Big|_{t=0}^{t=3\lambda} \qquad \text{Equation B.4}$$

$$I^{t}_{decay} = \lambda \cdot I^{\infty}_{\text{substrate}} \left[-e^{\left(-\frac{3\lambda}{\lambda}\right)} + e^{\left(\frac{0}{\lambda}\right)}\right] \qquad \text{Equation B.5}$$

$$I^{t}_{decay} = I^{\infty}_{\text{substrate}}(0.9502\lambda) \qquad \text{Equation B.6}$$

and analogously

$$I^{\infty}_{no\ decay} = I^{\infty}_{\text{substrate}}(3\lambda). \qquad \text{Equation B.7}$$

Equation B.6 shows that, indeed, 95 % of the signal originates from within a distance of 3λ from the surface. This information can then be used to obtain a correction factor as

shown in Equation B.8 for the ratio of an instance where no decay takes place to that where experimental decay is observed, thereby removing the effect of signal decay from experimental data.

$$\frac{I^{\infty}_{no\ decay}}{I^{t}_{decay}} = \frac{I^{\infty}_{\text{substrate}}(3\lambda)}{I^{\infty}_{\text{substrate}}(0.9502\lambda)} = 3.16 \qquad \text{Equation B.8}$$

This ratio of no decay to the case where decay occurs is thus $\frac{3\lambda}{0.95\lambda} = 3.16$. Graphically, this is represented in Figure B.2 and can be thought of as the ratio of the area from the rectangle 1 × 3λ (where no decay occurs, bounded by the dashed blue rectangle) to the area bounded by the exponential decay that experimentally occurs (the area underneath the red curve). Thus, in order to bring experimental data in line with an instance where no signal decay occurs, the experimental data must be multiplied by a factor of 3.16. This correction factor was subsequently used in 3.7in order to bring experimentally determined F/In atomic ratios (which have signal decay) in line with the same atomic ratio as determined from a theoretically modelled slab of ITO (where no signal decay exists).

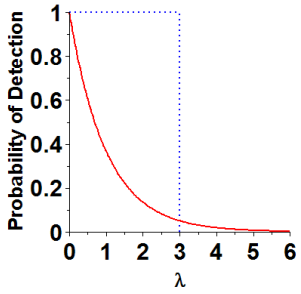

Figure B.2 Graphical representation for the origin of the correction factor to account for signal attenuation in experimental XPS data. The red curve is the same signal decay shown in Figure B.1 and the dotted blue line is the ideal case where no attenuation occurs. The ratio of these two areas provides the desired correction factor.

B.1 References

[1] Briggs, D.; Seah, P., *Practical Surface Analysis: Auger and X-Ray Photoelectron Spectroscopy*. Wiley: 1990.

[2] Seah, M. P.; Dench, W. A., Quantitative Electron Spectroscopy of Surfaces: A Standard Data Base for Electron Inelastic Mean Free Paths in Solids. *Surface and Interface Analysis* **1979,** *1*, 2-11.